2011

Ultraviolet Spectroscopic Analysis of the Binary Star System U Cephei

Peter Robert Tupa
Lehigh University

Ultraviolet Spectroscopic Analysis of the Binary Star System U Cephei

by

Peter Robert Tupa

A Dissertation
Presented to the Graduate Committee
of Lehigh University
in Candidacy for the Degree of
Doctor of Philosophy
in
Physics

Lehigh University
August 2011

Approved and recommended for acceptance as a dissertation in partial fulfillment of the requirements for the degree of Doctor of Philosophy.

Peter Robert Tupa
Ultraviolet Spectroscopic Analysis of the Binary Star System U Cephei

---

Date

Gary G. DeLeo, Dissertation Director, Chair

Accepted Date

Committee Members

A. Peet Hickman

John P. Huennekens

George E. McCluskey, Jr

Lawrence V. Snyder, Outside Member

Acknowledgements

First and foremost, I would like to thank my advisor, Professor Gary G. DeLeo for taking me on as graduate student, sharing his knowledge and aiding me on the journey to completing my doctorate. He has helped me develop professionally and provided much illumination on subjects I had not encountered before. His infectious good humor and sage wisdom have seen me through even the most trying and uncertain of times.

I would also most emphatically like to thank the Physics Department of Lehigh University for supporting my graduate studies through the Teaching Assistantship these past six years.

Professor George E. McCluskey, Jr. is owed a debt of gratitude for his advice and extensive knowledge on the subject of binary stars and always letting me know if I was on the right track.

In addition to Professors DeLeo and McCluskey, I would also like to thank the rest of my committee members: Professor A. Peet Hickman, Professor John P. Huennekens, and Professor Lawerence V. Snyder. They have endured many long meetings, but have always offered helpful and guiding commentary as I have progressed through my work. I would also especially like to thank Professor Huennekens for attending my committee meetings even before officially becoming a committee member, and Professor Snyder for his patience, while the rest of my committee and I descended into deep technical specificities outside of his realm of expertise.

I would like to acknowledge Professor Jerome Licini for his help in the development of my teaching career. Allowing the freedom to explore different teaching methods, as well as trusting me with teaching some of his lectures, have ultimately made me a better educator.

I would like to extend my deep appreciation to my family for their constant encouragement for all these years. I especially would like to thank my parents, Robert and Terry Tupa, for having faith in me and allowing me to leave the traditional school systems, teach myself and pursue my love of learning. It was a huge risk at the time, but the rewards have been so much greater than I could have imagined.

I share a special bond with the friends and colleagues I have met over the years at Lehigh. Even through the most stressful times of our studies, their constant shenanigans would lift my spirits. I will keep the memories our adventures together with me always.

To my daughters, Katharine and Abigail, their coming into my life has brought a joy that I never knew was possible before. And of course, this dissertation would not have been possible if not for my best friend and wife, Hisako. Her steadfast patience and encouragements have kept me going when times were down, and lifted me even higher when things were up.

I am lucky to have met so many wonderful and interesting people over these many years, and owe them all a debt of gratitude. Thank you all.

Contents

List of Tables

List of Figures

Abstract

Spectra from the International Ultraviolet Explorer (IUE) taken in September 1989 for over one full orbital period of U Cephei (U Cep, HD 5796) is analyzed.

A full and self consistent derivation is presented of the equations used to model various profile shapes, blending, and broadening mechanisms. The derivations cover such phenomena as the "intrinsic" absorption profile shape (including the contributions of natural broadening, collisional broadening, thermal broadening, and microturbulent broadening) and "extrinsic" macro-scale broadening processes (stellar rotational broadening, macroturbulent broadening, and differential rotation). A program is developed to simulate these absorption line profiles for both photospheric and gas stream absorption contributions.

The TLUSTY and SYNSPEC stellar atmospheric simulation programs are used to generate synthetic spectra to which U Cep continuum levels are normalized. Absorption lines attributed to the photosphere are divided out to isolate mass flow and accretion spectra. A radial velocity curve is constructed for conspicuous gas stream features, and shows evidence for a transient flow during secondary eclipse with outward velocities ranging between 200 and 350 km/s, and a number density of about $(8 \pm 2) \times 10^9 cm^{-3}$. The validity of C IV 1548 & 1550 and Si IV 1393 & 1402 lines are re-examined in the context of extreme rotational blending effects. A G-star to B-star mass transfer rate of $1 \times 10^{-9} M_{\odot}$/yr is calculated as an approximate upper limit, and a model of the system is presented.

Chapter 1

Introduction

The knowledge of the universe is locked within a ray of light. Almost everything that humanity has learned about existence beyond the shores of our planet was gained from the study of electromagnetic radiation, whether it was Kepler analyzing the motion of the planets or the Hubble space telescope staring deeply at the galaxies beyond our own. Most of the visible light from outside of our solar system comes from stars. This dissertation endeavors to add to the vast body of scientific knowledge on this topic.

It has been estimated that roughly half of the stars we observe are actually gravitationally bound as *binary* or *multiple* systems [19]. These are uniquely suited for astrophysical study, as their interactions with each other lead to subtle changes in their radiated light and allow for us to measure and analyze their physical properties. This dissertation concentrates on a specific subset of binary stars, the Algols. Algol type binaries are in a short term stage (relative to astrophysical time scales) of active mass transfer. Algols are typically higher mass stars with short orbital periods and a hot primary star.

Work on Algol type binaries at Lehigh University has had a long and storied development over the years. Professors George McCluskey and Gary DeLeo have overseen several graduate students through the doctoral process and many more undergraduate researchers. Over the years, the group's body of knowledge has grown and evolved

with new expertise and analytical tools. The group has specialized in the use of images taken by the International Ultraviolet Explorer (IUE) satellite, that flew from 1978 until 1996. The IUE satellite was one of the most prolific scientific instruments ever launched, both in terms of amount of data taken and the number of papers based on that data. Much of the spectral data is archived in a public access data base, and has yet to be fully analyzed. IUE has taken over 100 images of the target star of this dissertation alone.

This dissertation focuses on one particular Algol-type binary, U Cephei (U Cep) (HD 5796, α(J2000): $1^h2^m18.35^s$, δ: $+81°52'32.12''$). U Cep was among the first Algol systems discovered over 100 years ago. The system consists of a main sequence B7/8 V primary star and a G5/8 III-IV sub giant. The two companions orbit about a common center of mass every 2.49 days [2]. This system is of particular interest because it is amongst the most active Algols, and it is known to cycle through periods of extremely active mass exchange and times of relative quiescence.

This dissertation contains a detailed treatment of the atomic and astrophysical equations needed to describe such a system accurately, and we have endeavored to do this using a transparent and consistent nomenclature, which is often lacking in common sources.

This study also builds on previous works with new approaches to improve upon the data analysis techniques [2, 6, 8–12, 17, 18, 20–38]. The primary star of U Cep has an extremely fast equatorial rotational velocity, which serves to depress the apparent continuum of the spectra. A technique was developed to account for this fact and avoid undervaluing the continuum levels. It was also discovered that the effects of the high rotation can serve to blend absorption lines together in such a way as to create a pseudo line. Previous studies may have mis-identified these pseudo lines as features that would require temperatures far exceeding what is actually present in the system. This dissertation presents an argument that these ions may not truly be present (see, for example, reference [30]).

In addition to reporting a continuum spectrum for the ultraviolet region, we extract photospheric rotational velocities as a function of binary phase and estimate the number densities of various photospheric ionic species. Most importantly, we identify and characterize gas flow features as they move from the highly evolved G star toward the B star, and perhaps out of the binary system altogether.

This project endeavors to analyze an extremely complicated system and develop as accurate a model as possible, based on the data at hand. The early chapters lay the solid groundwork for a unique spectral line synthesis program and other techniques that can be expanded later on for future works.

Chapter 2

Background

2.1 Stellar Formation and Evolution

Stars begin their formation with the coalescence of large collections of dust and gas, where the gas is composed mainly of giant molecular clouds of hydrogen. Local dense pockets of gas and debris will attract more matter via gravitation, and eventually form a denser proto-stellar object. As the mass of this object increases, more and more gravitational pressure is exerted on the inner regions and core, increasing the central temperature. This process will continue until the pressure raises the temperature to the ignition point of hydrogen fusion. The outward thermal pressure of the fusion reactions will bring about an equilibration with the gravitational forces, halting any further contraction at this time. Once this process has settled, then the star is officially on the main sequence, or in the period of its lifetime during which it primarily burns hydrogen at its core [4].

After some time, the core will exhaust its hydrogen fuel and fusion will diminish, allowing the gravitational contraction to resume. As the pressure and temperature again begin to increase, the outer shell layers will initiate their burning of hydrogen as core burning ceases. Helium, the main ash (i.e., product) left from the hydrogen burning which has steadily accumulated at the core, will continue to contract, producing increasing pressure and temperature. Due to shell burning, the outer envelope will expand outward and cool. Additional energy transport via convection between

the deep interior and the upper atmosphere will further cause the star to expand outward. The energy produced by the star is spread out over a larger surface area and consequently lowers the average surface temperature, shifting its spectra more toward the red [4]. Thus the star has entered its red giant phase.

Depending on the star's initial mass, it could follow one of several paths [4]. The star may continue in the giant phase, eventually reaching sufficient conditions for helium core burning. Once the core of helium has been depleted, heavier elements will serve as the central fuel, but each new cycle of heavier elements will last for shorter and shorter periods. Stars with much higher initial masses may continue far along the core burning sequence up until iron, beyond which they cannot progress. Once the iron has been accumulated in the core and other elements have been depleted, the star will not be able to fend off the gravitational pressure and the core will undergo a catastrophic collapse, leading to a supernova explosion and the formation of either a neutron star or a black hole. Low mass stars will not progress very far along that cycle, the sequence ending long before iron is reached. At the end of the sequence, instead of a supernova, they will eject much of their outer layers and condense into a white dwarf. White dwarfs consist mainly of electron-degenerate matter and radiate light predominately via stored thermal energy.

The initial mass greatly dictates how a star will appear and evolve over time. The more massive a star, the greater the pressure and temperature in the core. The higher temperature will cause the star to burn through its hydrogen much faster, and exhibit a greater luminosity. Table 2.1 lists the relationship between a star's mass and how quickly it will burn itself off the main sequence.

Stars can be sorted into *spectral types* determined by their luminosity, temperature, and chemical composition. The *Hertzsprung-Russell* (HR) *Diagram* is commonly used to map out these various relations. Figure 2.1 shows a typical example of such a plot. Along the bottom axis is a log scale of average stellar surface temperature descending to the right, and the vertical axis is a log scale of the luminosity of the object. Hydrogen-burning stars of various masses plotted on these graphs will form a

Spectral Type	Mass ($M_\odot$)	Temperature (K)	Lifetime (yrs)
O5	40	38000	1 Million
B0	18	30000	7.3 Million
B5	6.5	16400	93 Million
A0	3.2	10800	550 Million
A5	2.1	8620	1.6 Billion
F0	1.7	7240	2.7 Billion
F5	1.29	6540	5.3 Billion
G0	1.1	6000	8 Billion
G2	1	5920	10 Billion
G5	0.93	5610	12 Billion
K0	0.78	5150	19 Billion
K5	0.69	4640	25 Billion
M0	0.47	3920	66 Billion
M5	0.21	3120	500 Billion

Table 2.1: Relation of main sequence mass to temperature and lifetime. Table adapted from [1]

continuous line, called the main sequence, starting from low mass stars on the lower right and leading to very high mass stars to the upper left. Along the top of the the graph are the main sequence spectral type labels (O,B,A,F,G,K,M,L, and T), placed to correspond with the average surface temperature of those stars. Numbers, ranging from 0 to 9, attached to the spectral type indicate the gradation, in tenths, within a certain spectral designation, where 0 is the hotter and 9 the cooler of the range. White dwarfs, stars that have reached the final stage of evolution, occupy a diffuse region to the lower left. Due to their small radiating surface area they appear in the less luminous portion of the HR diagram. Stars which are in the interim giant stage of evolution populate the upper right region of the diagram. In general, their outer atmospheric envelopes are cooler and less dense than those of the stars on the main sequence, but their expanded size greatly increases the radiating surface area and consequently places them high on the luminosity scale. Additionally, a suffix can be added to a star's spectral type label to indicate its *luminosity class*. The numeral 0 indicates a hyper-giant, I is a super-giant, II is a bright giant, III is a normal giant, IV is a subgiant, V indicates a main sequence star, VI is a subdwarf, and VII is a white dwarf. For example, the primary in U Cep is estimated to be a B7/8 V star, or a B spectral type main sequence star in the cooler 7 to 8 range. The secondary is

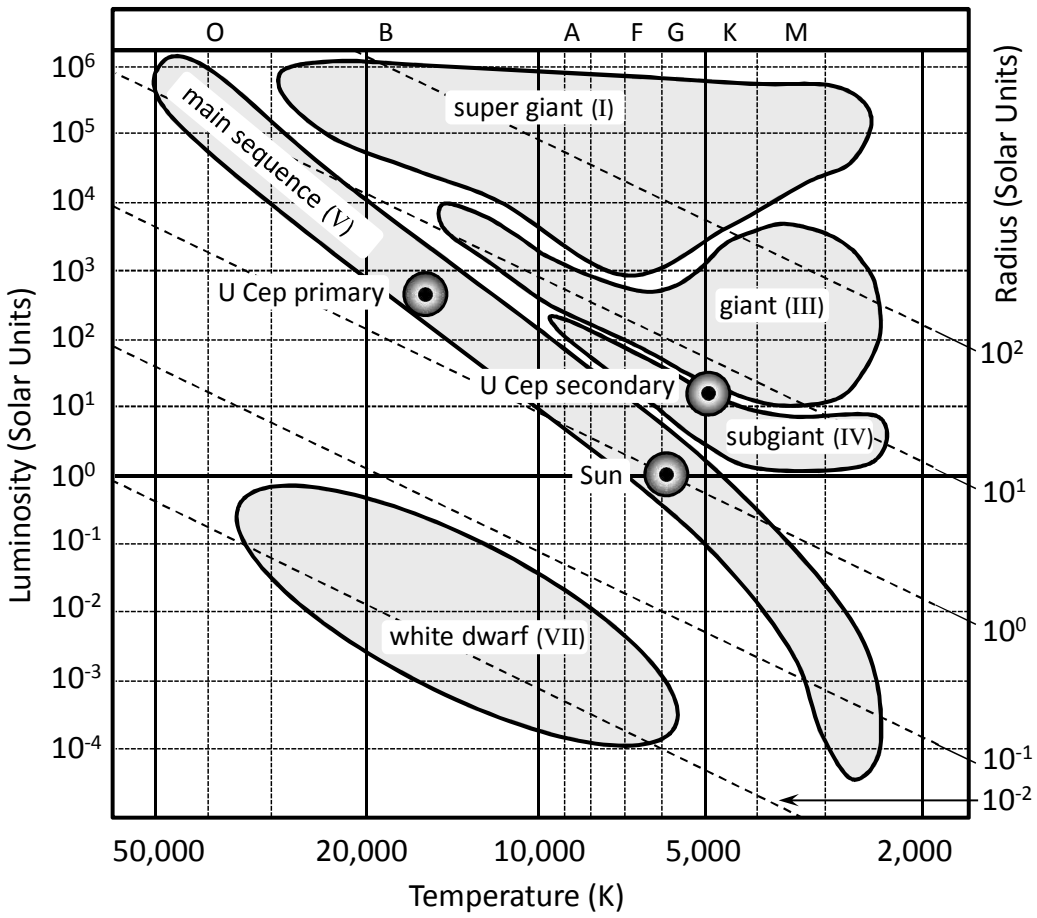

Figure 2.1: Hertzsprung-Russell Diagram.

a G5/8 III-IV, or a G type giant-subgiant in the mid to cool range of that spectral type.

2.2 Blackbody Radiation and Ultraviolet Light

In this section we will explore some of the basic characteristics of the light we observe, and motivate our choice to use ultraviolet wavelengths to explore U Cep. All heated matter radiates electromagnetic energy. Typically, a star's radiative spectrum can be modeled as a black body radiator, as shown in figure 2.2. As the object gets hotter, it will radiate over a wider range of wavelengths and, as Wien's Law states, its peak energy emission will move to shorter and shorter wavelengths. The distribution of

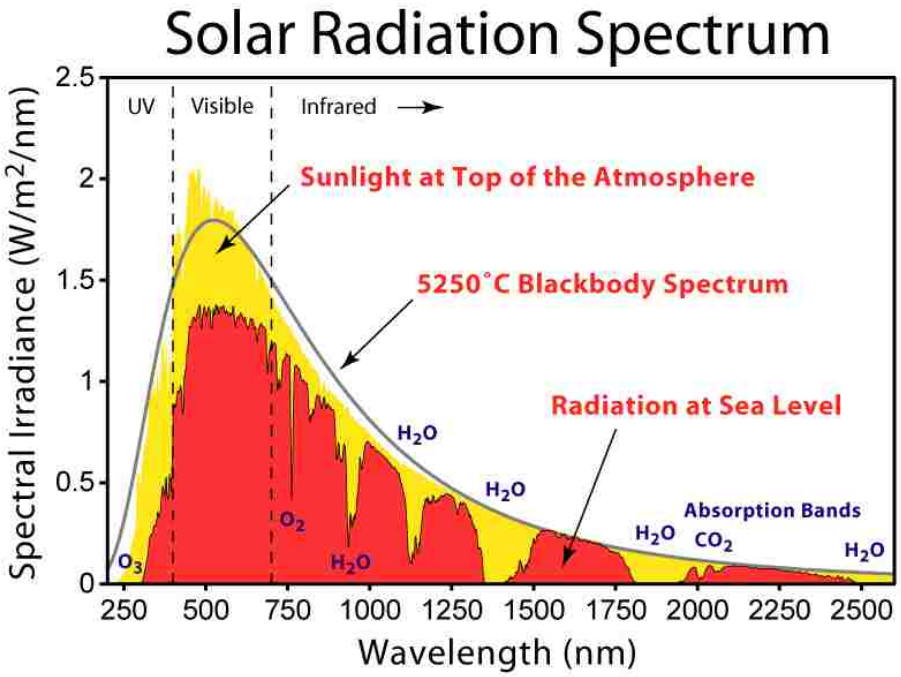

Figure 2.2: Black body curve compared with solar spectra obtained above the Earth's atmosphere and at sea level. [3]

radiation intensity is given by Planck's Law and illustrated in figure 2.3. The formal expression is

$$I_\lambda(T) = \frac{2hc^2}{\lambda^5} \frac{1}{e^{\frac{hc}{\lambda kt}} - 1}, \tag{2.1}$$

where h is Planck's constant, c is the speed of light, k is Boltzmann's constant, and λ is the wavelength.

It should be noted that the black body curve is only an approximation. The actual spectrum will be distorted by variations in the depth of the stellar atmosphere that allow views through various temperature regions, as well as by contamination by multitudinous absorption lines and bound-free transitions. Figure 2.3 illustrates the Planck distribution curves for three different temperatures. Note that the object at 13,000 K dominates the graph. Such is the case with most Algols, where the primary main sequence star is an O or B spectral type that has an average surface temperature anywhere from 10,000 to 20,000 K. The secondary sub giant star usually has an average surface temperature around 5,000 K. U Cep's primary is a B7/8 V star

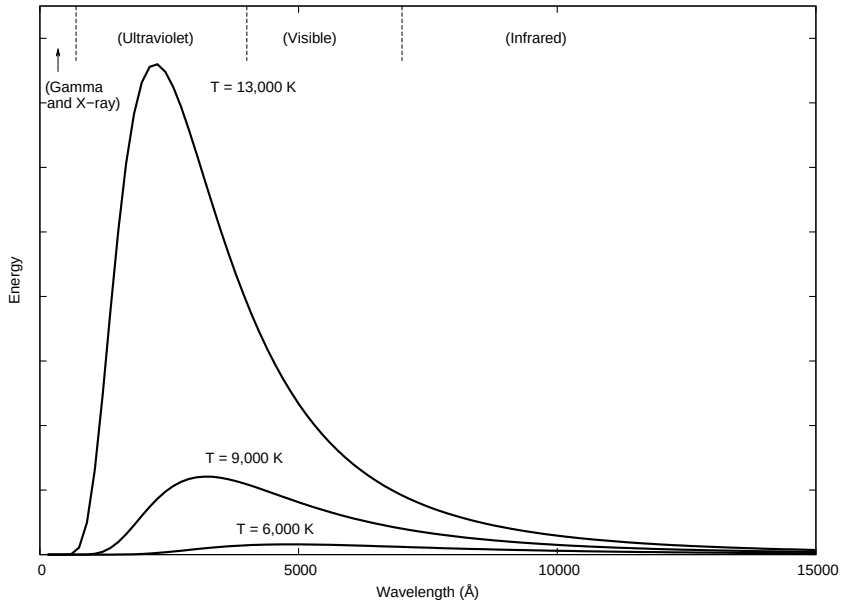

Figure 2.3: Sample blackbody curves. At higher temperatures, the peak is shifted to shorter wavelengths. Note that the 13,000 K curve dominates in the ultraviolet region.

with a surface temperature estimated between 11,250 K and 13,000 K. Its secondary is a G5/8 III-IV star with a surface temperature around 5,000 K [2]. We can use this fact to our advantage in the analysis of Algol type binaries. Many studies have been done on these types of binaries in the visible spectrum, particularly with light curve analysis to determine the physical parameters of the systems, i.e. period, masses, stellar radii, and distances. Binary star observations have to take into account the fact that some portion of the light comes from each star. But as one moves to shorter wavelengths, the secondary radiates very little compared to the primary. In effect, we can 'filter' out the light of the cooler star and choose to view only the contributions of the hotter primary by observing in the ultraviolet portion of the spectrum.

Unfortunately, ground based observation of UV light is difficult. The Earth's atmosphere has selective windows through which visible, some infrared and radio radiation can pass, but it is opaque to other wavelengths. Figure 2.4 shows the bands of light that can reach the Earth's surface. To get at the inaccessible regions of the spectrum, we need to move above the atmosphere and use satellites.

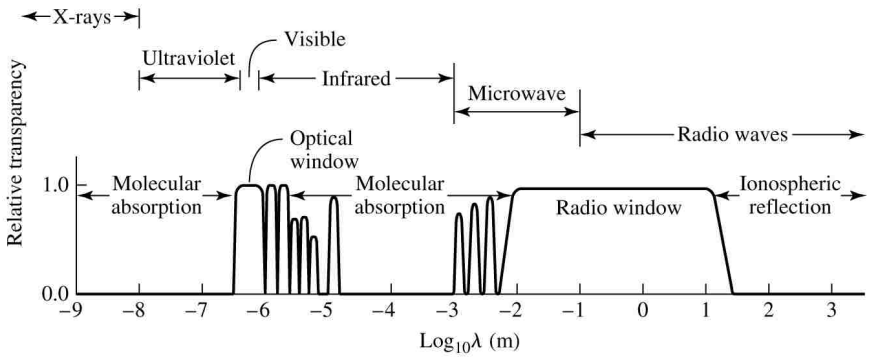

Figure 2.4: Spectral windows of Earth's atmosphere. Peaks describe ranges in the electromagnetic spectrum that can penetrate to the surface of the planet. CARROLL, BRADLEY W.; OSTLIE, DALE A., INTRODUCTION TO MODERN ASTROPHYSICS, 2nd Edition, ©2007. Reprinted by permission of Pearson Education, Inc., Upper Saddle River, NJ [4]

2.3 Binary Stars

2.3.1 Overview

It may be the case that not only one, but two or more stars may form in close proximity and be gravitationally bound to one another. Indeed, it is estimated that about one half of the observable stars in the night sky are binary or multiple star systems [19]. These stars orbit about a common center of mass, as shown in figure 2.5. As per Kepler's Laws, the shape of the star's orbit about the center of mass is an ellipse, defined by the semi major axis, a, and its eccentricity, e. Systems where the stars are close to one another will tend to circularize (i.e. $e = 0$) their orbits due to tidal interactions [39].

The orbit of a two body system is confined to a plane, but that plane can be in any orientation with respect to Earth. So a series of geometrical definitions has been employed to standardize the spatial orientations of the planes, as shown in figure 2.6. What is seen from Earth is the two dimensional projection of the orbital path on the plane of the sky, the *apparent orbit*. As per Kepler's Laws and basic trigonometry, both paths will be elliptical. The center of these ellipses will coincide, but their foci do not coincide [40]. Typically, the brighter of the two stars will be designated the

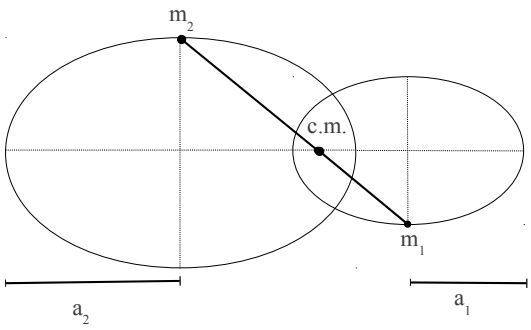

Figure 2.5: Binary Star Orbits about common center of mass

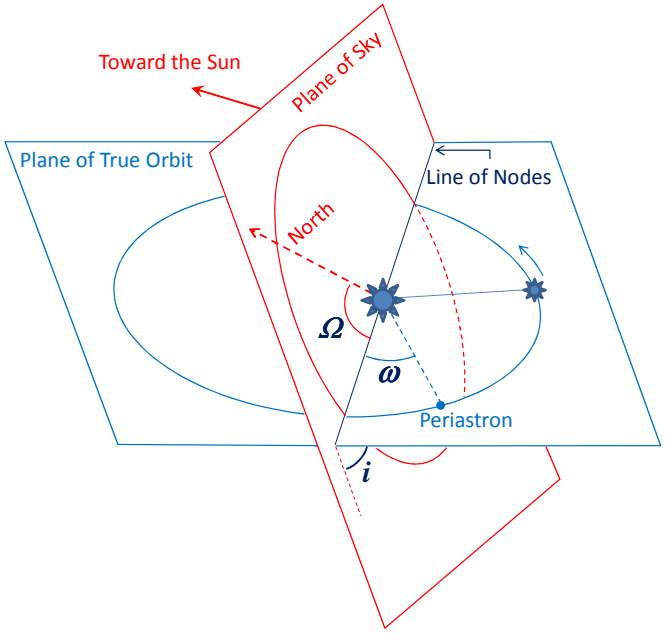

Figure 2.6: Binary Orbital Elements

primary and the fainter is called the *secondary*. We now consider the motion of the secondary with respect to the primary. For this relative orbit, the primary is located at one of the two foci of the true orbit (again, this focus does not map onto the focus of the apparent orbit), which is usually placed at the intersection of the two planes [40]. The angle between the plane of the sky and the orbital plane is the *inclination*, i. With an inclination of 0° we see a perpendicular view of the whole orbit, while an inclination of 90° gives us an edge on view. The line of nodes is the intersection of the two planes, true orbit and a plane perpendicular to the line of site [19]. Ω is the angle between the line of nodes and the direction toward the Celestial North Pole, which essentially gives the orientation of the apparent orbit in the plane of the sky. ω is the angle between the line of nodes and the position of periastron and defines the rotational orientation of the ellipse in the true orbital plane. Periastron is the point of closest approach for the two stars. Two further parameters, T, the time of periastron passage, and P, the period of orbit, complete the set of seven parameters, $a, e, i, \Omega, \omega, T$, P, allowing one to define a system's orbital path and orientation with respect to Earth.

There are many different types of observable binary systems [4]. The *optical double* is not a true binary, but merely two stars that lie along the same line of sight. A *visual binary* is a system where both companions can be optically resolved and are spatially separated, allowing for tracking of each star individually. An *astrometric binary* appears as only a single discernible star, but having an oscillatory motion that reveals the gravitational pull of its partner. In a *spectrum binary* system, the different components cannot be resolved separately, but the spectral data shows evidence of two sets of spectral lines blue- and red-shifted relative to the rest wavelength. However, the orbital motion of the stars may be so slow that the lines do not move significantly with time. Finally, a *spectroscopic binary*, while similar to a spectrum binary, can have a much shorter orbital period, thus the shift of the spectral lines will be much more apparent and oscillatory, as figure 2.7 shows.

Spectroscopic binaries can give us information about the motion of the components of a system via their Doppler shift. Since the displacement of a spectral line from its

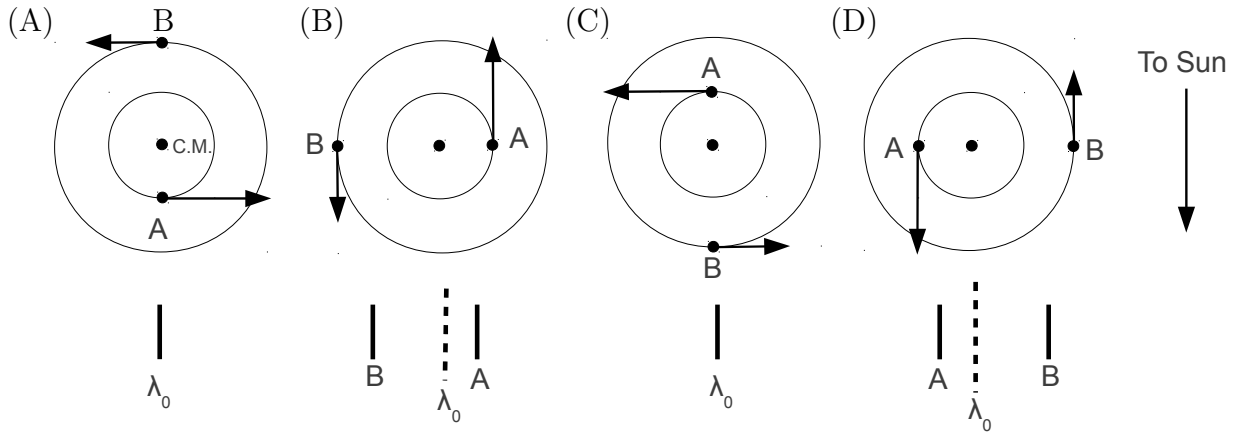

Figure 2.7: Line shifts in spectroscopic binaries. Four top down views of orbital motions relative to Earth accompanied by their relative line shift. (A) Both stars' motions are tangent to the line of sight of Earth, thus no shifting is apparent. (B) Star B approaches Earth, blue shifting its spectra to shorter wavelengths, or left of the laboratory rest wavelength. Star A recedes from Earth and redshifts its spectra to longer wavelengths to the right. (C) Again the stars move perpendicular to the line of sight of Earth and no spectral shift occurs. (D) Star A now moves towards Earth and blue shifts its spectra while star B moves away and red shifts its spectra.

laboratory rest wavelength can give us its radial velocity with respect to the observer via $v_{\text{radial}} = \frac{\Delta\lambda}{\lambda}c$, we can map out the radial velocities of the components of a binary star system over time. Figure 2.8b shows how a circular system's radial velocity plot would appear. Each star's velocity curve appears sinusoidal. The projection of the velocities depends on the inclination of the orbit as $v_{\text{radial}} = v \sin i$ [4]. Again, if we view the system perpendicularly, with $i = 0°$, we would see no radial projection towards us, and with $i = 90°$ we would see disk edge on. The inclination only affects the amplitude of the curves, not the shapes. Eccentricity, on the other hand, can have a significant impact on the velocity curve shape, as shown in figure 2.9b. U Cep has been determined to have a circular orbit, so deviations from the sinusoidal radial velocity plot can be used to discover other interesting properties of the system [34].

The Rossiter-McLaughlin effect can further skew the radial velocity curve. In cases where the inclination is between 70° and 90° and the angular separation between stars is sufficiently small, eclipsing of one star by the other will occur [4]. The Rossiter effect manifests itself when the secondary star begins its transit in front of and blocking

one quadrant of the brighter primary star. Due to the primary star's rotation, light emitted from the side rotating away from the observer will appear red shifted and light coming from the side rotating towards the observer will be blue shifted [19]. As the transit occurs, radiation from one side is blocked, causing the mean Doppler shift of the light to deviate in favor of the unblocked portion of the star. For instance, if the secondary first blocks the side of the star rotating towards the observer, blocking the blue shifted light, then spectral lines would appear slightly red shifted. And as the secondary crosses over to the side of the primary that rotates away from the observer, then the spectral lines would appear more blue shifted. A measure that is frequently used in these cases is the F value, or the ratio of measured equatorial rotational velocity to the synchronized rate based on the orbital velocity. In the case of the primary star of U Cep, the estimated equatorial rotational velocity is ~ 300 km/s, and if the system were synchronized (tidally locked) the rate would be ~ 62 km/s. Thus $F(B) = V_{\text{rot}}/V_{\text{sync}} \approx 5$. Figure 2.10 shows a simulation, created with the Binary Maker program [5], of how the Rossiter effect would appear on U Cep.

The eclipsing phenomenon will be evidenced by a dimming of the total light coming from the system as one star blocks the light of the other. Figure 2.11 demonstrates the effects of the blocked light on a light curve. Here the smaller star is the brighter companion. By convention, the brightest star is referred to as the primary. First contact occurs at point a, where the edges of both disks just touch. The total light from the system is rapidly diminished as the primary begins to pass behind the larger dimmer star, called the secondary. When the primary is fully occulted and transits behind the secondary, the only light being received comes from the secondary. This period is called primary eclipse. When the primary passes in *front* of the secondary, a portion of the secondary's contributed light is removed from the light curve. This is known as secondary eclipse. Figure 2.12 shows how a light curve would appear with only a partial eclipse. Light is diminished rapidly until the point of maximal occultation, followed by a rapid rise in luminosity as the primary disk is uncovered again. A further factor to consider is the actual shapes of the stars. One might assume a star to be spherical, but other factors such as oblateness due to rotation or the gravitational pull of a companion star can also be considered. Binary systems

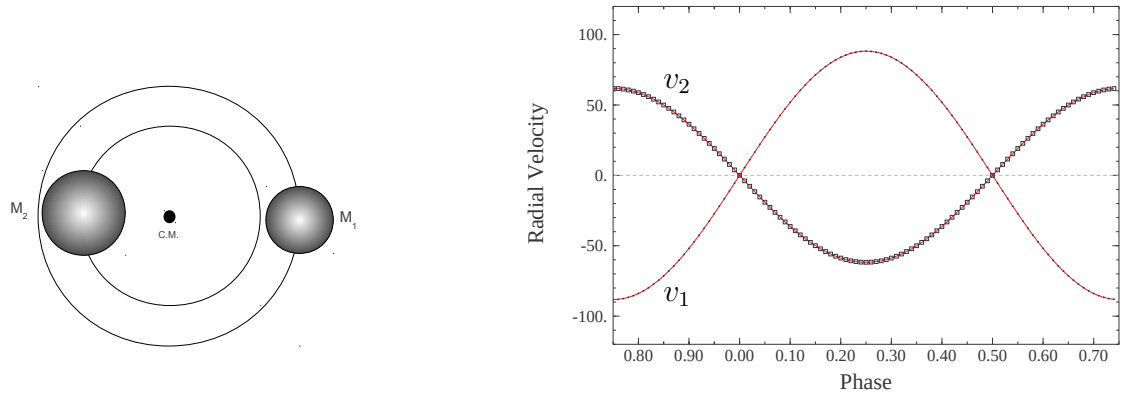

(a) Plane of Orbit **(b)** RV Curve

Figure 2.8: A simulated system where $M_1 = 1M_\odot$ and $M_2 = 2M_\odot$. (a) A top down view of the plane of the orbit. Both stars follow their respective circular orbital paths about a common center of mass. (b) The observed radial velocities for such a system. Plot generated via Binary Maker [5].

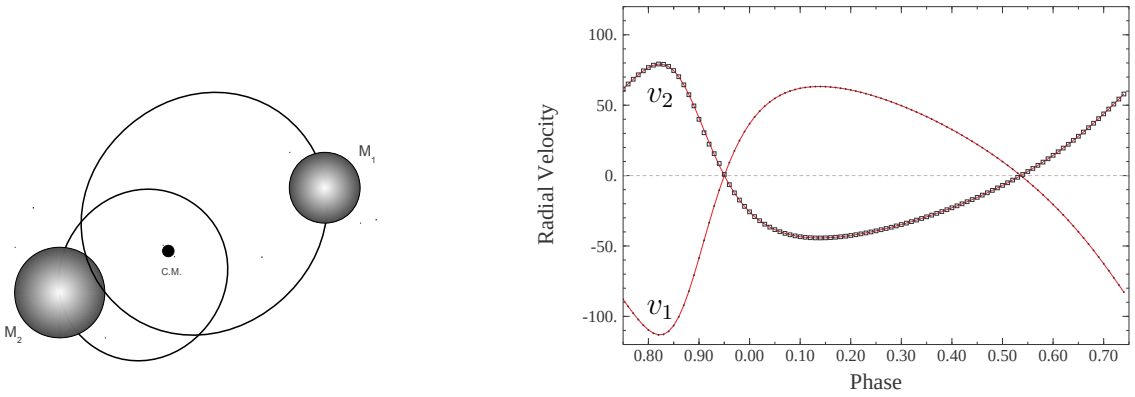

(a) Plane of Orbit **(b)** RV Curve

Figure 2.9: The same system as in figure 2.8, but with a highly eccentric orbit of $e = 0.4$ and the point of closet approach shifted 45° from observers line of sight. Plot generated via Binary Maker [5].

can be grouped into several categories based on how they affect one another. Systems with large separations relative to their stellar radii and roughly spherical shapes due to low gravitational distortions are known as *detached* systems. Systems where one of the companion stars has been distorted and increased in size past a certain critical point such that it can begin transferring mass to the other star are known as *semidetached* systems. And systems that are so close that they share a common

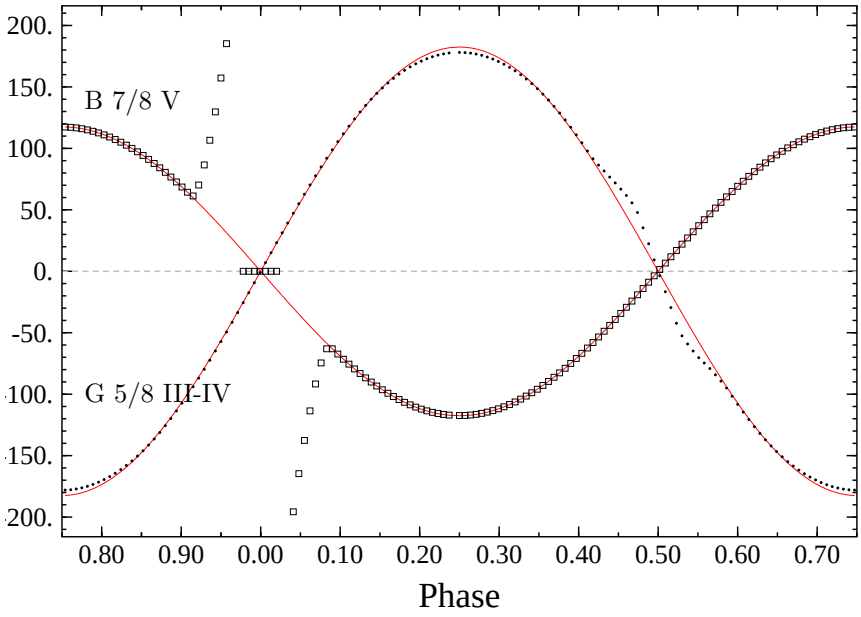

Figure 2.10: A simulation of the radial velocity curves of U Cep (dotted curves), including the Rossiter effect, using parameters found in [6]. The orbital velocity of the B7/8 V star is given as 120 km/s, while the G5/8 III-IV star is 180 km/s. Here, the B-star's simulated equatorial rotational velocity is 300 km/s. The solid curves represent actual orbital velocities. Plot generated via Binary Maker [5].

atmospheric envelope and take on the shape of a peanut are called *contact* binaries, as shown in figure 2.13 [7].

The close proximity of such massive bodies can have quite drastic effects on the local gravitational field strengths. A slowly rotating single star will have a spherically symmetric mass distribution with a gravitational field pointing radially inwards to the star with a spherical distribution. Equipotential surfaces, or surfaces of constant gravitational potential energy, will all be spherically symmetric, centered on the star. Introducing another massive body will complicate things by distorting the equipotential surfaces. Close to each star, they will have spherical equipotential surfaces, and positions far away from the center of mass of the system will show spherical surfaces encompassing both objects. The intermediate surfaces will be distorted by

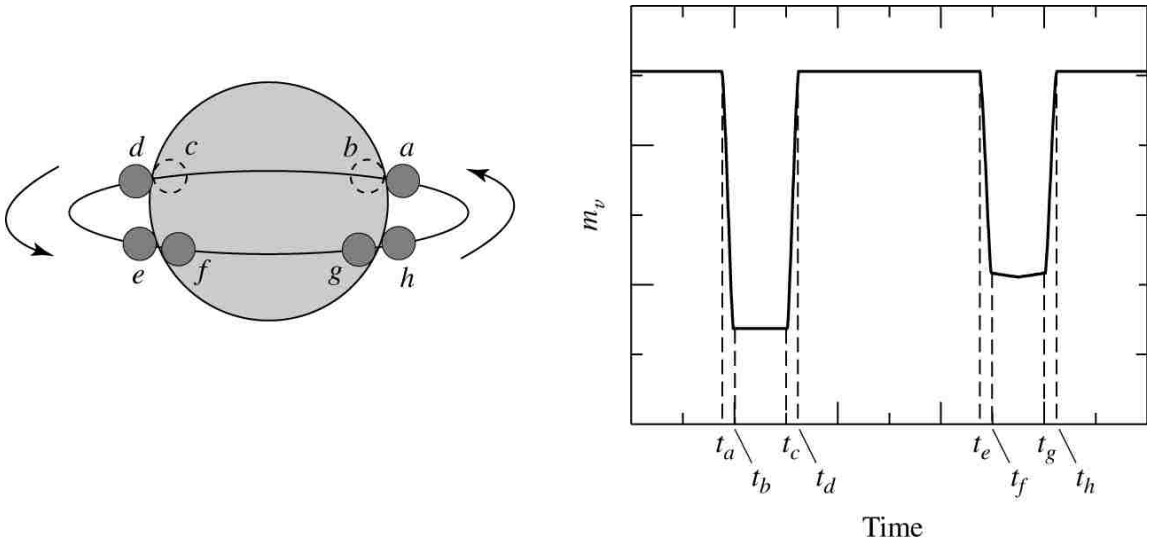

Figure 2.11: Light curve for a totally eclipsing binary. Time t_a is first contact of the smaller and brighter star moving behind the larger star. The primary is completely eclipsed from t_b until t_c. The primary emerges from eclipse during time t_c to t_d. Secondary eclipse follows accordingly from t_e until t_h. CARROLL, BRADLEY W.; OSTLIE, DALE A., INTRODUCTION TO MODERN ASTROPHYSICS, 2nd Edition, ©2007. Reprinted by permission of Pearson Education, Inc., Upper Saddle River, NJ[4]

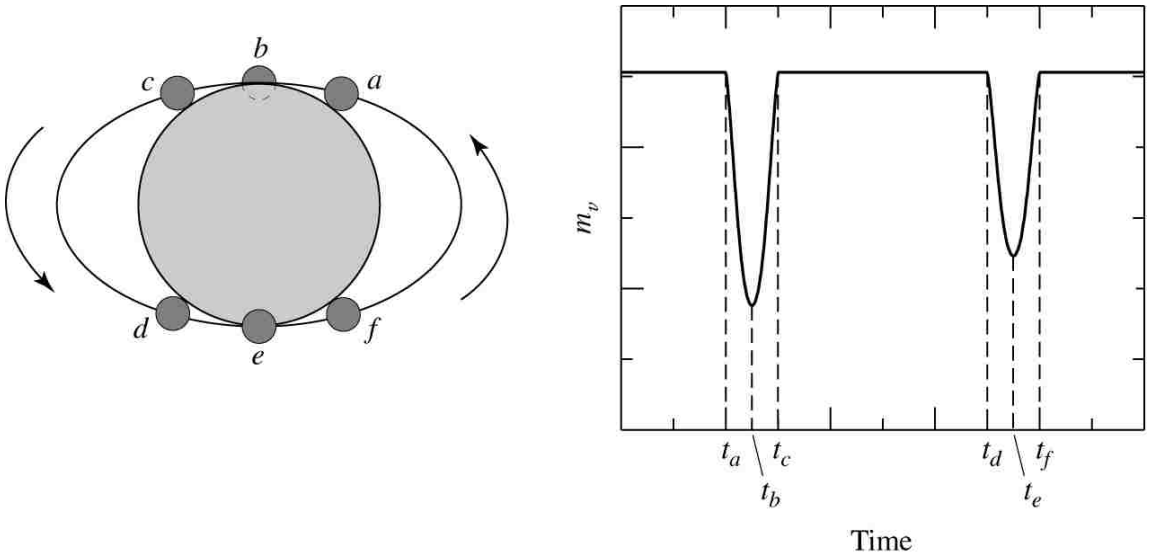

Figure 2.12: Partial eclipse light curve for a system with a non-negligible inclination. The process is similar to that in figure 2.11, except total eclipse does not occur. CARROLL, BRADLEY W.; OSTLIE, DALE A., INTRODUCTION TO MODERN ASTROPHYSICS, 2nd Edition, ©2007. Reprinted by permission of Pearson Education, Inc., Upper Saddle River, NJ [4]

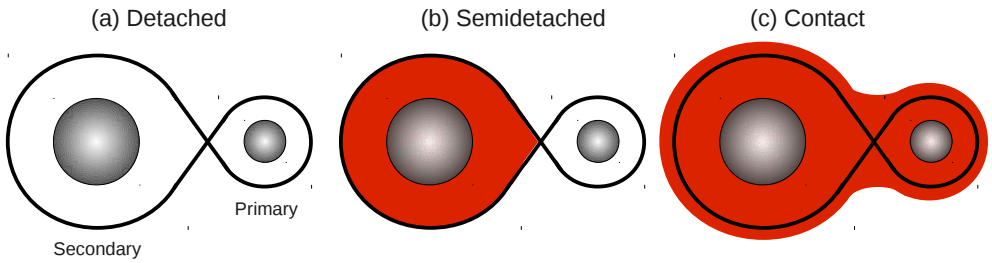

Figure 2.13: Three types of binary systems. Areas filled with gray indicate the mass distribution in each system. (a) Detached: Both stars are well within their Roche lobes. (b) Semidetached: One star completely fills its Roche lobe. (c) Contact: The two stars fill all of the Roche lobe space and consequently share a common envelope.

the competing fields, but an effective potential, Φ, can be represented by,

$$\Phi = \Phi_g + \Phi_c = -\left(\frac{GM_1}{r_1} + \frac{GM_2}{r_2}\right) - \frac{\Omega^2}{2}r^2, \tag{2.2}$$

where Φ_g is the combined gravitational term, M_1 and M_2 are the masses of the two stars, r_1 and r_2 are the distances from the stars to a point being measured, Ω is the orbital angular velocity, and Φ_c is the centrifugal term introduced to account for the fact that the system is in a rotating reference frame [41]. Figure 2.14 shows an example of an equipotential surface mapping. The points labeled L_1 through L_5 are the Lagrange points. These are places in the fields where a test particle, affected only by gravity (and, of course, the fictitious centrifugal force), could maintain a fixed position relative to the two larger bodies. But L_1, L_2, and L_3 are unstable positions since they are at local maxima in the potential field. A slight perturbation in any direction produces a force away from the point, and a test particle would be pulled along by the field to a new location or orbit. The L_4 and L_5 points are relatively stable, and allow for mass to maintain a stable orbit in these regions that lead (L_4) and follow (L_5) the secondary star, like the Trojan asteroids precede and trail Jupiter. A special surface to notice is that defined by equipotential lines encircling both stars in a figure eight shape that intersects at the inner Lagrange point, L_1 (see figures 2.13 and 2.14). This is the critical surface, called the *Roche lobe*. If a star were to expand past this surface, matter would be pulled off of it, funneled through the L_1 point, and fall onto the other companion star.

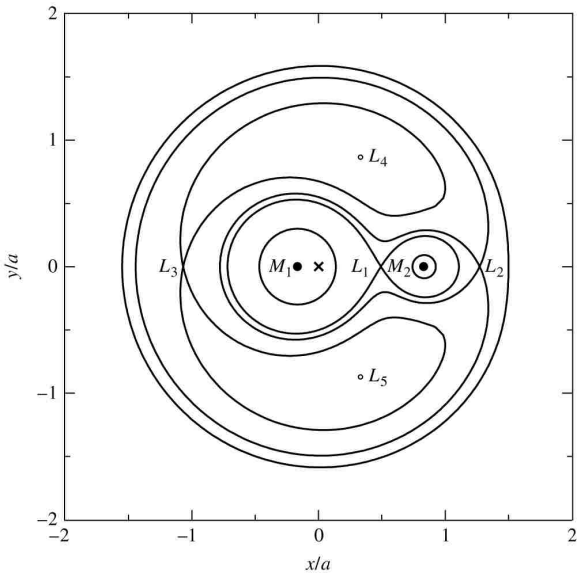

Figure 2.14: Equipotential surface map for a co-rotating binary system. Axes are given in terms of fractional semi-major axis. The center of mass is noted at the origin by "x". Immediately surrounding each star, the surfaces are circular, dominated by that star's local gravitational field. The Roche lobe surface makes a figure eight shape that encompasses both stars and meets at the L_1 point. Further out from both stars, the equipotential surface is greatly distorted into a tear drop shape that contains the "Trojan" Lagrange points, L_4 and L_5. Even further out from the binary, the equipotential again returns to a circular shape surrounding the entire system.CARROLL, BRADLEY W.; OSTLIE, DALE A., INTRODUCTION TO MODERN ASTROPHYSICS, 2nd Edition, ©2007. Reprinted by permission of Pearson Education, Inc., Upper Saddle River, NJ[4]

2.3.2 Algols

The previous section ended with a description of interacting binaries. A particular class of such binaries is called an Algol type binary system, of which U Cep is one, and they exhibit interesting characteristics. The first such star discovered to have these properties was β Persei, also known as Algol, which is where the binary class derives its name [42]. An Algol type binary is a semidetached binary with one main sequence star and another sub giant or giant phase companion. Historically, these systems displayed a unique peculiarity known as the *Algol Paradox*. We have already indicated that a star's mass dictates its rate of evolution, and it is assumed that stars in a binary system form at the same time. So naturally one would assume that in binary systems such as these, the giant phase star must be the more massive

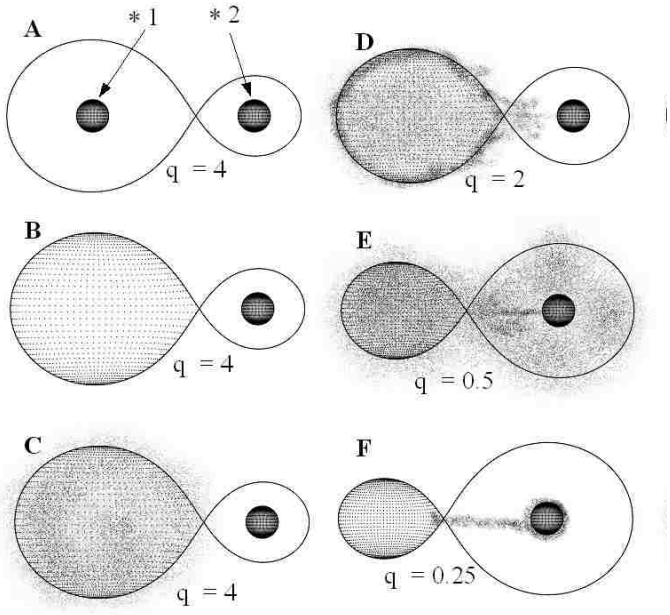

Figure 2.15: Possible sequence of Algol evolution. The mass ratio of star *1 to star *2 is given by q. (A) Detached binary system. Star *1 at this point in time is the more massive companion. (B) Star *1 evolves off the main sequence into the red giant phase and thus expands to fill its Roche lobe. (C) through (F) Active mass transfer through the inner Lagrange point onto star *2, now the primary. Note the change in Roche lobe size around both stars as the mass from star *1 is transferred to star *2. Adapted from [7].

companion, and the star still on the main sequence must be the less massive of the two. But, in many cases, the observed masses are opposite the classical understanding. The primary main sequence star *is more massive* than the more highly evolved companion star. This seemingly contradictory situation was resolved by Crawford in 1955 when he postulated that a mass reversal occurs [43]. The more advanced star was originally the more massive star, but it evolved into the sub giant phase, filled its Roche lobe and started to transfer matter onto its companion. So much matter flowed through the inner Lagrange point over time that the smaller star ended up with most of the mass in the system. Figure 2.15 illustrates the sequence of steps leading to a typical Algol system.

2.4 Previous U Cep Research

U Cep has been for centuries a star of considerable interest and posed many perplexing puzzles. Real notice was taken after Ceraski determined U Cep to be indeed a variable binary star, with a dimming of its light occurring every 2.5 days [20]. At the time, it was the seventh eclipsing binary to have been discovered [2], and it, up to that point, had the deepest drop in light (near 2 magnitudes) during the totality of primary eclipse. U Cep (HD 5796, α(J2000): $1^h2^m18.35^s$, δ: $+81°52'32.12''$) is known for being one of the more reliably active mass transferring Algol type binaries. The activity varies in intensity roughly over 9 years through violence and quiescence. Its ever changing nature has led to many revisions and refinements in the system's orbital parameters, period, structure, and even spectral class. Annie Jump Cannon originally classified the primary as a cool A0 [21]; Olson once estimated the primary to be as hot as a B 6 V [24], although the generally agreed standard is in the B7/8 V range for the primary and G5/8 III-IV for the secondary [12, 31]. Some evolution of the analysis of other parameters in the system are detailed in the sections that follow.

2.4.1 Radial Velocity Curves

The radial velocity curve can be used for the determination of mass ratios and other orbital parameters, and thus was the subject of early analyses. Carpenter in 1930 obtained a highly distorted RV curve (see figure 2.16) which led to an abnormally high eccentricity of 0.47 [8]. Struve in 1944 pointed out that this spectroscopically determined value did not agree with the well behaved light curve: a nearly symmetric total primary eclipse of 2.2 hours followed by a shallow, but well formed, secondary eclipse precisely at phase 0.5 [22]. With more observations, Struve produced another distorted RV curve and determined a lesser eccentricity of 0.2, but he also noted that absorption mediums, such as tidal bulges or gas streams, could introduce asymmetries in the absorption lines that would lead to the skewed RV plots. Later, Hardie in 1950 developed a way of correcting the systematic line asymmetries and produced a sinusoidal RV curve, as shown in figure 2.17, giving a circular orbital determination that finally resolved the long standing disparity between the photometric and spectroscopic observations. His work also highlighted a large equatorial rotational

velocity of 220 km/s [9].

Figure 2.16: Early U Cep Radial Velocity (top) and Light Curve (bottom) Plots from Carpenter 1930. Solid squares represent observational data points and circles around those points indicate the probable error. Susequent analyses indicated a more circular orbit. [8]

2.4.2 Rotational Velocity

Struve later revised Hardie's number with a combination of Rossiter affected RV-curves and a graphical extrapolation to set $v_{rot} = 300$ km/s [23]. Had the stars been tidally locked, the system's synchronized equatorial rotational velocities would be $v_{rot}(B) = 62$ km/s and $v_{rot}(G) = 100$ km/s, giving an F value for the primary of $F(B) = 5$. Even though Struve made some approximations (setting $i = 90°$ when the inclination is somewhere between 81° and 86°), this value is the generally accepted and oft quoted rotational rate. While some have made minor adjustments to the F value to better fit orbital and velocity curve solutions, only Mukherjee *et al.* actually reexamined rotational rates in Algols [34–36]. Their method of analysis used a least squares fit of a simulated absorption features to Mg II 4481 lines. They obtained an F

Figure 2.17: Corrected Radial Velocity Plot from Hardie 1950 [9].

value of 7.84, or $v_{rot} = 434$ km/s. Though, they admit that due to differential rotation and extended spun up accretion disks, their estimates may tend to be higher than that actually present in the photosphere. However, as will be shown in subsequent sections, the photosphere of U Cep is also subject to 'spinning up' and gaining angular momentum from in falling matter. The actual rotational rate, or even a profile of changing velocities, has not been satisfactorily determined yet. This dissertation has adopted the Struve estimate.

2.4.3 Changing Period

Another characteristic of U Cep, and indeed of virtually all mass transferring Algols, is the curious variability of its period. Many early observers noted periodic and abrupt changes to the times of primary minima [8]. The long term trend is a period increase. After 100 years of observation, the period has increased by roughly 20 seconds [4]. Period increases are indicative of mass transfer. The streaming matter carries with it angular momentum, taken from the donor star and given to the receiving star. In

a strictly Keplarian orbit, assuming mass and angular momentum conservation, the orbital separation will increase as well as the period. But, as detailed by Hall, there are drastic *decreases* in the period every 9 ± 4 years for U Cep [10]. Figure 2.18 shows O-C curve (Observed Minus Calculated) for the short term decreases in period over a century long trend of period increase. An O-C diagram takes the difference between observed period of orbit durations and a predicted constant period. A flat line about zero would indicate a correctly modeled and unchanging period. An incorrectly calculated period will result in an inclined straight line on the O-C graph, since the error will accumulate over time. A curved O-C line indicates a changing orbital period and the possiblity of mass exchange.

Biermann and Hall postulated that the decreases could be due to the sudden and extreme outbursts of matter that could not fully and immediately be absorbed by the gainer, and thus the angular momentum was 'stored' either in an accretion disk or spun up asynchronous equatorial material in the upper photosphere [25]. The matter integration involved two time scales: the time scale over which the mass transfer took place, τ_M (also called the dynamical time scale), and the time scale over which the angular momentum is fully reintegrated with the mass gainer, τ_J (essentially the tidal friction and turbulence that synchronizes the orbits). Equal time scales will give rise to a stable circular and synchronized orbit. When the mass transfer rate far exceeds the τ_J time scale, then there is a backlog of matter that the star cannot fully incorporate. The angular momentum of this extra material is effectively 'stored up' and removed from the consideration of the total orbital angular momentum, thus decreasing the period. The decreasing period can effectively shrink the Roche lobe of the giant star, encouraging further mass transfer. The stored angular momentum can take the form of an accretion disk structure surrounding the gainer, or increase the rotational rates of the equatorial regions in the star's photosphere. Biermann-Hall further postulated that as the sheer turbulence and various instabilities began to dominate the disk structures, frictional forces would begin to catch up with returning angular momentum to the orbit, increasing the period, and slightly expanding the Roche lobe around the donor.

The Biermann-Hall (BH) model, however, is not complete. The 1974 outburst of U Cep drew considerable attention, and as such, much detailed data was accumulated. Over the course of that decade, serveral abrupt period changes occured, but O-C curves were better modeled with linear segments, as shown in figure 2.19, rather than the parabolic curves the BH-model proposed. Olson speculated that these behaviors, and the uncharacteristic O-C curve for this time period, could be a mixture of factors in addition to the BH theory [11]. The gas stream was calculated to strike the primary star at 45° with respect to normal of the surface. The component striking the photosphere normally would serve to deliver an impulse to the star, push it away and increase the period, while the component tangential to the surface would spin up the photospheric rotation and thus store up the angular momentum (via the BH theory). Olson goes on to point out that matter leaving the system entirely would permanently remove some of the angular momentum from the system. Note that at the time of that work, Kondo and McCluskey had already shown that matter did, in fact, leave the system [28]. Additionally, the calculations would be further obfuscated by the possibility of mass distribution asymmetries in the disk structure (as shown by Piirola 1980) [29].

2.4.4 The 1974 to 1977 Outbursts

Starting in late 1974, U Cep underwent frequent and sometimes violent outbursts. The proliferation of photometrics and updated optics increased the accessibility of these events to observers, thereby allowing a significant amount of data to be recorded. Just prior to these outbursts, Batten published an exhaustive study on the system based on all the prior available data [2]. While determining the orbital and mass parameters, Batten attempted to tackle the problem of the asymmetrical eclipse light curve. In quiescent epochs, the ingress curve was marked by a shallower slope and was depressed slightly when compared to the egress curve. Figure 2.20 shows ingress and egress light curves for both quiescent and active epochs of U Cep. The most probable explanation put forward, and echoed by many authors later on, was that there was a thick stream of matter that began dimming the light, through electron scattering, in the phases leading up to first contact. At the time of his observations, U Cep was actively engaging in mass transfer (but at a steady rate), and this was assumed

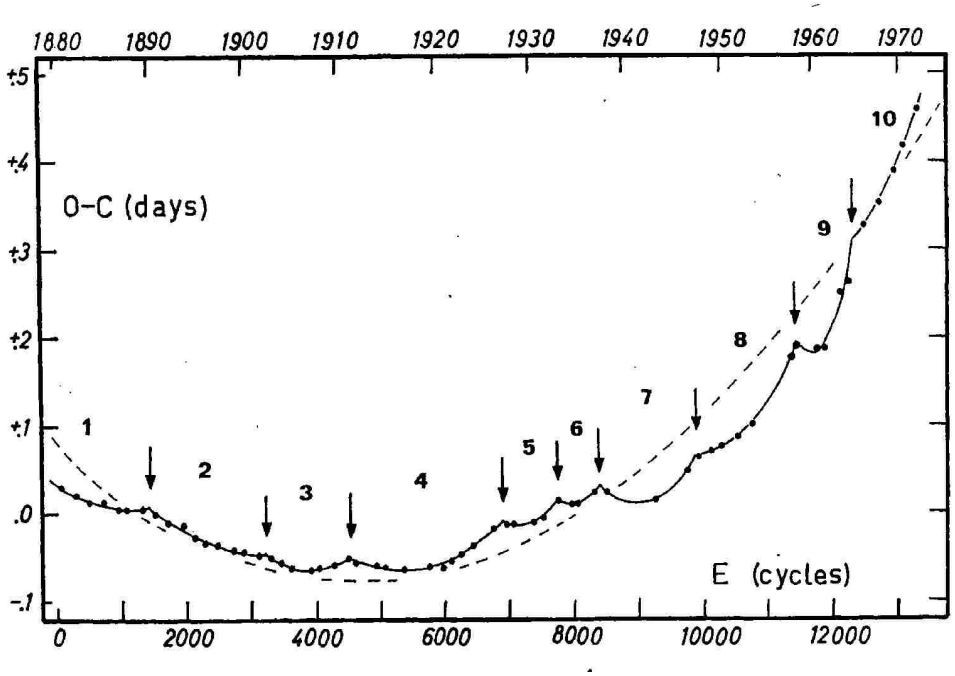

Figure 2.18: U Cep O-C period change versus epoch curve from from 1880 to 1972 [10]. Dashed parabolic line is the fit from Batten [2]. The numerous solid curves are fits of individual period decreases made by Hall. The average cycle of the period decreases is 9 ± 4 yrs.

to be a quiescent epoch, since the light curve, when out of eclipse, was relatively level.

Following the 1974 outbursts, many tried to codify the various phenomena and changes to the gas flow and accretion structure [37, 38]. Piirola used polarmetric (measuring the degree of polarization of light, possibly reflected off the accretion disk) data to determine the extent of the disk asymmetry. The disk structure of the trailing hemisphere of the B star seemed not to be confined to the orbital plane but extend quite diffusely over that hemisphere of the star [26]. The leading side of the star showed evidence for a disk structure that was confined to the orbital plane and extended further out, about 1.7 times the radius of the B star [29].

Estimates and interpretations varied considerably. Indeed the definition of what

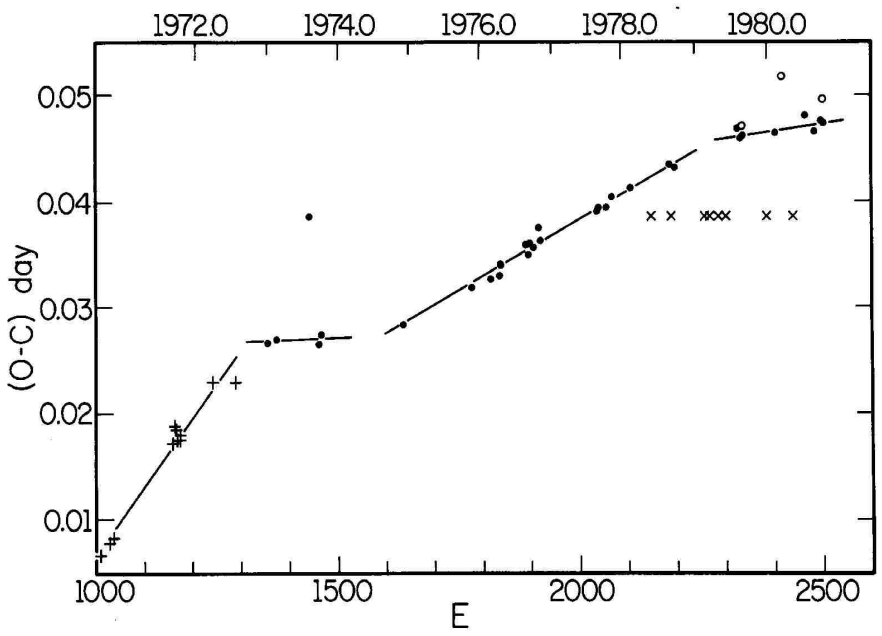

Figure 2.19: U Cep O-C period change versus epoch curve during the period of activity from 1972 until 1981. Olson noted that epochs leading to more horizontally oriented O-C segments indicated a period decrease relative to that expected for the system [11].

was meant by 'disk' changed from author to author. Different interpretations of the observations included a flat distribution of matter in the orbital plane; others interpreted disk to mean the excesses of a tidal bulge, the extended mass stream curving around the star, the effects of the spun up equatorial matter, a pseudo photosphere, or even a generic cloud that encompassed the entire system. An explanation favored by some involved the incorporation of all of these structures to explain as much of the data as possible, as we now summarize [31]. Close to the surface of the B star is a 'pseudo photosphere' that extends out approximately an additional 0.1-0.2 R_B [29] [33]. The vertical thickness seems to vary with the amount of activity U Cep is experiencing. The vertical extension of the pseudo photosphere was estimated by Olson to have ranges of 20% to 60% of the B-star's height [12] and Plavec surmised 80% [31]. During extreme cases, Piirola showed that the entire surface of the photosphere / pseudo-photosphere can swell and add an additional 15 to 20%, causing the eclipsed light curves to appear very rounded. This pseudo-photosphere contributes weakly

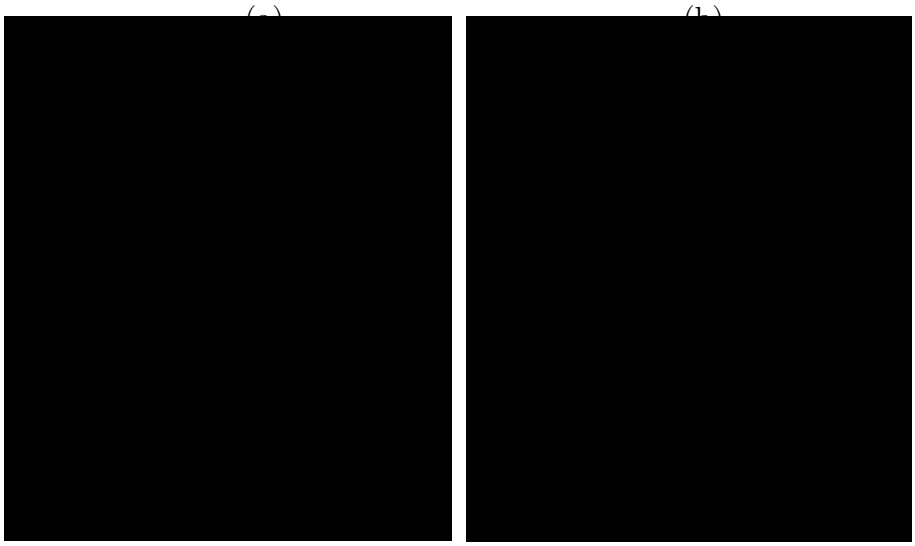

Figure 2.20: Light curves of U Cep eclipse at various stages of activity; triangles are data points taken during a period of high activity in October 1975, squares were taken during a night of moderate activity in July 1976, circles were taken over several periods of low activity. Note the totality of eclipse appears much shorter during the active period. The solid line is the averaged egress curve reflected about mid eclipse onto the ingress, indicating the amount of dimmed light prior to 2nd contact. (a) Ingress (b) Egress [12].

to the continuum, while there is an extended orbitally confined accretion disk that provides possible emission features [33]. This disk can stretch out as far as 1.7 R_B, but is highly transient. In as little as 10 observational days, this disk structure can change from showing strong emission lines to exhibiting no evidence of existence at all [27]. Kaitchuck et al. [33] and Nazarenko et al. [18] have suggested separately that the transient disk feature could be brought about by a 'splash' effect of the impacting gas stream ejecting photospheric material into an unstable orbit. Plavec estimated the disk to have an effective electron temperature of around 10,000 K and an internal turbulent velocity of approximately 100 km/s [31]. Another frequently cited feature is a small hot spot ($\sim$20,000 K) that produces a light excess and is apparent just after the gas stream has been eclipsed ($\phi = 0.965$), but right before 2nd contact [12]. This hot spot is directly attributed to the impact region of the gas stream. The gas stream itself is estimated to have an impact velocity between 620 [31] and 800 km/s [12] and has been estimated to have a variable mass transfer rate of 10^{-7} to $10^{-4} M_{\odot}$/yr.

Table 2.2: Stellar Parameters [2]

Stellar Parameters			**System Parameters**	
Parameter	**Primary**	**Secondary**	**Parameter**	**Published**
Spectral Type	B 7/8 V	G 5/8 III-IV	Period (days)	2.4928
T (K)	13,600	4,950	a ($R_\odot$)	14.7
Mass ($M_\odot$)	4.2	2.8	e	0.0
Radius ($R_\odot$)	2.9	4.7	i	83°
K (km/s)	120	180	γ (km/s)	2
			Distance (lyr)	550

Table 2.2 lists the commonly used stellar and system parameters of U Cep, derived by Batten [2]. Average photopshere temperatures for the B-star have been estimated between 11,500 K and 13,600 K. This work uses a value of 13,000 K, as it has provided the best agreement between our data and simulated spectra of TLUSTY & SYNSPEC, discussed later [44]. The value of the inclination listed in the literature also varies (82° to 88°), but we have set $i = 90°$, as is commonly done and has negligible impact on any calculations.

Chapter 3

Absorption Lines

3.1 Intensity and Flux

Some stars in the night sky appear very bright, while others are barely visible to the unaided eye. The amount of light that reaches us depends both on the distance of that star and how much light is actually emitted. In this section we will carefully lay out the various definitions describing the radiation we observe. Figure 3.1 illustrates a source of radiation and a detector. The energy per unit time, or power, $\mathrm{d}P_\nu$, at frequency ν, flows from a source element of area, $\mathrm{d}A_s$, onto the detector surface, $\mathrm{d}A_d$. The *specific intensity*, I_ν, is defined in terms of $\mathrm{d}P_\nu$ as ,

$$I_\nu = \frac{\mathrm{d}P_\nu}{\cos\theta\,\mathrm{d}A\,\mathrm{d}\Omega\,\mathrm{d}\nu}, \tag{3.1}$$

which is $\mathrm{d}P_\nu$ per unit cross-sectional area, $\cos\theta\,\mathrm{d}A$, per unit solid angle, $\mathrm{d}\Omega$, per unit frequency, $\mathrm{d}\nu$, radiated in the direction θ relative to the normal of the surface element [13]. As we shall see shortly, the terms appearing in equation (3.1) can be appropriate to either source or detector. Each of the terms can be taken to an infinitesimal limit, thus defining the specific intensity as radiated from a point source and received at a point detector. The term specific intensity is frequently shortened to merely intensity. The two terms are often used synonymously, which will be the case for the rest of this dissertation. Intensity can be recast from frequency units into wavelength units via

$$I_\nu\,\mathrm{d}\nu = I_\lambda\,\mathrm{d}\lambda. \tag{3.2}$$

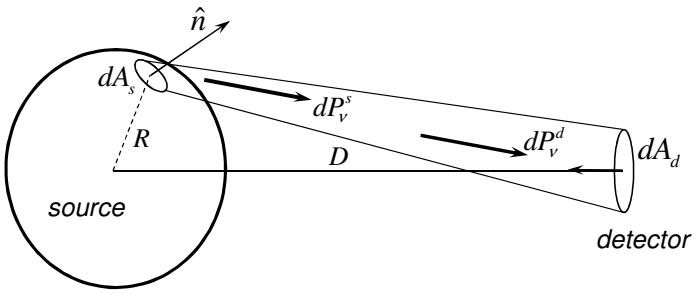

Figure 3.1: Radiation, $\mathrm{d}P_\nu^s$, emanating from surface element, $\mathrm{d}A_s$, towards a detector of area $\mathrm{d}A_d$ a distance D away. The detector receives an amount of radiation, $\mathrm{d}P_\nu^d$. $\widehat{n}$ indicates the normal vector of the surface element.

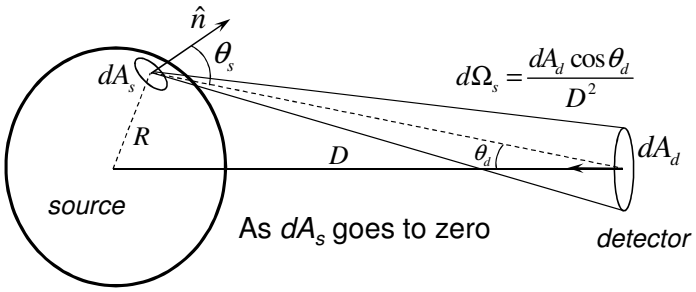

Figure 3.2: Same as figure 3.1, but with source end of channel shown as a point, thereby defining the solid angle of the detector with respect to the source.

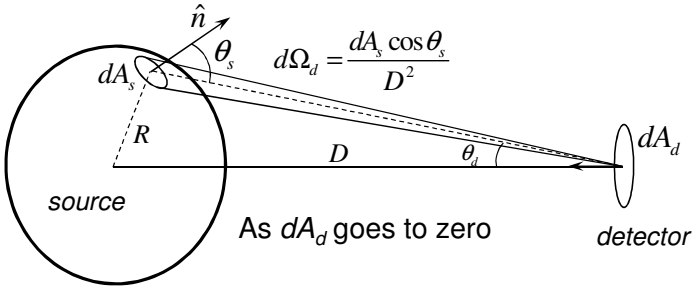

Figure 3.3: Same as figure 3.1, but with the detector end of channel shown as a point, thereby defining the solid angle of the source with respect to the detector.

The units of intensity are given as (erg s^{-1} cm^{-2} rad^{-2} Hz) and (erg s^{-1} cm^{-2} rad^{-2} Ang^{-1}) in (mostly) cgs units for I_ν and I_λ, respectively. One must be careful when converting between frequency and wavelength, since $c = \nu\lambda$ and $d\nu = -(c/\lambda^2)\, d\lambda$, where the minus sign tells us that the direction of the ν and λ coordinate systems run opposite one another. As λ increases, ν decreases and vice versa. This also translates into changes in the incremental step sizes across spectral distributions. On a plot of wavelength with a constant $\Delta\lambda$ grid spacing, a corresponding frequency plot would see a changing $\Delta\nu$ increment. To expound further on the potency of the concept of intensity, we will demonstrate the behavior of intensity at the source and how it is received at the detector. First, we will demand that the power radiated from the source along the channel shown in figure 3.1 be equal to the power collected at the detector; hence,

$$dP_\nu^s = dP_\nu^d. \tag{3.3}$$

We can rearrange equation (3.1) in terms of both the power emitted,

$$dP_\nu^s = I_\nu^s\, dA_s \cos\theta_s\, d\Omega_s\, d\nu, \tag{3.4}$$

and captured,

$$dP_\nu^d = I_\nu^d\, dA_d \cos\theta_d\, d\Omega_d\, d\nu. \tag{3.5}$$

Figure 3.2 shows how, as we shrink the radiating surface element to a point, we can obtain an expression for the solid angle of the detector as viewed from the source,

$$d\Omega_s = \frac{dA_d \cos\theta_d}{D^2}, \tag{3.6}$$

where D is the distance between source and detector. Figure 3.3 shows a similar argument for the solid angle of the source viewed from the detector,

$$d\Omega_d = \frac{dA_s \cos\theta_s}{D^2}. \tag{3.7}$$

By combining all of these expressions into equation (3.3), we find that

$$I_\nu^s\, dA_s \cos\theta_s \frac{dA_d \cos\theta_d}{D^2}\, d\nu = I_\nu^d\, dA_d \cos\theta_d \frac{dA_s \cos\theta_s}{D^2}\, d\nu. \tag{3.8}$$

Thus,

$$I_\nu^s = I_\nu^d \equiv I_\nu. \tag{3.9}$$

We have shown here that the intensity is independent of the separation distance between the source and the detector. It is essentially the energy moving along a thin ray of light.

A further quantity that we must carefully explore is the *flux*. Flux, F_ν, is the energy per unit time, per unit frequency interval flowing in all directions (though the directionality condition can be redefined) through a unit area element; hence,

$$\mathrm{d}F_\nu = \frac{\mathrm{d}P_\nu}{\mathrm{d}A\,\mathrm{d}\nu} = I_\nu \cos\theta\,\mathrm{d}\Omega, \tag{3.10}$$

or

$$F_\nu = \int I_\nu \cos\theta\,\mathrm{d}\Omega. \tag{3.11}$$

For example, let us consider the radiation of a constant specific intensity, but only outward through a source element, $\mathrm{d}A_s$. We will make the assumption that at the detector, $\cos\theta_d \approx 1$, as is most often the case in stellar astronomical situations. We will also integrate the detector area element over the visible hemisphere of the star. Aligning the normal of our detector element with the vector pointing towards the source, the area element is,

$$\mathrm{d}A_d = D^2 \sin\theta_s\,\mathrm{d}\theta_s\,\mathrm{d}\phi_s. \tag{3.12}$$

Thus the flux flowing through the source element, $\mathrm{d}A_\nu^s$, is,

$$\begin{aligned} F_\nu^s &= \int I_\nu \cos\theta_s \frac{\mathrm{d}A_d \cos\theta_d}{D^2} \\ &= I_\nu \int_0^{2\pi} \mathrm{d}\phi_s \int_0^{\pi/2} \sin\theta_s \cos\theta_s\,\mathrm{d}\theta_s \\ &= \pi I_\nu. \end{aligned} \tag{3.13}$$

Note that this result, commonly appearing in astrophysics textbooks, would be zero for a constant intensity if the integral were to include both the flux into and out of the area element (i.e. deep within a stellar atmosphere). But since we have

placed the area element at the stellar surface, only calculating the out flowing flux is appropriate. A more relevant example in the context of this work is the calculation of the flux through the detector element, $\mathrm{d}A_d$, radiated from the visible portion of the star. Assuming once again that I_ν is constant, and integrating over the hemisphere pointed toward the detector,

$$\begin{aligned} F_\nu^d &= \int I_\nu \cos\theta_d \, \mathrm{d}\Omega_d \\ &= \int I_\nu \cos\theta_d \frac{\mathrm{d}A_s \cos\theta_s}{D^2} \\ &= I_\nu \frac{1}{D^2} \int \mathrm{d}A_s \cos\theta_s \\ &= \pi R^2 I_\nu \frac{1}{D^2}. \end{aligned} \tag{3.14}$$

We have highlighted the ideas of intensity and flux to distinguish between the desired measurement and what is actually attainable. The intensity, as it is constructed, is independent of distance from the source. It is a means of describing the light emitted from each specific point on the surface of the radiating body and propagating along some direction. However, in order to measure intensity, the object must be resolvable, as is the case for our Sun. Due to its close proximity, satellites and ground based telescopes have been able to determine variations in brightness on the Sun's surface, such as sunspots and solar granulation. But for far distant objects, where the object's angular size is smaller than the resolving power of the detector, intensity cannot truly be measured. Flux, as we have defined it, sums the intensity function over the observable hemisphere of the star. We will be working with a measure of flux at the detector, though mostly in a normalized form, throughout this work.

3.2 Absorption Coefficient and Optical Depth

Among the fundamental quantities associated with spectral line analysis are the absorption coefficient, which describes the form and shape of an absorption line, and the optical depth, which relates an amount of matter to how far light can penetrate through such a medium. Figure 3.4 shows the observable disk of a radiating source,

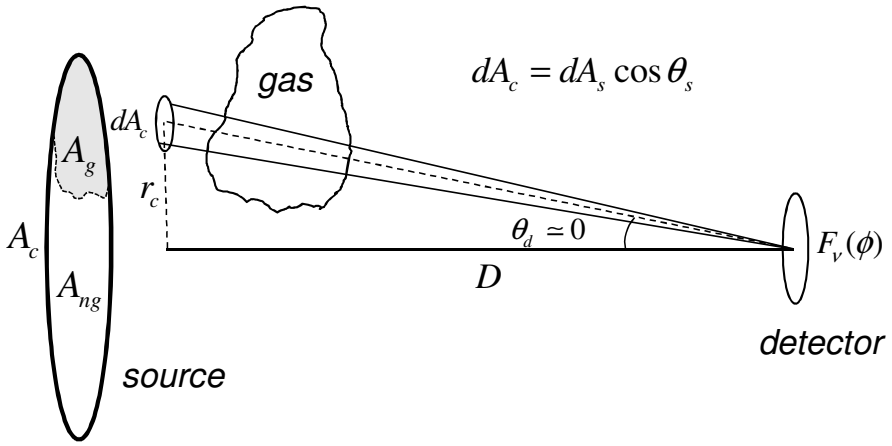

Figure 3.4: Apparent disk of radiation from source of projected area A_c. An intervening gas cloud covers an area of the disk, A_g, leaving an uncovered area, A_{ng}, $\mathrm{d}A_s$ is defined in figure 3.1.

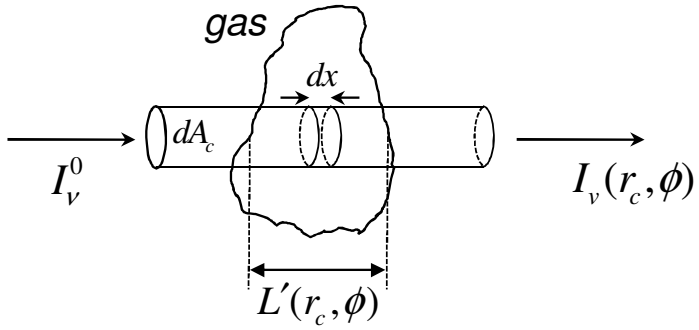

Figure 3.5: Light is extinguished as it passes through a column of an absorbing medium. The column depth is dependent on phase angle, ϕ, and disk position, r_c.

with an intervening gas cloud. The total disk area, A_c, has been divided into subsections consisting of those occulted by the gas cloud, A_g, and those not occulted, A_{ng} ("g" and "ng" refer to "gas" and "no gas", respectively). We will further define a radial vector, r_c, that describes any position on the surface of the disk. With these sectional divisions and $\mathrm{d}A_c \equiv \mathrm{d}A_s \cos\theta_s$, we can expand equation (3.14) to include the amount of light that falls on the detector from both regions as,

$$
\begin{aligned}
F_\nu(\phi) &= \frac{1}{D^2}\int I_\nu(r_c,\phi)\,\mathrm{d}A_c \\
&= \frac{1}{D^2}\int_{ng} I_\nu(r_c,\phi)\,\mathrm{d}A_c + \frac{1}{D^2}\int_{g} I_\nu(r_c,\phi)\,\mathrm{d}A_c \\
&= A_{ng} I^0_\nu \frac{1}{D^2} + \frac{1}{D^2}\int_{g} I_\nu(r_c,\phi)\,\mathrm{d}A_c, \qquad (3.15)
\end{aligned}
$$

where ϕ is the time dependent phase angle of the binary star system. Phase runs from 0 to 1 over one orbit. Since we can treat the radiated intensity as a pencil thin beam of light, let us consider a column of light passing through the intervening gas cloud, as shown in figure 3.5. We can describe this medium as an arbitrary cloud of gas with a position dependent number density $n'(x, r_c, \phi)$ (units = L^{-3}). The density of the gas may vary at any given position x, but we can define an *average* number density, $n'(r_c, \phi)$ over the full length of the cloud as,

$$
n'(r_c,\phi) \equiv \frac{1}{L'(r_c,\phi)}\int_0^{L'(r_c,\phi)} n'(x, r_c, \phi)\,\mathrm{d}x. \qquad (3.16)
$$

The total depth, $L'(r_c, \phi)$, is also phase dependent, as the cloud's morphology may change as we view it from different angles over the course of an orbital period. If we simply integrate over the length of the cloud, we can obtain the *column density* $\mathscr{N}'(r_c, \phi)$ (units = L^{-2}),

$$
\mathscr{N}'(r_c,\phi) \equiv \int_0^{L'(r_c,\phi)} n'(x, r_c, \phi)\,\mathrm{d}x = n'(r_c,\phi)L'(r_c,\phi). \qquad (3.17)
$$

In practice, the column density is obtainable from the data. Extracting the number density of the medium requires either *a priori* knowledge of the structure and dimension of the gas, or a sophisticated estimate.

Naturally, if there is a substantial number of particles between the radiation source and the detector, we would expect the light to have been dimmed during its passage through the cloud. We can express the extinction of light over an incremental distance, $\mathrm{d}x$, as

$$
\mathrm{d}I_\nu(x, r_c, \phi) = -\alpha_\nu I_\nu(x, r_c, \phi) n'(x, r_c, \phi)\,\mathrm{d}x, \qquad (3.18)
$$

where we have introduced α_ν, the *atomic optical absorption coefficient* (units = L^2), which effectively acts as an absorption cross section (Note: In many fields, the entire quantity $\alpha_\nu\ n'$, is called the absorption coefficient). The absorption coefficient is constant for a given ion species, and unique to each different electronic transition. Of course the energy is not actually destroyed during its passage through the medium, but merely redirected out of the path of observation by various mechanisms. When a photon of a sufficient frequency is incident on an atom, ionization can occur through bound-free absorption, tearing away an electron and sending it into the gas, where the photon's energy has been transfered into the electron's kinetic energy. Scattering serves to change the direction of the photon and remove it from the solid angle of observation. And finally, a photon can excite an electron to a higher energy level, but when the electron relaxes and falls back to its original state, it will re-radiate a photon. This relaxation can happen via a drop back to original state all at once, or through a series of intermediate states. But in either case, each photon is re-emitted in a random direction, most likely out of the original solid angle.

We can begin to solve for intensity as follows:

$$\frac{\mathrm{d}I_\nu(x, r_c, \phi)}{I_\nu(x, r_c, \phi)} = -\alpha_\nu n'(x, r_c, \phi)\,\mathrm{d}x, \tag{3.19}$$

$$\int_0^{L'(r_c,\phi)} \frac{\mathrm{d}I_\nu(x, r_c, \phi)}{I_\nu(x, r_c, \phi)} = -\int_0^{L'(r_c,\phi)} \alpha_\nu n'(x, r_c, \phi)\,\mathrm{d}x, \tag{3.20}$$

$$\ln \frac{I_\nu(r_c, \phi)}{I_\nu^0} = -\alpha_\nu \mathscr{N}'(r_c, \phi), \tag{3.21}$$

$$I_\nu(r_c, \phi) = I_\nu^0 e^{-\alpha_\nu \mathscr{N}'(r_c,\phi)}, \tag{3.22}$$

$$I_\nu(r_c, \phi) = I_\nu^0 e^{-\tau'_\nu(r_c,\phi)}, \tag{3.23}$$

where we have defined the *optical depth*, τ_ν, as

$$\tau'_\nu(r_c, \phi) = \int_0^{L'(r_c,\phi)} \alpha_\nu n'(x, r_c, \phi)\,\mathrm{d}x = \alpha_\nu \mathscr{N}'(r_c, \phi). \tag{3.24}$$

The optical depth is essentially a measure of the transparency of the gas. If the medium is substantially dense or if it is likely to absorb or scatter the light, then less

light can penetrate through the gas and reach the observer.

With the concepts of intensity and flux, the various density treatments of the gas and the basic properties of light extinction laid out, we can now begin a development of some of the practical applications of these quantities. We can combine equations (3.22) and (3.15) to obtain the flux in terms of $\alpha_\nu \mathscr{N}'$,

$$F_\nu(\phi) = A_{ng}(\phi) I_\nu^0 \frac{1}{D^2} + I_\nu^0 \frac{1}{D^2} \int_g e^{-\alpha_\nu \mathscr{N}'(r_c,\phi)} \, \mathrm{d}A_c \tag{3.25}$$

$$= \frac{I_\nu^0}{D^2} \left[A_{ng}(\phi) + \int_g e^{-\alpha_\nu \mathscr{N}'(r_c,\phi)} \, \mathrm{d}A_c \right]. \tag{3.26}$$

Thus far, we have been using primes to denote unaveraged quantities ($L'(r_c,\phi)$, $n'(r_c,\phi)$, $\mathscr{N}'(r_c,\phi)$, and $\tau'(r_c,\phi)$) at specific positions on the observable disk. We will now define the quantities of $L(\phi)$, $n(\phi)$, $\mathscr{N}(\phi)$ and $\tau(\phi)$ as the averages of their primed counterparts over the the area of the occulting gas cloud,

$$L(\phi) \equiv \frac{1}{A_g} \int_g L'(r_c,\phi) \, \mathrm{d}A_c, \tag{3.27}$$

$$n(\phi) \equiv \frac{1}{A_g} \int_g n'(r_c,\phi) \, \mathrm{d}A_c, \tag{3.28}$$

$$\mathscr{N}(\phi) \equiv \frac{1}{A_g} \int_g \mathscr{N}'(r_c,\phi) \, \mathrm{d}A_c, \tag{3.29}$$

$$\tau(\phi) \equiv \frac{1}{A_g} \int_g \tau'(r_c,\phi) \, \mathrm{d}A_c. \tag{3.30}$$

A further expansion of the column density shows its simple relation to the number density and the cloud depth,

$$\mathscr{N}(\phi) = \frac{1}{A_g} \int_g \mathscr{N}'(r_c,\phi) \, \mathrm{d}A_c \tag{3.31}$$

$$= \frac{1}{A_g} \int_g n'(r_c,\phi) L'(r_c,\phi) \, \mathrm{d}A_c \simeq \frac{1}{A_g} n(\phi) L(\phi) A_g \tag{3.32}$$

$$= n(\phi) L(\phi), \tag{3.33}$$

$$n(\phi) \simeq \mathscr{N}(\phi)/L(\phi). \tag{3.34}$$

Note that this can also serve as the defining relation for $\mathscr{N}(\phi)$, and using

$$\int_g e^{-\alpha_\nu \mathscr{N}'(r_c,\phi)}\, \mathrm{d}A_c \simeq A_g(\phi) e^{-\alpha_\nu \mathscr{N}(\phi)}, \tag{3.35}$$

equation (3.26) becomes,

$$F_\nu(\phi) = \frac{I_\nu^0}{D^2}\left[A_{ng}(\phi) + A_g(\phi) e^{-\alpha_\nu \mathscr{N}(\phi)}\right]. \tag{3.36}$$

Defining $\beta(\phi)$ as the fractional coverage of the intervening gas over the radiating disk,

$$A_g(\phi) = \beta(\phi) A_c, \tag{3.37}$$

and

$$A_{ng}(\phi) = (1 - \beta(\phi)) A_c, \tag{3.38}$$

the flux simplifies to

$$F_\nu(\phi) = \frac{A_c I_\nu^0}{D^2}\left[(1 - \beta(\phi)) + \beta(\phi) e^{-\alpha_\nu \mathscr{N}(\phi)}\right] \tag{3.39}$$

$$= \frac{A_c I_\nu^0}{D^2}\left[1 + \beta(\phi)(e^{-\alpha_\nu \mathscr{N}(\phi)} - 1)\right]. \tag{3.40}$$

The factor to the left of the square brackets in equation (3.40) represents the amount of flux the detector would receive had there been no intervening gas. For convenience, we refer to this factor as follows,

$$F_\nu^0 \equiv \frac{A_c I_\nu^0}{D^2}, \tag{3.41}$$

so that

$$F_\nu(\phi) = F_\nu^0\left[1 + \beta(\phi)(e^{-\alpha_\nu \mathscr{N}(\phi)} - 1)\right], \tag{3.42}$$

or,

$$F_\nu^n(\phi) = 1 + \beta(\phi)(e^{-\alpha_\nu \mathscr{N}(\phi)} - 1), \tag{3.43}$$

where $F_\nu^n(\phi)$ is normalized flux,

$$F_\nu^n(\phi) \equiv \frac{F_\nu(\phi)}{F_\nu^0(\phi)}. \tag{3.44}$$

Rewriting these in terms of the optical depth,

$$F_\nu(\phi) = F_\nu^0 \left[1 + \beta(\phi)(e^{-\tau_\nu(\phi)} - 1)\right], \tag{3.45}$$

$$F_\nu^n(\phi) = 1 + \beta(\phi)(e^{-\tau_\nu(\phi)} - 1), \tag{3.46}$$

$$\tau_\nu(\phi) = \alpha_\nu \mathscr{N}(\phi), \tag{3.47}$$

where $\tau_\nu(\phi)$ is the average optical depth across $A_g(\phi)$ (unitless). If F_ν^0 is the "continuum" flux into the detector, the line depth, $D_\nu(\phi)$ (unitless), and *equivalent width*, $W_\nu(\phi)$ (units of Hz), which will be examined more closely in a later section, are,

$$D_\nu(\phi) \equiv \frac{F_\nu^0 - F_\nu(\phi)}{F_\nu^0} \tag{3.48}$$

$$= \beta(\phi)(1 - e^{-\alpha_\nu \mathscr{N}(\phi)}) = \beta(\phi)(1 - e^{-\tau_\nu(\phi)}), \tag{3.49}$$

$$W_\nu(\phi) \equiv \int_0^\infty D_\nu(\phi)\, \mathrm{d}\nu \tag{3.50}$$

$$= \int_0^\infty \beta(\phi)(1 - e^{-\alpha_\nu \mathscr{N}(\phi)})\, \mathrm{d}\nu = \int_0^\infty \beta(\phi)(1 - e^{-\tau_\nu(\phi)})\, \mathrm{d}\nu. \tag{3.51}$$

In cases where the gas is optically thin, $\tau_\nu \ll 1$, we can make a Taylor expansion of the exponential term and obtain the following relations,

$$F_\nu(\phi) \simeq F_\nu^0[1 - \beta(\phi)\alpha_\nu \mathscr{N}(\phi)] = F_\nu^0[1 - \beta(\phi)\tau_\nu(\phi)], \tag{3.52}$$

$$D_\nu(\phi) \simeq \beta(\phi)\alpha_\nu \mathscr{N}(\phi) = \beta(\phi)\tau_\nu(\phi). \tag{3.53}$$

Now let us examine several special cases to see how the presence of the gas affects these equations. If the gas was not present at all so that $\mathscr{N}$ and τ_ν were zero, then all the initial radiation within the solid angle would reach the detector, the normalized flux would be unity, and the line depth zero.

$$\beta(\phi) = 0 \qquad F_\nu(\phi) = F_\nu^0 \qquad F_\nu^n(\phi) = 1 \qquad D_\nu(\phi) = 0 \tag{3.54}$$

If the gas covered the entire surface of the radiating disk, then all of the terms would be fully dependent on the exponential extinction terms.

$$\beta(\phi) = 1 \qquad F_\nu(\phi) = F_\nu^0 e^{-\tau_\nu(\phi)} \qquad F_\nu^n(\phi) = e^{-\tau_\nu(\phi)} \qquad D_\nu(\phi) = 1 - e^{-\tau_\nu(\phi)} \tag{3.55}$$

If if the gas is optically thin, with $\beta(\phi) = 1$, we can make the approximations,

$$F_\nu(\phi) \simeq F_\nu^0(1 - \tau_\nu(\phi)) \qquad F_\nu^n(\phi) \simeq 1 - \tau_\nu(\phi) \qquad D_\nu(\phi) \simeq \tau_\nu(\phi), \tag{3.56}$$

producing linear dependencies on optical depth. If the cloud half covered the disk, with $\beta(\phi) = 0.5$, the fluxes become,

$$F_\nu(\phi) = F_\nu^0 \left[1 + 0.5(e^{-\tau_\nu(\phi)} - 1)\right] = 0.5F_\nu^0(1 + e^{-\tau_\nu(\phi)}), \tag{3.57}$$

$$F_\nu^n(\phi) = 0.5(1 + e^{-\tau_\nu(\phi)}) \qquad D_\nu(\phi) = 0.5(1 - e^{-\tau_\nu(\phi)}). \tag{3.58}$$

In the optically thin regime we get

$$F_\nu(\phi) \simeq 0.5F_\nu^0(2 - \tau_\nu(\phi)) = F_\nu^0(1 - 0.5\tau_\nu(\phi)), \tag{3.59}$$

$$F_\nu^n(\phi) \simeq 1 - 0.5\tau_\nu(\phi) \qquad D_\nu(\phi) \simeq 0.5\tau_\nu(\phi). \tag{3.60}$$

And in the optically very thick regime, $\tau_\nu \gg 1$, we get

$$F_\nu(\phi) \simeq 0.5F_\nu^0 \qquad F_\nu^n(\phi) \simeq 0.5 \qquad D_\nu(\phi) \simeq 0.5. \tag{3.61}$$

where the intervening cloud has completely darkened one half of the disk; i.e., the portion it covers.

Since much of the actual work in astrophysics is done with respect to the wavelength of light, we will now convert the pertinent equations of this section. Recall that since wavelength is inversely proportional to frequency, the conversions are not necessarily straightforward. Any expression containing or utilizing a differential term must be handled with care.

$$F_\nu = \int I_\nu \cos\theta_d \, \mathrm{d}\Omega_d \sim I_\nu \tag{3.62}$$

$$\nu = \frac{c}{\lambda} \tag{3.63}$$

$$I_\lambda \, \mathrm{d}\lambda = I_\nu \, \mathrm{d}\nu \tag{3.64}$$

$$I_\nu = I_\lambda \left| \frac{\mathrm{d}\nu}{\mathrm{d}\lambda} \right|^{-1} \tag{3.65}$$

$$I_\nu = I_\lambda \frac{\lambda^2}{c} \tag{3.66}$$

$$F_\nu = F_\lambda \frac{\lambda^2}{c} \tag{3.67}$$

$$F_\lambda^0 = \frac{A_c I_\nu^0}{D^2} \frac{c}{\lambda^2} \tag{3.68}$$

$$F_\lambda(\phi) = F_\lambda^0 \left[1 + \beta(\phi)(e^{-\alpha_\lambda \mathscr{N}(\phi)} - 1)\right] = F_\lambda^0 \left[1 + \beta(\phi)(e^{-\tau_\lambda(\phi)} - 1)\right] \tag{3.69}$$

$$F_\lambda^n(\phi) = 1 + \beta(\phi)(e^{-\alpha_\lambda \mathscr{N}(\phi)} - 1) = 1 + \beta(\phi)(e^{-\tau_\lambda(\phi)} - 1) \tag{3.70}$$

$$D_\lambda(\phi) \equiv \frac{F_\lambda^0 - F_\lambda(\phi)}{F_\lambda^0} = \beta(\phi)(1 - e^{-\alpha_\lambda \mathscr{N}(\phi)}) = \beta(\phi)(1 - e^{-\tau_\lambda(\phi)}) \tag{3.71}$$

Before proceeding to the next section, we will make a few comments regarding $\beta(\phi)$. Distinguishing $\beta(\phi)$ from a value of unity would be difficult-to-impossible for the system we examine. In this dissertation, $\beta(\phi)$ will be set equal to one wherever numerical values are determined. However, it will be maintained through much (though not all) of the subsequent developments as an aid to future work, or work on other systems, where its determination may be possible.

3.3 Atomic Transitions and Absorption Strength

With appropriate photon energies, atoms can be stimulated into higher energy states and some time later spontaneously transition again back into lower states (see DeLeo [45], Merzbacher [46], and other quantum mechanical texts). The probability for these transitions to occur is governed by the oscillator strength, sometimes called the transition strength. If a certain transition is more likely to occur, the higher rate of excitation will cause more light to be diverted out of the solid angle of observation, and thus an absorption line would appear deeper relative to other weaker lines. The oscillator strength depends on the transition rate per atom, $\mathscr{W}_{mk}(\omega)$, from state m to state k as,

$$\mathscr{W}_{mk}(\omega) = \frac{2\pi\hbar e^2}{m^2 c^2} |A_0|^2 |\langle k|\hat{e} \cdot \overrightarrow{\bigtriangledown}|m\rangle|^2 \delta(\hbar\omega_{mk} - \hbar\omega), \tag{3.72}$$

where $\hat{e}$ is the polarization direction, ω is angular frequency, and ω_{mk} is that associated with the transition energy given by

$$\omega_{mk} \equiv \frac{E_k - E_m}{\hbar}. \tag{3.73}$$

The equivalent equation in terms of frequency is given by

$$\mathscr{W}_{mk}(\nu) = \frac{e^2}{m^2c^2}|A_0|^2|\langle k|\hat{e}\cdot\overrightarrow{\bigtriangledown}|m\rangle|^2\delta(\nu_{mk}-\nu), \tag{3.74}$$

where the transition frequency, ν_{mk}, is

$$\nu_{mk} \equiv \frac{E_k - E_m}{2\pi\hbar}, \tag{3.75}$$

and the δ-function has been converted as follows:

$$\delta(\hbar\omega_{mk} - \hbar\omega) = \delta(2\pi\hbar\nu_{mk} - 2\pi\hbar\nu) = \frac{1}{2\pi\hbar}\delta(\nu_{mk}-\nu). \tag{3.76}$$

Additionally, the vector potential is given by

$$\overrightarrow{A} = A_0\hat{e}e^{-i(\omega t - \overrightarrow{k}\cdot\overrightarrow{r})} + \text{complex conjugate}. \tag{3.77}$$

We can then find the energy per unit area per unit time (the magnitude of the Poynting vector) averaged over one period, as

$$\frac{\mathrm{d}P_\nu}{\mathrm{d}A_c} = \frac{2\pi\nu^2}{c}|A_0|^2, \tag{3.78}$$

or

$$|A_0|^2 = \frac{c}{2\pi\nu^2}\frac{\mathrm{d}P_\nu}{\mathrm{d}A_c}. \tag{3.79}$$

Recalling equation (3.1),

$$I_\nu \equiv \frac{\mathrm{d}P_\nu}{\cos\theta\,\mathrm{d}A\,\mathrm{d}\Omega\,\mathrm{d}\nu} = \frac{\mathrm{d}P_\nu}{\mathrm{d}A_c\,\mathrm{d}\Omega\,\mathrm{d}\nu} \tag{3.80}$$

or

$$\frac{\mathrm{d}P_\nu}{\mathrm{d}A_c} = I_\nu\,\mathrm{d}\Omega\,\mathrm{d}\nu. \tag{3.81}$$

Combining equations (3.79) and (3.81) we find

$$|A_0|^2 = \frac{c}{2\pi\nu^2}I_\nu\,\mathrm{d}\Omega\,\mathrm{d}\nu. \tag{3.82}$$

The transition rate per unit solid angle, per unit frequency, can be written

$$\frac{\mathscr{W}_{mk}(\nu)}{\mathrm{d}\Omega\,\mathrm{d}\nu} = \frac{e^2}{2\pi m^2 c}\frac{1}{\nu^2} I_\nu |\langle k|\hat{e}\cdot\overrightarrow{\bigtriangledown}|m\rangle|^2 \delta(\nu_{mk}-\nu). \tag{3.83}$$

We can expand the expression in the bra-ket using the well known result (see DeLeo [45], Merzbacher [46], and other quantum mechanical texts)

$$\langle k|\hat{e}\cdot\overrightarrow{\bigtriangledown}|m\rangle = \frac{-2\pi m\nu_{mk}}{\hbar}\langle k|\hat{e}\cdot\overrightarrow{r}|m\rangle. \tag{3.84}$$

Thus, using equations (3.84) and (3.83),

$$\frac{\mathscr{W}_{mk}(\nu)}{\mathrm{d}\Omega\,\mathrm{d}\nu} = \frac{2\pi e^2}{\hbar^2 c} I_\nu |\langle k|\hat{e}\cdot\overrightarrow{r}|m\rangle|^2 \delta(\nu_{mk}-\nu). \tag{3.85}$$

Or in the case of unpolarized light,

$$\mathscr{W}_\nu \equiv \frac{\mathscr{W}_{mk}^{unpol}(\nu)}{\mathrm{d}\Omega\,\mathrm{d}\nu} = \frac{2\pi e^2}{3\hbar^2 c} I_\nu |\langle k|\overrightarrow{r}|m\rangle|^2 \delta(\nu_{mk}-\nu). \tag{3.86}$$

Note that $\mathscr{W}_\nu$ is the transition rate per unit frequency per solid angle for all transitions in a band of frequencies of width $\mathrm{d}\nu$ at ν. It should not be viewed as ν dependent since line broadening has not yet been addressed. The loss of energy per unit time per unit area per unit frequency per unit solid angle at frequency ν is

$$\mathrm{d}I_\nu = -\mathscr{W}_\nu (2\pi\hbar\nu) n'(x, r_c, \phi)\,\mathrm{d}x \tag{3.87}$$

$$= -\frac{4\pi^2 e^2}{3\hbar c}\nu |\langle k|\overrightarrow{r}|m\rangle|^2 \delta(\nu_{mk}-\nu) I_\nu n'(x, r_c, \phi)\,\mathrm{d}x. \tag{3.88}$$

Comparing this to equation (3.18), we can solve for the atomic absorption coefficient,

$$\alpha_\nu = \frac{4\pi^2 e^2}{3\hbar c}\nu |\langle k|\overrightarrow{r}|m\rangle|^2 \delta(\nu_{mk}-\nu). \tag{3.89}$$

The *oscillator strength*, f, is defined as [46]

$$f \equiv \frac{2m\omega}{3\hbar}|\langle k|\overrightarrow{r}|m\rangle|^2 = \frac{4\pi m}{3\hbar}\nu|\langle k|\overrightarrow{r}|m\rangle|^2. \tag{3.90}$$

Using equation (3.90), equation (3.89) can be rewritten as

$$\alpha_\nu = \frac{\pi e^2}{mc} f \delta(\nu_{mk}-\nu). \tag{3.91}$$

Real optical absorption coefficients are broadened by various mechanisms, which are addressed next. These can be represented by replacing the Dirac delta function with a normalized line profile, $\varphi_\nu(\nu-\nu_0)$ (units=t) where ν_0 is just the transitional frequency, ν_{mk}, so that

$$\int_0^\infty \varphi_\nu(\nu-\nu_0)\,\mathrm{d}\nu = 1. \tag{3.92}$$

Equation (3.89) can now be written as a product of two important terms: the collection of constants that together represent the strength of the transition and a normalized broadening term, φ_ν, which describes the spread of the absorption function; hence,

$$\alpha_\nu = \frac{4\pi^2 e^2}{3\hbar c}\nu_0 |\langle k|\overrightarrow{r}|m\rangle|^2 \varphi_\nu(\nu-\nu_0). \tag{3.93}$$

In terms of oscillator strength, equation (3.93) becomes

$$\alpha_\nu = \frac{\pi e^2}{mc} f \varphi_\nu(\nu-\nu_0). \tag{3.94}$$

When we integrate over all wavelengths, we obtain

$$\int_0^\infty \alpha_\nu\,\mathrm{d}\nu = \frac{\pi e^2}{mc} f. \tag{3.95}$$

Note that for the thin gas approximation, the equivalent width becomes

$$W_\nu(\phi) \equiv \int_0^\infty D_\nu(\phi)\,\mathrm{d}\nu \tag{3.96}$$

$$= \int_0^\infty \beta(\phi)(1-e^{-\alpha_\nu \mathscr{N}(\phi)})\,\mathrm{d}\nu \tag{3.97}$$

$$\simeq \beta(\phi)\mathscr{N}(\phi)\int_0^\infty \alpha_\nu\,\mathrm{d}\nu \tag{3.98}$$

$$\simeq \frac{\pi e^2}{mc} f \beta(\phi)\mathscr{N}(\phi). \tag{3.99}$$

For expressions in terms of wavelength, define $\varphi_\lambda(\lambda-\lambda_0)$; hence,

$$\int_0^\infty \varphi_\lambda(\lambda-\lambda_0)\,\mathrm{d}\lambda = 1, \tag{3.100}$$

$$\varphi_\lambda(\lambda-\lambda_0)\,\mathrm{d}\lambda = \varphi_\nu(\nu-\nu_0)\,\mathrm{d}\nu, \tag{3.101}$$

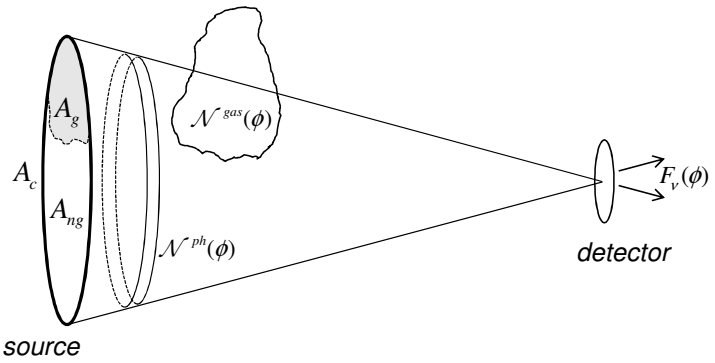

Figure 3.6: Viewable disk of radiation covered both by a photosphere and a gas cloud.

$$\varphi_\nu(\nu-\nu_0) = \varphi_\lambda(\lambda-\lambda_0)\left|\frac{\mathrm{d}\nu}{\mathrm{d}\lambda}\right|^{-1} = \varphi_\lambda(\lambda-\lambda_0)\frac{\lambda_0^2}{c}. \tag{3.102}$$

Therefore,

$$\alpha_\lambda = \frac{4\pi^2e^2}{3\hbar c}\lambda_0|\langle k|\overrightarrow{r}|m\rangle|^2\varphi_\lambda(\lambda-\lambda_0), \tag{3.103}$$

$$\alpha_\lambda = \frac{\pi e^2}{mc^2}\lambda_0^2 f\varphi_\lambda(\lambda-\lambda_0), \tag{3.104}$$

$$\int_0^\infty \alpha_\lambda\,\mathrm{d}\lambda = \frac{\pi e^2}{mc^2}\lambda_0^2 f, \tag{3.105}$$

$$W_\lambda(\phi) \equiv \int_0^\infty D_\lambda(\phi)\,\mathrm{d}\lambda = \int_0^\infty \beta(\phi)(1-e^{-\alpha_\lambda\mathcal{N}(\phi)})\,\mathrm{d}\lambda. \tag{3.106}$$

In the thin-gas approximation,

$$W_\lambda(\phi) \simeq \frac{\pi e^2}{mc^2}\lambda_0^2 f\beta(\phi)\mathcal{N}(\phi). \tag{3.107}$$

Now let us consider the previous treatment in the case where there are multiple layers of intervening gas that have unique properties. The example we explore here is the case of a gas cloud in front of a photospheric atmosphere above and spherically symmetric with the spherical radiating "surface" of the star, as shown in figure 3.6. Adapting equation (3.70) for each layer separately, we can write the flux from the normalized photosphere as

$$F_\lambda^{n,ph}(\phi) = 1+\beta^{ph}(\phi)(e^{-\tau_\lambda^{ph}(\phi)}-1) = e^{-\tau_\lambda^{ph}(\phi)}, \tag{3.108}$$

and the normalized gas as

$$F_{\lambda}^{n,gas}(\phi) = 1 + \beta^{gas}(\phi)(e^{-\tau_{\lambda}^{gas}} - 1), \tag{3.109}$$

where $\beta^{ph}(\phi) = 1$. The normalized flux appropriate to the passage through both gases is the product of the separate normalized fluxes. That is, the flux after passing through the first gas becomes the "F^0" for the second gas. Hence,

$$F_{\lambda}^{n,ph+gas}(\phi) = F_{\lambda}^{n,ph}(\phi) F_{\lambda}^{n,gas}(\phi). \tag{3.110}$$

But if we wish to examine only the contribution from the gas flow, we can divide the total flux by the photospheric contribution,

$$F_{\lambda}^{n,gas}(\phi) = F_{\lambda}^{n,ph+gas}(\phi) / F_{\lambda}^{n,ph}(\phi). \tag{3.111}$$

As we describe later, this expression enables us to distinguish the gas flow since $F_{\lambda}^{n,ph+gas}$ is determined from the data, and $F_{\lambda}^{n,ph}$ can be simulated for a given star using such modeling programs as TLUSTY and SYNSPEC [44].

Equating the right side of equation (3.109) and that of equation (3.111) gives

$$1 + \beta^{gas}(\phi)(e^{-\tau_{\lambda}^{gas}(\phi)} - 1) = F_{\lambda}^{n,ph+gas}(\phi) / F_{\lambda}^{n,ph}(\phi). \tag{3.112}$$

Solving for the optical depth and recalling that $\tau_{\nu}^{gas}(\phi) = \alpha_{\nu} \mathscr{N}(\phi)$,

$$\tau_{\lambda}^{gas}(\phi) = -\ln \left\{ \left[\frac{\left(F_{\lambda}^{n,ph+gas}(\phi) / F_{\lambda}^{n,ph} \right) - 1}{\beta^{gas}(\phi)} \right] + 1 \right\} = \alpha_{\lambda} \mathscr{N}(\phi). \tag{3.113}$$

Using the expression for α_{λ} in equation (3.104), we can now solve for the product of column density and normalized line profile,

$$\mathscr{N}(\phi)\phi_{\lambda}(\lambda - \lambda_0) = -\frac{mc^2}{\pi e^2 \lambda_0^2 f} \ln \left\{ \left[\frac{(F_{\lambda}^{n,ph+gas}(\phi) / F_{\lambda}^{n,ph}) - 1}{\beta^{gas}(\phi)} \right] + 1 \right\}. \tag{3.114}$$

If $\beta^{gas}(\phi) = 1$, this becomes

$$\mathscr{N}(\phi)\phi_{\lambda}(\lambda - \lambda_0) = \frac{mc^2}{\pi e^2 \lambda_0^2 f} \ln \left(\frac{F_{\lambda}^{n,ph}(\phi)}{F_{\lambda}^{n,ph+gas}(\phi)} \right), \tag{3.115}$$

and upon integration over λ,

$$\mathscr{N}(\phi) = \frac{mc^2}{\pi e^2 \lambda_0^2 f} \int_0^\infty \ln\left(\frac{F_\lambda^{n,ph}(\phi)}{F_\lambda^{n,ph+gas}(\phi)}\right) \mathrm{d}\lambda. \tag{3.116}$$

In cases where all of the flux broadening contributions are contained within $\phi(\lambda - \lambda_0)$, this expression provides the column density, and through

$$n(\phi) \simeq \mathscr{N}(\phi)/L(\phi), \tag{3.117}$$

an estimate of the particle number density. However, as we shall see, rotation and macroturbulant contributions must be handled differently.

3.4 Spectral-Line Broadening

3.4.1 Overview of Line Broadening

In the following sections, we will develop the mathematical formulation that determines the shape of the absorption profile, $\varphi_\lambda(\lambda - \lambda_0)$, for various broadening mechanisms. All spectral lines have a natural, or intrinsic, width which is present even for a motionless, isolated, and otherwise unperturbed atom. A spectral line is further broadened by interactions with other particles (collisional, or pressure, broadening), random thermal motions (thermal broadening), and the wholesale motion of "packets" of atoms whose dimensions are small compared with photon mean free paths (microturbulent broadening). All of these contributions, sometimes called the *intrinsic* terms, may be collected into the line profile, $\varphi_\lambda(\lambda - \lambda_0)$.

There are two additional sources of flux broadening that cannot be incorporated into the line profile. These involve macroscopic collective motions with "packet" sizes much larger than photon mean free paths. These include large scale surface convective motions (macroturbulent broadening), such as those observed on our sun as granulation, and that due to stellar rotation (rotational broadening). These are sometimes called the *extrinsic* contributions.

3.4.2 Natural Line Broadening

To develop an expression for a line profile due to natural broadening we will first consider the classical case of photons interacting with atom cores with bound electrons. The positively charged atomic cores and their negatively charged electrons can be treated as oscillating dipoles. We will treat the photons as an electromagnetic field, $\overrightarrow{E}(x,t)$, pointing (oscillating) in the y direction and propagating in the x direction, and satisfying the wave equation [47],

$$\frac{\partial^2 E}{\partial t^2} = v^2 \frac{\partial E}{\partial x^2}, \tag{3.118}$$

where E refers to the y component of vector $\overrightarrow{E}(x,t)$. Here v is the velocity of an electromagnetic wave (derived from Maxwell's equation and using Gaussian units) passing through a medium with,

$$v = \frac{c}{\sqrt{\epsilon}} = \frac{c}{n_C}, \tag{3.119}$$

where ϵ is the permitivity. With equation (3.118) extended to the complex plane, the complex index of refraction of the medium, n_C, can be expressed as

$$\sqrt{\epsilon} = n_C = n_R + i n_I = n_R - iK. \tag{3.120}$$

The solution of equation (3.118) can be written in sinusoidal complex form as

$$E(x,t) = E_0 e^{i\omega(t-x/v)} = E_0 e^{i2\pi\nu(t-xn_C/c)}. \tag{3.121}$$

We can then find the intensity of the wave by multiplying $E(x,t)$ by its complex conjugate,

$$I_\nu(x) = E^*(x,t)E(x,t) = E_0^2 e^{\frac{-i2\pi\nu x}{c}(n_C - n_C^*)} = I_0 e^{\frac{-4\pi K_\nu \nu}{c}x}, \tag{3.122}$$

where we have simplified $E_0^2 \equiv I_0$ and $(n_c - n_c^*) = -2Ki$. We also placed a subscript on K to indicate its frequency dependence. As the electromagnetic waves pass through the dipole medium, the accelerated electrons will radiate some of the energy away, decreasing the intensity over the path traveled. If we assume the region of space that the medium occupies to have an arbitrary depth of length L, the intensity becomes

$$I_\nu(L) = I_0 e^{\frac{-4\pi K_\nu \nu}{c}L}. \tag{3.123}$$

Compare this expression to the previously derived intensity extinction equation,

$$I_\nu(L) = I_0 e^{-\tau_\nu(\phi)} = I_0 e^{-\alpha_\nu \mathscr{N}(\phi)} = I_0 e^{-\alpha_\nu n(\phi) L(\phi)}, \tag{3.124}$$

recalling that τ_ν is the optical depth, α_ν is the atomic absorption coefficient, $\mathscr{N}$ is the column density, and n is the number density. We can thus equate the exponential terms of equations (3.123) and (3.124),

$$\tau_\nu = \frac{4\pi K_\nu \nu}{c} L = \alpha_\nu n L. \tag{3.125}$$

Solving for the absorption coefficient yields

$$\alpha_\nu = \frac{4\pi K_\nu \nu}{nc}. \tag{3.126}$$

Hence, we find that the absorption coefficient depends on the imaginary component of the index of refraction of the gas, which in turn depends on the permitivity, $K = -\mathrm{Im}\sqrt{\epsilon}$. This dielectric constant comes from the fact that we have the electromagnetic wave acting on our atomic dipoles and inducing charge separations. We can find ϵ by taking a ratio of the sum of the applied electric field, $E(x,t)$, and the induced field, to the applied field,

$$\epsilon = \frac{E(x,t) + 4\pi N e\, y(t)}{E(x,t)} = 1 + 4\pi N e \frac{y(t)}{E(x,t)}, \tag{3.127}$$

where e is the electron charge, N is now the number of dipoles per unit volume, and $y(t)$ is the induced dipole charge separation. Since the EM field only causes a small amplitude of displacement, we can make a Taylor expansion,

$$\sqrt{\epsilon} \simeq 1 + 2\pi N e \frac{y(t)}{E(x,t)} = n_R - iK. \tag{3.128}$$

When the electromagnetic wave interacts with the atom, it causes the electron to oscillate in the y direction . The accelerated electron radiates energy, thus damping its motion. This motivates the use of a classical damped-driven oscillator in the development of these equations (in actuality the electron only radiates energy when it is undergoing an electronic transition). Combining the acceleration, damping, and restoring force terms and setting them equal to the driving force, we obtain the damped-driven harmonic oscillator equation,

$$\frac{\mathrm{d}^2 y}{\mathrm{d}t^2} + \Gamma \frac{\mathrm{d}y}{\mathrm{d}t} + \omega_0^2 y = \frac{e}{m} E_o \exp\left(i 2\pi \nu t\right) = \frac{e}{m} E(t), \tag{3.129}$$

where Γ is the damping constant and m is the electron mass. The solution for $y(t)$ is given by,

$$y(t) = \frac{e}{m}\frac{E(t)}{\omega_0^2 - \omega^2 + i\Gamma\omega}. \tag{3.130}$$

The oscillator amplitude of the electron is a maximum when ω approaches the resonant frequency of ω_0. We now use $K = -Im(\sqrt{\epsilon})$ along with equations (3.128) and (3.130) to produce an expression for K, which can be expanded as

$$K = -\mathrm{Im}\left(1 + \frac{2\pi ne^2}{m}\ \frac{1}{\omega_0^2 - \omega^2 + i\Gamma\omega}\right) \tag{3.131}$$

$$= -\mathrm{Im}\left(1 + \frac{2\pi ne^2}{m}\ \frac{(2\omega\Delta\omega - i\Gamma\omega)}{(4\omega^2\Delta\omega^2 + \Gamma^2\omega^2)}\right) \tag{3.132}$$

$$= \frac{2\pi ne^2}{m\omega}\ \frac{\Gamma}{4\Delta\omega^2 + \Gamma^2} \tag{3.133}$$

$$= \frac{ne^2}{4m\nu}\ \frac{\Gamma/4\pi^2}{\Delta\nu^2 + (\Gamma/4\pi)^2}, \tag{3.134}$$

where $\Delta\omega \equiv \omega_0 - \omega$ and the approximation of $\omega_0^2 - \omega^2 \simeq 2\omega\Delta\omega$ was used in an intermediary step. The absorption coefficient now becomes

$$\alpha_\nu = \frac{4\pi K_\nu \nu}{nc} = \frac{\pi e^2}{mc}\ \frac{\Gamma/4\pi^2}{\Delta\nu^2 + (\Gamma/4\pi)^2}. \tag{3.135}$$

The normalized line profile function, $\varphi_\nu(\nu - \nu_0)$, therefore has the form,

$$\varphi_\nu(\nu - \nu_0) = \frac{\Gamma/4\pi^2}{\Delta\nu^2 + (\Gamma/4\pi)^2}. \tag{3.136}$$

Note that this result was derived using a classical electromagnetic treatment. If we compare this equation to the result obtained in the previous section via quantum mechanics,

$$\alpha_\nu = \frac{\pi e^2}{mc}\ f\ \varphi_\nu(\nu - \nu_0), \tag{3.137}$$

we see that the classical expression is missing the oscillator strength term. Recall that the oscillator strength was a purely quantum mechanical construction based on transition probability. In laboratory measurements on single, active-electron systems the absorption value is found to be a little less than what equation (3.135) predicts, the inclusion of the oscillator strength making up for the discrepancy. We rewrite

the absorption coefficient in terms of wavelength, since that is how the data will be utilized; hence,

$$\alpha_\lambda = \frac{\pi e^2}{mc^2}\lambda_0^2 \; f \; \varphi_\lambda(\lambda - \lambda_0). \tag{3.138}$$

In terms of wavelength, and with superscript or subscript "N" denoting "Natural", the normalized line profile and absorption coefficient appropriate to natural line broadening are, respectively,

$$\varphi_\lambda^N(\lambda - \lambda_0) = \frac{\Gamma_N \lambda_0^2/4\pi^2 c}{\Delta\lambda^2 + (\Gamma_N \lambda_0^2/4\pi c)^2} \tag{3.139}$$

and

$$\alpha_\lambda^N = \frac{\pi e^2}{mc^2} \; \lambda_0^2 \; f \; \frac{\Gamma_N \lambda_0^2/4\pi^2 c}{\Delta\lambda^2 + (\Gamma_N \lambda_0^2/4\pi c)^2}. \tag{3.140}$$

Equation (3.139) has been called by many names, such as the Cauchy curve, the Witch of Agnesi, natural profile, damping profile, or finally the Lorentzian profile [13]. It essentially gives us the dispersion profile of the absorption of a photon via bound-bound transition. These equations give the absorption profile for a single ion in the shape of a Lorentzian curve with a width determined by the Γ parameter. The damping term can be determined by considering a damped (but not driven) harmonic oscillator,

$$\frac{\mathrm{d}^2 y}{\mathrm{d}t^2} + \Gamma \frac{\mathrm{d}y}{\mathrm{d}t} + \omega_0^2 y = 0, \tag{3.141}$$

with its associated solution,

$$y(t) = y_0 e^{-\Gamma t/2} \cos\omega_0 t = y_0 e^{-\Gamma t/2} \cos 2\pi\nu_0 t. \tag{3.142}$$

The value of maximum displacement, due to the damping, decays over time,

$$y_{max}(t) \simeq y_0 e^{-\Gamma t/2}. \tag{3.143}$$

Since the resonant frequency is much greater than the damping term, $\omega_0 \gg \Gamma/2$, we can approximate y_{max} to be constant over the course of one cycle. Thus we can write the oscillation energy as

$$\mathscr{E}_{osc}(t) \simeq \frac{1}{2} m(2\pi\nu_0)^2 y_{max}(t)^2 = 2\pi^2 m\nu_0^2 y_0^2 e^{-\Gamma t}. \tag{3.144}$$

Since the oscillations are being damped out, we can find the equivalent energy lost per cycle,

$$\frac{\mathrm{d}\mathscr{E}_{osc}(t)}{\mathrm{d}t} \simeq -2\pi^2 \Gamma m\nu_0^2 y_0^2 e^{-\Gamma t}. \tag{3.145}$$

Due to energy conservation, the energy lost over time *must* equal the energy radiated away,

$$\frac{\mathrm{d}\mathscr{E}_{osc}(t)}{\mathrm{d}t} + \frac{\mathrm{d}\mathscr{E}_{rad}(t)}{\mathrm{d}t} = 0. \tag{3.146}$$

We can average over one cycle to find the power radiated (dipole radiation in the case of natural line broadening), using the well known expression

$$\frac{\mathrm{d}\mathscr{E}_{rad}(t)}{\mathrm{d}t} = \langle P(t)\rangle = \frac{2e^2\langle \ddot{y}^2(t)\rangle}{3c^3}. \tag{3.147}$$

The average of the second time derivative can be found by differentiation and averaging over one cycle,

$$\ddot{y} = y_0 e^{\Gamma t/2}\left[\left(\left(\frac{\Gamma}{2}\right)^2 - (2\pi\nu_0)^2\right)\cos 2\pi\nu_0 t + 4\pi\nu_0\frac{\Gamma}{2}\sin 2\pi\nu_0 t\right], \tag{3.148}$$

$$\langle \ddot{y}^2(t)\rangle = \frac{1}{2}y_0^2 e^{-\Gamma t}\left[\left(\frac{\Gamma}{2}\right)^2 + (2\pi\nu_0)^2\right]^2, \tag{3.149}$$

$$\langle \ddot{y}^2(t)\rangle \simeq \frac{1}{2}(2\pi\nu_0)^4 y_0^2 e^{-\Gamma t} \qquad \omega_0 \gg \Gamma/2. \tag{3.150}$$

Thus the power radiated becomes [48]

$$\frac{\mathrm{d}\mathscr{E}_{rad}(t)}{\mathrm{d}t} \simeq \frac{2e^2}{3c^3}\frac{1}{2}(2\pi\nu_0)^4 y_0^2 e^{-\Gamma t}. \tag{3.151}$$

Equating equation (3.151) with the negative of equation (3.145), we find for the natural damping terms, Γ_N,

$$\Gamma_N = \frac{8\pi^2 e^2}{3mc^3}\nu_0^2, \tag{3.152}$$

or in terms of wavelength,

$$\Gamma_N = \frac{8\pi^2 e^2}{3mc}\,\frac{1}{\lambda_0^2}. \tag{3.153}$$

Here we have derived the final form of the damping constant in the classical treatment of dipole radiation. This term governs the full width at half max of the dispersion profile of the absorption coefficient in equation (3.138). This expression can be further reduced, by evaluating all of the constants, to $\Gamma_N \simeq 0.22\lambda_0^{-2}$ with Γ in sec^{-1} and λ_0 in cm. However, again there is a slight discrepancy between this value and what can be measured in a laboratory setting. A quantum mechanical treatment of this parameter

gives improved results. An archive of these values has been computed and compiled for use in stellar atmospheric simulation programs such as SYNTHE, and TLUSTY [44]. The line absorption profile program, discussed later, utilizes these archives for the acquisition of the Γ constant. However, in cases where the value has not been provided, the classical approximation above is used.

3.4.3 Collisional Broadening

Collisional broadening, or as it is sometimes called, pressure broadening or electron damping, is a consequence of collisional interactions of atoms and other particles *during* the process of absorbing photons. In a quantum mechanical view, impact events have the effect of shifting the upper and lower energy levels of a transition, where the upper level is usually more susceptible to larger changes. The amount of distortion depends on the distance, r, between the interacting particles. There are three main types of collisions with varying degrees of strength, distinguished by the type of interacting particles, which can result in line shifts, asymmetries, and broadening. The broadening will be our main focus for this dissertation. The energy change due the collision events can be approximated with a power law relation [13, 49, 50],

$$\Delta E = \text{const.}/r^j, \tag{3.154}$$

where j depends on the type of collision. Linear Stark interactions ($j = 2$) occur when protons and electrons disturb hydrogen atoms. The Quadratic Stark interactions ($j = 4$) are dominant when various ions collide with electrons or other ions in hot stars and can broaden most absorption lines. Van der Waals interactions ($j = 6$), caused by neutral hydrogen collisions, also affect most spectral lines, but mainly dominate in cooler stars.

3.4.3.1 The Impact Approximation

Following the presentation of Emerson [50], which is based upon the original work of Lorentz [51], we can model the collisional process during a transition by imagining the atom producing essentially an infinite train of electromagnetic waves of some constant frequency, ν_0. We first consider an emission process since it is the easiest way to

visualize the collision mechanism. In a simple classical picture, the electromagnetic wave is interrupted and phase shifted by a collisional disturbance occurring at time t_0. Hence,

$$E(t) = \begin{cases} E_0 e^{i2\pi\nu_0 t} & \text{for } t \leq t_0 \\ E_0 e^{i2\pi\nu_0 t+\delta} & \text{for } t > t_0. \end{cases} \tag{3.155}$$

Fourier analysis can be used to describe this in terms of a set of monochromatic waves with

$$E(t) = \int_0^\infty E_\nu e^{i2\pi\nu t} d\nu, \tag{3.156}$$

where the Fourier amplitudes are given by

$$E_\nu = \int_0^{t_0} E(t) e^{-i2\pi\nu t} dt = \int_0^{t_0} E_0 e^{i2\pi\nu_0 t} e^{-i2\pi\nu t} dt, \tag{3.157}$$

and phase shifts (δ) lead to cancellations for $t > t_0$. Upon carrying out the integral, we find

$$E_\nu = \frac{E_0 e^{i\pi(\nu_0-\nu)t_0}}{\pi(\nu_0-\nu)} \sin\left(\pi(\nu_0-\nu)t_0\right). \tag{3.158}$$

Thus the instantaneous emission intensity at time t_0 is

$$I_\nu^{e\prime}(t_0) = E_\nu^* E_\nu = \frac{E_0^2}{\pi^2(\nu_0-\nu)^2} \sin^2\left(\pi(\nu_0-\nu)t_0\right). \tag{3.159}$$

Now average over the range of possible t_0, where P is the probability of a disruption at time t_0, to arrive at

$$I_\nu^e = \int_0^\infty I_v^{e\prime}(t_0) P(t_0) dt_0 \tag{3.160}$$

$$= \frac{E_0^2}{\pi^2(\nu_0-\nu)^2} \int_0^\infty P(t_0) \sin^2\left(\pi(\nu_0-\nu)t_0\right) dt_0. \tag{3.161}$$

Let N represent the number of particles out of N_0 in the medium that have yet to be hit. The change in the number disrupted from t to $t + \mathrm{d}t$ is

$$dN \propto -N dt = kN dt. \tag{3.162}$$

The solution is

$$N(t_0) = N_0 e^{-kt_0} = N_0 e^{-t_0/T_0}, \tag{3.163}$$

where T_0 is the average time between collisions. The probability of a disruption at time t_0, in terms of N_0, can be written as,

$$P(t_0) = \frac{N(t_0)/N_0}{\int_0^\infty (N(t_0)/N_0)dt_0} = \frac{e^{-t_0/T_0}}{\int_0^\infty e^{-t_0/T_0}dt_0} = \frac{1}{T_0}e^{-t_0/T_0}. \tag{3.164}$$

The emission intensity function can now be evaluated and simplified,

$$I_\nu^e = \frac{E_0^2}{\pi^2(\nu_0-\nu)^2}\frac{1}{T_0}\int_0^\infty e^{-t_0/T_0}\sin^2\left(\pi(\nu_0-\nu)t_0\right)dt_0 \tag{3.165}$$

$$= \frac{2E_0^2}{\left(\frac{1}{T_0}\right)^2 + 4\pi^2(\nu_0-\nu)^2}. \tag{3.166}$$

Since absorption and emission line profiles have the same frequency dependence, I_ν^e is proportional to the corresponding absorption in an infinitesimal length of column, $\mathrm{d}I_\nu$, which is in turn proportional to the line profile, $\varphi_\nu(\nu-\nu_0)$. Hence, after normalizing the intensity, we obtain the normalized collisional line profile,

$$\varphi_\nu^C(\nu-\nu_0) = \frac{\Gamma_C/4\pi^2}{\Delta\nu^2 + (\Gamma_C/4\pi)^2}, \tag{3.167}$$

in terms of frequency, with a broadening parameter $\Gamma_C = 2/T_0$. In terms of wavelength, the profile can be written as

$$\varphi_\lambda^C(\lambda-\lambda_0) = \frac{\Gamma_C\lambda_0^2/4\pi^2c}{\Delta\lambda^2 + (\Gamma_C\lambda_0^2/4\pi c)^2}. \tag{3.168}$$

Here we have another Lorentzian profile, the same shape as the natural transition line shape. This is not surprising, since the finite lifetime of an excited state similarly can be viewed as a truncation of a wave train. Later, we will show how advantageous similar line profile shapes can be when considering their combined effect on the final absorption profile.

3.4.3.2 Collisional Damping

The collisional damping term, Γ_C, dictates the width of the Lorentzian profile, and is itself determined by the mean time between collisions. To obtain either of these figures, one must consider the state of the gas not only in terms of density and pressure, but also in terms of what constitutes a collision. It should be noted that

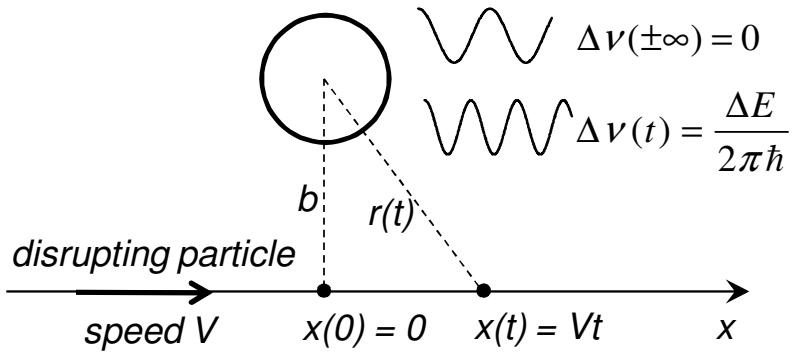

Figure 3.7: Passage of disrupting particle by radiating atom or ion.

collision does not actually mean a hard sphere impact, but the effects of the electric field produced by a rapidly passing particle on the radiating atom, as shown in figure 3.7. Unperturbed, the atom will radiate at a constant frequency, but when disturbed it will experience for certain types of interactions (long-range interactions predominant under conditions of interest here) a frequency shift given by

$$\Delta\nu(t) = \frac{\Delta E}{2\pi\hbar} = \frac{C}{2\pi r^j}. \tag{3.169}$$

The energy shift of equation (3.154) can be re-expressed as follows,

$$\Delta E = \frac{\hbar C}{r^j}, \tag{3.170}$$

where C is a constant related to the specific transition and the structure of the atom. The total phase shift resulting from the collision can be written as

$$\eta = 2\pi \int_{-\infty}^{\infty} \Delta\nu(t)dt = C \int_{-\infty}^{\infty} r(t)^{-j} dt. \tag{3.171}$$

We set b as the impact parameter as shown in the geometry of figure 3.7. If we assume that the perturbing particle maintains a straight line path as it passes, we can write the separation distance as a function of time as $r(t) = (b^2 + (Vt)^2)^{1/2}$, where V is the speed of the disturbing particle. Hence,

$$\eta = C \int_{-\infty}^{\infty} (b^2 + V^2 t^2)^{-j/2} dt. \tag{3.172}$$

The integral contains a numerical term which depends on the type of collision process, given by the order j. Hence,

$$\eta(b) = C J_j b^{1-j} V^{-1}, \tag{3.173}$$

where the J_j values are π for j=2, $\pi/2$ for j=4, and $3\pi/8$ for j=6. If b_{max} represents the "maximum" impact parameter that produces a disruption, then expressed in terms of the corresponding maximum phase shift, we have

$$b_{max} = \left(\frac{CJ_j}{\eta_{max}}\right)^{1/(j-1)} V^{1/(1-j)}. \tag{3.174}$$

This allows us to define the effective target area of impact, or the collisional cross section, σ, as

$$\sigma = \pi b_{max}^2 = \pi \left(\frac{CJ_j}{\eta_{max}}\right)^{2/(j-1)} V^{2/(1-j)}. \tag{3.175}$$

If we equate the mean free path of a passing particle using the well-known expression $\frac{1}{n\sigma}$, with $VT_0 = 2V/\Gamma_C$, we can solve for the damping parameter [52],

$$\Gamma_C = 2\pi \left(\frac{CJ_j}{\eta_{max}}\right)^{2/(j-1)} nV^{(3-j)/(1-j)}. \tag{3.176}$$

The ideal gas law combined with kinetic theory leads to $n \propto p/T$ and $V \propto \sqrt{T}$; hence,

$$\Gamma_C \propto nT^{(j-3)/2(j-1)} \propto pT^{-(j+1)/2(j-1)}. \tag{3.177}$$

For quadratic Stark broadening ($j = 4$), the dominant term in our case,

$$\Gamma_C \propto nT^{1/6} \sim n, \tag{3.178}$$

or

$$\Gamma_C \propto pT^{-5/6} \sim p/T. \tag{3.179}$$

For the purposes of the line simulation program described later, we have adopted the approximation of Kurucz in the spectrum synthesis program SYNTHE [53]. The quadratic stark effect is primarily caused by fast moving charged particles, thus the number density of perturbers per unit volume can be approximated by the electron density, n_e, since hydrogen atoms, the predominant species, are fully ionized and helium atoms are not. The collisional damping term becomes

$$\Gamma_C = constant\ n_e. \tag{3.180}$$

Note that equation (3.180) is a general result of the impact model, rather than a result for the specific case of Stark broadening.

A data base of constant values specific to each transition, as calculated by the SYNTHE program, is available at http://kurucz.harvard.edu/.

3.4.4 Thermal Broadening

Another source of spectral line broadening is random thermal motion. In the case of an isotropic gas, the particles are moving in all directions. However, spectroscopically, an observer on earth will only see the projected radial component of their motion, towards or away from Earth. Some particles will seem to be receding, while others will be approaching. Wavelength shifts for emission or absorption due to bound-bound transitions result from the Doppler effect,

$$\frac{\Delta\nu}{\nu_0} = \frac{\Delta\lambda}{\lambda_0} = \frac{v_{\rm rad}}{c}, \tag{3.181}$$

where $\Delta\nu$ and $\Delta\lambda$ are the differences from the line center (ν_0 or λ_0) and v_{rad} is the radial velocity. A large number of particles in a thermal distribution produces a Gaussian, or Maxwellian, distribution of velocities,

$$\frac{{\rm d}N}{N} = \frac{1}{\sqrt{\pi}v_0}\exp\left[-\left(\frac{v_{\rm rad}}{v_0}\right)^2\right]{\rm d}v_{\rm rad}. \tag{3.182}$$

The most probable speed is given by $v_0^2 = 2kT/M$, where M is the mass of the ion and k is the Boltzmann constant. We can now define the characteristic Doppler shift as [13]

$$\begin{aligned}\Delta\nu_D &= \frac{v_0}{c}\nu_0 = \frac{\nu_0}{c}\left(\frac{2kT}{M}\right)^{1/2}\\ \Delta\lambda_D &= \frac{v_0}{c}\lambda_0 = \frac{\lambda_0}{c}\left(\frac{2kT}{M}\right)^{1/2}.\end{aligned} \tag{3.183}$$

Thus the distribution of $\Delta\lambda$ is

$$\begin{aligned}\frac{{\rm d}N}{N} &= \frac{1}{\sqrt{\pi}\Delta\nu_D}\exp\left[-\left(\frac{\Delta\nu}{\Delta\nu_D}\right)^2\right]{\rm d}\nu\\ &= \frac{1}{\sqrt{\pi}\Delta\lambda_D}\exp\left[-\left(\frac{\Delta\lambda}{\Delta\lambda_D}\right)^2\right].{\rm d}\lambda\end{aligned} \tag{3.184}$$

Finally, as in the case of collisional broadening, we construct the normalized thermal line profile in terms of frequency and wavelength:

$$\varphi_\nu^T(\nu - \nu_0) = \frac{1}{\sqrt{\pi}\Delta\nu_D} e^{-(\Delta\nu/\Delta\nu_D)^2} \tag{3.185}$$

$$\varphi_\lambda^T(\lambda - \lambda_0) = \frac{1}{\sqrt{\pi}\Delta\lambda_D} e^{-(\Delta\lambda/\Delta\lambda_D)^2} \tag{3.186}$$

3.4.5 Microturbulance

While thermal Doppler broadening is due to the thermalized motions of individual particles, there can also be the wholesale motion of packets of gas. This phenomena is considered 'microturbulence' when the dimensions of the gas groupings are small compared to the photon mean free path. Typically one selects a Gaussian form for the range of velocities for the clumps of gas, and consequently the math can be treated in the same way as the thermal Doppler broadening. The only change is that we define a new variable, v_{mic}, to serve as the velocity dispersion term, replacing the $(2kT/M)^{1/2}$ term in $\Delta\lambda_D$ and $\Delta\nu_D$. Hence,

$$\varphi_\nu^{mic}(\nu - \nu_0) = \frac{1}{\sqrt{\pi}\xi} e^{-(\Delta\nu/\xi)^2}, \tag{3.187}$$

$$\varphi_\lambda^{mic}(\lambda - \lambda_0) = \frac{1}{\sqrt{\pi}\xi} e^{-(\Delta\lambda/\xi)^2}. \tag{3.188}$$

Here, $\xi = \frac{\nu_0}{c} v_{mic}$ or $\frac{\lambda_0}{c} v_{mic}$ in the two forms above, respectively.

3.4.6 Bringing It Together So Far: The Voigt Profile

Thus far, we have analyzed four different mechanisms that determine the shape and width of an absorption line, with normalized line profiles given by

$$\varphi_\lambda^N(\lambda-\lambda_0) = \frac{\Gamma_N\lambda_0^2/4\pi^2c}{\Delta\lambda^2+(\Gamma_N\lambda_0^2/4\pi c)^2}$$

$$\varphi_\lambda^C(\lambda-\lambda_0) = \frac{\Gamma_C\lambda_0^2/4\pi^2c}{\Delta\lambda^2+(\Gamma_C\lambda_0^2/4\pi c)^2}$$

$$\varphi_\lambda^T(\lambda-\lambda_0) = \frac{1}{\sqrt{\pi}\,\Delta\lambda_D}e^{-(\Delta\lambda/\Delta\lambda_D)^2}$$

$$\varphi_\lambda^{mic}(\lambda-\lambda_0) = \frac{1}{\sqrt{\pi}\,\xi}e^{-(\Delta\lambda/\xi)^2}. \tag{3.189}$$

Acting alone, each of these would produce an absorption coefficient equal to $\frac{\pi e^2\lambda_0^2 f}{mc^2}$ times the corresponding normalized line profile. However, in reality, all of these mechanisms occur simultaneously. So we need to develop a method to account for the accumulated effect since the line shape produced by one process is modulated by contributions from another process. Hence, they must be combined through the method of convolutions. The convolution of two functions is given by

$$k(\sigma) = f(\sigma) * g(\sigma) = \int_{-\infty}^{\infty} f(\sigma_1)g(\sigma-\sigma_1)\,\mathrm{d}\sigma_1. \tag{3.190}$$

It can be easily shown that the convolution of two Gaussian functions is another Gaussian where the characteristic broadening parameter is a combination of the separate parameters, [13]

$$G_a(x) * G_b(x) = G_c(x) = \frac{1}{\beta_c\sqrt{\pi}}e^{-x^2/\beta_c^2} \tag{3.191}$$

$$\beta_c^2 = \beta_a^2 + \beta_b^2. \tag{3.192}$$

Similarly, two Lorentzians convolute into another Lorentzian profile, where the broadening parameter γ is the sum of each separate line's damping value,

$$L_a(x) * L_b(x) = L_c(x) = \frac{\gamma_c}{\pi}\,\frac{1}{x^2+\gamma_c^2} \tag{3.193}$$

$$\gamma_c = \gamma_a + \gamma_b. \tag{3.194}$$

The convolution of a Gaussian and Lorentzian can be carried out to yield

$$\begin{aligned} G(x) * L(x) &= \frac{\gamma/\pi}{x^2+\gamma^2} * \frac{1}{\sqrt{\pi}\beta} e^{-x^2} \\ &= \frac{1}{\sqrt{\pi}\beta}\frac{\gamma}{\pi} \int_{-\infty}^{\infty} \frac{e^{-x_1^2}}{(x-x_1)^2+\gamma^2}\,\mathrm{d}x_1 \qquad (3.195) \\ &= \frac{1}{\sqrt{\pi}\beta} H(x,\gamma) = V(x,\gamma). \qquad (3.196) \end{aligned}$$

$H(x,\gamma)$ is known as the Hjerting function and $V(x,\gamma)$ is the normalized Hjerting function, known as the Voigt function [54, 55].

Applying these convolutions to the previously derived absorption coefficients, we obtain

$$\alpha_\lambda = \left(\frac{\pi e^2}{mc^2}\lambda_0^2 f\right) \varphi_\lambda^N * \varphi_\lambda^C * \varphi_\lambda^T * \varphi_\lambda^{Mic}. \tag{3.197}$$

Combining the profile shape with the energy removed from a unit beam gives us

$$\begin{aligned} \alpha_\lambda &= \frac{\pi e^2}{mc}\, f\, \frac{\lambda_0^2}{c} \frac{\Gamma\lambda_0^2/4\pi^2 c}{(\Delta\lambda)^2 + (\Gamma\lambda_0^2/4\pi c)^2} * \frac{1}{\sqrt{\pi}\Delta\lambda_D} e^{-(\Delta\lambda/\Delta\lambda_D)^2} \qquad (3.198) \\ &= \frac{\pi e^2 \lambda_0^2}{mc^2}\, f\, V(u,a) \qquad (3.199) \end{aligned}$$

where

$$\Delta\lambda = \lambda - \lambda_0 \tag{3.200}$$

$$\Gamma = \Gamma_N + \Gamma_C \tag{3.201}$$

$$\Delta\lambda_D = \frac{\lambda_0}{c}\left(\frac{2kT}{m} + \xi^2\right)^{1/2} \tag{3.202}$$

$$a = \frac{\Gamma\lambda_0^2}{4\pi c \Delta\lambda_D} \tag{3.203}$$

$$u = \Delta\lambda/\Delta\lambda_D \tag{3.204}$$

$$V(u,a) = \frac{a}{\pi}\int_{-\infty}^{\infty} \frac{e^{-u_1^2}}{(u-u_1)^2+a^2}\,\mathrm{d}u_1. \tag{3.205}$$

Note that $\Delta\lambda_D$ has been redefined to include microturbulance. Equation (3.199) is the main work horse equation to get the basic line shape of any electronic bound-bound transition. In the following sections we will apply various macro scale phenomena to this basic profile to see how it can be further affected.

3.4.7 Rotational and Macroturbulant Broadening

Large scale motions of stellar material can greatly affect the shapes of absorption lines as well. In the following sections we will develop the treatment of the *extrinsic* effects due to the high rotational rates of the star, differential rotation at varying latitudes, and convective motion in the stellar atmosphere.

First, recall that in section 3.2 we developed a treatment to describe the flux received at a detector in terms of the fractional coverage of a radiating disk by an intervening gas cloud.

$$F_v^{gas} = \frac{F_\nu^0}{A_c I_\nu^0} \int_g I_\nu(r_c) dA_c, \tag{3.206}$$

where the intensity radiated is location-specific to the disk, so that

$$I_\nu(r_c) = \int_L dI_\nu(x, r_c), \tag{3.207}$$

and the intensity is related to the absorption coefficient and profile function in the usual way:

$$dI_\nu(x, r_c) = -\alpha_\nu I_\nu(x, r_c) n'(x, r_c) dx \tag{3.208}$$

$$\alpha_\nu = \frac{\pi e^2}{mc} f\varphi(\nu - \nu_0) \equiv C\varphi(\nu - \nu_0) \tag{3.209}$$

This gives an overall function describing the occulting gas flux with respect to the position over the disk,

$$F_v^{gas} = -C \frac{F_\nu^0}{A_c I_\nu^0} \int_g dA_c \int_L dx \varphi(\nu - \nu_0) I_\nu(x, r_c) n'(x, r_c). \tag{3.210}$$

Now consider a "macroscopic" scale Doppler shift, $\Delta\nu_{0,p}$ that depends on the disk position, r_c. Divide the area covered by the gas cloud, A_g, into N_p small but macroscopic elements (long compared to the photon mean free path) of area Δa and identified by

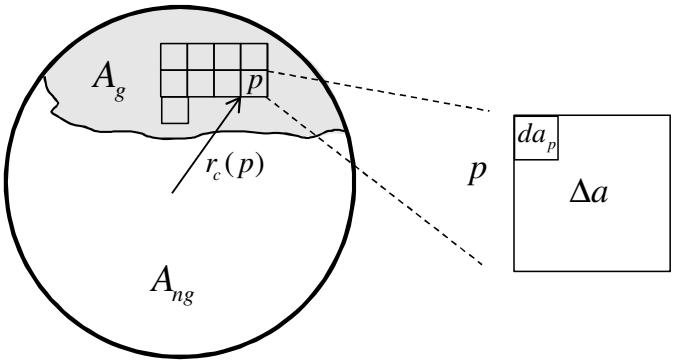

Figure 3.8: Subdivision of A_g into small but macroscopic elements.

p, as shown in figure 3.8. Each Δa is in turn divided into "infinitesimal" elements $\mathrm{d}a_p$ so that, for an arbitrary function, $f(r_c)$,

$$\int_g dA_c f(r_c) = \sum\nolimits_{p=1}^{N_p} \int_{\Delta a} da_p f(r_c(p)) \tag{3.211}$$

and

$$F_v^{gas} = -C\frac{F_\nu^0}{A_c I_\nu^0} \int\limits_L dx \sum\nolimits_{p=1}^{N_p} \int_{\Delta a} da_p \varphi(\nu - \nu_0 - \Delta\nu_{0,p}) I_\nu(x, r_c) n'(x, r_c), \tag{3.212}$$

where

$$\Delta\nu_{0,p} = -\frac{V(r_c)}{c}\nu_0 = -\frac{V(p)}{c}\nu_0 \tag{3.213}$$

and V is the radial velocity. Integrating over the infinitesimal small elements yields

$$F_v^{gas} = -C\frac{F_\nu^0}{A_c I_\nu^0}\Delta a \int\limits_L \mathrm{d}x \sum_{p=1}^{N_p} \varphi(\nu - \nu_0 - \Delta\nu_{0,p}) I_\nu(x, r_c) n'(x, r_c). \tag{3.214}$$

Upon making the following substitutions,

$$\Delta a = \frac{\beta A_c}{N_p}, \tag{3.215}$$

$$n'(x, r_c) = n'(x, r_c(p)) \simeq n'(x), \tag{3.216}$$

$$I(x, r_c) = I(x, r_c(p)) \equiv I(x, p), \tag{3.217}$$

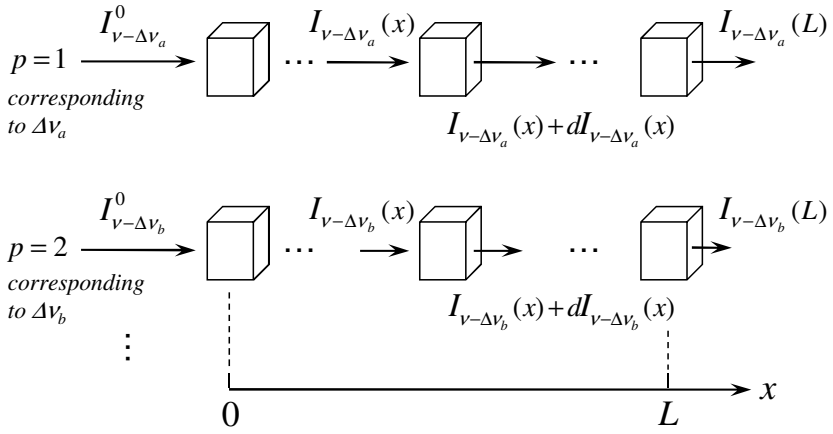

Figure 3.9: Pictured here is an example of how light may be extinquished by different amounts depending on the local absorption properties. $\Delta\nu_a$ and $\Delta\nu_b$ represent various values of $\Delta\nu_0$.

we find

$$F_\nu^{gas} = -C\frac{\beta F_\nu^0}{I_\nu^0 N_p}\int_L \mathrm{d}x \sum_{p=1}^{N_p} \varphi(\nu-\nu_0-\Delta\nu_{0,p}) I_\nu(x,p) n'(x). \tag{3.218}$$

Many area elements identified by different values of p will correspond to the same Doppler frequency shift, $\Delta\nu_0$. Let $G(\Delta\nu_0)$ represent the number of frequency shifts with values between $\Delta\nu_0$ and $\Delta\nu_0 + \Delta(\Delta\nu_0)$, per unit frequency-shift interval, $\Delta(\Delta\nu_0)$. This distribution function can be found by noting that $G(\Delta\nu_0)\Delta(\Delta\nu_0)$ is the fractional number of area elements (or the fractional area) corresponding to frequency shifts in the range $\Delta(\Delta\nu_0)$ about $\Delta\nu_0$. With this definition, we can convert the sum over area elements, p, to a sum over frequency shifts, $\Delta\nu_0$, using

$$\sum_{p=1}^{N_p} f(p) = \sum_{\Delta\nu_0} N_p G(\Delta\nu_0)\left(\Delta(\Delta\nu_0)\right) f(\Delta\nu_0). \tag{3.219}$$

We also replace the position dependence of I_ν by a frequency dependence as shown in figure 3.9 so that

$$I(x,p) = I_{\nu-\Delta\nu_0}(x). \tag{3.220}$$

Therefore,

$$F_\nu^{gas} = -C\frac{\beta F_\nu^0}{I_\nu^0}\int_L \mathrm{d}x \sum_{\Delta\nu_0} G(\Delta\nu_0)\left(\Delta(\Delta\nu_0)\right)\varphi(\nu-\nu_0-\Delta\nu_0) I_{\nu-\Delta\nu_0}(x) n'(x). \tag{3.221}$$

In terms of α_ν,

$$F_\nu^{gas} = -\frac{\beta F_\nu^0}{I_\nu^0} \sum_{\Delta\nu_0} G(\Delta\nu_0)\,(\Delta(\Delta\nu_0)) \int_L \mathrm{d}x \alpha_{\nu-\Delta\nu_0} I_{\nu-\Delta\nu_0}(x) n'(x). \tag{3.222}$$

Using

$$\int_L \alpha_{\nu-\Delta\nu_0} I_{\nu-\Delta\nu_0}(x) n'(x)\,\mathrm{d}x = -\int_L \mathrm{d}I_{\nu-\Delta\nu_0} = -I_{\nu-\Delta\nu_0} \tag{3.223}$$

$$= -I^0_{\nu-\Delta\nu_0} e^{-\tau_{\nu-\Delta\nu_0}} \tag{3.224}$$

with $I^0_{\nu-\Delta\nu} \simeq I^0_\nu$, and $F^0_{\nu-\Delta\nu_0} \simeq F^0_\nu$, we find

$$F_\nu^{gas} = \beta \sum_{\Delta\nu_0} G(\Delta\nu_0)\,(\Delta(\Delta\nu_0))\, F^0_{\nu-\Delta\nu_0} e^{-\tau_{\nu-\Delta\nu_0}}, \tag{3.225}$$

or, with a shift in the summation variable, now called ν',

$$F_\nu^{gas} = \beta \sum_{\nu'} F^0_{\nu'} e^{-\tau_{\nu'}} G(\nu-\nu')\Delta\nu'. \tag{3.226}$$

The first two terms in the sum constitute the flux in the absence of extrinsic (macroscopic) motional terms. Using the superscript "nm" to denote "no (macroscopic) motion,"

$$F_\nu^{gas} = \beta \sum_{\nu'} F^{\mathrm{nm}}_{\nu'} G(\nu-\nu')\Delta\nu'. \tag{3.227}$$

Finally, converting the sum to an integral, we find

$$F_\nu^{gas} = \beta \int_{-\infty}^{\infty} F^{\mathrm{nm}}_{\nu'} G(\nu-\nu')\,\mathrm{d}\nu'. \tag{3.228}$$

Notice that this is a convolution; hence,

$$F_\nu^{gas} = \beta (F^{\mathrm{nm}} * G)_\nu. \tag{3.229}$$

This expression is the starting point for the determination of either macroturbulent or rotational broadening. The next task is to derive expressions for G.

3.4.7.1 Rotational Broadening without Macroturbulance

As a star rotates, parts of the star move toward the observer, while other parts move away. One can determine the contributions to the Doppler shift across the viewable

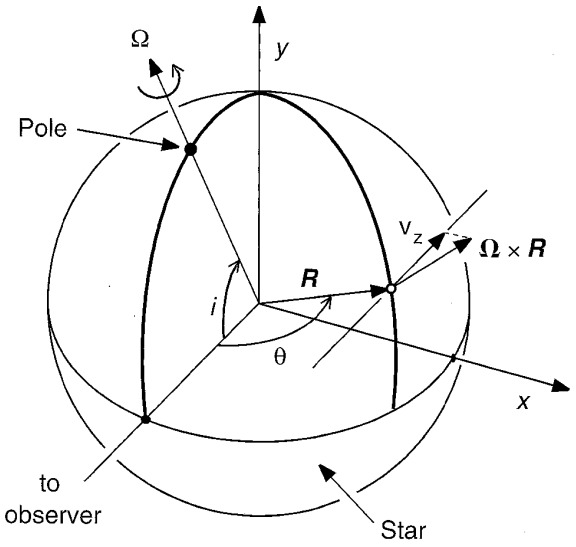

Figure 3.10: Schematic of the geometry for a rotating star of radius R. Rotation axis ω (indicated as Ω in this figure) is inclined at an angle i from the observer's line of sight axis, z [13]. Reprinted with the permission of Cambridge University Press.

portions of the stellar disk. The distribution of projected radial velocities will give us a profile of Doppler shifts. We describe in this section how this Doppler distribution results in rotationally broadened spectral lines.

The degree of broadening depends on the equatorial rotational speed and the orientation of the star relative to the observer. If the star is viewed along the polar axis, no rotational broadening will be observed since there are no radial components to the velocity. The more a star is inclined so that one could see edge on to the equator, the higher the proportion of rotational broadening that will be applied to the spectra. We will first assume the star to be a rigidly rotating sphere with an angular velocity of ω . We set up the coordinate system, shown in figure 3.10, where the line of sight to the star is along the negative z-axis. The inclination, as defined previously, is the angular difference between the polar axis of the star and the line of sight z-axis. The surface velocity of any point on the sphere is given by the cross product,

$$\mathbf{v} = \boldsymbol{\omega} \times \mathbf{r}, \tag{3.230}$$

where r is the radius vector from the center of the star to that point. We are only concerned with Doppler shifts along the z-axis; hence, $v_z = y\omega_x - x\omega_y$. In our coordinate system, there is no ω_x component, and the y-component is $\omega_y = \omega \sin i$, where i is the inclination angle, giving radial velocity

$$v_z = x\omega \sin i. \tag{3.231}$$

Notice that the radial velocity depends only on the x coordinate of the projected stellar disk, assuming a maximum value at x=R. A star's rotational speed is often reported as its equatorial speed,

$$v_{eq} = R\omega. \tag{3.232}$$

The wavelength Doppler shift as a function of x is given by

$$\Delta\lambda_0 = \frac{v_z\lambda_0}{c} = \frac{xv_{eq}\lambda_0 \sin i}{Rc} \tag{3.233}$$

and this assumes a maximum value of

$$\Delta\lambda_0^{max} = \frac{Rv_{eq}\lambda_0 \sin i}{Rc} = \frac{v_{eq}\lambda_0 \sin i}{c}. \tag{3.234}$$

Expressing the Doppler shift in terms of the maximum value yields

$$\Delta\lambda_0 = \frac{x}{R}\Delta\lambda_0^{max}. \tag{3.235}$$

We seek the distribution function, G, described in the previous section. Noting this relationship between position on the stellar disk and Doppler wavelength shifts, we can say that the fractional number of "macro-regions" with shifts between $\Delta\lambda_0$ and $\Delta\lambda_0 + \mathrm{d}\Delta\lambda_0$ is equal to the corresponding fraction of stellar disk area producing those shifts (see figure 3.11); hence,

$$G(\Delta\lambda_0)\,\mathrm{d}(\Delta\lambda_0) = \frac{2y(x)\,\mathrm{d}x}{\pi R^2}. \tag{3.236}$$

Using $y(x) = (R^2 - x^2)^{1/2}$ and $\Delta\lambda_0 = \frac{x}{R}\Delta\lambda_0^{max}$, we solve for G,

$$G^{Rot}(\Delta\lambda_0) = \frac{2}{\pi\Delta\lambda_0^{max}}\left(1 - \left(\frac{\Delta\lambda_0}{\Delta\lambda_0^{max}}\right)^2\right)^{1/2}. \tag{3.237}$$

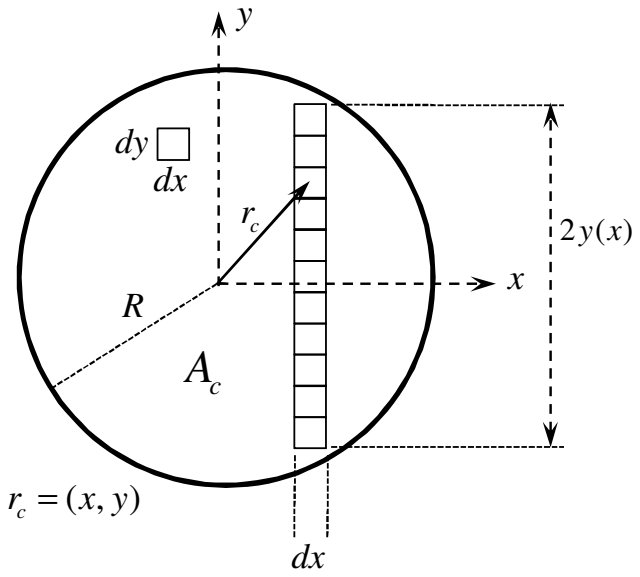

Figure 3.11: Disk integration via vertical strips of the apparent disk of the star. The line of sight of the observer is parallel to the z axis here.

This expression is appropriate for $\Delta\lambda_0$ less than or equal to $\Delta\lambda_0^{max}$, otherwise G is zero. We could use this result to add the effect of rotational broadening to our Voigt profile by applying the convolution described at the end of the last section. Before examining the consequences of rotational broadening, we add in the effect known as limb darkening. Up until now, we have assumed that we have a uniform pre-absorption intensity emitted across the viewable stellar disk. But stars are giant balls of gas, not rigid spheres. The density and temperature of the gas can decrease towards the upper altitudes of the star's photosphere. Our view of the edges of the viewable stellar disk is essentially of the upper photosphere at a penetrative oblique angle, and thus the star appears less luminous there. We look deeper into the stellar atmosphere, to higher temperature regions, near the center of the apparent disk. The relative dimming due to limb darkening can be approximated by

$$I/I^0 = 1 - \epsilon + \epsilon \cos\theta, \tag{3.238}$$

where θ is the angular limb distance measured from the apparent center of the star, and ϵ is the limb darkening coefficient [13]. A value of $\epsilon = 0$ means that no limb darkening takes place and you have a uniformly illuminated disk, while $\epsilon = 1$ gives a

"fully darkened" stellar limb. In this work, we have taken U Cep to have $\epsilon = 0.5$ (a common approximation) for the purposes of spectral line simulations [13]. ϵ can vary slowly over wide spectral regions, but not so much that we cannot assume it constant over the lines analyzed in this dissertation. In a relatively straightforward approach, we begin with the Doppler broadening expression,

$$G(\Delta\lambda_0)\,\mathrm{d}(\Delta\lambda_0) = \frac{2y(x)\,\mathrm{d}x}{\pi R^2},$$

and make the following substitutions,

$$y(x)\,\mathrm{d}x \rightarrow \mathrm{d}x \int_0^{y(x)} (1 - \epsilon + \epsilon\cos\theta)\,\mathrm{d}y, \tag{3.239}$$

$$\pi R^2 \rightarrow 4\int_0^R \mathrm{d}x \int_0^{y(x)} (1 - \epsilon + \epsilon\cos\theta)\,\mathrm{d}y = \pi R^2(1 - \frac{\epsilon}{3}), \tag{3.240}$$

where

$$\cos\theta = \left[R^2 - (x^2 + y^2)\right]^{1/2}/R, \tag{3.241}$$

and $y(x)$ is defined by figure 3.11. The first substitution accounts for the variation in intensity, and the second correspondingly normalizes the distribution to unity. The integration is straight forward, and we find (consistant with Gray's result [13])

$$G^{Rot+Limb}(\Delta\lambda_0) = \frac{2(1-\epsilon)\left(1 - \left(\frac{\Delta\lambda_0}{\Delta\lambda_0^{max}}\right)^2\right)^{1/2} + \frac{\pi\epsilon}{2}\left(1 - \left(\frac{\Delta\lambda_0}{\Delta\lambda_0^{max}}\right)^2\right)}{\pi(1 - \frac{\epsilon}{3})\Delta\lambda_0^{max}}. \tag{3.242}$$

The rotation profile has been reduced to the sum of two terms. The first has the form of an ellipse and the second the shape of a parabola. Again, in the case where $\epsilon = 0$, the star is uniformly illuminated and absorption is dominated by the elliptical shape, and as we approach $\epsilon = 1$, the parabolic distribution takes over. Figure 3.12 displays the contributions of the two distribution shapes.

Because the G function is normalized, it mainly serves to redistribute the area of an absorption line, making it wider and shallower. It cannot add to or take away from the area of that curve. In cases of extreme rotation, this type of broadening can have a major impact on the appearance of a spectrum. Many lines closely packed together can be blended by the rotational broadening, appearing to be a new line

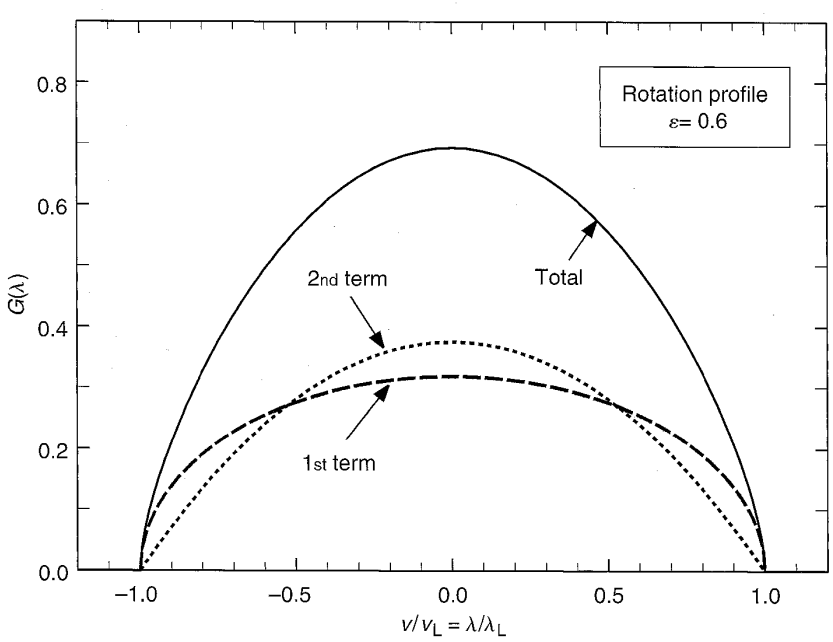

Figure 3.12: $G^{Rot+Limb}(\Delta\lambda)$ rotational velocity profile. The dashed line indicates the contribution from the elliptical term, and the dotted line gives the contribution from the parabolic term [13]. Reprinted with the permission of Cambridge University Press.

entirely, or even broadened so much that they appear flat and modify the continuum of the spectrum. Figure 3.13 shows a simulated spectrum of a star with the effects of higher and higher rotational velocities. Notice how the spectrum becomes increasingly smooth, and many of the minor absorption lines seem to disappear. Horizontal lines, using the fitting method described in section 4.5, indicate where an observer might measure the local continuum. However, it is clear that at higher rotational rates, the apparent continuum is significantly lower than the true value. This effect will have a significant impact on the analysis of continuum levels, described in a later section.

3.4.7.2 Macroturbulant Broadening without Rotation

We know from our own Sun that there are convective cells of uprising and sinking gas whose appearance has lent them the name of 'solar granulation'. These granules consist of bright patches of hot matter bubbling up from below, surrounded by darker lanes where the gas has cooled off, been pushed aside and begun to sink. On

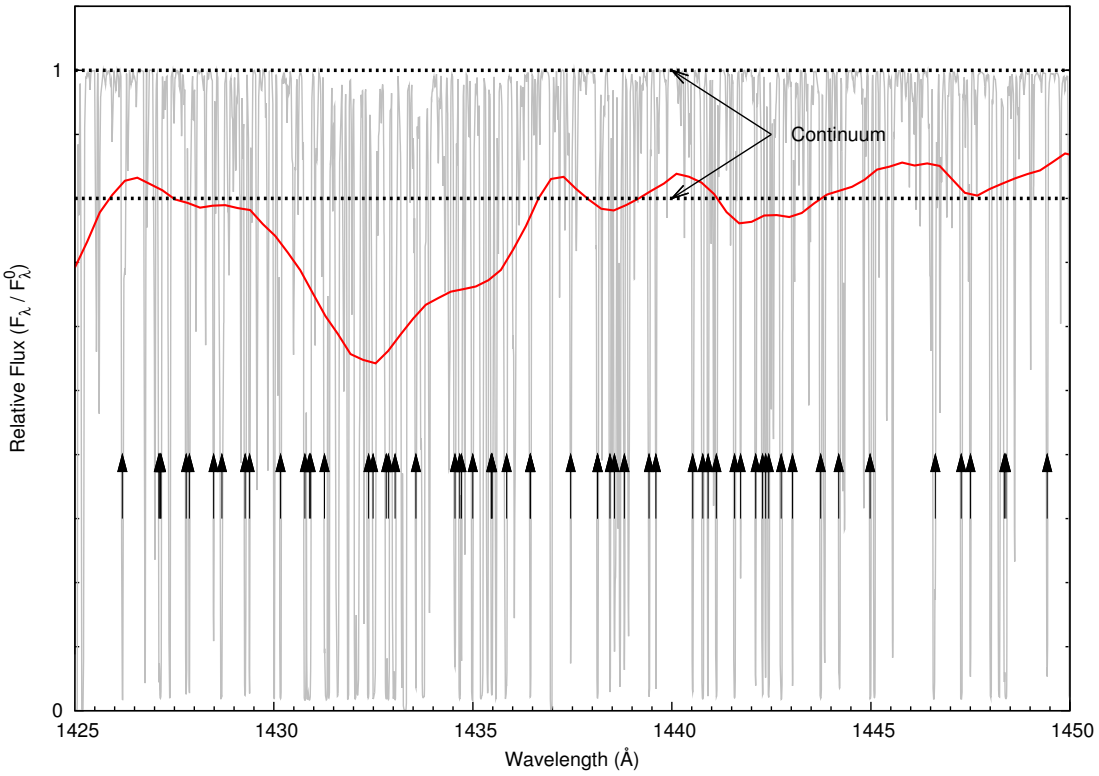

Figure 3.13: Synthetic spectra showing the effect of stellar rotation. The solid line is after the unbroadened spectrum (in gray) has been broadend with a rotational rate of $v_{eq} \sin i =$ 300 km/s. Dashed lines have been placed for the unbroadened and broadened apprent continuum. For the broadened spectrum, the apparent continuum has been depressed to 80% of normal. Black arrows mark the location of many Fe II absorption lines that seem to disappear at higher rotational velocities. Also note that these Fe II lines convolve together to form a quite large absorption feature around 1432 Å, which is in fact a pseudo line.

the Sun, cells last an average of 10 minutes, are typically 1300 km across, and have a temperature difference on the order of 100 K between the hot and cool regions [13]. This difference accounts for about a 20% reduction of brightness from the patches to the lanes. The hot regions flow upwards at around 1 to 2 km/s, while the cool lanes are twice as fast. This is due in part to the lanes covering less than half the stellar surface area and conservation of mass flow necessitates that the sinking matter move faster. Additionally, the cooler regions have a lower continuous opacity and allow a deeper view to where convective velocities are higher [13].

Modeling the effects of these granules, or similar macroscopic motions, on a spectrum can become quite complex, especially if one considers the hydrodynamics of large scale velocity fields or the interactions of magnetic field lines, getting twisted by flowing ionized matter, as is the case with sunspots. But the commonly used approach of micro-macroturbulence modeling will be sufficient to tell us the general effects of the bulk matter flow. In modeling microturbulence, we consider motion of the gas on the scale of the mean free path of a photon, and convolute those contributions into the overall thermal Doppler profile. The macroturbulent case involves turbulent cells large enough to contain a newly created photon until it can escape from the star. Another definition is that the cells are much larger than unit optical depth.

Similarly to the derivation outlined in the rotation section, we can assume that the motion of the local medium will govern the range of Doppler shifts applied to the spectrum produced at those regions. Thus we can describe the modified spectrum as a convolution of F^{nm} (no motion) with the velocity distribution of the macroturbulence, G^{Mac}.

The shape of the distribution profile can be approximated using the radial-tangential model of Gray [56]. Remember that the convective cells we are modeling first come up, radially outwards from the center of the star, and that the dark lanes would sink downwards, radially towards the center of the star. But we must also account for matter flowing tangentially across the surface of the star from where it welled up to where it reaches its sinking destination. So, we can essentially break down the surface of the star into fractions of radial and tangential motion, denoted by A_T and A_R respectively. We further assume the velocity distribution of each component to be of a Gaussian form with dispersion parameters $\zeta_R \cos\theta$ and $\zeta_T \sin\theta$ projected towards the observer's line of sight (e.g.; the distribution of tangential velocities projected along the line of sight is Gaussian with exponential argument $-(\,\Delta\lambda_0/\zeta_T \sin\theta)^2\,$). Here, θ is the angle from the line of sight to the limb. With A_R and A_T as adjustable parameters defining the fractional amounts of stellar surface exhibiting the radial or transverse motion, the distribution function becomes

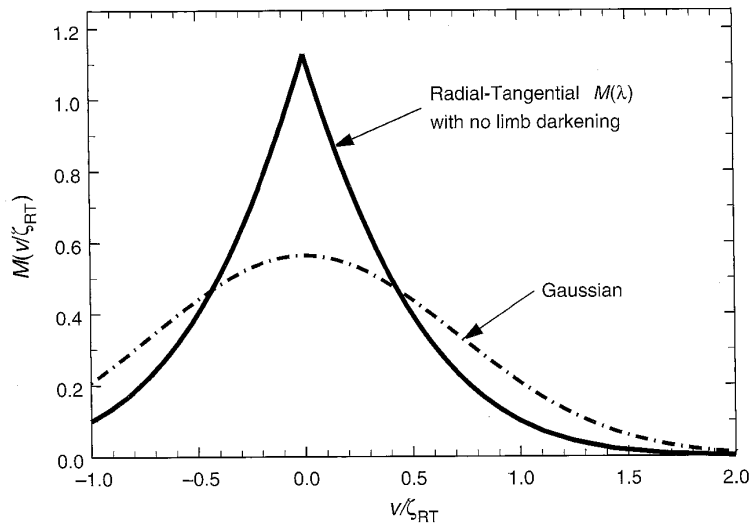

Figure 3.14: The solid line represents the integrated macroturbulent velocity profile. The accompanying profile is a Gaussian profile using the same broadening parameters for comparison [13]. Reprinted with the permission of Cambridge University Press.

$$g^{Mac}(\Delta\lambda_0) = \frac{A_R}{\sqrt{\pi}\zeta_R \cos\theta} e^{(-\Delta\lambda_0/\zeta_R \cos\theta)^2} + \frac{A_T}{\sqrt{\pi}\zeta_T \sin\theta} e^{(-\Delta\lambda_0/\zeta_T \sin\theta)^2}. \qquad (3.243)$$

The use of a lower-case "g" indicates that this function is defined for a certain location on the stellar surface. Upon integrating over the azimuthal angle and using the substitution suggested by Gray, $u = \zeta_R \cos\theta/\,\Delta\lambda_0 = \zeta_T \sin\theta/\,\Delta\lambda_0$, we get

$$G^{Mac}(\Delta\lambda_0) = \frac{2A_R\Delta\lambda_0}{\sqrt{\pi}\zeta_R^2} \int_0^{\zeta_R/\Delta\lambda_0} e^{-1/u^2}\,\mathrm{d}u + \frac{2A_T\Delta\lambda_0}{\sqrt{\pi}\zeta_T^2} \int_0^{\zeta_T/\Delta\lambda_0} e^{-1/u^2}\,\mathrm{d}u. \qquad (3.244)$$

Even though the radial and tangential functions are Gaussian in nature, the resultant profile shape of $G^{Mac}(\,\Delta\lambda_0)$ is a cuspy shape with broad wings, nearly the opposite of the rotational broadening profile with its flat middle and discontinuous limbs. Most often, the values of the dispersion parameter are chosen to be $\zeta = \zeta_R = \zeta_T$ and $A_R = A_T = 0.5$. One of the drawbacks of this formulation is that it does not account for thermal differences between the rising and sinking flows, thus the end profile is symmetric as shown in figure 3.14.

3.4.7.3 Rotation, Limb Darkening, and Macroturblence Combined

The macroturbulence model describes how the motion of convective cells on a stellar surface will affect spectral lines, even to the limb of a star, but neglects rotation. We have seen previously that high rotational rates can have a significant impact on the broadening of a spectrum. But it is possible to merge these broadening mechanisms. Unfortunately, the process is not as simple as adding, multiplying, or even convoluting all of the processes. We follow the procedure of Gray [56] whereby the rotational Doppler broadening is incorporated into the macroturbulent distribution prior to the stellar disk integration over the viewable hemisphere. Including limb darkening, we find

$$G^{Rot+Limb+Mac}(\Delta\lambda_0) = \frac{1}{\pi(1-\frac{\epsilon}{3})}\int_0^{2\pi}\int_0^{\pi/2}(1-\epsilon+\epsilon\cos\theta)g^{Mac}(\Delta\lambda_0 - \Delta\lambda_{0,R})\cos\theta\sin\theta\,\mathrm{d}\theta\,\mathrm{d}\phi, \quad (3.245)$$

where in terms of spherical coordinates the rotational Doppler shift is

$$\Delta\lambda_{0,R} = v_{eq}\sin i\frac{\lambda_0}{c}\sin\theta\cos\phi. \quad (3.246)$$

(Note: Here, ϕ represents the azimuthal spherical coordinate where the z axis is pointing toward the Earth.) One must be mindful that there are sufficient grid points to cover the whole disk adequately, as different phenomena dominate at different positions on the disk. The radial marcoturbulent term is strongest at the center of the disk, while the tangential turbulent term is strongest along all of the edges. Rotation will contribute to the tangential term strongly at the equatorial edges, but not at the polar regions. The best rule of thumb is that in a macro-turbulent dominated situation, if the cuspy section of the profile is clear and sharp, then you have a good grid size.

3.4.8 Differential Rotation

Thus far, we have assumed the star to be a rigid rotating sphere. This has allowed us to quantify the effects of rotation as the edges of the star rotate towards and away from us, and also to analyze the convective motion covering the surface. But stars are also giant balls of gas, and much like a cup of coffee when you spin it, it does not

rotate with the same angular velocity at all positions. The best example to imagine is Jupiter. Its striated clouds give a stark example of differential rotation. The various lanes stream past one another quite rapidly at the lower latitudes, but near the poles they are considerably slower. Our Sun, while not as highly contrasting, displays the same properties. The angular velocity near the solar poles is about 70% of that at the equator.

The differential rotation can be approximated by

$$\omega(\psi) = \omega_0 - \omega_1 \sin^2 \psi = \omega_0(1 - \alpha \sin^2 \psi), \tag{3.247}$$

where $\alpha = \omega_1/\omega_0$, the ratio of the polar to equatorial velocities, and ψ is the heliographic latitude measured from the equator [13, 57]. This correction can easily be included in the previous macro-rotation profile simply by modifying the $v_{eq} \sin i$ term,

$$v_{eq} \sin i \rightarrow v_{eq} \sin i \sin\theta \cos\phi \left[1 - \alpha(\sin i \sin\theta \sin\phi + \cos i \cos\theta)^2\right], \tag{3.248}$$

where θ and ϕ are the polar coordinates described earlier. One of the primary effects of differential rotation is that the contribution of rotational broadening in the polar regions can be significantly reduced. As figure 3.15 shows, more absorption is concentrated at the core of the line, forming an almost triangular shape.

3.5 Equivalent Width

Equivalent width was defined earlier in terms of fluxes as

$$W^{nm}(\phi) \equiv \int_0^\infty \frac{F_\lambda^0 - F_\lambda^{nm}(\phi)}{F_\lambda^0} d\lambda = \int_0^\infty (1 - F_\lambda^{nm,n}(\phi))\, d\lambda, \tag{3.249}$$

and it was noted that for an optically thin gas, there was a linear relation between equivalent width and column density. The equivalent width has a simple interpretation in terms of measured flux: it is the width (generally in Å) of a manufactured rectangular spectral line of unit depth with the same area as the original line (as shown in figure 3.16).

We also noted in section 3.3 that if we worked with the logarithm of the flux, we

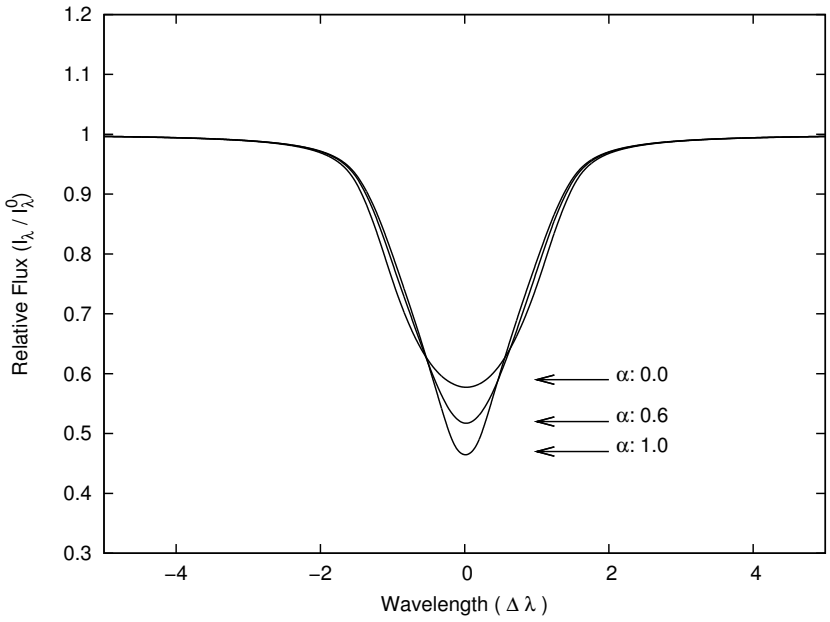

Figure 3.15: Effect of differential rotation with increasing α.

did not need to invoke a thin gas approximation to relate properties of an observed spectral line and the column depth of the corresponding species. Indeed, equation (3.116) shows a simple relation between the area under the natural log of the spectral line and column density. However, it is important to note that these relations were developed without consideration of the effects of extrinsic broadening contributions, such as rotation and macroturbulence. In order to address this issue, we return to equation (3.228), with $\beta = 1$,

$$F_\lambda = \int_0^\infty F^{nm}_{\Delta\lambda_0} G(\lambda - \Delta\lambda_0) d(\Delta\lambda_0). \tag{3.250}$$

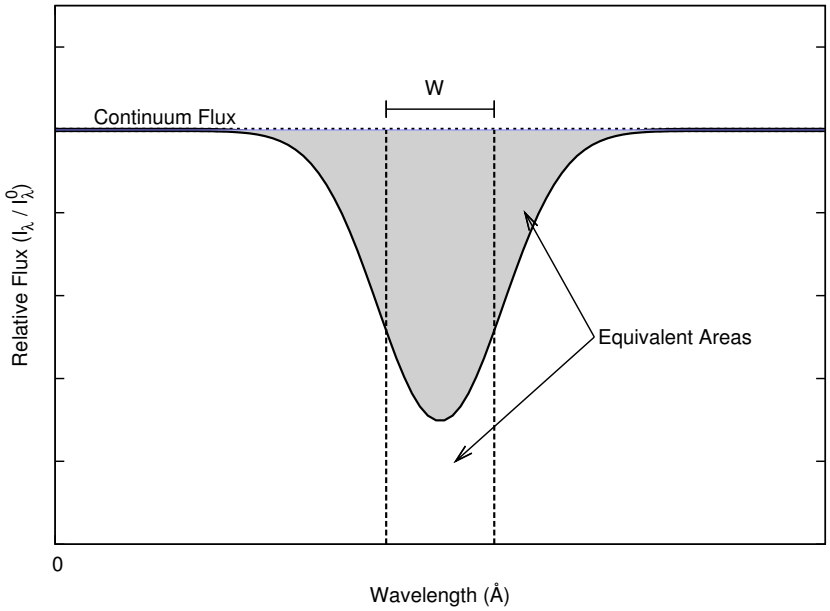

Figure 3.16: Equivalent width matches the area of an absorption line to that of a box relative to the continuum [14].

In the following series of steps, we demonstrate that the equivalent width is unchanged by the addition of extrinsic broadening mechanisms:

$$W(\phi) \equiv \int_0^\infty \frac{F_\lambda^0 - F_\lambda(\phi)}{F_\lambda^0} d\lambda \tag{3.251}$$

$$= \int_0^\infty d\lambda \int_0^\infty \left(1 - F_{\Delta\lambda_0}^{nm,n}\right) G(\lambda - \Delta\lambda_0) d(\Delta\lambda_0) \tag{3.252}$$

$$= \int_0^\infty d(\Delta\lambda_0) \left(1 - F_{\Delta\lambda_0}^{nm,n}\right) \int_0^\infty d\lambda G(\lambda - \Delta\lambda_0) \tag{3.253}$$

$$= \int_0^\infty d\lambda' \left(1 - F_{\lambda'}^{nm,n}\right) \int_0^\infty d\lambda G(\lambda - \lambda'). \tag{3.254}$$

Let Δ be a number considerably greater than the non-vanishing spectral width of F or G. Using this and changes in variables, we find

$$\begin{aligned} W(\phi) &= \int_{\lambda_0-\Delta}^{\lambda_0+\Delta} d\lambda' \left(1 - F_{\lambda'}^{nm,n}\right) \int_{\lambda'-\Delta}^{\lambda'+\Delta} d\lambda G(\lambda - \lambda') \\ &= \int_{\lambda_0-\Delta}^{\lambda_0+\Delta} d\lambda' \left(1 - F_{\lambda'}^{nm,n}\right) \int_{-\Delta}^{+\Delta} d\lambda'' G(\lambda'') \qquad (3.255) \\ &= \int_{\lambda_0-\Delta}^{\lambda_0+\Delta} d\lambda' \left(1 - F_{\lambda'}^{nm,n}\right) (1) \\ &= \int_{\lambda_0-\Delta}^{\lambda_0+\Delta} \left(\frac{F_\lambda^0 - F_\lambda^{nm}}{F_\lambda^0}\right) d\lambda = W^{nm}(\phi), \qquad (3.256) \end{aligned}$$

thereby demonstrating our assertion of the invariance of equivalent width.

Unfortunately, we no longer have the nice relationship between column density and the integrated area under the natural log of the normalized flux (equation (3.116)). However, we can make use of the relationship between column density and the integral of a function containing optical depth, which is, in turn, related to column density. Hence, using

$$W(\phi) = W^{nm}(\phi) = \int_0^\infty (1 - e^{-\tau_\lambda}) d\lambda \qquad (3.257)$$

along with

$$\tau_\lambda(\phi) = \alpha_\lambda \mathscr{N}(\phi), \qquad (3.258)$$

$$\alpha_\lambda = \frac{\pi e^2 \lambda_0^2}{mc^2} f \varphi_\lambda(\lambda - \lambda_0), \qquad (3.259)$$

$$\int_0^\infty \varphi_\lambda(\lambda - \lambda_0) d\lambda = 1, \qquad (3.260)$$

produces an integral equation for the column density. Although this equation cannot be solved for the column density in the general case, one can determine three expressions, each appropriate to one of the three density regimes. These expressions are derived in the next three sections.

Up until this point, the various velocity profiles and absorption coefficients we have derived have been nicely framed to see their key features. But the optical depth is

a function of the profile shape and the number of absorbers. As the number of particles in the line of sight increases, the depth of the line will also scale accordingly. Eventually, the feature will saturate and bottom out at $F = 0$. Yet the number of absorbers can still be increased, and little additional light will be removed from the line of sight. Eventually, enough absorbers can be added to the point that damping wing features become apparent and dominant. These various scaling relations are called the linear, logarithmic, and square root regimes [13, 50]. Figure 3.17 gives a plot of column density vs equivalent width, called the curve of growth, that shows the progression of these various regimes. Figure 3.18 shows the corresponding flux profiles.

3.5.1 Linear Regime

When the optical depth at line center is quite small, $\tau_0 \ll 1$, the gas is optically thin. With τ being sufficiently small, a series expansion gives us $\exp(-\tau_\lambda) \simeq -\tau_\lambda$; hence,

$$W(\phi) = \int_{-\infty}^{\infty} \tau_\lambda(\phi)\,\mathrm{d}\lambda = \mathscr{N}(\phi) \int_{-\infty}^{\infty} \alpha_\lambda\,\mathrm{d}\lambda. \tag{3.261}$$

We can now expand the absorption coefficient,

$$W(\phi) = \frac{\pi e^2 \lambda_0^2}{mc^2}\, f\mathscr{N}(\phi) \int_{-\infty}^{\infty} \varphi_\lambda(\lambda - \lambda_0)\,\mathrm{d}\lambda = \frac{\pi e^2 \lambda_0^2}{mc^2}\, f\mathscr{N}(\phi), \tag{3.262}$$

since the profile function has been normalized. Equation (3.262) is the energy removed from a photon beam by a single absorber multiplied by the column density. In this region of the curve of growth, the equivalent width scales linearly with the column density. As more absorbers are added, we see the line's core deepen substantially. After measuring the equivalent width, the column density can be found with

$$\mathscr{N}(\phi) = \frac{mc^2}{\pi e^2 \lambda_0^2} \frac{1}{f} W(\phi). \tag{3.263}$$

3.5.2 Logarithmic Regime

As the optical depth increases to between $10 \leq \tau_0 \leq 10^3$, the Gaussian core dominates and the Lorentzian damping wings contribute very little. To simplify the calculations,

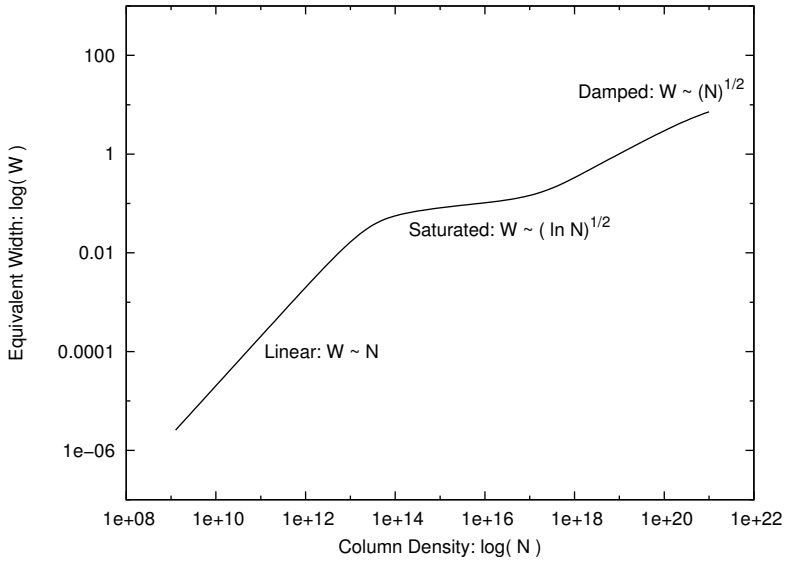

Figure 3.17: Curve of growth and the relation of column density of an absorbing medium to the equivalent width of a line.

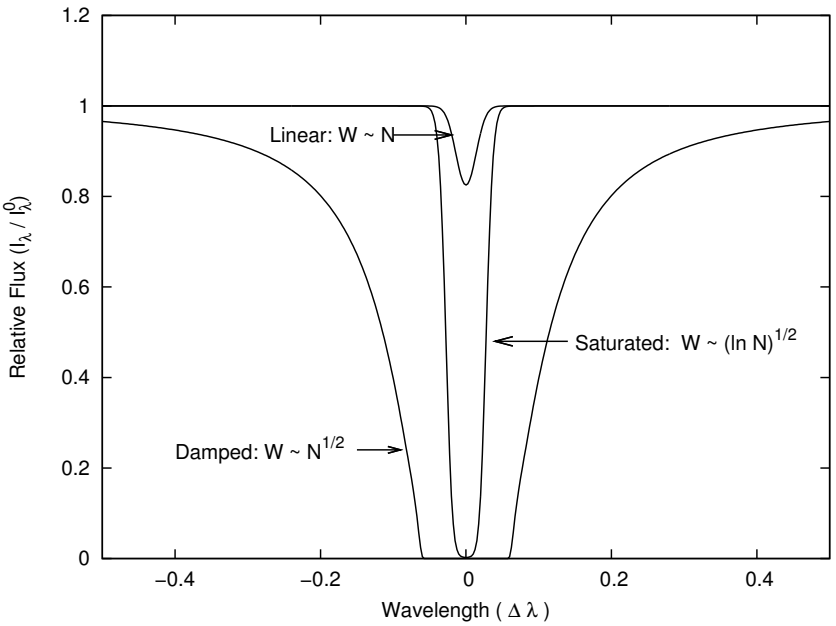

Figure 3.18: Evolution of absorption line shape with increasing column density. In the linear regime, the line is Gaussian in form. Once the line is fully saturated, line growth slows considerably. Once the damping regime is reached, the Lorentzian wings dominate the absorption.

we can take convolution equation (3.198) and approximate the Lorentzian term as a δ function, effectively removing it. The optical depth can then be written as

$$\tau_\lambda(\phi) = \alpha_\lambda \mathscr{N}(\phi) \simeq \frac{\pi e^2 \lambda_0^2}{mc^2} f \frac{1}{\sqrt{\pi}\,\Delta\lambda_D} e^{-(\,\Delta\lambda/\,\Delta\lambda_D)^2} \mathscr{N}(\phi). \tag{3.264}$$

We will condense all the constants into $\tau_0 = (\pi e^2 \lambda_0^2)/(mc^2)(1/\sqrt{\pi}\,\Delta\lambda_D) f\mathscr{N}$ and simplify the argument of the exponential to $x = (\,\Delta\lambda/\,\Delta\lambda_D)$ so that

$$\tau_\lambda(\phi) = \tau_0\, e^{(-x^2)}. \tag{3.265}$$

The equivalent width equation becomes

$$W(\phi) = \,\Delta\lambda_D \int_{-\infty}^{\infty} \left[1 - e^{(-\tau_0\, e^{(-x^2)})}\right] \mathrm{d}x. \tag{3.266}$$

Evaluating the integral gives us

$$W(\phi) = 2\,\Delta\lambda_D \left(\ln\left[\frac{\pi e^2 \lambda_0^2}{mc^2} \frac{1}{\sqrt{\pi}\,\Delta\lambda_D} \mathscr{N} f\right]\right)^{1/2}. \tag{3.267}$$

So as more absorbers are added, most of the flux is removed via the Gaussian wings and core. The equivalent width increases at a much slower rate, scaling with $W \propto \sqrt{\ln \mathscr{N}}$. This region along the curve of growth is the most prone to error. A measurement of an equivalent width from the spectral data, even if is a little bit off, could yield a result that is incorrect by many orders of magnitude. Solving for the column density yields

$$\mathscr{N}(\phi) = \frac{mc^2}{\pi e^2 \lambda_0^2}\, \frac{1}{f} \sqrt{\pi}\,\Delta\lambda_D\; e^{-\left(\frac{W(\phi)}{2\,\Delta\lambda_D}\right)^2}. \tag{3.268}$$

3.5.3 The Square Root Regime

As the optical depth increases to even larger values, $\tau_0 \geq 10^4$, the line core will have long since saturated, and the Lorentzian damping wings will show a greater effect and overtake the Gaussian wings. Since the Gaussian features play no significant role, we can take equation (3.198) and set the Gaussian term as a δ function, giving us

$$\tau_\lambda(\phi) = \alpha_\lambda \mathscr{N}(\phi) \simeq \frac{\pi e^2 \lambda_0^2}{mc^2}\; f\; \frac{\Gamma \lambda_0^2 / 4\pi^2 c}{(\Delta\lambda)^2 + (\Gamma\lambda_0^2/4\pi c)^2} \mathscr{N}(\phi), \tag{3.269}$$

which can be simplified using $\gamma \equiv \Gamma\lambda_0^2/4\pi c$; hence,

$$\tau_\lambda(\phi) = \frac{e^2\lambda_0^2}{mc^2}\, f\, \frac{\gamma}{(\Delta\lambda)^2+\gamma^2}\mathscr{N}(\phi). \tag{3.270}$$

Since the the dominant line absorption takes place in the wings, which are far from the line center, we can again gather the constants into $\tau_0 = (e^2\lambda_0^2/mc^2)f\gamma\mathscr{N}$ and make the approximation that $\Delta\lambda \gg \gamma$; hence,

$$\tau_\lambda(\phi) = \frac{e^2\lambda_0^2}{mc^2}\, f\, \frac{\gamma}{(\,\Delta\lambda)^2}\frac{1}{(1+(\gamma/\,\Delta\lambda)^2}\mathscr{N}(\phi) \simeq \frac{\tau_0}{(\,\Delta\lambda)^2}. \tag{3.271}$$

Therefore the equivalent width becomes

$$W(\phi) \simeq \int_{-\infty}^{\infty}[1-e^{(-\tau_0/(\,\Delta\lambda)^2)}]\,\mathrm{d}\lambda. \tag{3.272}$$

Making the substitution $u^2 = (\,\Delta\lambda)^2/\tau_0$ and $\mathrm{d}u = \mathrm{d}\lambda/\sqrt{\tau_0}$, the integral becomes

$$W(\phi) \simeq (\tau_0)^{1/2}\int_{-\infty}^{\infty}[1-e^{(-1/u^2)}]\,\mathrm{d}u. \tag{3.273}$$

The evauluation of the above integration yields $2\sqrt{\pi}$, hence using the definition of γ above, we arrive at

$$W(\phi) = \lambda_0^2\left[\frac{e^2}{mc^3}f\Gamma\mathscr{N}\right]^{1/2}. \tag{3.274}$$

Thus the equivalent width in this regime goes as $W \propto \sqrt{\Gamma\mathscr{N}}$. Therefore this section along the curve of growth is referred to as the "square root" or "damping" regime. The solution for the column density can be found as

$$\mathscr{N}(\phi) = \frac{mc^3}{\Gamma f e^2}\left(\frac{W(\phi)}{\lambda_0^2}\right)^2. \tag{3.275}$$

3.6 Computational Applications

3.6.1 TLUSTY and SYNSPEC

A vital component of the techniques used in this project are the TLUSTY and SYNSPEC programs, first developed by Hubeny in 1988 [44]. Together, the two programs can simulate a stellar atmosphere and its associated spectra. TLUSTY uses the

hybrid complete linearization/accelerated lambda iteration (CL/ALI) method to compute a *non local thermodynamic equilibrium* (LTE) model of the stellar atmosphere [58]. The program simultaneously solves the radiative transfer equation, hydrostatic equilibrium equation, radiative equilibrium equation, the set of statistical equilibrium equations for specified atomic energy levels, charge and particle conservation, and the equations for opacities. The CL/ALI computationally optimizes the whole process and results in a set of vectors, ψ_d, at all possible optical depths. The vectors are given by

$$\psi_d = \{J_1, ...J_{NF}, N, n_e, n_1, ...n_{NL}\} \tag{3.276}$$

where J_i is the mean radiation intensity at each frequency point, NF is the number of frequency points, N is the total particle number density, n_e is the electron density, n_i is the number density (population) of energy level i, and NL is the number of atomic energy levels being considered. The model atmosphere is then passed to the SYNSPEC program which then generates the model photospheric spectrum. The initial spectrum factors in the model atmosphere and given atomic abundances, and then calculates basic Voigt profiles based on the mechanisms of natural broadening, all applicable collisional broadenings, microturbulence, and thermal broadening. A subsequent program, ROTINS3, may then be used to simulate rotational broadening or instrumental broadening. SYNSPEC does not handle macroturbulence nor differential rotation, but can be used to simulate accretion disk structures. The output of SYNSPEC includes multiple diagnostic files, as well as the flux output and continuum output. A further program was introduced by the author to interpolate the output flux and continuum onto a uniform wavelength grid for ease of use in Gnuplot programs and for comparison with U Cep data.

3.6.2 Tupaspec

Tupaspec was developed by the author to synthesize a theoretical absorption line while taking into consideration as many contributions to the line shape as possible. The program begins with determining the various factors that create the Voigt profile: natural broadening, collisional broadening, microturbulence, and thermal broadening. The original thrust of the program was to simulate photospheric lines, so a velocity distribution profile that includes rotation, macruturbulance, and differential rotation

is computed. There is even a further option that allows one to simulate the inclination of the star. Later in the development, it became obvious that features such as gas streams could not be adequately modeled using rotation and macroturbulence velocity distributions. An added function was implemented to allow one to switch to a user defined velocity distribution. This distribution function could be any best guess of the structure of the absorbing medium, such as a box function or a Gaussian.

The intrinsic line profile and velocity distribution profile can then be convolved together to create the synthetic profile shape. Further calculations determine the line's equivalent width and position on the curve of growth. The main strength in the program lies in the ability to control all of the available physical parameters that make up the line. Many of these parameters are set by the situation, such as gas temperature or various atomic properties. The most important free parameter is the column density. When we successfully fit an absorption feature in the data with this program, we can directly measure the column density via the input parameters.

3.7 Ions of Interest - Practical Considerations

As the unbroadened synthetic stellar atmosphere model indicates, there are innumerable absorption lines contributing to the total spectra. To extract any meaningful data regarding the system, an abbreviated list of lines for close examination must be compiled. Due to the high rotation of U Cep, many of the smaller lines will be blended away, others in denser collections will create false absorption lines. The main lines of interest are the strong ground state transitions that have enough optical depth to survive the blending process, yet maintain a definitive shape. Dr. Wecht compiled a comprehensive list of possible lines that are viewable in the spectral window given by the IUE data [59]. Lines that could be present in temperature regions from 10,000 K to 30,000 K were included. Not only did a spectral line have to be present, but it had to be sufficiently analyzable. The signal to noise ratio had to be high enough to actually distinguish the morphology of the line, making Fe II 2599 Å an unlikely candidate. Blending with other lines had to be treated carefully. The forest of strong Si II and Si III lines in the 1294 Å – 1310 Å region were so closely packed together

Ion	Wavelength (Å)	Configuration	$J_i \rightarrow J_k$	f_{ij}
Si II 1260	1260.42	$3s^2 3p - 3s^2 3d$	$\frac{1}{2} - \frac{3}{2}$	1.22
Si II 1264	1264.74	$3s^2 3p - 3s^2 3d$	$\frac{3}{2} - \frac{5}{2}$	1.09
C II 1334	1334.53	$2s^2 2p - 2s 2p^2$	$\frac{1}{2} - \frac{3}{2}$	0.127
C II 1335	1335.71	$2s^2 2p - 2s 2p^2$	$\frac{3}{2} - \frac{5}{2}$	0.114
Si IV 1393	1393.76	$2p^6 3s - 2p^6 3p$	$\frac{1}{2} - \frac{3}{2}$	0.513
Si IV 1402	1402.77	$2p^6 3s - 2p^6 3p$	$\frac{1}{2} - \frac{1}{2}$	0.255
Si II 1526	1526.72	$3s^2 3p - 3s^2 4s$	$\frac{1}{2} - \frac{1}{2}$	0.133
Si II 1533	1533.45	$3s^2 3p - 3s^2 4s$	$\frac{3}{2} - \frac{1}{2}$	0.133
C IV 1548	1548.2	$1s^2 2s - 1s^2 2p$	$\frac{1}{2} - \frac{3}{2}$	0.19
C IV 1550	1550.77	$1s^2 2s - 1s^2 2p$	$\frac{1}{2} - \frac{1}{2}$	0.095
Al II 1670	1670.79	$2p^6 3s^2 - 3s 3p$	0 – 1	1.83
Al III 1854	1854.72	$2p^6 3s - 2p^6 3p$	$\frac{1}{2} - \frac{3}{2}$	0.557
Al III 1862	1862.79	$2p^6 3s - 2p^6 3p$	$\frac{1}{2} - \frac{1}{2}$	0.277

Table 3.1: Lines of Interest

that it is impossible to tell where one line ends and the other begins. However, the C II 1334 & 1335 Å doublet was blended enough to appear almost as one line, but had a predictable enough behavior that it could be examined. Table 3.1 lists the ions of focus in this study, all of which are located in the SWP IUE images. Additional details appear in Appendix A. The few lines present in the LWP/R images were either too weak to be seen or presented an untenable absorption structure for analysis. It should also be noted that all of the lines, save the Al II 1670 Å transition, are part of doublet pairs, which allow for additional insights from our method of analysis.

3.7.1 Interstellar Lines

Due to U Cep's quite substantial distance from Earth, there is a high occurrence of intervening gas between the IUE satellite and the observation target. This gas comes in the form of diffuse hot gas clouds. This gas does not contribute any light to the observed flux, but can contaminate the data with its own absorption lines. Fortunately, these intervening lines are normally easy to distinguish from the stellar lines. They appear as deep and sharp Voigt profiles superimposed on the stellar

Line	Wavelength (Å)	Radial Velocity (km/s)
Al II	1670	20
C II	1334	15
C II	1334	35
Si II	1526	15
S II	1255	15
SI II	1260	20

Table 3.2: Interstellar Lines. Radial velocities were determined by this work.

data. Most often these profiles appear in our data as double peaks, with blue shifts of approximately 15 and 35 km/s, as indicated in table 3.2. The saturation of the optical depth could be attributed to the cloud(s) being quite thick. There is slight thermal broadening, which is to be expected as the transitions occur with lines that typically exist in temperature regions of 5,000 – 18,000 K. But most importantly, the interstellar lines do not change position or shape with the phases of the binary star. There are some slight fluctuations from image to image, but that is most likely due to varying exposure times of the images and noise. Due to their static nature, these lines can later be removed by dividing the data by the average interstellar line profile shape. Further discussions of interstellar lines appear in the sections describing line morphology.

3.7.2 Ionization Fractions

If the temperature is high enough in a gas, the atoms will have sufficient energy due to thermal collisions to ionize some of those atoms; that is, strip off or eject electrons from parent atoms. The common notation to indicate the degree of ionizations uses the roman numeral I for neutral atoms and increments the numerals for each subsequent electron removed; i.e., C IV is a carbon atom that is missing three electrons. The Saha equation allows for the estimation of the proportion of various ionic species for a given temperature and electron pressure [60]; hence,

$$\frac{N_{i+1}}{N_i} = \frac{2kTZ_{i+1}}{P_e Z_i} \left(\frac{2\pi m_e kT}{h^2}\right)^{3/2} e^{-\chi_i/kT}, \tag{3.277}$$

where i is the ionization state, N_i is the state population, Z_i is the partition function for a given state, χ_i is the ionization energy, and P_e is the electron pressure. The

partition functions are given by

$$Z = \sum_{j=1}^{\infty} g_j e^{-(E_j - E_1)/kT}, \tag{3.278}$$

where g_j is the degeneracy of the j^{th} level of ionization state and E_j is the energy for the j^{th} level. Additionally, the electron pressure is given by

$$P_e = n_e kT, \tag{3.279}$$

where n_e is the electron density. The ionization fraction is given by the ratio of the number of atoms in that state to the total number of that type of atom, so that

$$X_i = \frac{N_i}{N_0 + N_1 + ... + N_{imax}} \tag{3.280}$$

$$= \frac{1}{\frac{N_0}{N_i} + \frac{N_1}{N_i} ... + 1 + ... \frac{N_{imax}}{N_i}}. \tag{3.281}$$

We can then construct plots of the various expected ionization fractions to help us predict what lines to expect in the spectral data as well as get a sense of their relative strength. Figure 3.19 shows how the ion populations vary with changing electron pressure and figure 3.20 shows how the populations change with temperature. For a full list of the various ionization fractions, see Appendix D. Aller computed an electron pressure for U Cep of $P_e = 320$ dynes/cm^2 or $\log(P_e) \sim 2.5$ [49]. The ionization fraction plots suggest that for a stellar atmosphere around 11,000 to 15,000 K and an electron pressure of $\log(P_e) \sim 2.5$ we would expect to see C II, and the second (about 30%) and third (about 70%) ionization states of both Si and Al. This is supported by the observational data, and the list of major absorption lines that are found in the spectra is given in table 3.1. The only two anomalous lines in that list are the C IV and Si IV features. As figure 3.20 indicates, you would need much higher temperatures for those lines to be present. Anywhere between 18,000 and 33,000 K for Si IV and 25,000 to 43,000 K for C IV would yield an appreciable absorption feature for the given atmospheric electron pressure. Naturally, those temperature ranges would be lower with a smaller electron pressure or higher with a larger P_e, but we would still not expect to see those lines in the photosphere. To account for their presence it could be considered that there is a extremely hot region of gas in the observer's line of sight, but as we will show in section 4.7, this is not necessarily the case.

When considering possible gas stream effects, we cannot know immediately the stream's average temperature or electron pressure. But if we can isolate line features for the gas stream for different ions of the same atomic type, we can determine what the temperature and pressure could be.

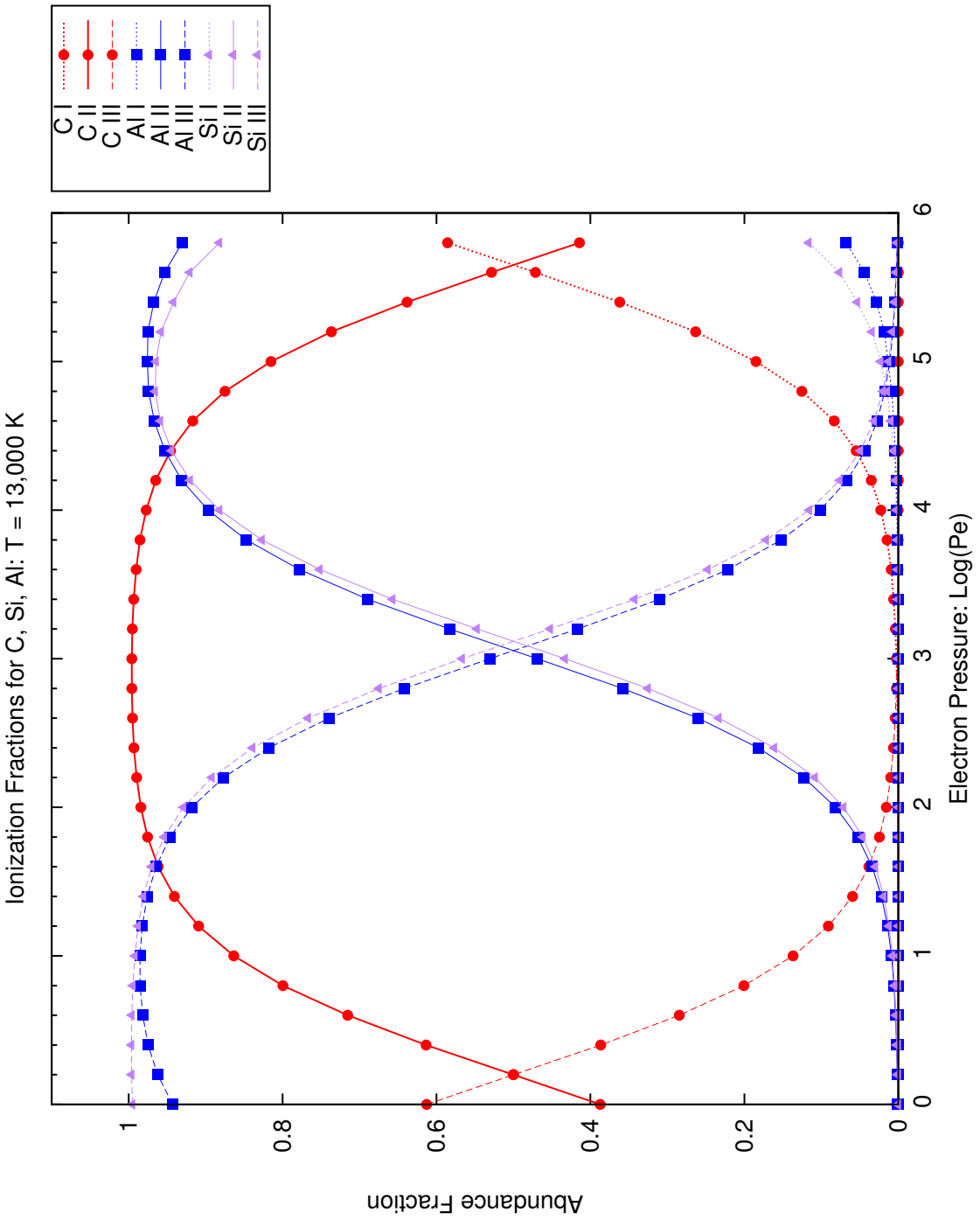

Figure 3.19: Abundance ratios for the elements C, Si, and Al at an average temperature of 13,000 K varying with electron pressure, P_e. As P_e increases, it is more likely for an atom to capture an electron and exist in a lower ionization state.

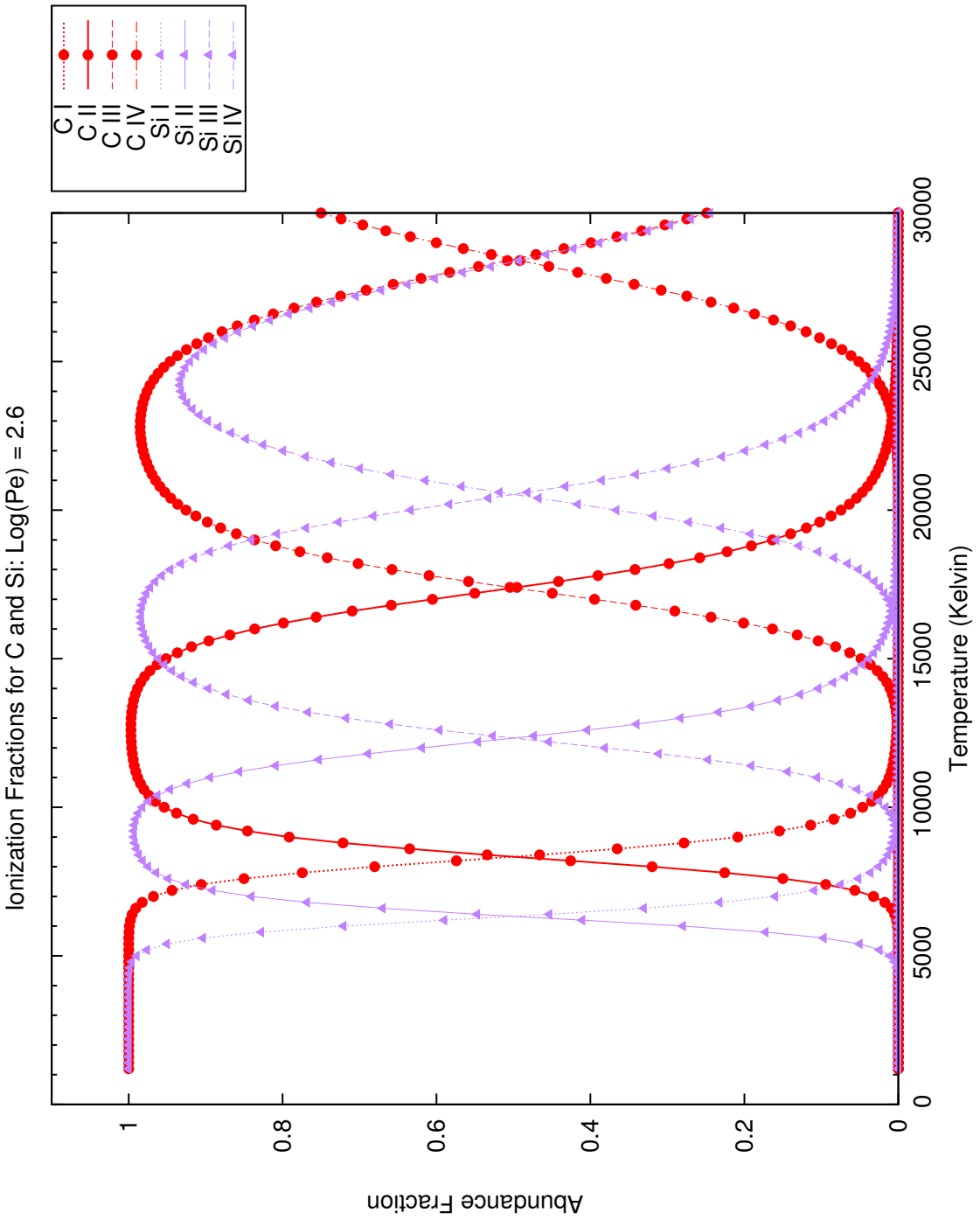

Figure 3.20: Abundance ratios for the elements C and Si at a given $log(P_e) = 2.6$ varying with temperature. As T increases, it is more likely for an electron to be stripped from its parent atom, leading to higher and higher ionization states.

Chapter 4

Data Analysis Techniques and Results

4.1 Overview

In this chapter we will discuss the various analytical techniques utilized to quantify the properties of U Cep. Some methods have been built upon those used in past works, while others had to be created and adapted to suit the peculiarities presented by this particular binary system. The techniques we apply to the various absorption lines are sound in theory, but occasionally other factors conspire to contaminate and obfuscate the phenomena we wish to understand. In the end, we will employ the data to present a coherent model of U Cep.

4.2 IUE Data

All of the analyzed data was obtained by the *International Ultraviolet Explorer* (IUE) (pictured in figure 4.1). This satellite was launched in 1978 with an expected program lifetime of 3 years, but lasted far longer than anyone could have anticipated, finishing its mission nearly 19 years later [61]. With over 100,000 images obtained, and over 3,000 refereed journal articles arising from the mission, IUE is considered one of the most productive satellites ever launched. IUE was a collaborative effort of 31 countries, including such organizations as the US National Aeronautics and Space

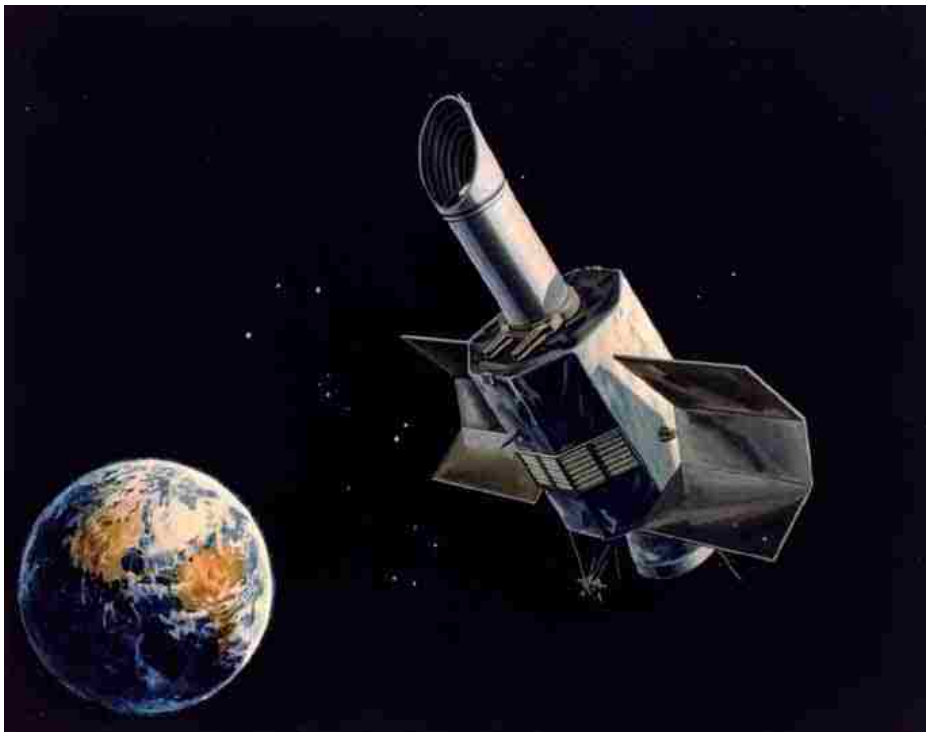

Figure 4.1: IUE Satellite Promotional Image [15]

Administration (NASA), the UK Science and Engineering Research Council (SERC), and the European Space Agency (ESA).

The satellite had two types of imaging tools: the short-wave cameras had a spectral range of 1150 – 2000 Å and the long-wave cameras could view wavelengths from 1850 – 3400 Å. A simplified schematic is shown in figure 4.2. Each type had a primary and backup, or redundant, camera. Since the short-wave redundant was not operational for most of the mission, operational imaging systems consisted of the long-wave primary (LWP), long-wave redundant (LWR), and short-wave primary (SWP) cameras [61]. All of the cameras could be operated in high dispersion or low dispersion modes. The low dispersion spectra were primarily used for spectrophotometric studies and only had a resolution of about 6 Å. The high dispersion mode was used for spectroscopic studies and had a much finer resolution of 0.1 – 0.3 Å.

During the mission lifetime there were some operational difficulties. IUE was launched

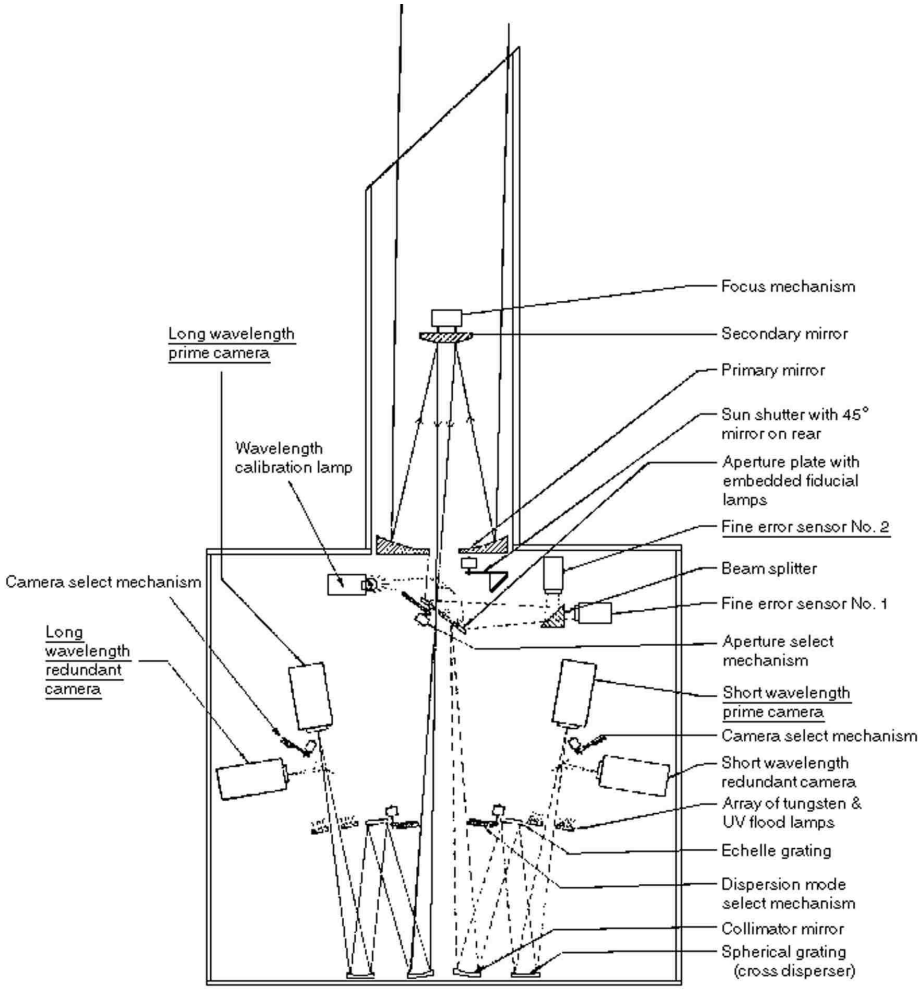

Figure 4.2: Cutaway of internal scientific instruments on board IUE. [16]

with 6 stabilizing gyroscopes, and needed only 3 to work properly. But by 1985, eight years into the mission, four of the gyroscopes had ceased working [61]. Fortunately, using the *Fine Sun Sensor* as a substitute gyroscope allowed the mission to continue for another 11 years. Other technical difficulties included vibrations emanating from the IUE TV camera tubes, which may have contributed to the noise in spectral images taken with the satellite. The LWR camera's heating element introduced "pings" that affected its images. And it was later determined that there were non-random, systematic noise patterns introduced into the data that arose due to a misalignment with the 2-D *Intensity Transfer Functions* (ITF). The ITF were used in the data processing when the raw two dimensional images were corrected for various sensitivities

Table 4.1: IUE SWP Observations of U Cep

Data ID	Obs. Start Time (UT)	Exp. Time (s)	Disp.	UCep Phase
SWP36990	09/11/89 10:35	2700	HIGH	0.335
SWP36991	09/11/89 12:01	2400	HIGH	0.358
SWP36994	09/11/89 19:37	2400	HIGH	0.485
SWP36995	09/11/89 21:02	2520	HIGH	0.509
SWP36997	09/12/89 00:00	2280	HIGH	0.558
SWP36998	09/12/89 01:24	2520	HIGH	0.582
SWP37000	09/12/89 07:46	2400	HIGH	0.688
SWP37004	09/12/89 15:32	2400	HIGH	0.818
SWP37007	09/12/89 23:26	3600	HIGH	0.953
SWP37012	09/13/89 07:19	3600	HIGH	0.084
SWP37015	09/13/89 14:09	2400	HIGH	0.196
SWP37018	09/13/89 20:24	2400	HIGH	0.300
SWP37022	09/14/89 04:14	2400	HIGH	0.431
SWP37024	09/14/89 10:02	2400	HIGH	0.528

of the camera and converted into linearized flux data [62]. The entire data archive was re-reduced to minimize the effect of this error and reduce signal to noise ratios by up to 40%. The subsequent updated archive was titled NEWSIPS, and included quality flags that noted the reliability of the data points.

The IUE satellite took 104 images of U Cep over a 10 year period, sometimes one image at a time, other times in groups during a certain period, or epoch. The longest continuous series of pictures was obtained in September 1989, where IUE took 29 images, one after another, alternating between the SWP and LWP/R cameras. These images cover just over a full period of orbit for the system, and the high dispersion set forms the basis for most of the research conducted in this dissertation. Orbital orientations for the phases of the SWP images are shown in figure 4.3. Tables 4.1 and 4.2 list all of the U Cep observations taken by IUE for the September 1989 epoch. Tables identifying the full set of U Cep images can be found in appendix B.

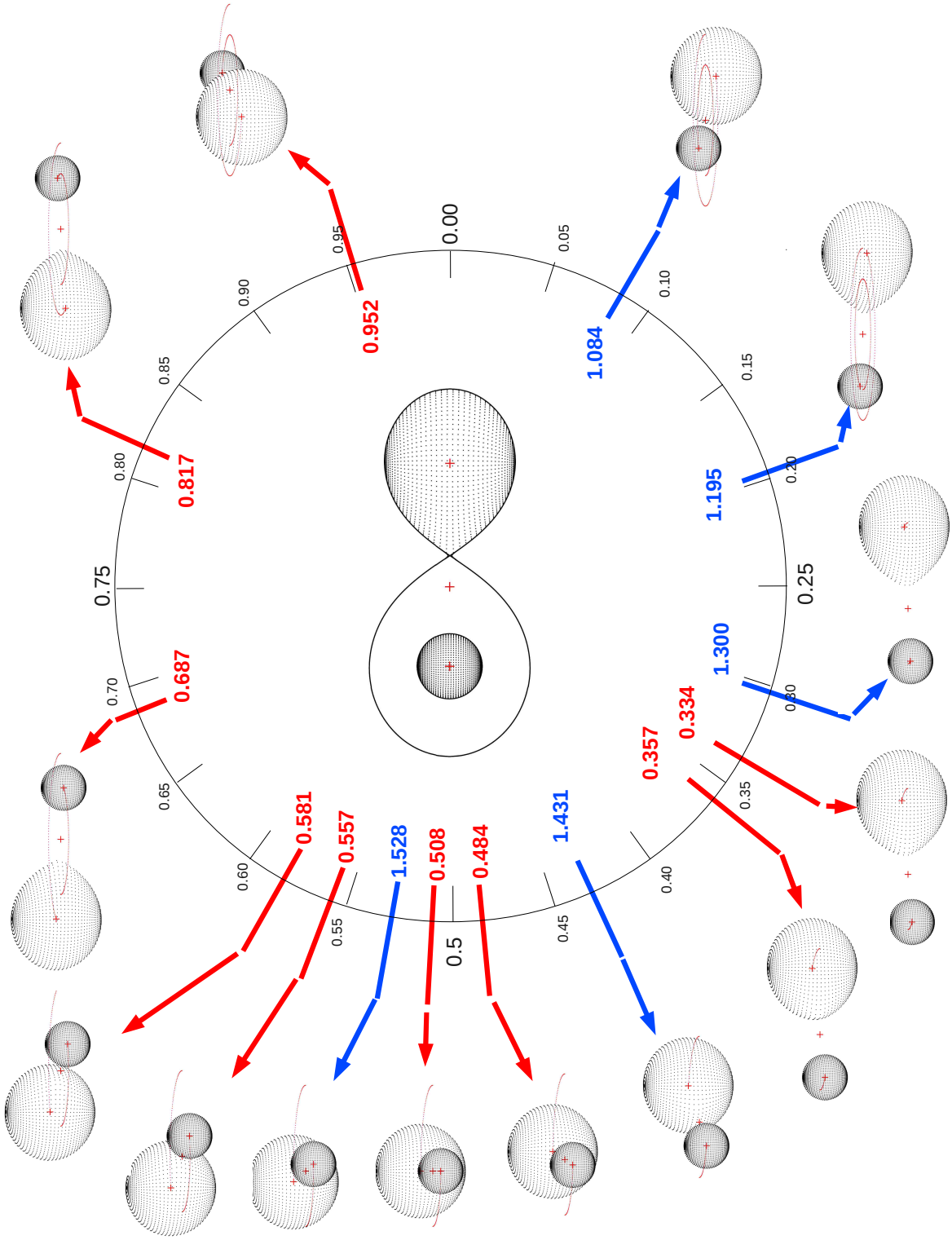

Figure 4.3: U Cep orbital orientations during SWP images.

Table 4.2: IUE LWP/R Observations of U Cep

Data ID	Obs. Start Time (UT)	Exp. Time (s)	Disp.	UCep Phase
LWP16328	09/11/89 11:29	1320	HIGH	0.35
LWP16331	09/11/89 19:09	1200	HIGH	0.47
LWP16332	09/11/89 20:26	1260	HIGH	0.5
LWP16334	09/12/89 00:48	1200	HIGH	0.57
LWP16335	09/12/89 02:18	1200	HIGH	0.59
LWP16337	09/12/89 07:17	1200	HIGH	0.68
LWP16341	09/12/89 16:20	1200	HIGH	0.83
LWP16344	09/12/89 22:28	1800	HIGH	0.93
LWP16346	09/13/89 02:14	4200	HIGH	0
LWP16348	09/13/89 08:39	1800	HIGH	0.1
LWP16351	09/13/89 14:59	1200	HIGH	0.21
LWP16354	09/13/89 21:13	1200	HIGH	0.31
LWP16345	09/13/89 00:34	3000	HIGH	0.97
LWP16357	09/14/89 05:05	1200	HIGH	0.44
LWP16359	09/14/89 10:50	1200	HIGH	0.54

4.3 Overview of U Cep and Standard-Star Analysis

Standard stars allow us to check our theoretical calculations against real world situations. If a TLUSTY spectrum does not match the raw U Cep data, what does that imply? Is the simulated spectrum simply incorrect or are there other physical phenomena occurring in the actual system that warrant closer examination? A comparison with less complicated systems can help remove several layers of uncertainty. Among the many candidates to use in a comparison, Regulus (HD 87901) stands out as almost ideal. Regulus and U Cep are the same spectral type B7/8 V, have roughly the same surface temperature (10,000 – 15,000 K), and have similar rotational rates (300 – 315 km/s). Regulus is known to be quite oblate due to its high rotation. This property of Regulus was discovered via advanced interferometric techniques, aided by the fact that it is much closer to Earth than U Cep (77 ly vs 550 ly) [63]. The two stars share an extremely high rotational velocity, so it is possible for this oblateness feature to develop in the primary of U Cep, but there has been no treatment of this in the literature. Of course, such features in the U Cep primary would be affected by

the presence of a companion.

In comparing Regulus and U Cep, we find both coinciding spectral features, and sometimes differences. Another approach to the problem is to compare U Cep with a similar binary system exhibiting less noise and blending. Algol is a good candidate for this task. Algol has a similar spectral type and temperature as U Cep, but its rotational velocity is much lower, (65 km/s) [59] . This system allows us to view possible features common to mass transfer binaries that would not appear in the spectra of an isolated star such as Regulus. Figure 4.4 gives a comparative plot of the two standard stars and U Cep for the Si II 1526 & 1533 lines. Each observed spectrum has been fitted with a TLUSTY simulated spectrum appropriate to each star's rotational velocity. Algol (top) presents lines that are narrow with excess absorption at the line core, while Regulus's (middle) absorption lines are quite broad, shallow and bowl shaped. The U Cep data (bottom) presents a more complicated combined morphology of the other two stars. But it should be noted that we are not saying U Cep should look like a superposition of both Regulus and Algol. We are merely using these two exemplary stars as a point of reference to identify commonalities as well as divergences. The standard stars help us in identifying what could be a well understood feature or point us to a more interesting occurrence that warrants further investigation.

4.4 Overview of the Application of TLUSTY/ SYNSPEC and Tupaspec to U Cep

As described earlier, TLUSTY/SYNSPEC only requires user input values of surface temperature, gravimetric field, and rate of rotation. (Note: "TLUSTY" may at times be used to refer to the full sequence of programs described in section 3.6.1.) These values were selected from a range identified by measurements reported in previous publications. Although we did select a temperature of 13,000 K and an equatorial

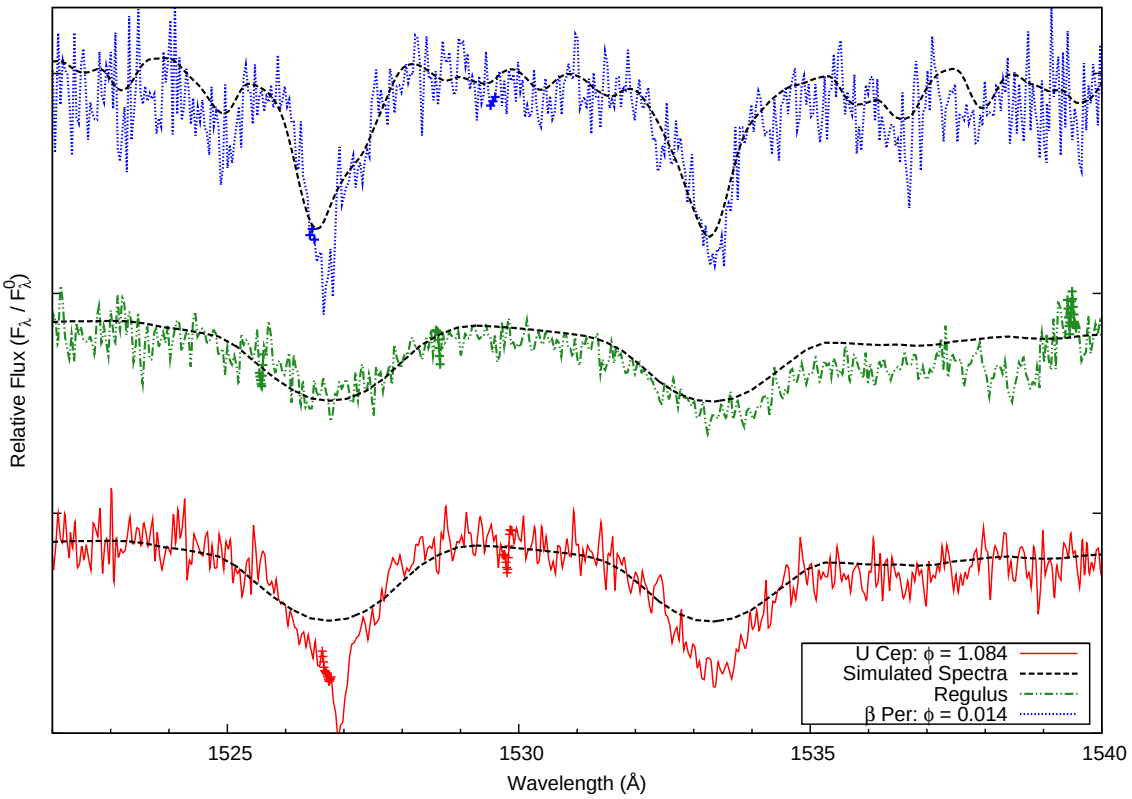

Figure 4.4: Standard stars β Per (top) and Regulus (middle) compared with U Cep spectra of the Si II 1526 & 1533 region for phase 1.084. A simulated spectrum (dashed line) for each spectrum has been calculated for rotational velocities appropriate to each star.

rotational velocity of 300 km/s to optimize the overall agreement with our data, selecting other values from over most of the accepted ranges would have made little difference. Furthermore, no specific feature of interest was chosen for a best fit in selecting our values of temperature and velocity. Therefore, in the context of an isolated B-star, TLUSTY parameters were not fit to any specific feature in our data. However, there is a connection between TLUSTY and our data that results from the use of TLUSTY in the normalization of our data. As we describe in greater detail in subsequent sections, by scaling the observational (unnormalized) flux data to best match TLUSTY simulations in each 20-30 Å wavelength interval, we normalized the data and establish wavelength-dependent continuum flux values. Note that in the context of flux, normalization means that flux values range from zero (complete absorption) to one (no absorption).

Since U Cep is a binary system, the B-star exhibits a radial motion with respect to the sun with velocities ranging from -120 km/s to +120 km/s. Of course, the spectra we observe result from a combination of a rotating and perhaps turbulent and disturbed photosphere, and other gases flowing within and out of the system. Even a cursory examination of the spectra reveals broadened lines that are Doppler shifted in a sinusoidal pattern with phase, as one would expect for a point emitter or absorber moving along the orbital path. However, instead of assuming such a path, we describe in this chapter a procedure by which we shift the TLUSTY simulated spectra to longer or shorter wavelengths so as to match the broader lines in the data, presumed to represent the photosphere rotating at 300 km/s and revolving around its companion. Hence, we establish the radial component of the orbital velocity of the star (the photosphere) as a function of phase. (One might describe this as a fit; however, it is more like a policeman determining the speed of a car by matching his or her speed to that of the car.)

All of the electronic transitions considered have line shapes that appear more cluttered on the short-wavelength side, yet more like TLUSTY simulations on the long-wavelength side. Furthermore, the short wavelength clutter seems to contain distinguishable features that we propose to be evidence of gas flow outside of and moving independently of the photosphere. On the basis of this hypothesis - which we show is supported by, or at least very consistent with, the analysis described in the next chapter - we Doppler shift TLUSTY simulations to match the long-wavelength side of the broad photospheric features. These Doppler-shifted TLUSTY spectra are then used to remove from the normalized, observed spectra those features associated with the photosphere of a B-type star rotating at 300 km/s and in orbit about its partner in the binary system.

This brings us now to the Tupaspec program. Tupaspec simulates the normalized flux produced by a gas moving independently of the photosphere. Since it is not part of a model-atmosphere simulation and does not necessarily move with the photosphere, the user must input column density, radial velocity, a macroscopic velocity

distribution, electron density, and temperature. Using the line shape formalism described earlier in this chapter, Tupaspec produces a spectral line shape for each ion species and transition under consideration. In the absence of other information, we use a temperature of 13,000 K (same as the photosphere). The electron density, equivalent in our case to hydrogen density, is determined self consistantly from the number density produced by the fit. Hence, it is not truly an adjustible parameter. Beyond this, Tupaspec uses three parameters to fit a set of features presumed to be due to a gas flow between the stars, as described in this chapter. These parameters provide us with the column density, radial velocity, and range of velocities for this flow feature. By estimating the length of the column, we can determine an approximate value for the number density.

4.5 Continuum Analysis

4.5.1 Project History-Continuum Fitting

In order to fully utilize the spectral data, we must first identify the location of the continuum. One can think of the continuum as the level of ambient flux if there were no absorptions or other features that would cause light extinction. The continuum might be roughly approximated by the black body curve of the radiating object. However, line blanketing, bound-free transitions and extreme rotation can seriously cloud the identification of the continuum. The continuum distribution curve can vary quite substantially over wide spectral regions, but plots of portions that are 10 Å to 50 Å wide will appear to be flat and level. We can determine the average level in these small sections to then construct a continuum plot. The data from the NEWSIPS archive come un-normalized and report fluxes on the order of $10^{-11}(\mathrm{erg/cm^2/s/\AA})$. Measuring the continuum values must be done carefully, as they set the baseline for all of the analysis to follow. In the normalized plots, this sets the $F^n_\lambda = 1$ level from which the absorption lines are measured.

In one time-honored technique, the normalization involves identifying the continuum level by manually drawing horizontal lines at the values of the fluxes in apparent line-absorption-feature-free regions of the data. Because some groupings of blended

absorption features could be quite wide, broad sections of 50 Å were analyzed at a time. This would give a reasonably constant continuum value over the region. This technique was applied to IUE data by McCluskey et al. [32] and later utilized by Dr. Kristen Wecht in her analysis of β Per [59]. The advantage of this technique is that the wide view allows one to avoid smaller local variations in the spectrum that could be due to multiple blended lines. One of the weaknesses of this method (although it could also be considered a strength) is the susceptibility to a subjective perception of where to place a continuum line. A fair amount of practice is required to know where it is reasonable to set the continuum.

On a subsequent project, Reed et al. developed a new method, utilizing the IDL programming language, which removed a large degree of subjectivity from the fit [7]. Part of his program would target narrow sections of the spectra that were assumed to be relatively free of absorption lines, and find the average flux level. This was done at the selected wavelength over all of the spectral image files available, and thus was very time efficient. This method was difficult to apply to U Cep since the high rotation rate creates wide swaths of blended lines. Especially in the lower wavelength regions of the SWP images, there are very few suitable line-free regions.

4.5.2 Continuum Damping via Blending

Over the course of this study, as familiarity with the project grew and techniques advanced, the continuum of U Cep was constantly revised. Initially, the manual method of Wecht was employed. Later, due to its extreme efficiency, the Reed IDL routine (Phillview) was employed to check for consistency. Figure 4.5 shows example placements arrived at via these two different methods. There is relatively good agreement in the placement of both continuum lines.

We later learned that this method could underestimate the actual continuum level for stars with high rotational velocities. This problem was discovered while using the TLUSTY output to investigate how the apparent spectra changes with increasing rotational velocities. The normalized TLUSTY spectra is densely packed with many thin but saturated absorption lines. Recall that rotational broadening conserves the

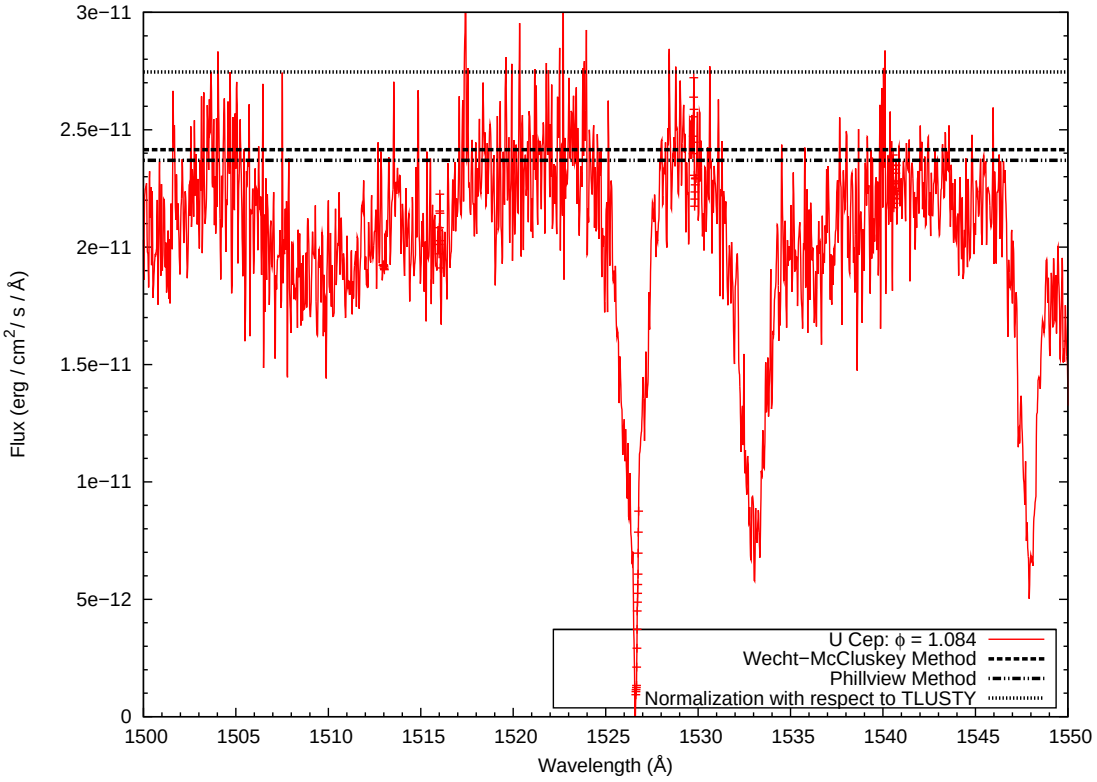

Figure 4.5: Example of Wecht-McCluskey and Phillview method applied by P. Tupa to U Cep over a 50 Å region. The Si II 1526 & 1533 doublet lines are shown.

equivalent width of a line, but redistributes the profile over a wider wavelength range as $v_{eq} \sin i$ increases. At very large $v_{eq} \sin i$, the absorption feature will appear almost flat and very wide. When gathering a large number of lines together and rotationally broadening them simultaneously, those flat absorption profiles will combine and seemingly depress the continuum. Figure 3.13 and 4.5 show how the apparent continuum levels can be as much as 20% below the actual value. Also note that areas in the figure that are more densely packed with these minor lines could be interpreted as a much larger single absorption line.

Considering that U Cep would have its apparent continuum dampened to the same degree as these simulations suggests that it may be underestimated by these approaches. But this poses the question of how do you determine a continuum level to correct for this issue? One method is to normalize the raw U Cep spectral data with

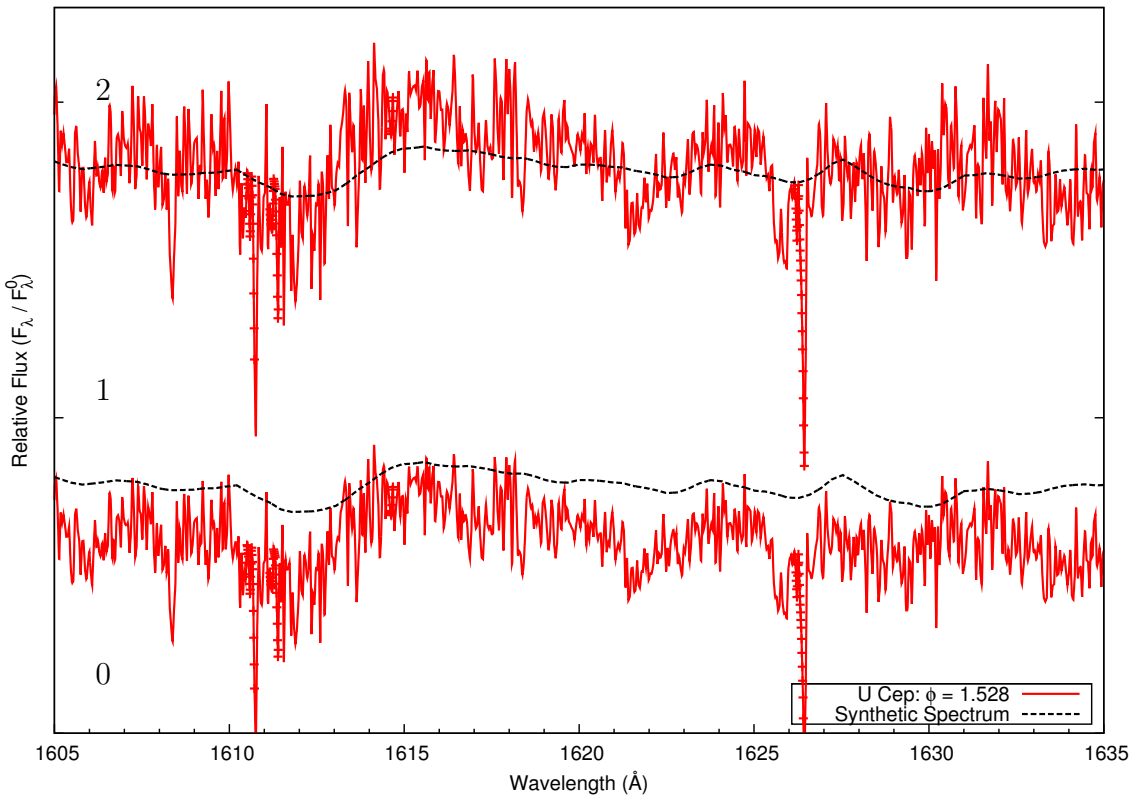

Figure 4.6: Example of continuum fitting of the data to synthetic spectrum. Top spectrum shows a fit of a TLUSTY simulation to the lowest possible value of the continuum, while the bottom spectrum is a fit for the highest possible value. The targeted region of 1615 to 1620 Å appeared relatively absorption line free and was used as a fitting point of reference.

respect to the simulated broadened and normalized TLUSTY output spectra. The basic procedure was to view 20 or 30 Å wide segments of the raw U Cep spectra, and divide the local data points by a value that would align the image with the rotationally broadened TLUSTY spectra. Figure 4.6 gives an example of the fitting process, fitting the simulated spectrum to the lowest and highest possible positions to obtain the best value and probable error.

There are some complications in practice. As mentioned earlier, TLUSTY only simulates the photosphere of a static solitary star, and does not account for the various anomalous features present in the U Cep spectra. To attempt to deal with this, first

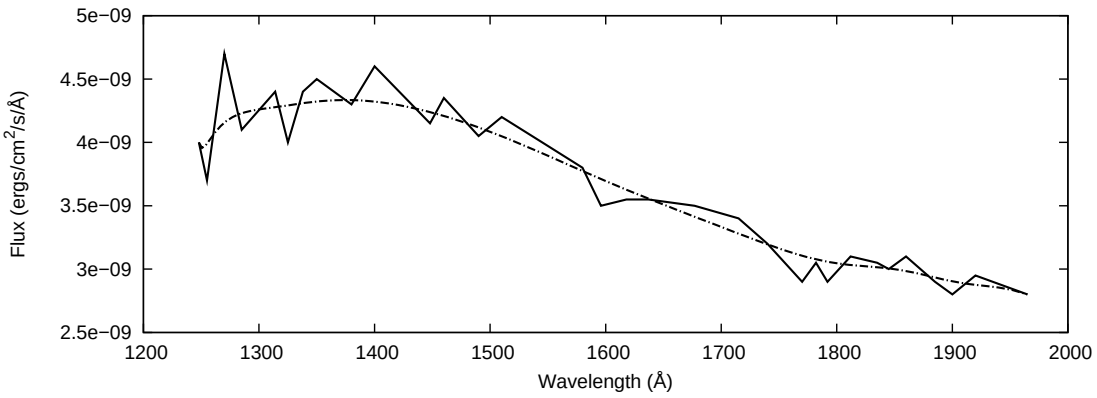

Figure 4.7: Continuum of Regulus.

we used the new normalization technique on the Regulus data as a test case. Over all, TLUSTY's synthetic spectra predicts and coincides with Regulus's spectra beautifully and finding its continuum posed no problem (results shown in figure 4.7). Then, we co-plotted the TLUSTY spectra, and normalized Regulus data, and focused on normalizing U Cep in regions that appeared similar to Regulus's photospheric spectra. U Cep data was also appropriately Doppler shifted to coincide with the TLUSTY and Regulus images. Regions that sat higher in the data were assumed to have been less affected by absorption lines and the extreme rotational broadening and were given preference for continuum-level identification. These regions were called 'peaks' or 'plateaus' in the data. The synthetic curve was matched with the highest and lowest portions of the noise in those regions. The resulting continuum values were averaged to obtain our final result, as well as giving error estimates. The continuum curve was then smoothed to avoid any discontinuous jumps in the normalized spectral data. Figure 4.8 shows the results obtained by the three different continuum fitting methods. The bottom two curves are the continuums obtained via the Wecht-McCluskey and the Phillview methods. The two curves show very good agreement with one another, but still underestimate the continuum found when considering the effects of extreme rotational broadening and line blending.

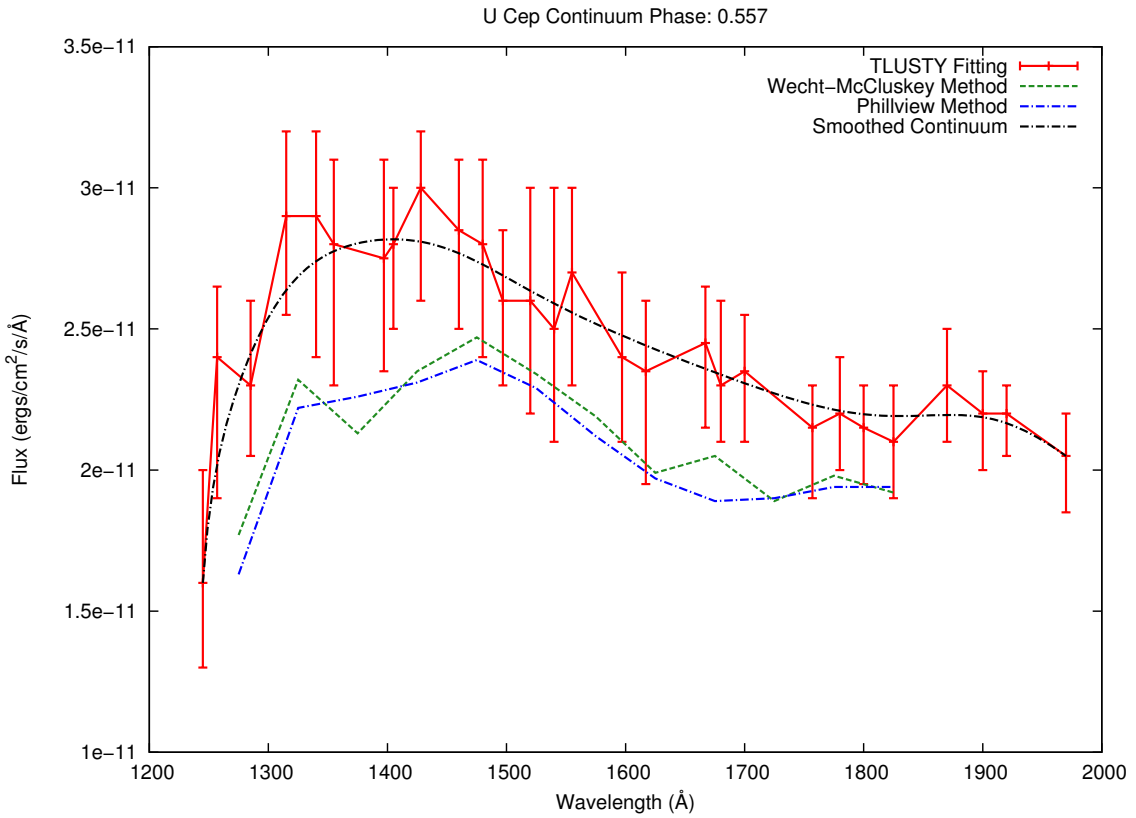

Figure 4.8: Continuum levels produced by three different methods. The Wecht-McCluskey method (short dash) and Phillview method (long dash dot) show good agreement with each other. However, fitting the TLUSTY simulation spectra (highest curve) produces a continuum curve 10 – 20 % higher when accounting for line broadening and blending mechanisms present in a rapidly rotating star.

4.6 Line Morphology

This section will detail the line morphologies as they evolve with phase. Plots appropriate to C II are located here, while those for the other atoms are in Appendix C.

4.6.1 C II 1334 & 1335

The C II doublet is one of the strongest and best defined absorption lines in the U Cep UV spectrum. The two separate lines are so close together that the high rotational broadening of U Cep blends them so that they seem to be one line; however, the

properties of each line can be teased out. Figures 4.9 and 4.10 show the normalized data along with TLUSTY simulations with respect to the sun. The normalized fluxes are layered in chronological order from the bottom to the top and then from figure 4.9 to 4.10. Associated phases (numbered 1 – 14 on the left) are given at the right. The location of number 1 on the left represents the zero flux for phase 0.358, etc. The TLUSTY simulated spectra match the broad feature in the data well, especially on the long wavelength side. Notice how the spectrum shifts left and then right according to phase, indicative of the orbital motion of the primary (B-type) star. Figures 4.11 and 4.12 are located here for convenience, but described later.

Deviations from the synthetic spectra are very interesting, and we attribute these departures largely to pseudo photospheric or other gas-flow features. A prominent pair of blue shifted features, presumed to be due to gas flow, begins to appear at phase 0.48 in the 1333–1335 Å range and persist through phase 0.69. Phases 0.82 and 0.95 show excess redward absorption. The absorption at phase 0.82 appears as a flat broad feature from 1336.2 to 1337 Å, though it is difficult to see in this figure. As we describe shortly, this feature may be related to the blue-shifted feature. The excess absorption at phase 0.95 can be attributed to the Rossiter effect, described earlier in section 2.3.1.

The phases of 0.69 and 0.82 are of particular interest since they occur right before and right after 3rd quadrature, or the point of maximum red shifted photospheric radial velocity. As such, one might expect that they would have the same radial velocity value of 110 km/s away from the sun (see figure 4.3). However, when plotted together (as shown in Figure 4.13) they reveal significant differences in behavior. Although the broad features show apparent photospheric shifts on the order of 110 km/s, there are obvious excess absorption features that differ drastically from one image to the next. The phase 0.69 image shows two sharp peaks, blue shifted from the main absorption feature, that seems to straddle the interstellar line and some bad data points. (Bad or suspicious data points are indicated by red + signs in the NEWSIPS IUE data base.) The separation between these two peaks is about 1.15 Å. The difference between the doublet lines of carbon in the laboratory rest frame is 1.18 Å. This close agreement

between the wavelength differences suggests that the two peaks in phase 0.69 are in fact sharply defined features of the C II doublet, blue shifted indicating an apparent velocity of about 260 km/s relative (towards) to the sun. In phase 0.82, there are much broader features evident that seem to be red shifted by about 160 km/s, away from the sun. The wavelength difference between the midpoints of these two features is about 0.98 Å, somewhat shorter than the rest frame difference. However, these two features are much more diffuse and broad, which would lead to more uncertainty in the difference. Notice that the phase 0.69 feature can be viewed as moving away from the B star at 360 km/s (260 km/s + 110 km/s), and the 0.82 feature toward the B star at 50 km/s (160 km/s - 110 km/s). Although these features are not much larger than the noise, we will see after examining a range of phases and ionic species that they are part of a consistant pattern.

It is important to note that any gas flow is likely to be an extended feature, following a trajectory around the B star, with parts possibly moving toward and away from the sun or the B star. However, we only see the absorption features associated with the part of the gas flow between us and the B star. The data is suggestive of a gas flow seen in front of the B star which is moving away from the B star at phase 0.69 and toward the B star at phase 0.82 (though this latter identification is not as definitive).

All images following primary eclipse, 1.08 through 1.52, appear mostly symmetric and do not display any prominent flow features. However, the left-most blue-shifted flow feature may be present in phases 1.3 through 1.52, but considerably weaker than in the previous orbit. Although the binary orientation is the same at, for example phase 0.48 and 1.43, we note that significant differences between those phases suggest that the flow did not substantially persist past the first orbit. We discuss this later.

We identify the double peaked saturated line, mostly visible in the latter phases and just left of the 1334 line center, as a pair of interstellar lines since they are independent of binary phase. They are blue shifted by amounts indicating velocities of 15 and 35 km/s. We fitted these lines by Gaussians at one phase and included them

with the TLUSTY simulation, as shown in figures 4.11 and 4.12. Note that the same Gaussian is used for all phases. In these figures, the orbital (photospheric) velocity of the B star has been set to zero. That is, both data and simulation appear as if viewed from the B star, or actually, a point in space moving with the B star. This, along with the fitting of the interstellar lines, will be important when we examine photospheric and flow features quantitatively in subsequent sections.

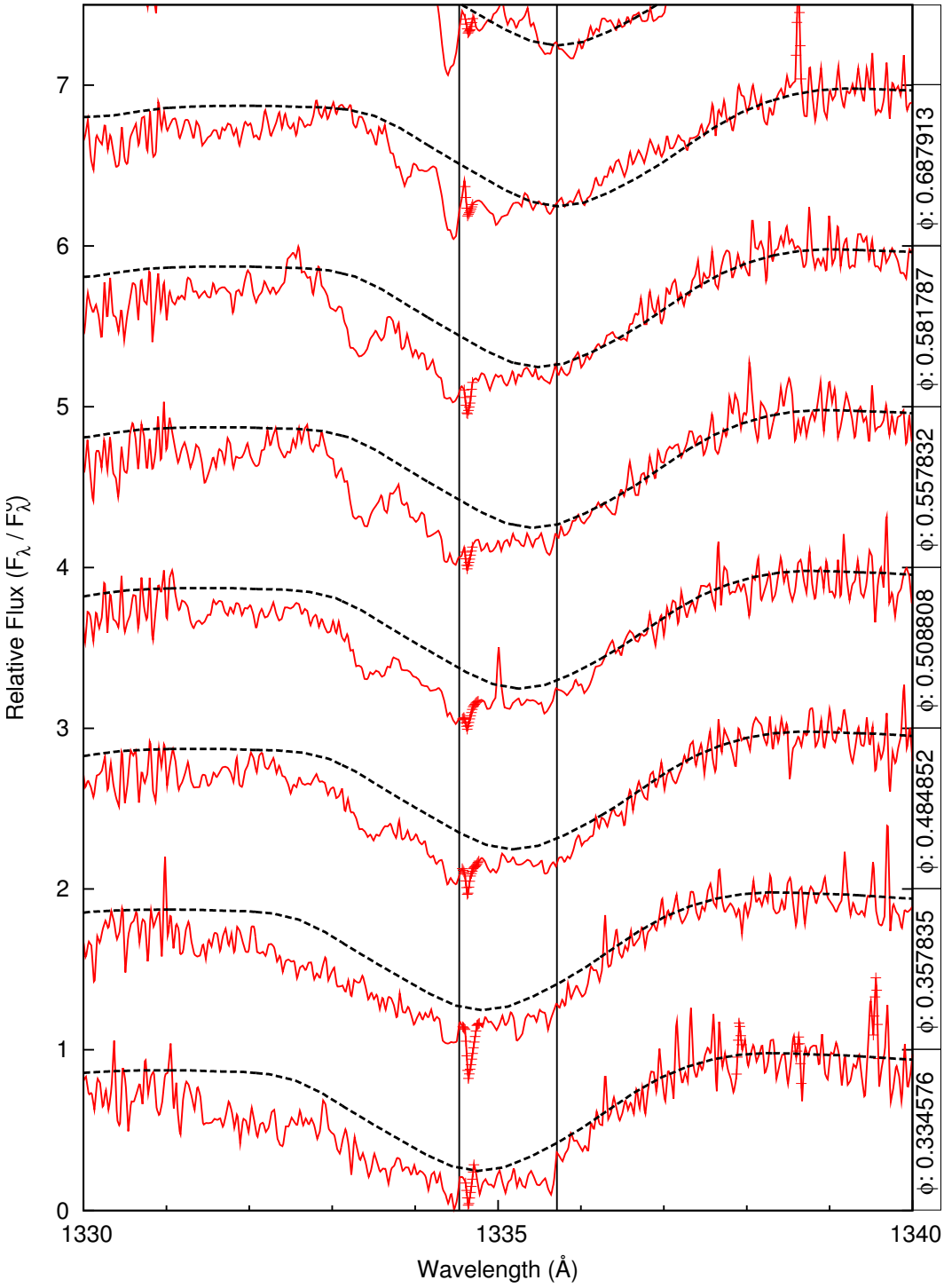

Figure 4.9: [A] (a) C II 1334 & 1335: Normalized U Cep data and synthetic spectra (dashed). The Doppler motion of the spectra is taken with respect to the Sun. (see text)

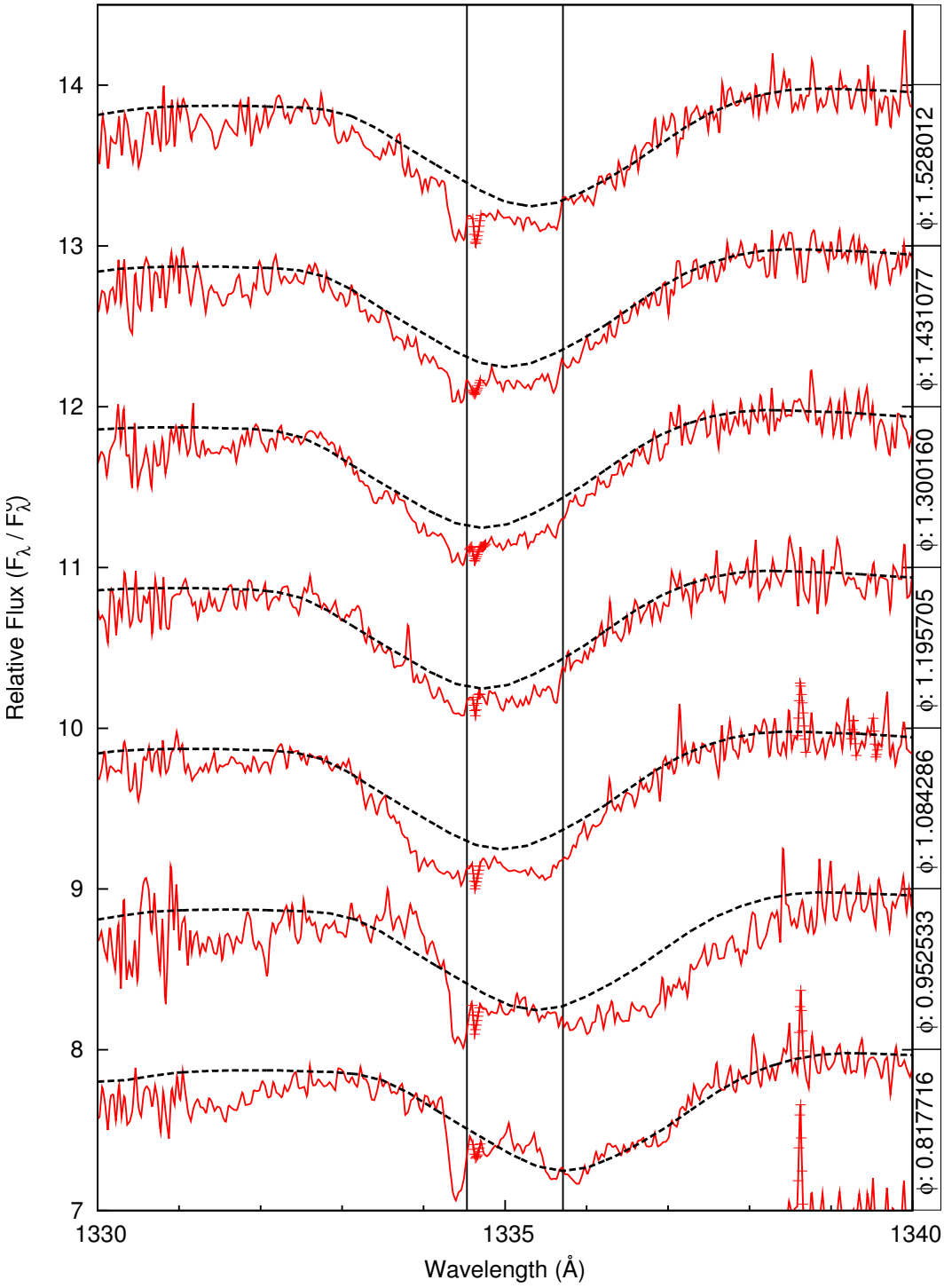

Figure 4.10: [A] (b) C II 1334 & 1335: Normalized U Cep data and synthetic spectra (dashed line). The Doppler motion of the spectra is taken with respect to the Sun.

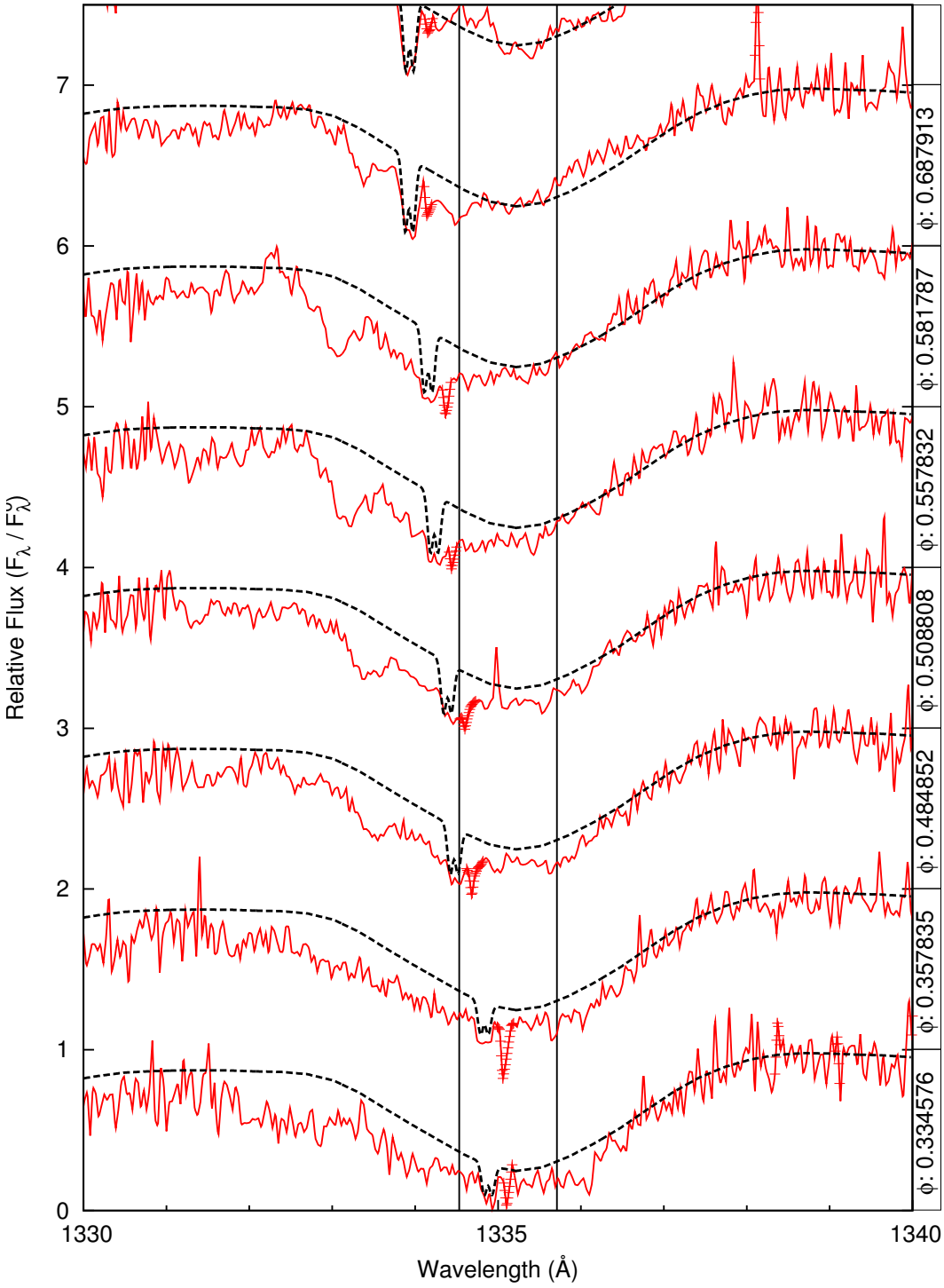

Figure 4.11: [B] (a) C II 1334 & 1335: Normalized U Cep data and synthetic spectra (dashed line). The Doppler motion of the spectra is taken with respect to the B-star. Interstellar line appoximations have been included into the synthetic spectra.

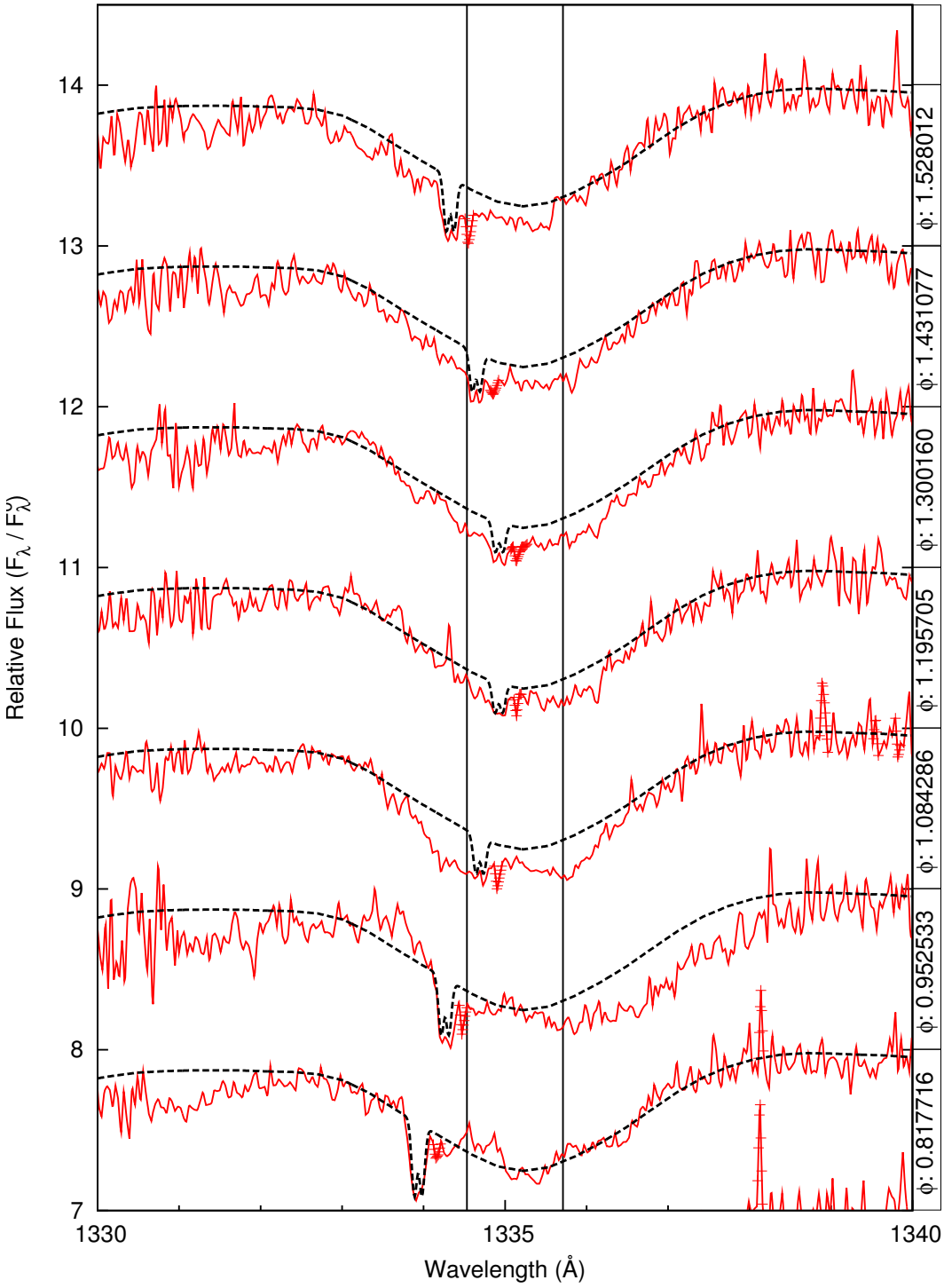

Figure 4.12: [B] (b) C II 1334 & 1335: Normalized U Cep data and synthetic spectra (dashed line). The Doppler motion of the spectra is taken with respect to the B-star. Interstellar line appoximations have been included into the synthetic spectra.

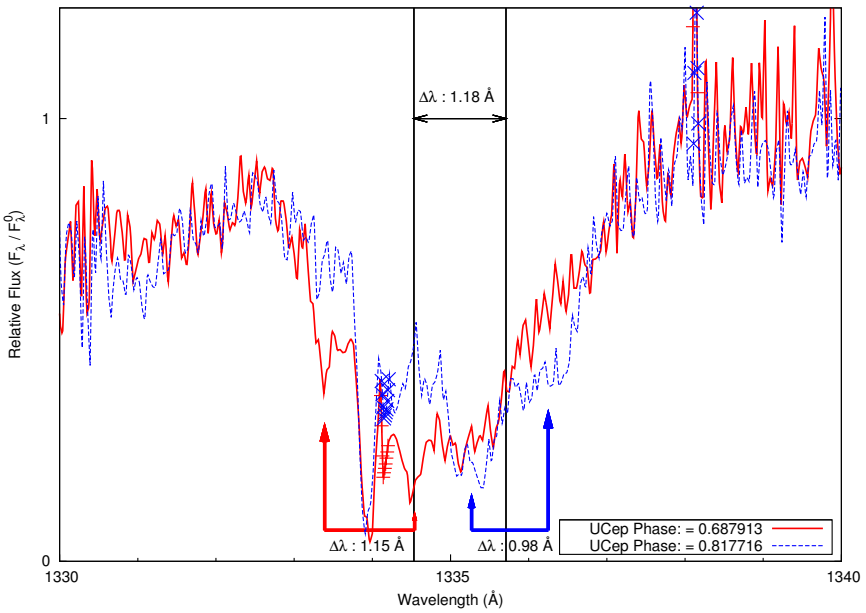

Figure 4.13: C II 1334 & 1335 Region: Comparison between phase 0.69 and 0.82. The narrow absorption line at approximately 1334 Å is an interstellar line.

4.6.2 Si II 1260 & 1264

As indicated earlier, observed and calculated flux plots for silicon and aluminum have been placed in Appendix C. For example, the Si II 1260 & 1264 figures analogous to C II figures 4.9 & 4.10 are identified as C.10 & C.11. The Si II 1260 & 1264 lines are strong and the two components are resolvable, though their shoulder features begin to overlap in the middle. TLUSTY matches the data reasonably well, but deviations are frequently apparent, particularly for the short wavelength component of the doublet pair.

The 1260 Å region shows two discernible interstellar lines: a Si II 1260 line blue shifted by 20 km/s and what we tentatively identify as a S II 1255 (sulfur) line shifted by 15 km/s. Much like C II, the spectrum displays prominent blue shifted gas flow features at phases 0.33 through 0.69, though that at 0.35 is weaker. The line appears clear and symmetrical just following primary eclipse at phase 1.08. Phases 1.31, 1.43, and 1.52 show possible blue shifted absorptions.

The 1264 line shows no sign of interstellar absorption. There is obvious blue shift absorption at phases 0.56 and 0.58. Phases 0.69 and 0.82 appear much shallower than TLUSTY predicts. Following primary eclipse, phases 1.08 through 1.52 appear well behaved and symmetrical.

4.6.3 Si II 1526 & 1533

The calculated flux plots discussed here appear in Appendix C as figures C.19 and C.20. The Si II 1526 and 1533 lines are well separated and do not overlap, but noise in the data in this region is quite high. TLUSTY has difficulty modeling the peaks and valleys of these lines. An interstellar line appears with the 1526 feature, but not the 1533 line.

The 1526 line appears to have a weak blue shifted feature at phases 0.48 and 0.51, which becomes stronger at phases 0.55 and 0.58. Excess red absorption presents at phase 0.95. Following primary eclipse, all phases appear relatively well behaved, symmetric, and with less noise.

The 1533 line displays a blue shifted feature at phases 0.51 through 0.58 and a red shifted feature at phase 0.95. The feature at 0.48 may be present, but it is difficult to resolve. Following primary eclipse the phase 1.31, 1.43, and 1.52 present a possible blue shifted feature.

4.6.4 Al II 1670

The calculated flux plots discussed here appear in Appendix C as figures C.28 and C.29. The Al II line presents as a shallow line with moderate noise levels. There is a prominent interstellar line at 1670.68 Å, with a blue shift of 20 km/s. Up until primary eclipse TLUSTY does not model this line very well, as the actual data appears much shallower and thinner than predicted. After primary eclipse at phases greater than 1.08, the data begin to match TLUSTY better. There are blue shifted gas flow features from phase 0.48 to 0.58, but no gas flow features seem apparent in subsequent phases.

4.6.5 Al III 1854 & 1865

The calculated flux plots discussed here appear in Appendix C as figures C.37 and C.38. The Al III doublet lines are well separated and thus do not contaminate one another. Both are far deeper and wider than TLUSTY or Regulus would predict. There is a small amount of noise and no apparent interstellar features.

The 1854 line displays obvious blue shifted flow features from phases 0.48 through 0.69, and an ambiguous feature in phase 0.33. Excess red absorption appears at phases 0.82 and 0.95. After primary eclipse, between phases 1.19 and 1.52, the line appears to have areas of flat troughs and asymmetries.

The 1862 line exhibits blue shifted absorption between the phases of 0.35 and 0.69 and red shifted absorptions in phases 0.82 and 0.95. Following primary eclipse the line appears well behaved and symmetric.

4.7 C IV and Si IV Analysis and the Effects of Extreme Line Blending

As mentioned previously, the purported C IV and Si IV lines pose many questions. There are certainly absorption features that correspond to the locations of those lines, but certain aspects of their behavior, morphology, and very existence give reason for pause. These two lines require extreme temperatures to reach this state of ionization and be observed in any appreciable amount: in excess of 18,000 K for Si IV and over 25,000 K for C IV. The photosphere of the hottest star in U Cep is only 13,000 K, far short of what is required. Kondo et al. speculated that a super heated "pseudo photosphere" or accretion disk structure, heated by in-falling matter to the primary star mainly in the equatorial region, might give rise to these lines [30]. While the present work does not discount the presence of a certain amount of these ions in the pseudo photosphere, we will postulate another explanation involving convolutions of velocity distributions that may account for the strength and variability of these absorption features, and does not need to invoke extremely high temperature regions.

Kondo et al. identified features as C IV and Si IV in 1979 using early IUE images [30]. They noted the peculiarity of their presence, as the B-star was far too cool to produce these absorptions naturally, and that even the hot spot (only visible right before second contact of primary eclipse) with an estimated temperature of 20,000 K was still too cool to produce significant amounts of C IV. They also noted line asymmetries, and although the features had a phase dependence consistent with the orbital motion of the B star, the C IV radial velocities appeared to be off by 30 – 50 km/s. Plavec in 1983 obtained definitive emission spectra of U Cep using the IUE telescope during eclipse [31]. There, he did observe strong lines of Si IV, C IV, Al III, and a weak N V 1240 line. However, even the strongest line, at best, was one fortieth the flux of the continuum out of eclipse. He did further analysis on the out-of-eclipse absorption features and noted the shape of the features did not match the typical bell shaped rotationally broadened feature one would expect of a line found in the photosphere. The assumption was that these were accretion disk formations, but attempts to pinpoint their exact location in the system were inconclusive. Indeed, across epochs, the emission lines showed variation in strength and whether they appeared or not.

Figures 4.14 and 4.15 are normalized flux plots of the C IV 1548 & 1550 Å region, while figures 4.16 and 4.17 are those for the Si IV 1393 & 1402 Å region. The normalized fluxes are layered in chronological order from the bottom to the top. Associated phases are given at the right. These plots display the high morphological variability of the lines. The lines suggestive of C IV and Si IV are most conspicuous at phases around 1.08. This feature is barely discernable between phases 0.48 and 0.58.

In our initial attempts to model C IV properly, we endeavored to isolate other contributing lines and interstellar features in the region. This method involved coplotting TLUSTY simulations, broadened with various rotational rates, and selectively omitting the calculation of certain atomic species with the synthetic spectra (referred to as "omission spectra"). As seen previously, there is a significant value attached to our ability to control the rotational rate in TLUSTY simulations. Lowering the rate

not only helps us to clarify line identifications and locations, but also in simulating features that may not be moving with the photosphere. Even for off-photosphere gas flows, adjusting the rotation rate is a convenient mechanism for introducing (in an approximate way) an effective range (or dispersion) of velocities. We noticed that at lower v_{eq} sin i, with carbon "turned off", the synthetic spectra did not appear to change very much (see figures 4.18 and 4.19 for C IV and 4.20 and 4.21 for Si IV) maintaining the C IV-like features. There seemed to be quite substantial absorption centered around the C IV line, yet the simulations were done assuming a photospheric temperature of 13,000 K, and C IV contributions inhibited. Upon further investigation, it was discovered that for both the C IV and Si IV lines, there were dense forests of mostly Fe II lines clustered around wavelengths associated with the main ions of interest, though not as pronounced for the long wavelength component of Si IV. An example of this behavior was first shown with figure 3.13 and the discussion of the effects of rotational broadening where another pseudo line was created purely with blended Fe II lines. The arrows on figures 4.22 and 4.23 indicate the strongest contributors of Fe II absorption. This phenomena of cooler absorption lines combining to appear as other lines has also been observed by Hubeny et al. [64].

In summary, adjustments to the simulated rotational speed can produce synthetic spectra that appear to match the data even more closely. While these simulations are not exact fits — they were created with a program that assumes a single photospheric temperature and rotational velocity — they do show how the blended lines of one species can mimic the line of another. With the inclusion of an accretion disk or pseudo photosphere, additional velocity distributions could add layers of absorption on top of the actual photosphere. This could also account for the discrepancies between the expected photospheric lines and simulated spectra.

With the knowledge of the extreme effects rotational broadening and blending can have on apparent absorption lines, we performed additional checks on our other lines of interest. We have included comparative simulations of important C II, Si II, Al II, and Al III spectral regions with and with out the associated atom. The C II 1334 & 1335 (figure 4.24) and Al II 1670 (figure 4.25) lines both appear clear of contamination

when their respective atoms are omitted from the synthetic spectra. The Si II 1526 & 1533 (figure 4.26) doublet exhibits slight excess absorption in the 1526 line, while the 1533 line is clean. Si II 1260 & 1264 (figure 4.27) exhibits significant excess absorption in the omission spectra for both features. While some of the contamination can be attributed to Fe II lines in this case, the majority of absorption is comprised of blended C I lines. Al III 1854 & 1862 (figure 4.28) also displays some excess absorption caused by blended lines. In the omission spectra, absorption around 1851 to 1854 and between 1858 to 1862 is comprised of Fe II.

4.8 Photospheric Radial Velocity

Radial velocity (RV) curves display radial velocities as a function of binary-pair phase. Anomalous departures from an expected sinusoidal curve will give a sense of any interesting physics that may be occurring.

4.8.1 History - Radial Velocity Measurements

Previous works at Lehigh utilized various Gauss fitting techniques to obtain radial velocity curves. Wecht used a method of manually fitting inverted Gaussian shapes to smoothed spectral lines. The positions and widths of the Gaussians were recorded [59]. Reed developed another IDL routine to aid and accelerate his line analysis. In this routine, the user identifies a line's peak position and width. The widths were determined by locating the half max absorption points along the walls of the feature [7], then the program would calculate a Gaussian shape appropriate to the given parameters. This process could then be iterated until a satisfactory fit was attained. In both cases of Wecht and Reed, the Gaussian area was later used in equivalent width analyses, and line centers yielded the RV curves.

Dr. Jess Johnson (in collaboration with McCluskey, DeLeo, and others) worked on a project with U Cep that mainly focused on mass flow characteristics through radial velocity curve analysis [17]. Since the U Cep data can be somewhat noisy, and it was assumed that a diffuse gas stream was being viewed along with photospheric motion, Johnson measured the positions of any conspicuous absorption feature. This

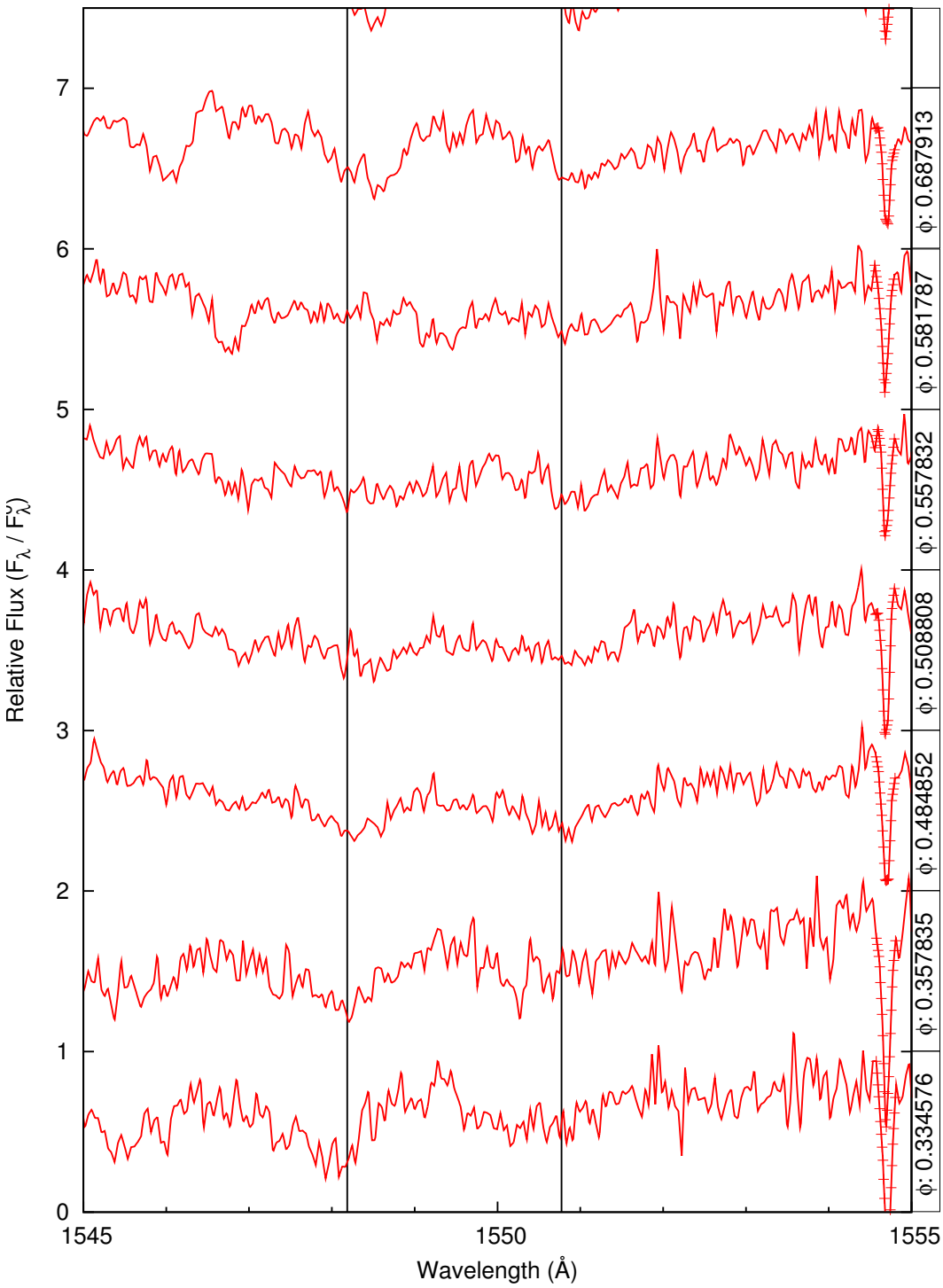

Figure 4.14: C IV 1548 & 1550 Region: Normalized U Cep data. Doppler motion with respect to the Sun. ϕ is the phase. Vertical lines correspond to the laboratory rest wavelengths of 1548.2 and 1550.77 Å.

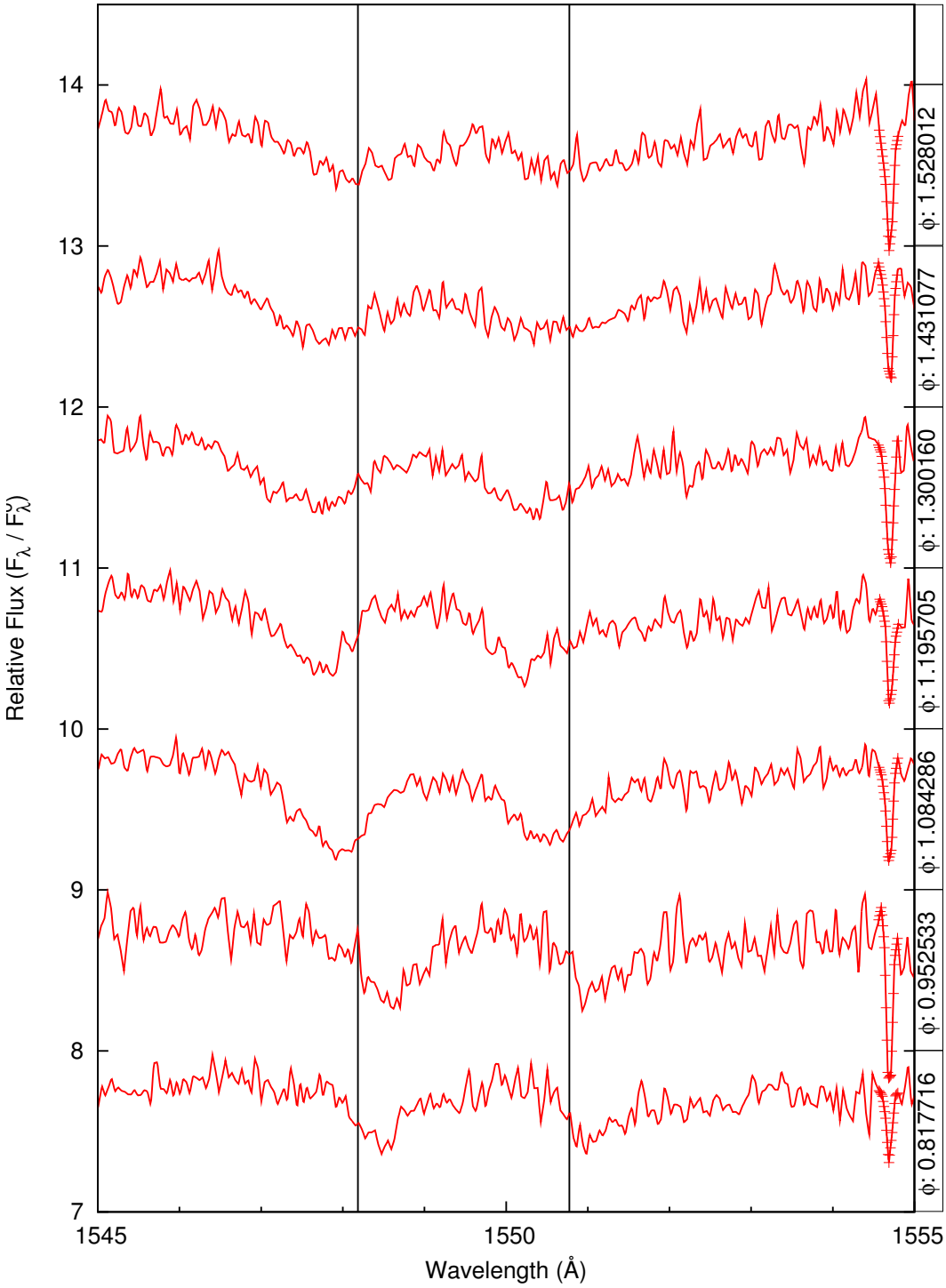

Figure 4.15: C IV 1548 & 1550 Region: Normalized U Cep data. Doppler motion with respect to the Sun. ϕ is the phase. Vertical lines correspond to the laboratory rest wavelengths of 1548.2 and 1550.77 Å.

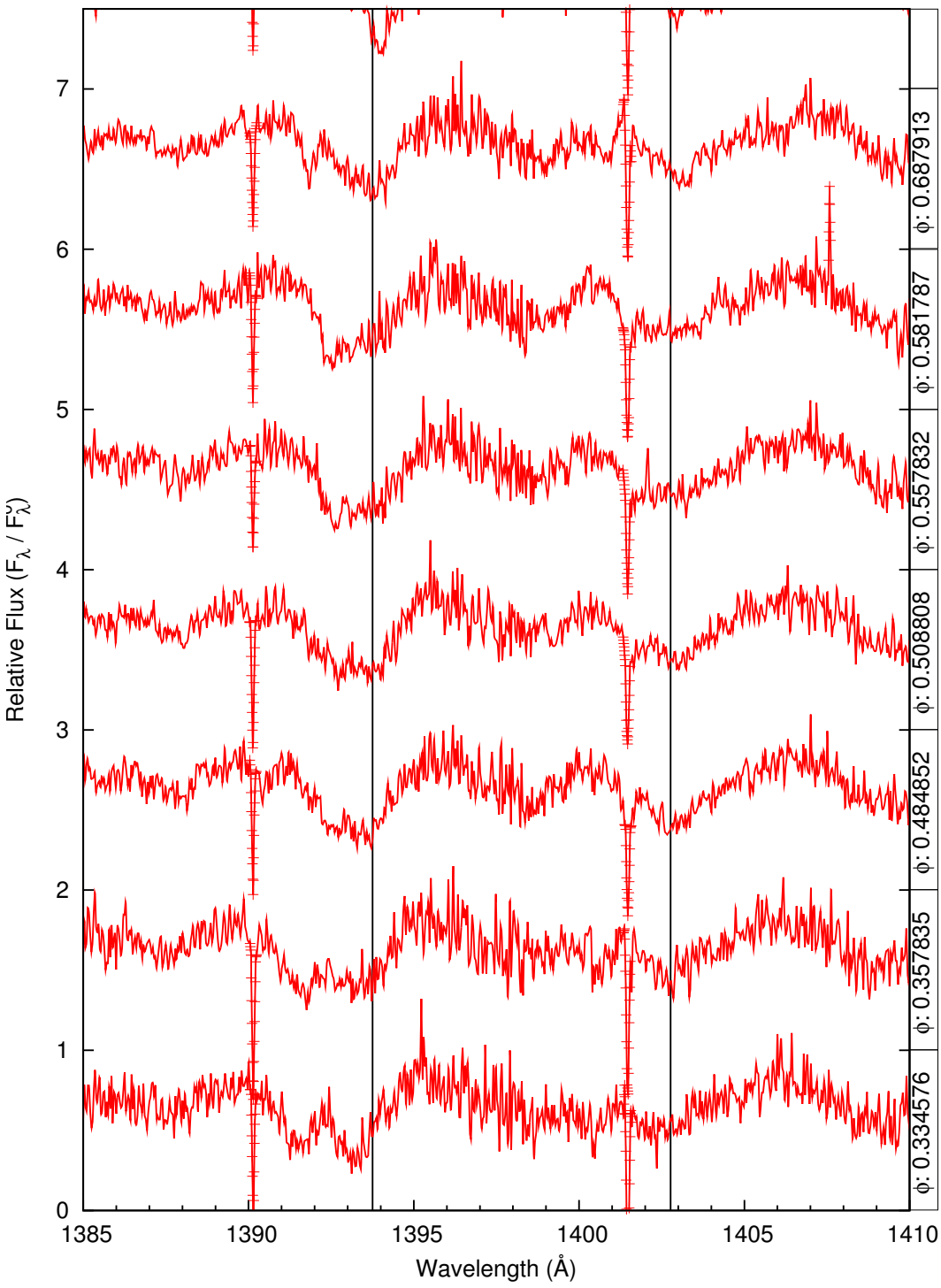

Figure 4.16: Si IV 1393 & 1402 Region: Normalized U Cep data. Doppler motion with respect to the Sun. ϕ is the phase. Vertical lines correspond to the laboratory rest wavelengths of 1393.76 and 1402.77 Å.

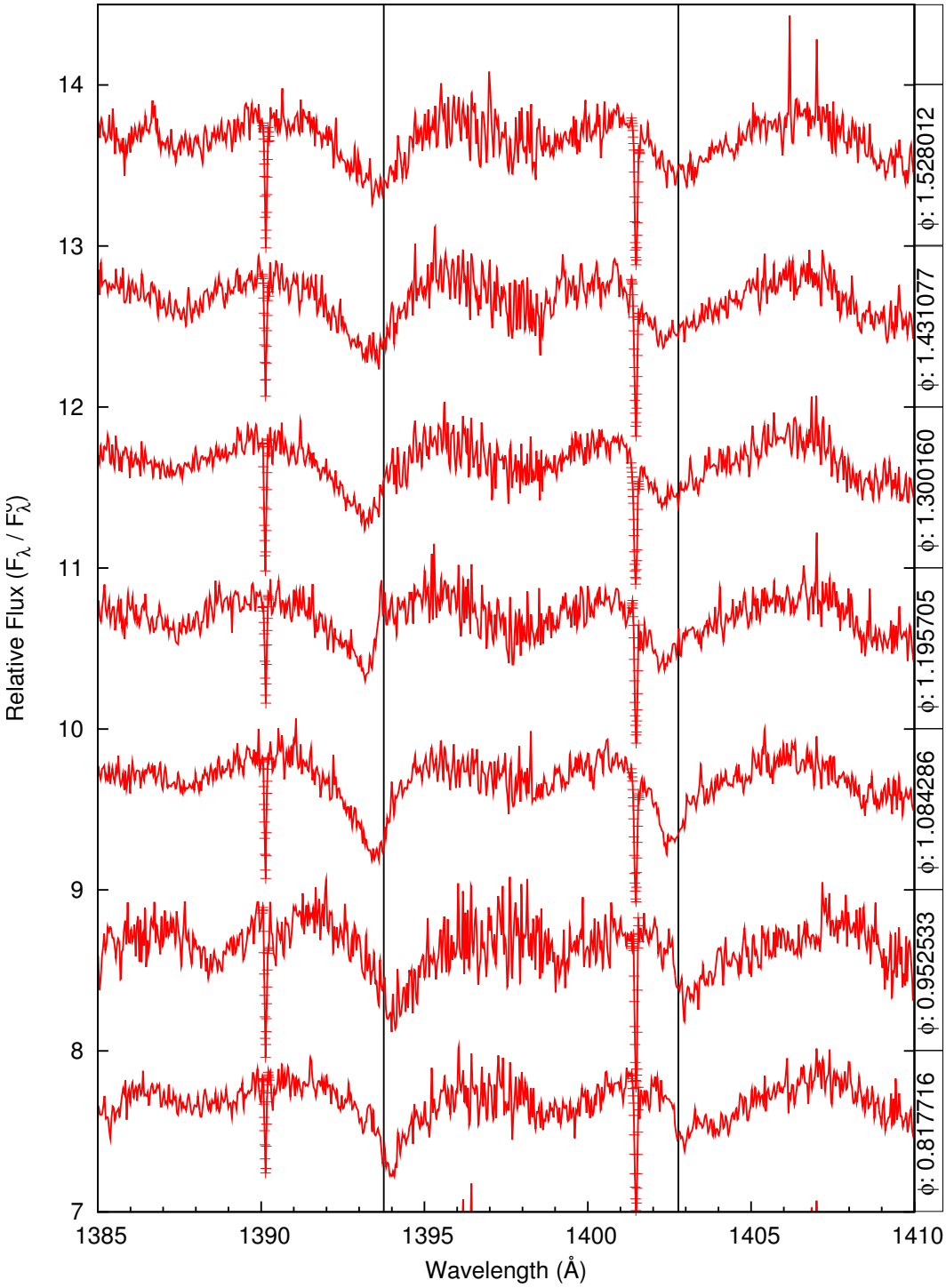

Figure 4.17: Si IV 1393 & 1402 Region: Normalized U Cep data. Doppler motion with respect to the Sun. ϕ is the phase. Vertical lines correspond to the laboratory rest wavelengths of 1393.76 and 1402.77 Å.

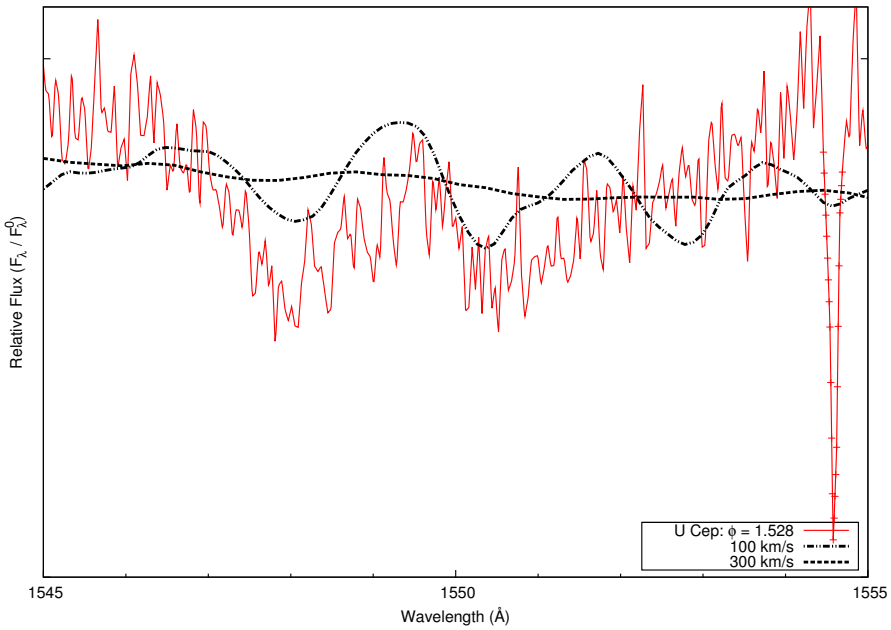

Figure 4.18: C IV 1548 & 1550 Region: Simulated spectra at 100 and 300 km/s

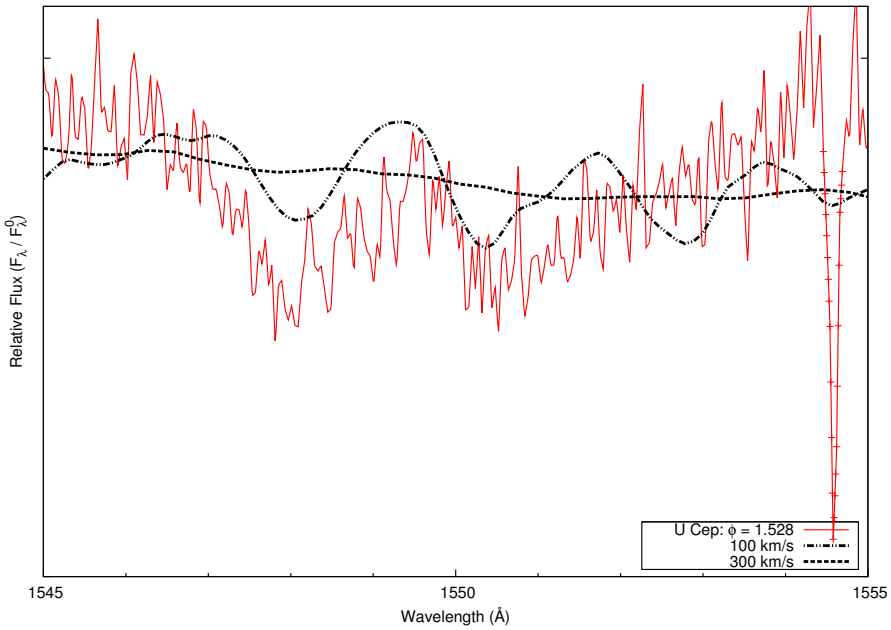

Figure 4.19: C IV 1548 & 1550 Region: Simulated spectra with carbon omitted at 100 and 300 km/s

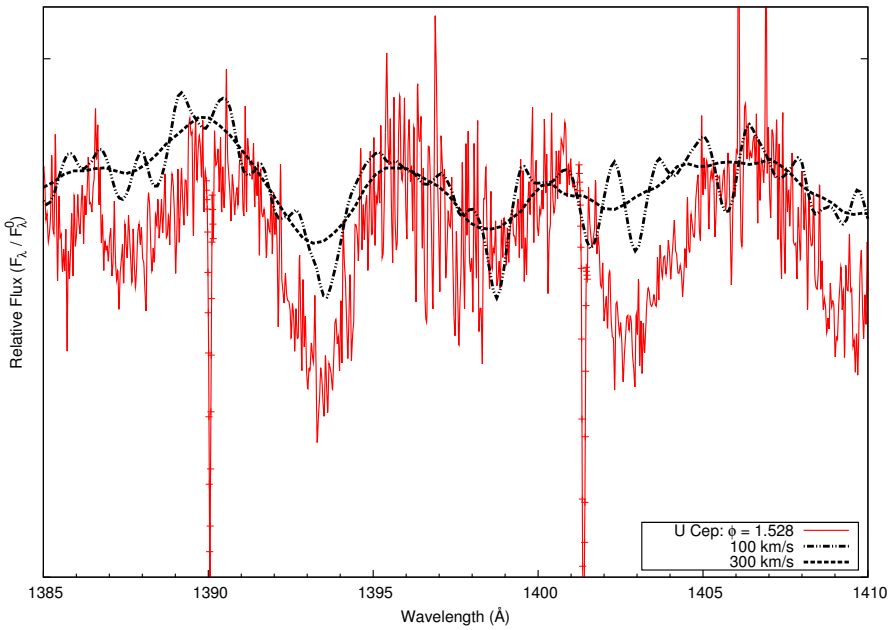

Figure 4.20: Si IV 1393 & 1402 Region: Simulated spectra at 100 and 300 km/s

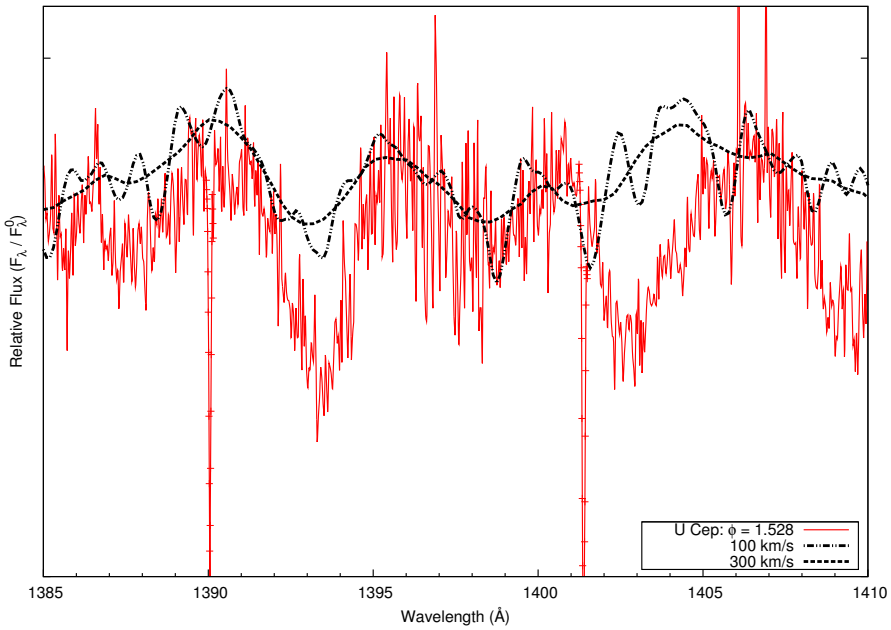

Figure 4.21: Si IV 1393 & 1402 Region: Simulated spectra with silicon omitted at 100 and 300 km/s

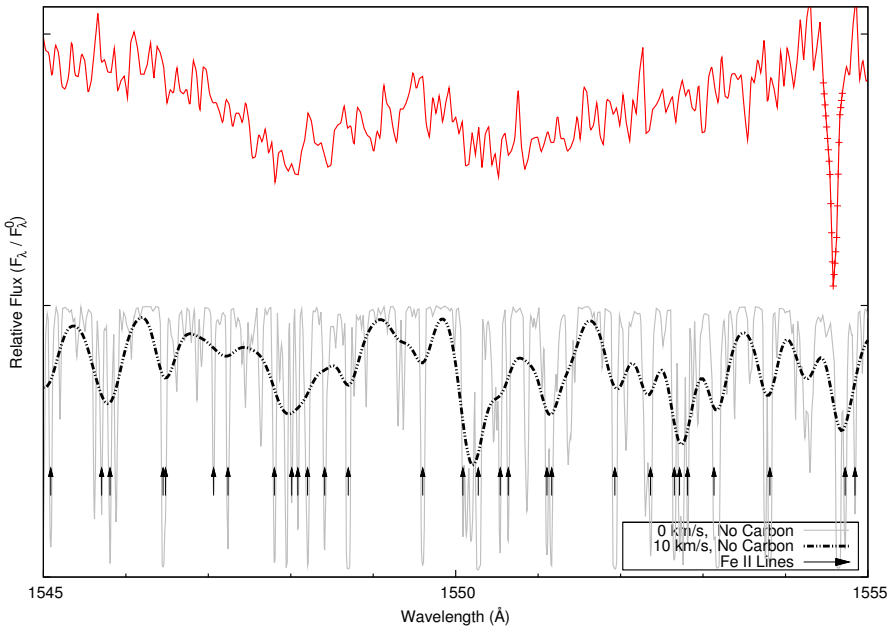

Figure 4.22: C IV 1548 & 1550 Region: (Upper Plot) Normalized U Cep at phase ϕ: 1.528. (Lower Plot) Omission spectra (carbon omitted) with no broadening (solid gray line) and slight broadening (dash line). Arrows indicate the presence of significant Fe II lines

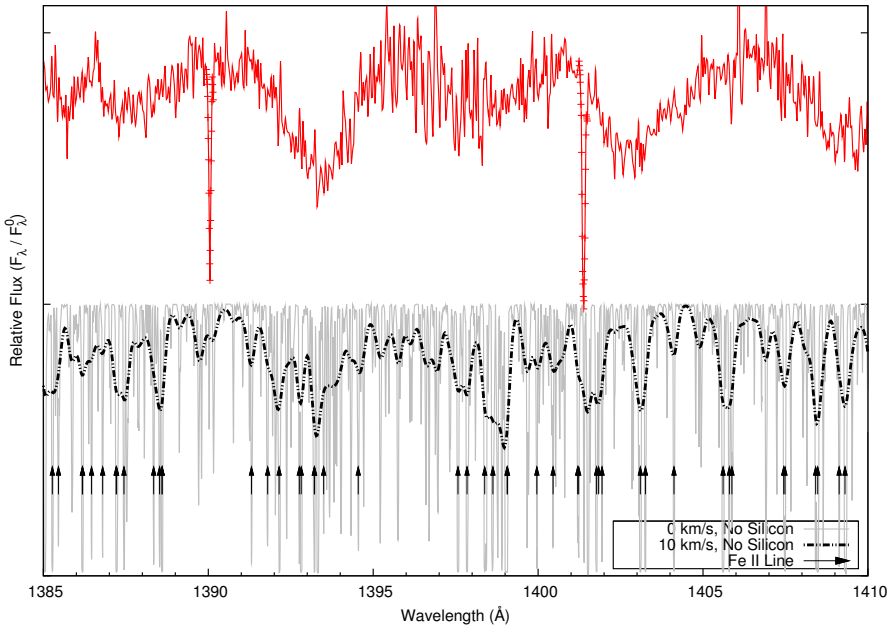

Figure 4.23: Si IV 1393 & 1402 Region: (Upper Plot) Normalized U Cep at phase ϕ: 1.528. (Lower Plot) Omission spectra (silicon omitted) with no broadening (solid gray line) and slight broadening (dash line). Arrows indicate the presence of significant Fe II lines

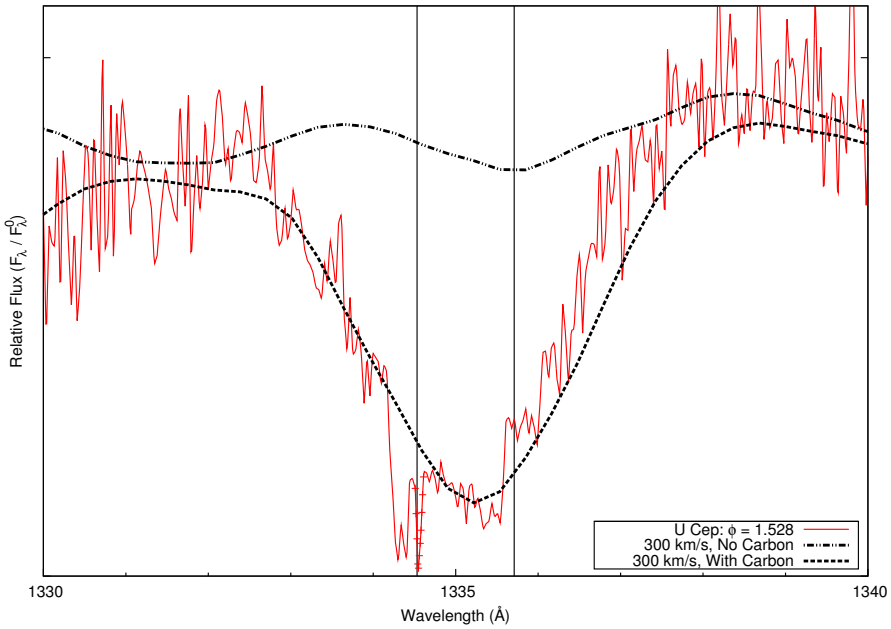

Figure 4.24: C II 1334 & 1335 Region: Simulated spectra with and without carbon.

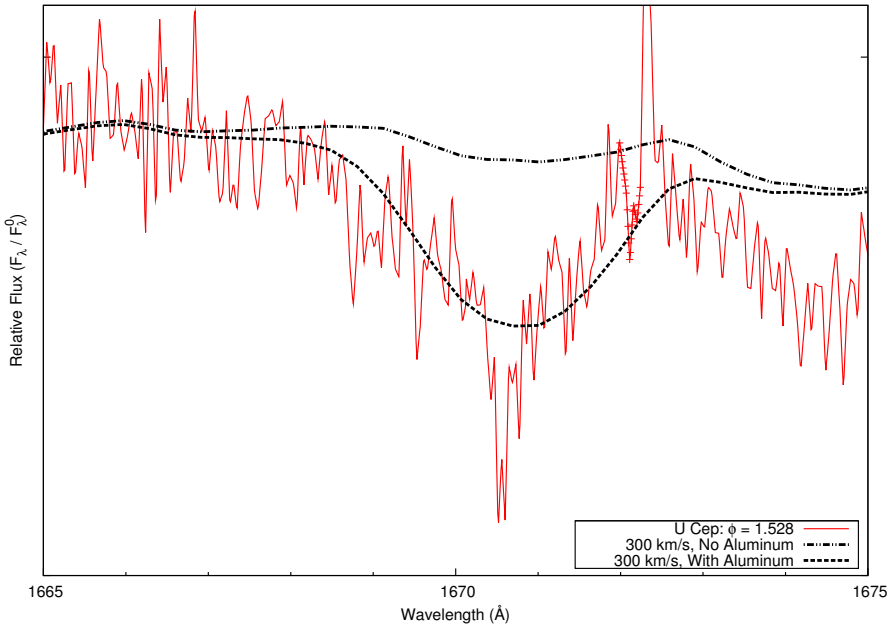

Figure 4.25: Al II 1670 Region: Simulated spectra with and without aluminum.

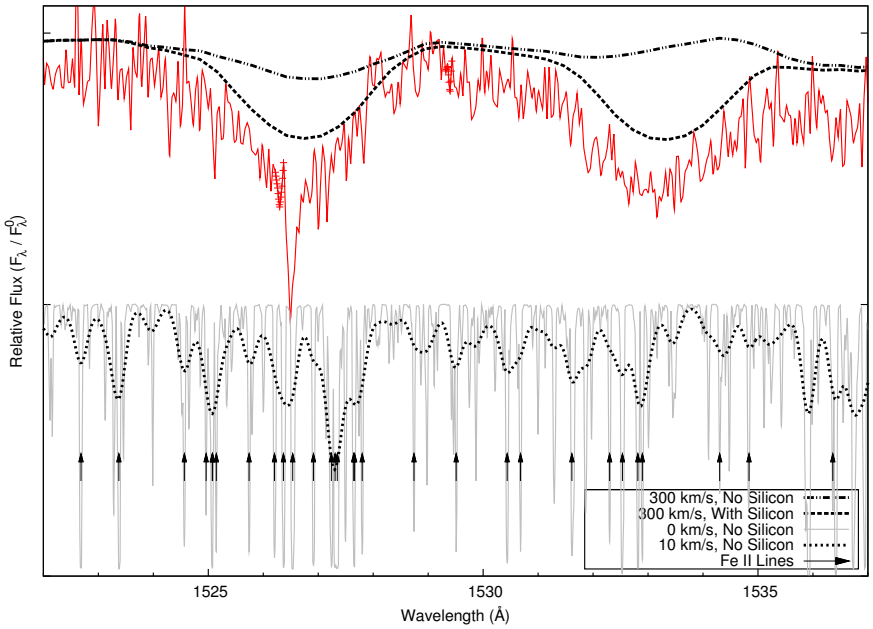

Figure 4.26: Si II 1526 & 1533 Region: Simulated spectra with and without silicon.

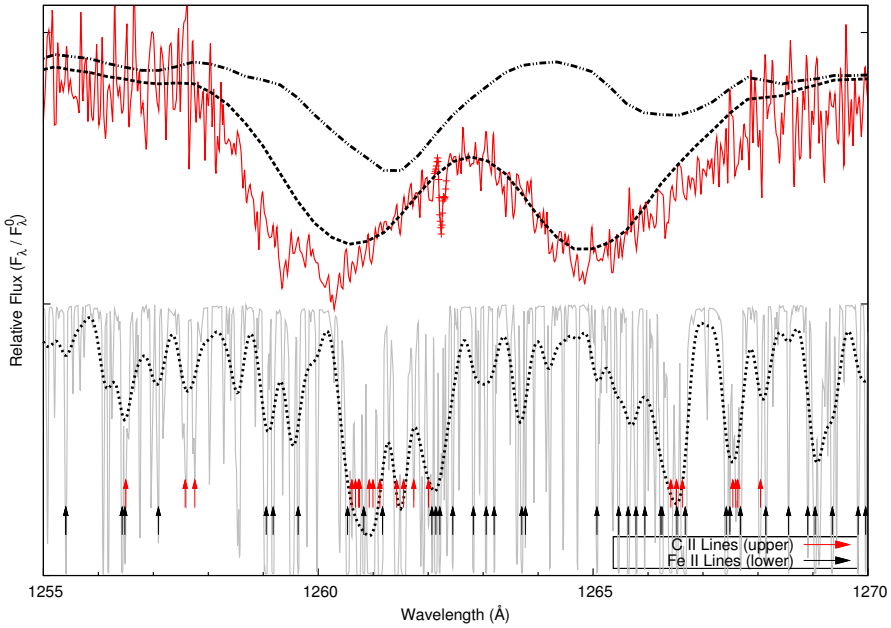

Figure 4.27: Si II 1260 & 1264 Region: Simulated spectra with and without silicon.

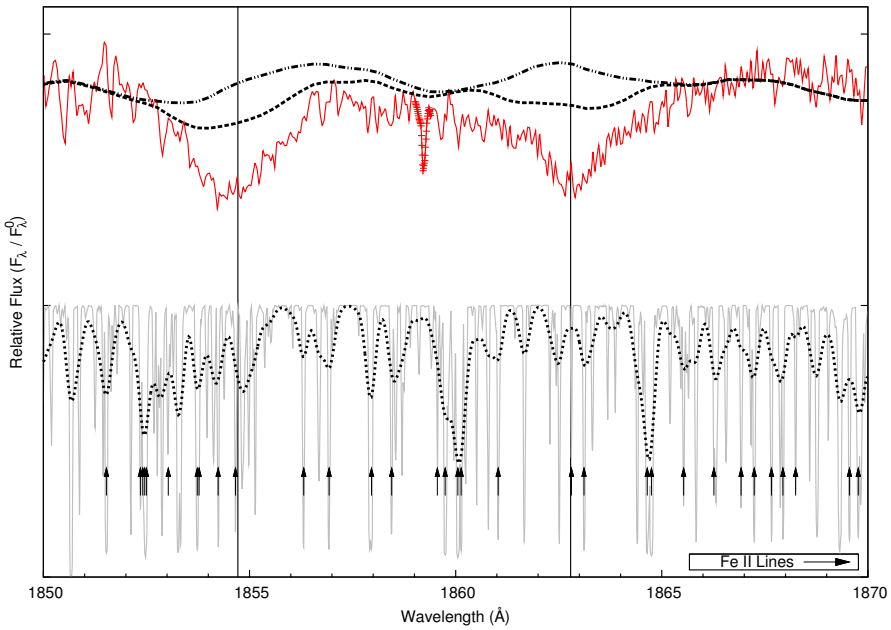

Figure 4.28: Al III 1854 & 1862 Region: Simulated spectra with and without aluminum.

method created a compelling plot (see figure 4.29) of the interesting behavior of this system, but did not adequately filter out false positive line identifications. The graph suggested a flow of gas moving with velocities of 200 to 300 km/s away from the system around secondary eclipse, and other features with red shifted velocities of 100 to 200 km/s relative to the system from past mid phase until primary eclipse. In the following sections, we isolate the photoshere and gas-flow motions. We shall see that our gas-flow results are consistent with the essential features of the Johnson scatter plot.

4.8.2 Measuring the Photosphere's Radial Velocity

Due to noise and the ambiguity of line centers caused by line blending, a new technique for determining radial velocity was developed. A synthetic spectrum was generated with TLUSTY and SYNSPEC using the photospheric parameters of U Cep. The output from TLUSTY assumes there is no relative motion of the star. We simply calculated a radial velocity that would cause a sufficient Doppler shifting of the synthetic data to align it with the absorption lines of U Cep. Due to noise in the U Cep

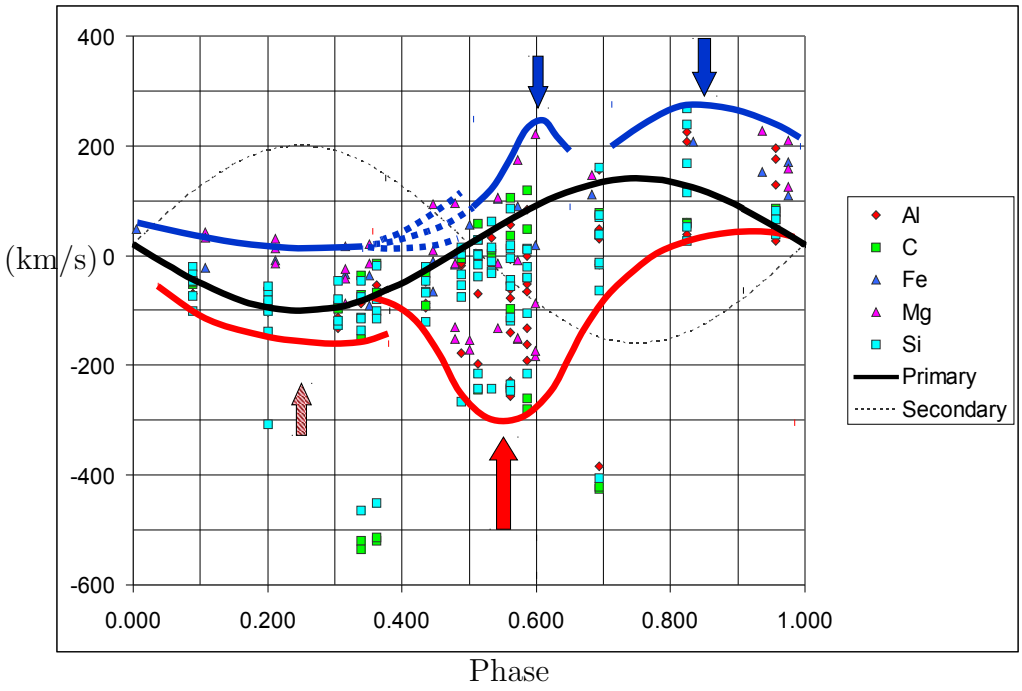

Figure 4.29: Radial velocity (relative to sun) scatter plot produced by Johnson et al. Around secondary eclipse, a number of significantly blue shifted absorption features were found [17].

data, and the failure of TLUSTY to perfectly match the data in all spectral regions, it was difficult to pinpoint an exact placement of the TLUSTY curves. Hence, a range of possible radial velocities was determined, again producing error bars. The synthetic curve was aligned with the right most and left most edges of noise patterns around the half max sides of the absorption line, as shown for the C II 1334 & 1335 doublet in figure 4.30. The walls of the absorption lines were typically the safest place to measure, as the deepest absorption areas of the lines did not always match up with the TLUSTY curves, and the wings had much greater noise. Where possible, alignments used both sides of the absorption line, but more often than not, extreme line blending or obvious gas flow features would obscure one wall or the other, as described previously in section 4.4. In those cases, the opposing wall was used. The RV-curves obtained with this method for C II 1334 & 1335 (figure 4.31), Al II 1670 (figure 4.32), Si II 1260 & 1264 (figure 4.33) and Si II 1526 & 1533 (figure 4.34) are

given below. TLUSTY could not adequately model the Al III 1854 & 1862 lines to reasonably match the U Cep data. So we did not feel confident applying this method in the case of Al III. The other four sets of lines did show remarkable agreement in following the predicted photospheric radial velocity, shown as a dashed line representing the radial projection of the B-star orbital velocity. Note the extreme divergence from the predicted path around phase 0.95. This can be attributed to the Rossiter effect during partial eclipse, where blocking the section of the star rotating away from Earth leads to line asymmetries in favor of the blue shifted light emanating from he unblock portion of the star.

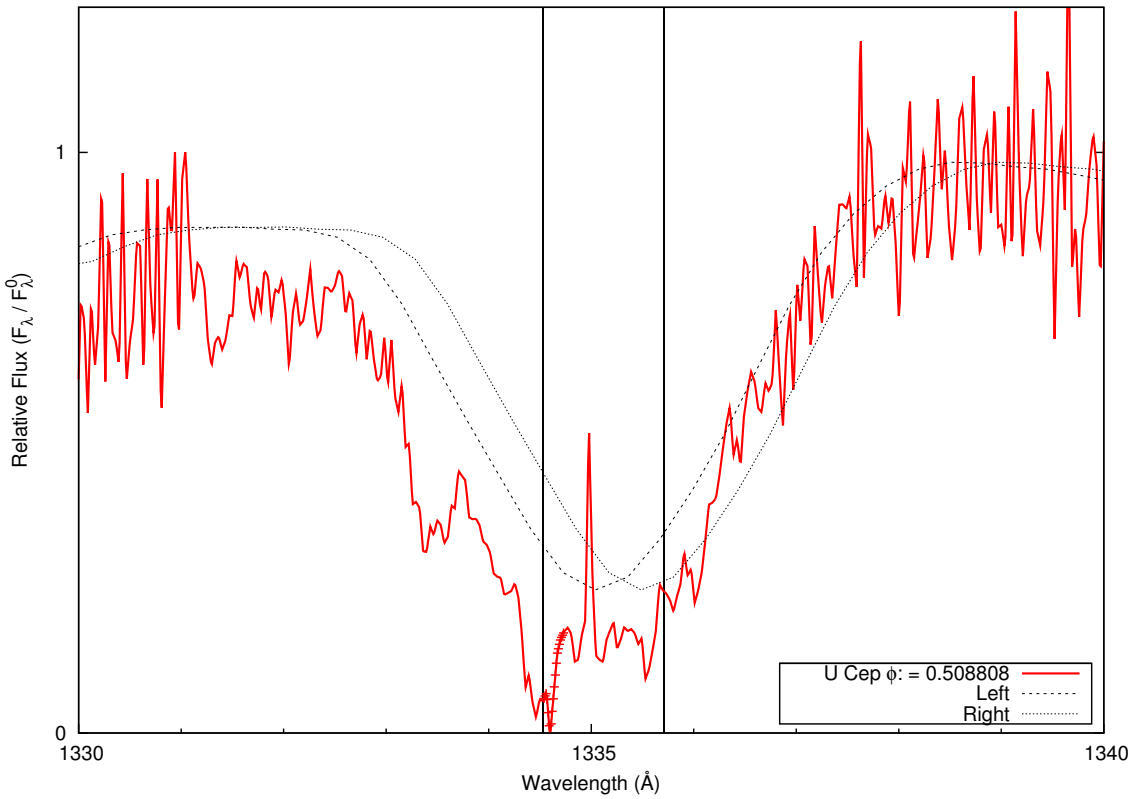

Figure 4.30: Example photoshere fit to the right side of feature C II 1334 & 1335.

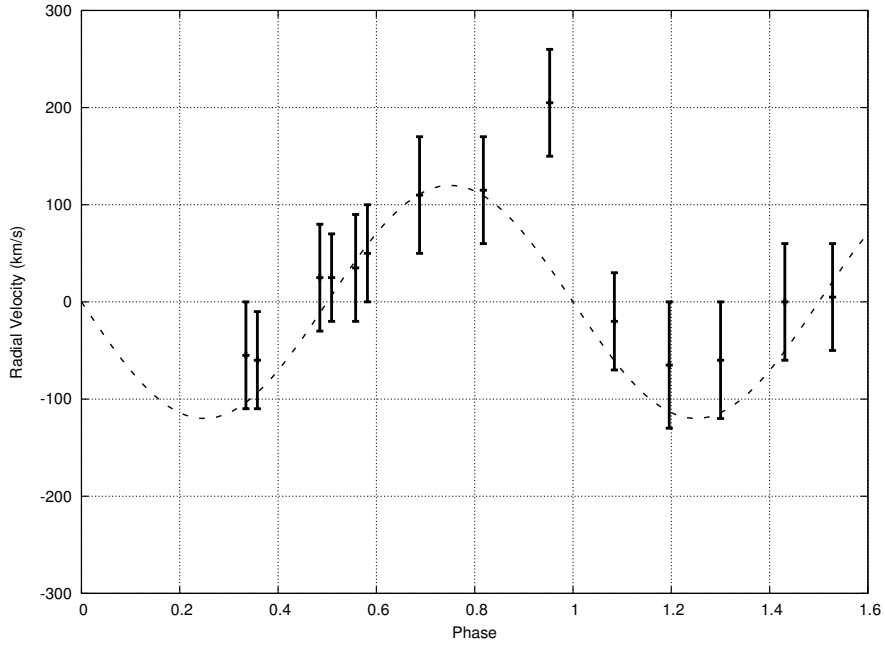

Figure 4.31: Photospheric Radial Velocity for C II 1334 & 1335. The dashed line is that appropriate to parameters from table 2.2.

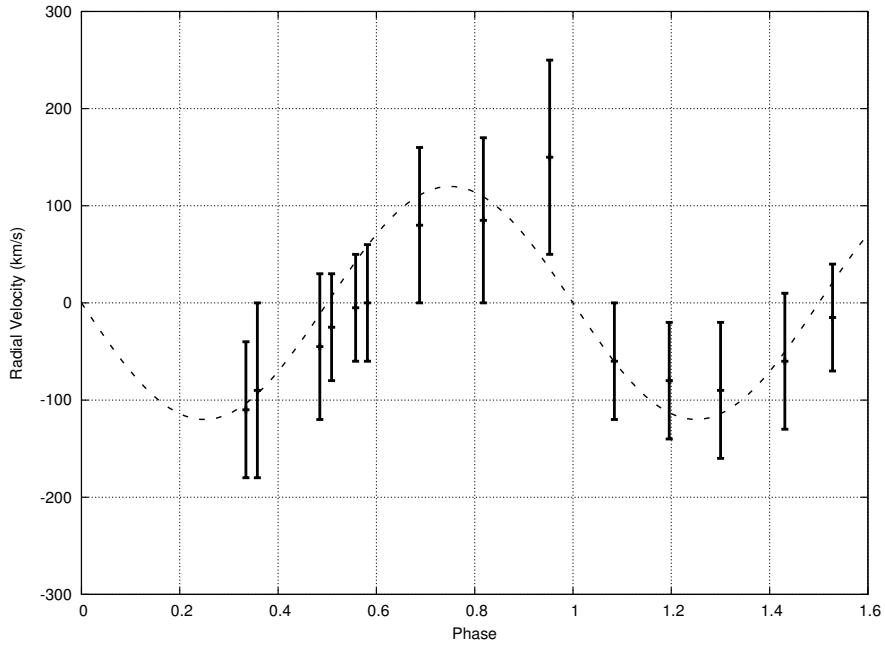

Figure 4.32: Photospheric Radial Velocity for Al II 1670. The dashed line is that appropriate to parameters from table 2.2.

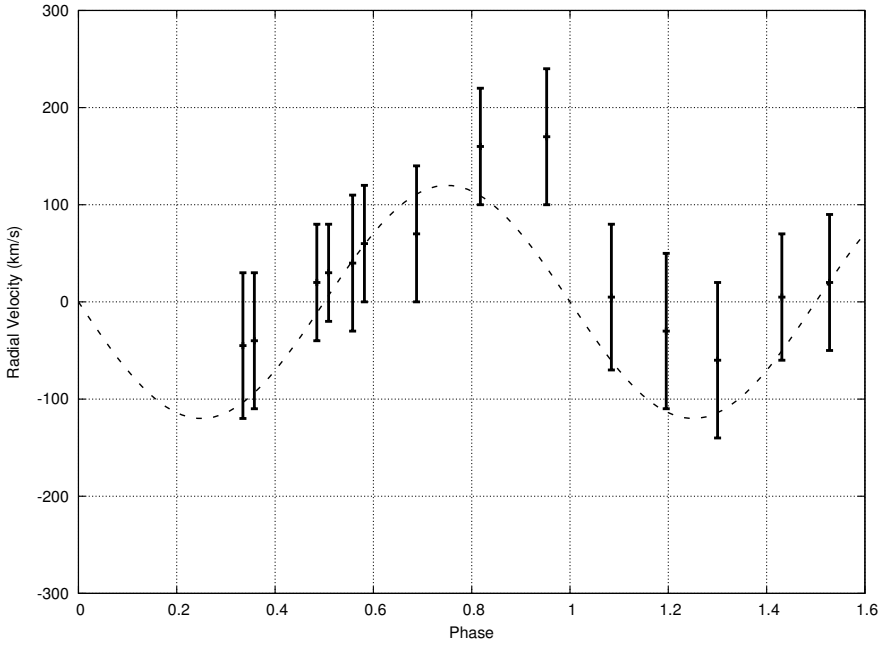

Figure 4.33: Photospheric Radial Velocity for Si II 1260. The dashed line is that appropriate to parameters from table 2.2.

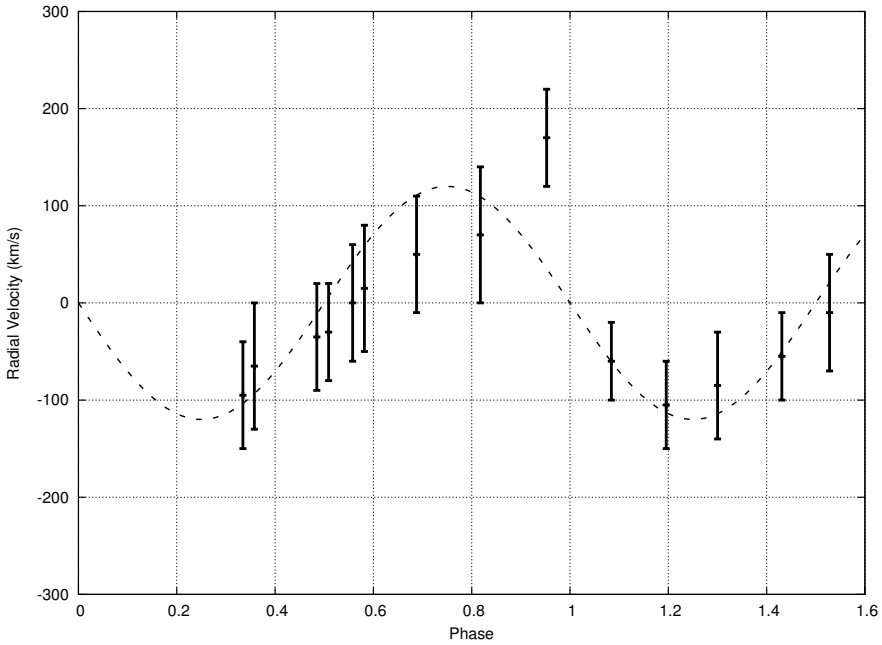

Figure 4.34: Photospheric Radial Velocity for Si II 1526. The dashed line is that appropriate to parameters from table 2.2.

4.9 Gas-Flow Velocity from Division Spectra

To properly analyze the gas flow features, we must isolate the excess spectral features from those attributed to a normal photosphere. In section 3.3 a formalism was developed to account for the absorption effects of several different intervening media before light would reach a detector. In order to remove the effects of both the photosphere (ph) and interstellar (IS) contributions, we apply (see equation (3.111))

$$F_\lambda^{n,gas}(\phi) = F_\lambda^{n,observed}(\phi) / \left(F_\lambda^{n,ph}(\phi) F_\lambda^{n,IS}(\phi) \right). \tag{4.1}$$

Therefore, by simply dividing the net flux received at the detector by the photospheric and interstellar flux profile, one could extract the flux profile of the gas stream. In applying this method to the data, several other steps were included to further refine the reliability of the measurements. Shifting to a frame of reference moving with the B-star, all of the U Cep spectral plots were shifted by an appropriate amount, according to the phase at which the image was taken, to zero-out the photospheric radial velocity. That is, the images were Doppler shifted so that there would be no apparent (orbital) motion of the photosphere. With these plots, any conspicuous absorption feature that was not centered on the laboratory rest wavelength of the line was considered a candidate for a non-photospheric flow feature. One unfortunate consequence of setting the radial velocity of the star to zero is that the interstellar lines would then shift back and forth according to phase. But since these lines are narrower and deeper than any other feature in the spectra, they were easily identified so they could be excluded from this part of the analysis. A further concern was the possible mismatch between the simulated photosphere, according to TLUSTY, and the true case for U Cep. The parameters utilized in the simulation were the best estimates to date, yet there is some uncertainty, and subsequently the division spectra could contain some measure of error. This is certainly the case with Al III, where there is considerable disagreement between the synthetic and real spectra. Factoring in the presence of an accretion disk and possible pseudo photosphere further complicates the matter. Previous researchers, going back to Struve in 1944, have noted that an accretion disk structure would introduce excess absorption at the line cores [22]. Given the fact that all of the lines being examined are already highly saturated at the line core, any deviation from the true value produced by TLUSTY could introduce

significant error. Hence, tracking gas flow or accretion disk structure at the line cores should be approached with caution.

However, flow features that appear very far away from the photospheric line center, where saturation due to the photospheric absorption is not as great, will be more reliable. Indeed, all five lines of interest do exhibit excess absorption features far removed from the line center, typically between phase 0.48 and 0.58. We follow features outside of this phase range as well; however, that is very speculative and it is not clear that we are even tracking the same flow. In fact, as we shall see, we are probably tracking a photospheric or pseudophotospheric contribution in the higher phase regions. However, at phase 1.52, the equivalent point in the orbit to phase 0.52, signs of the flow-feature doublet seem to have reappeared.

The process of extracting flow-feature fluxes and radial velocities requires several steps which we describe using C II as an example and illustrate with figures. The first two steps were described in section 4.6.1 using figures 4.9 – 4.12. Accordingly, total fluxes were normalized and presented relative to the sun according to phase in figures 4.9 & 4.10. Included were the corresponding TLUSTY simulations, shifted in wavelength to match the Doppler-shifted data. (Note that this is the only fitting parameter used that is based upon this IUE data. Other TLUSTY parameters, such as temperature and electron pressure, are based upon other measurements and theoretical models.) In figures 4.11 & 4.12, the fluxes are modified to include the interstellar contribution, and also wavelength-shifted so as to represent a view from a point moving with the B star.

Using equation (4.1) to remove the effects of both photospheric and interstellar contributions, we produce the results shown in figures 4.35 & 4.36. The dashed lines represent fits to the data using the sum of two Gaussian functions, but with constraints on their parameters. At all phases, the separation between Gaussian centers is maintained at the value appropriate to the doublet separation, and the relative amplitudes consistent with the relative oscillator strengths. In the case of C II, we fit the more conspicuous short-wavelength component (with the other component going

along for the ride). Hence, to obtain the radial velocities and error bars for these flow features, the Gaussian was fit to the shape of each absorption feature, and then shifted left and right to obtain a range of possible radial velocities, similar to the method used in finding the photospheric radial velocities. Note that these Gaussian profiles were used only to measure the line's position. No equivalent width data were taken at this point. Figures similar to 4.35 & 4.36 for the other ions of interest are included in Appendix C. For other lines, where doublet separations are large, each distinguishable component is fit separately with Gaussians.

The following figures for C II 1334 & 1335 (4.37), Al II 1670 (4.38), Si II 1260 & 1264 (4.39) and Si II 1526 & 1533 (4.40) show the measured radial velocities of the gas flow with respect to the Sun. All four lines lines show significant blue shifted velocities in the phases around secondary eclipse. After primary eclipse, any excess absorption fitted via the Gaussian profiles was mainly centered around the photospheric position and most likely due to accretion absorption or the mismatching of the TLUSTY spectra.

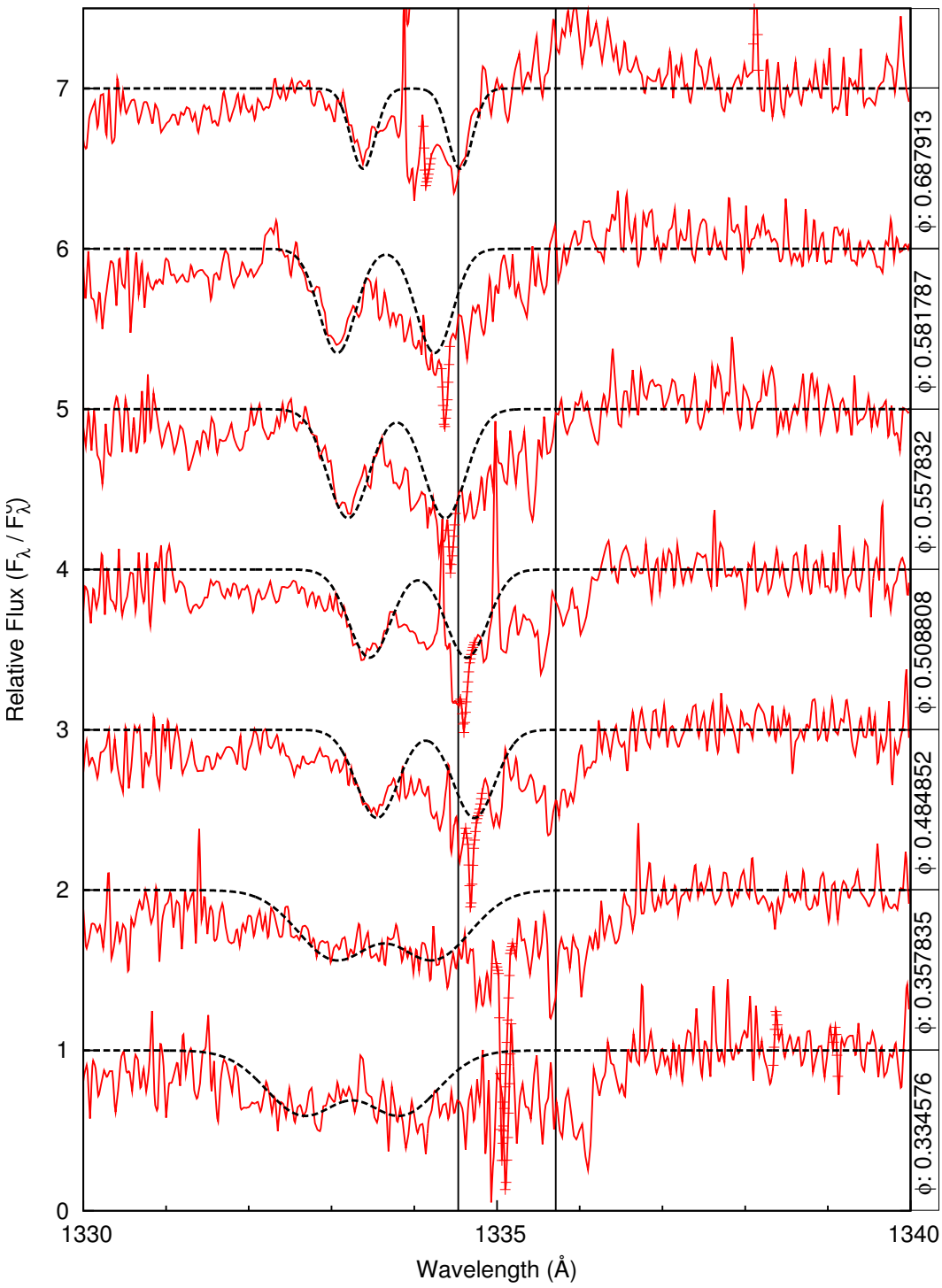

Figure 4.35: [C] (a) C II 1334 & 1335: Synthetic photosphere and interstellar lines divided out of U Cep data. Doublet Gaussian positioned at strongest flow features.

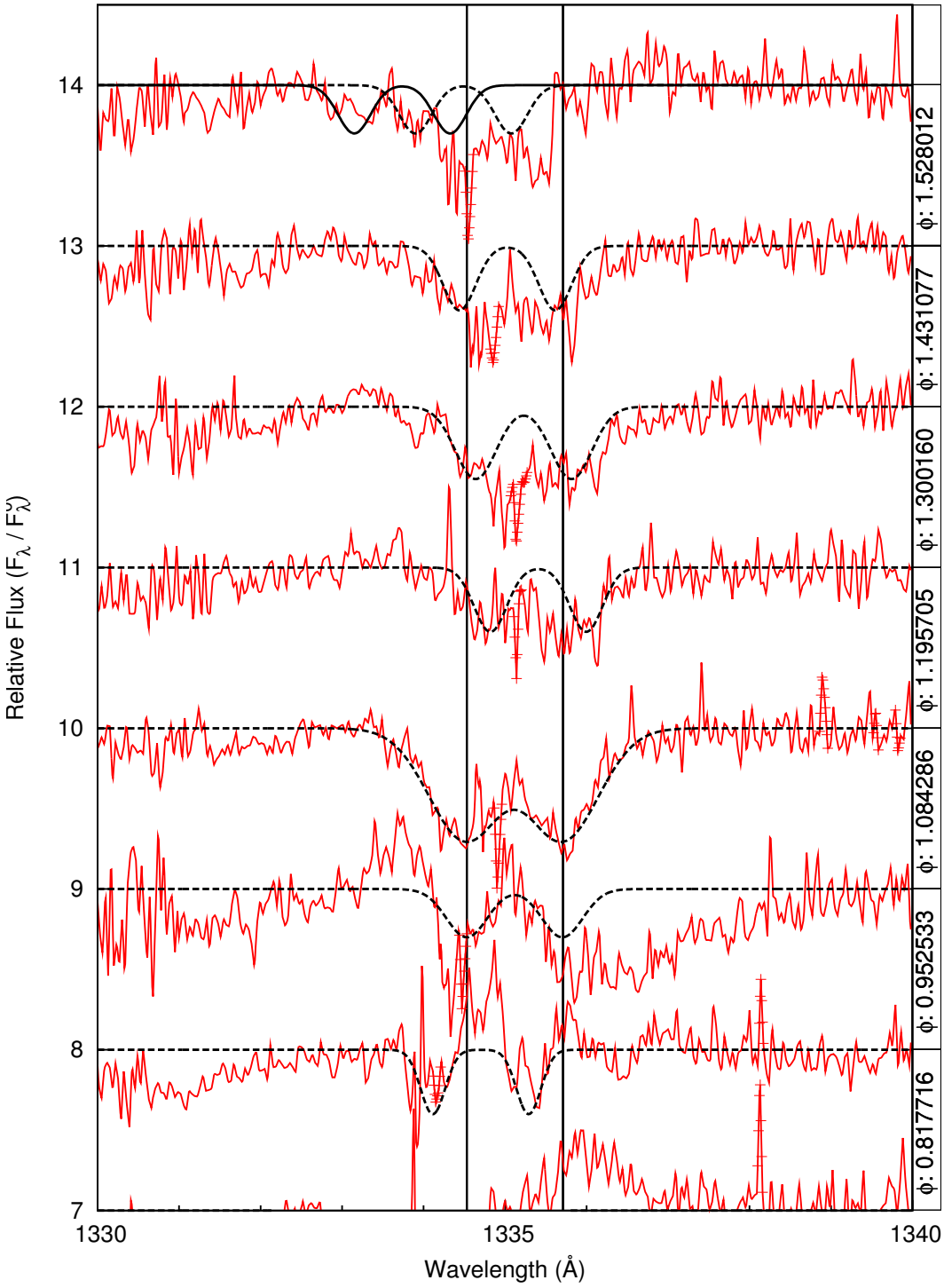

Figure 4.36: [C](b) C II 1334 & 1335: Synthetic photosphere and interstellar lines divided out of U Cep data. Doublet Gaussian positioned at strongest flow features. Solid-line double well at phase 1.52 is fit to the feature seen at phase 0.51.

Figure 4.41 displays only the more conspicuous flow feature velocities, but here viewed relative to the B-star. Dashed lines follow data in a roughly sinusoidal arc. The dash line is repeated exactly one period later to illustrate the mostly transitory nature of the gas flow. In the first orbit, the flow features are quite conspicuous, but one period later it is very difficult to find any repeatable evidence of their existence. It is possible that the flow feature seen in the first orbit was a quick mass outburst from the G star that either circled around the B-star, or impacted on the surface of the primary and splashed out what we see here. In the following orbit, we may not see signs of that flow feature either because the matter fell back onto the B-star or the matter was ejected from the system entirely and subsequently spread out and became diffuse enough as to not absorb a significant amount of light.

The sine curve is consistant with a (somewhat speculative) model of the flow feature whereby we are seeing its changing radial projection as we pass through phases approaching and around secondary eclipse. Furthermore, it indicates (rather more convincingly) a flow velocity of slightly more than 300 km/s relative to the B star.

4.10 Application of Tupaspec

Actually measuring the column density, and subsequently the number density, is best accomplished by a more sophisticated analysis than simply fitting a Gaussian to the data. The derivations contained in chapter 3 lay the ground work for the Tupaspec program. With input parameters specific to each electronic transition and the known properties of the stellar structure, Tupaspec was used to find the number of absorbers in both the photosphere of the B-star and the gas flow features. In each case, the free variable was the column density. This number was manually varied until the predicted profile coincided with the U Cep spectra. The extremes of highest and lowest column densities that could possibly fit the data were also found to establish probable error for the results. Different broadening profiles were used, depending on whether photospheric or gas flow lines were being measured. Each case started with a basic Voigt profile that considered the natural, collisional, thermal Doppler, and microturbulant broadening mechanisms. For photospheric measurements, the Voigt profile

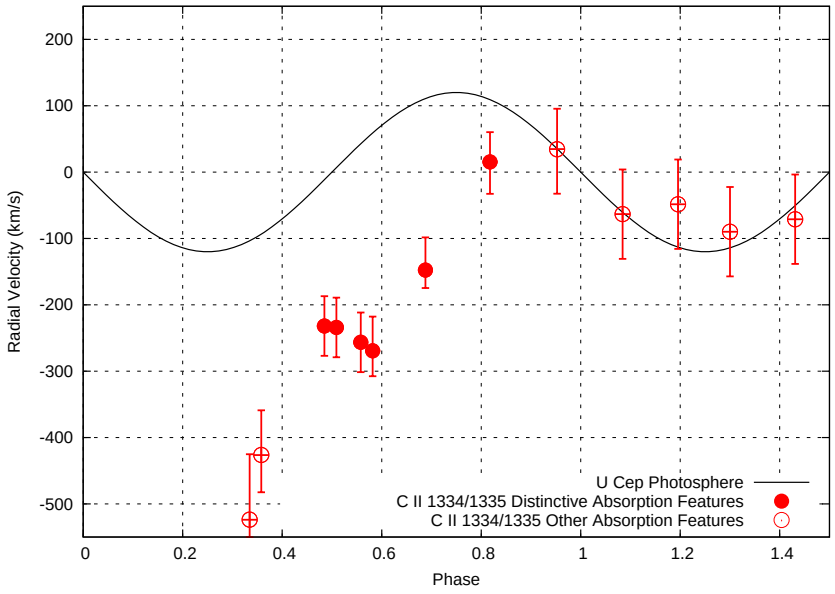

Figure 4.37: Radial velocity of C II 1334 with respect to the Sun.

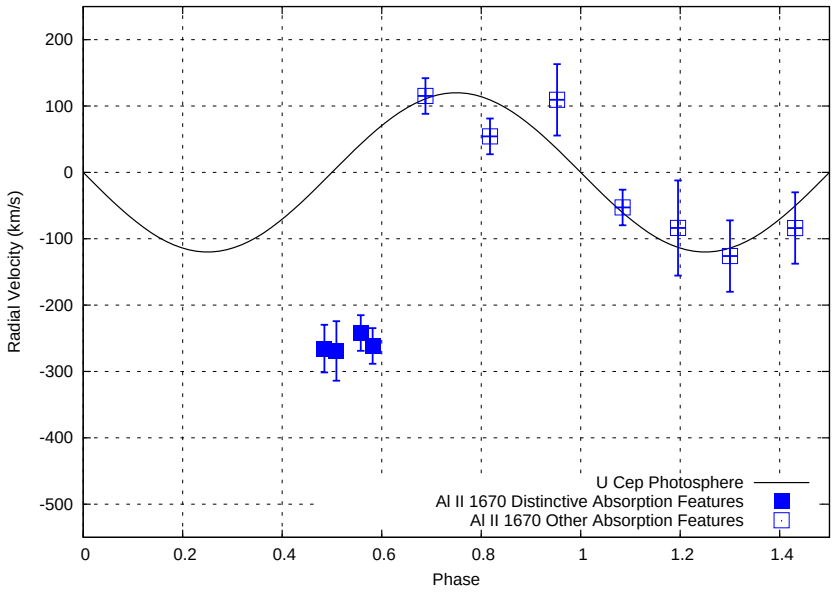

Figure 4.38: Radial velocity of Al II 1670 with respect to the Sun.

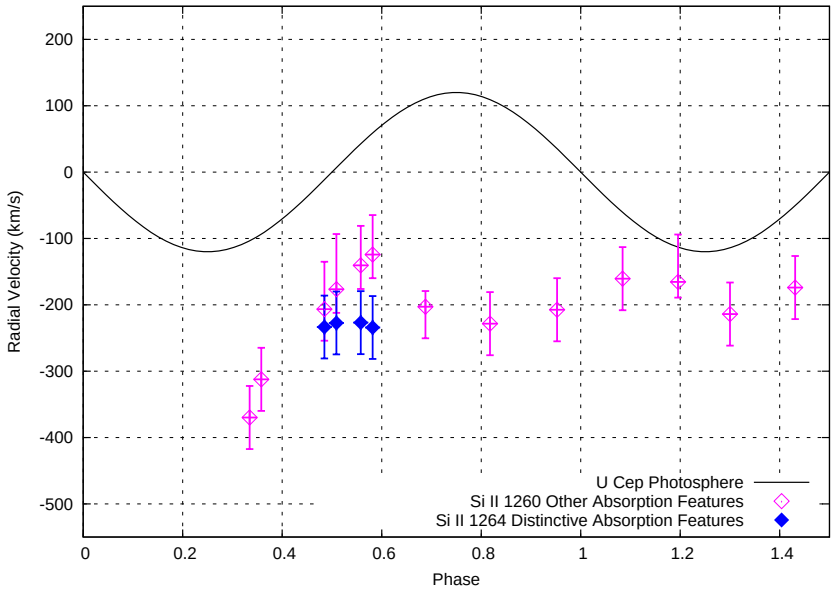

Figure 4.39: Radial velocity of Si II 1260 & 1264 with respect to the Sun.

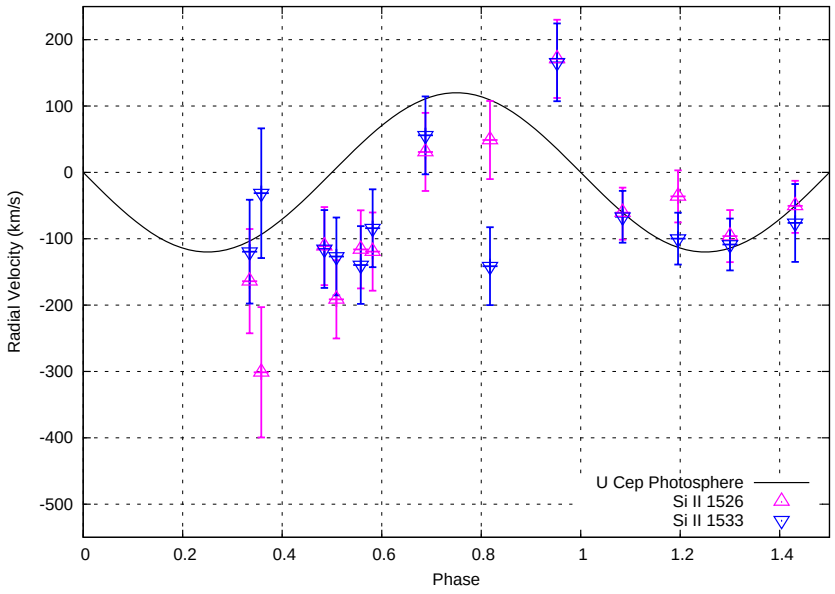

Figure 4.40: Radial velocity of Si II 1526 & 1533 with respect to the Sun.

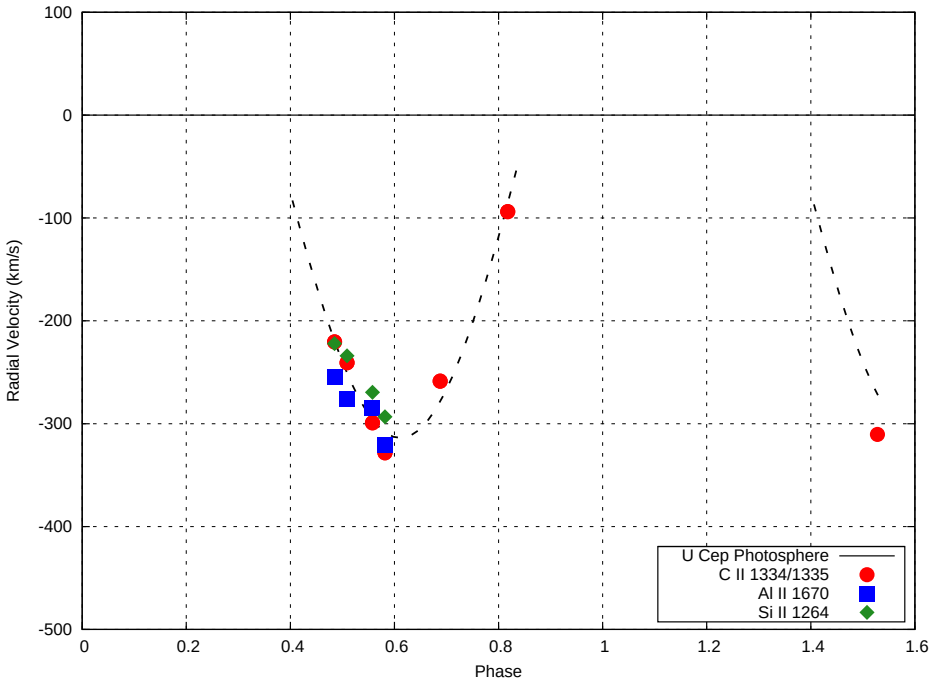

Figure 4.41: Radial velocity scatter plot of C II, Al II and Si II with respect to B-star.

was convoluted with the disk integrated macroturbulent-rotational profile function. Gas-flow-feature simulations used a convolution of the Voigt profile with a normalized Gaussian distribution function to represent the range of velocities present in the flow. The width parameter, σ, was varied to obtain a better fit with the data. The C II photospheric results versus phase are shown in figures 4.43 & 4.44 and corresponding flow-feature results in figure 4.45. In figure 4.45, note that the plots are of the log of the flux data. Hence, figure 4.45 is a plot of the optical depth. Plots appropriate to the other ions are collected in Appendix C.

In both cases, simulation fittings were done while examining the normalized flux as well as the log of the flux, as shown in detail in figure 4.42. In this way, the equivalent width as well as the optical depth could be determined by slightly different approaches to guard against any significant deviations between the two matches.

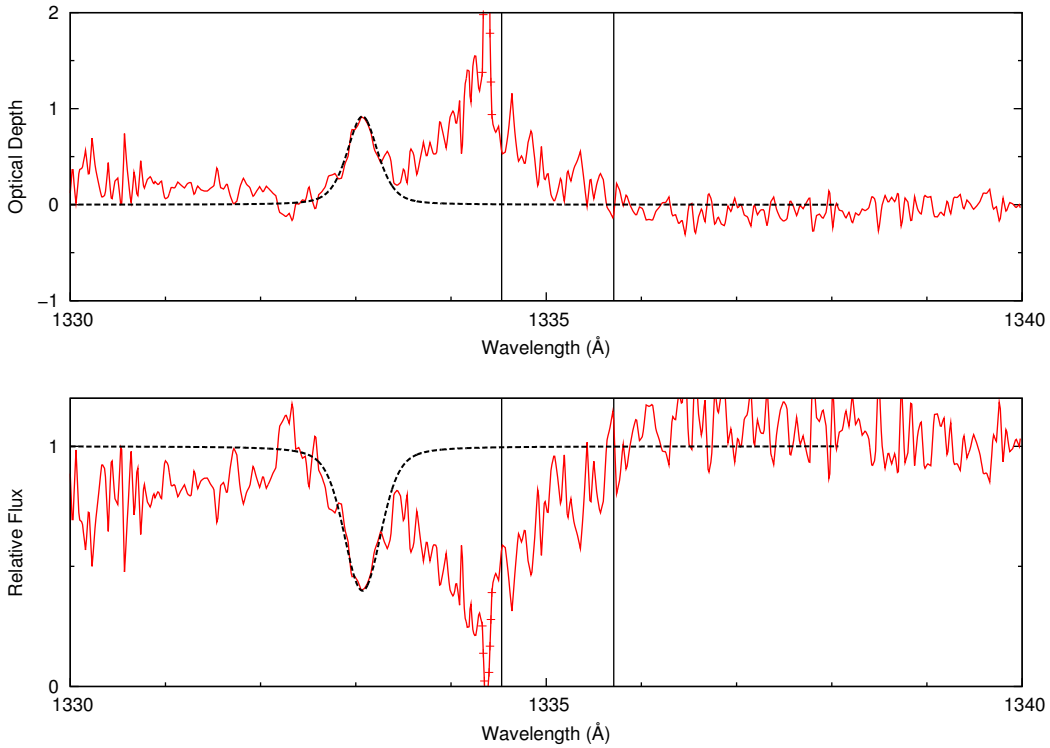

Figure 4.42: C II 1334 & 1335 Region: Example fitting of Tupaspec. The lower plot contains data obtained via the division of normalized U Cep data by a simulated photosphere. The dashed curve is a fit via Tupaspec. The upper plot is the log of the lower plot, representing optical depth. The dashed curve in this plot is the log of the Tupaspec fit.

Measurements of the gas flow spectra were only done for the most conspicuous features (i.e. those appearing between phases 0.48 and 0.58). Excess absorption features centered too close to photospheric line centers were too uncertain for useful analysis. The contribution of differential rotation, unaccounted for accretion structures, and artifacts of interstellar lines that were not completely divided out can have small contributions at the absorption line cores. These cores are already highly saturated due to just the photospheric lines, and as the log plots show, small changes in a line core may have a large impact on the log of the data. For this reason, we chose to concentrate on the conspicuous absorption features in regions with less saturation.

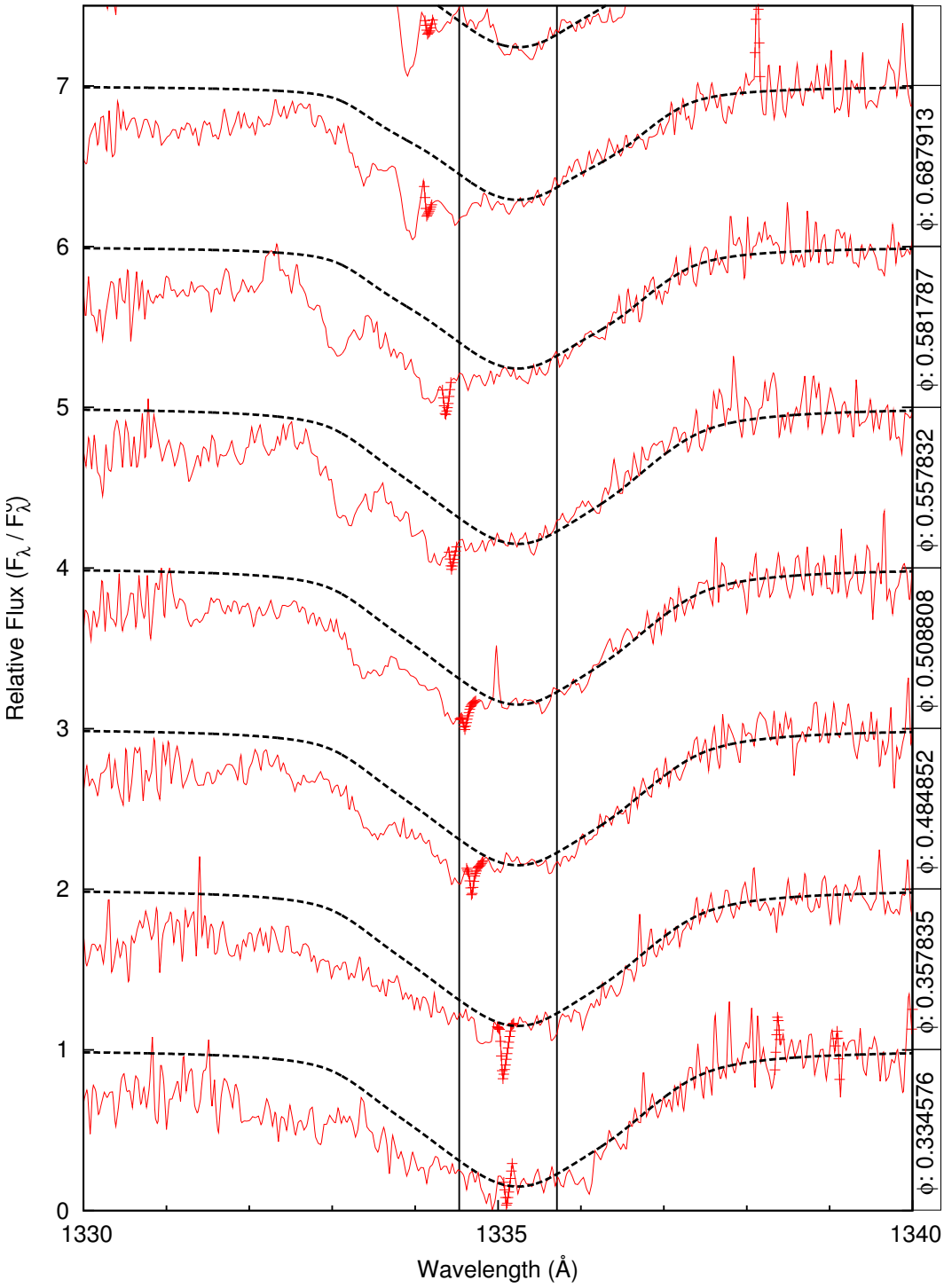

Figure 4.43: [D] (a) C II 1334 & 1335: Tupaspec fit to photosphere.

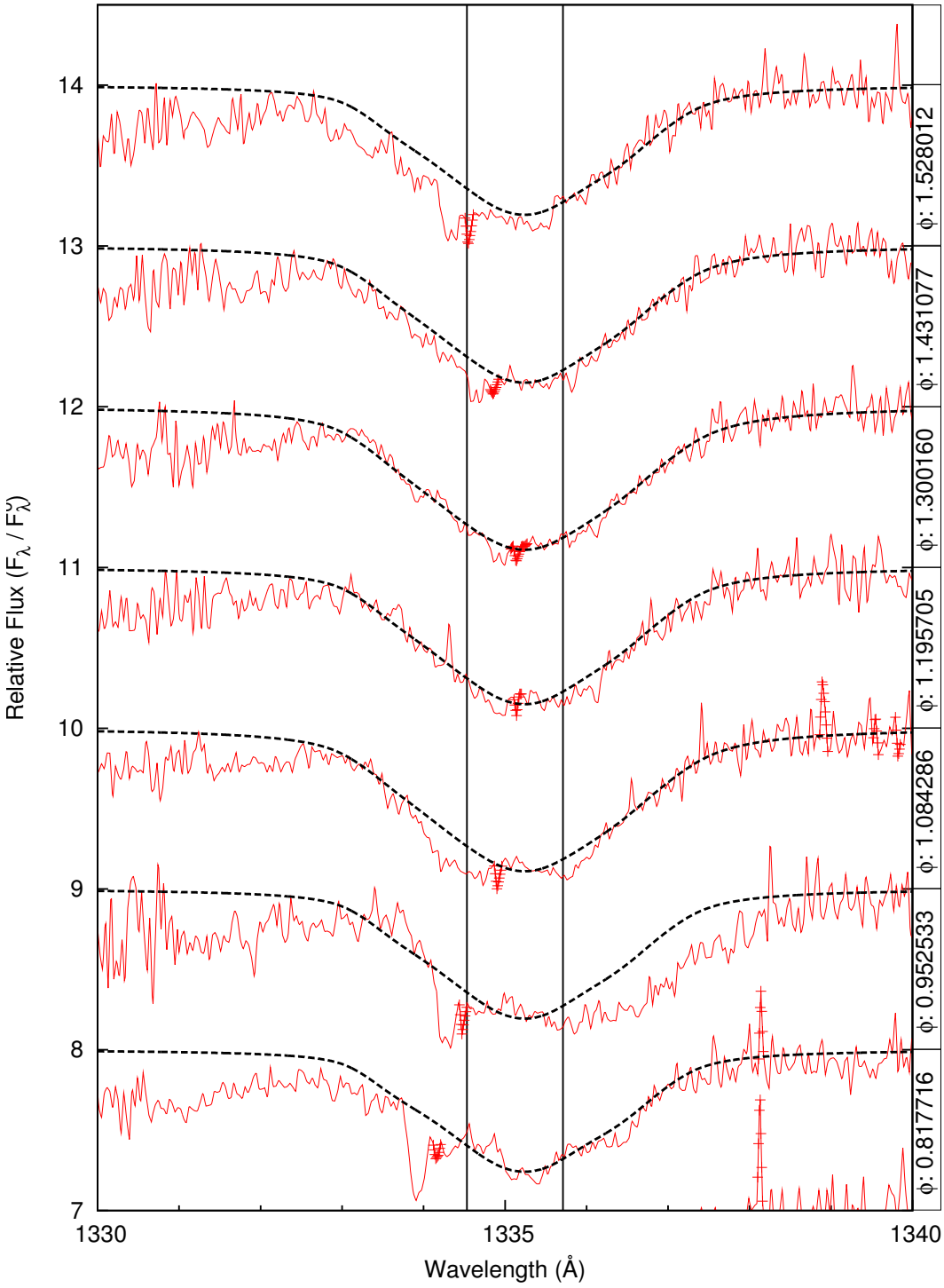

Figure 4.44: [D](b) C II 1334 & 1335: Tupaspec fit to photosphere.

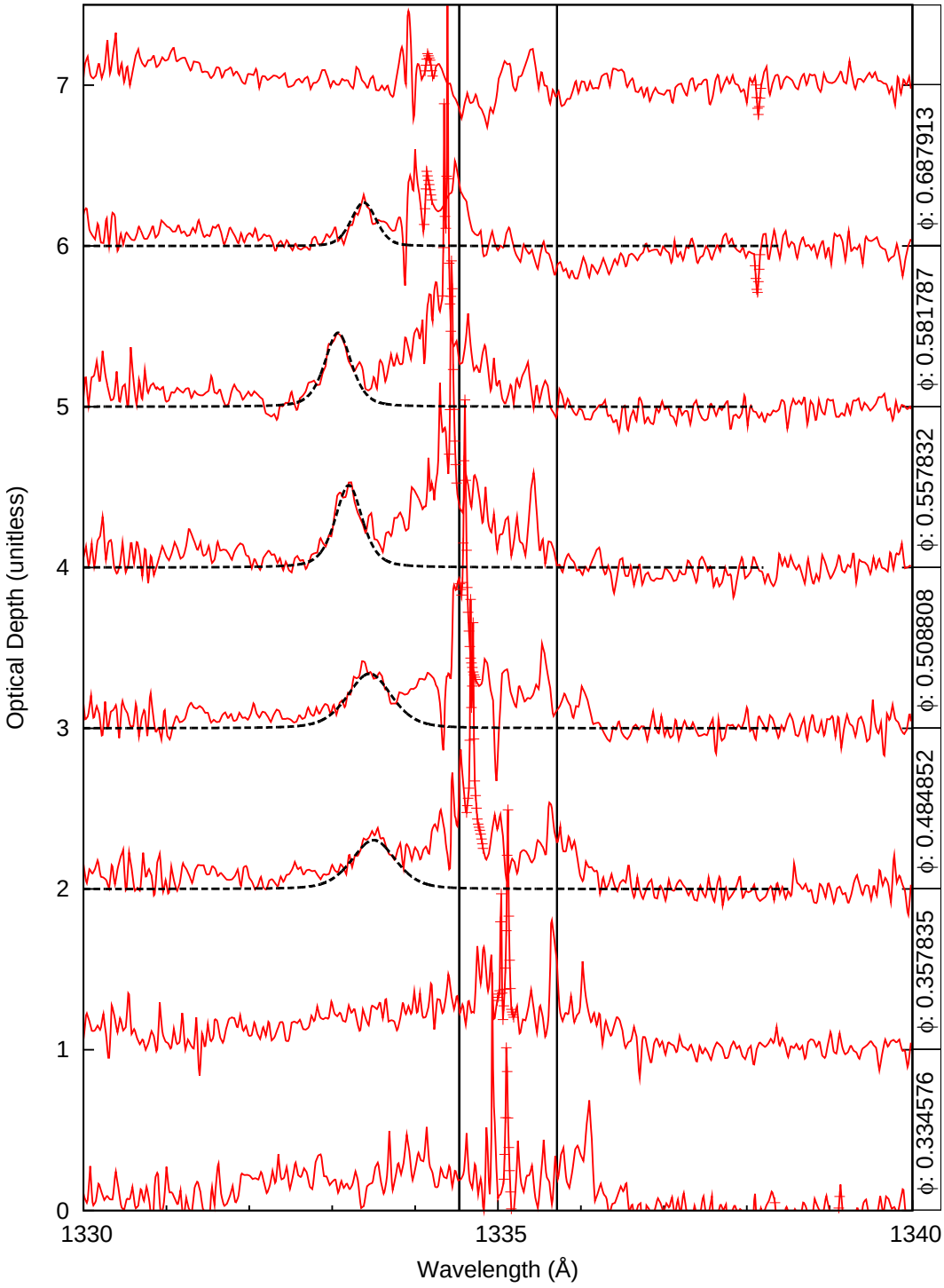

Figure 4.45: [E] C II 1334 & 1335: Tupaspec fit to optical depth of flow features isolated through divsion spectra method.

4.11 Number Densities and Mass Transfer

Once the fittings have been completed, the number density of the absorbing medium can be calculated. As described in section 3.3, the number density can be estimated using equation (3.117),

$$n(\phi) = \mathscr{N}(\phi)/L(\phi). \tag{4.2}$$

Notice that an estimate must be made of the average depth through which the light has passed.

4.11.1 Photosphere

In the case of the photosphere, many tables have been compiled for various models of stars. The photospheric depth can be defined as the point at which the gas becomes opaque, or effectively $\tau_\lambda \approx 2/3$ [41]. According to the model atmosphere tables compiled by Novotny, the depth of the photosphere for a B-star similar to U Cep's primary is roughly 1000 km or 10^8 cm [65]. We present our results for photospheric column and number densities in table 4.3. The hydrogen ion density can be estimated from the photospheric electron pressure, computed by Aller for the model atmosphere of a B-star similiar to U Cep, of approximately 320 dynes/cm^2 [49]. Since at a temperature of 13,000 K, all of the hydrogen and none of the helium atoms (together constituting over 99% of the number of atoms) will be ionized, the hydrogen number density will approximately equal the electron density. Hence, applying the ideal gas law

$$n_H = n_e = \frac{P_e}{kT} \simeq 1.8 \times 10^{14} \text{ cm}^{-3}. \tag{4.3}$$

With this information, we can estimate the element abundances relative to hydrogen. These values are reported in table 4.4. The silicon column density was determined by averaging the values for Si II 1260 & 1264 and Si II 1526 & 1533. Since these numbers should be the same, our values could be in error by a factor of two or more. Also, since Al II would account for only 33% of the aluminum abundance and Si II accounts for 33% of the silicon abundance, according to the Saha equations (see figure 3.19), we multiply our Al II and Si II values by three to account for all ionic species of aluminum and silicon.

Table 4.3: Calculated Photospheric Densities

Line	$\mathscr{N}$ (cm^{-2})	$n(cm^{-3})$
C II 1334 & 1335	1.12E+19	1.12E+11
Al II 1670	6.40E+16	6.40E+8
Si II 1260 & 1264	1.4E+18	1.4E+10
Si II 1526 & 1533	2.4E+18	2.4E+10

Table 4.4: Predicted Photospheric Densities (parenthetical H densities from other work; see text)

Calculated for U Cep (this work)					Solar
Atom	$N_c(10^{17}cm^{-2})$	$n_z(10^9cm^{-3})$	$\frac{n_z}{n_H}(10^{-6})$	$log(\frac{n_z}{n_H})+12$	$log(\frac{n_z}{n_H})+12$
Hydrogen	-	(180,000)	(1)	(12)	(12)
Carbon	112	112	6.2E-04	8.8	8.5
Silicon	57	57	3.2E-04	8.5	7.5
Aluminum	1.9	1.9	1.1E-05	7.0	6.5

The last two columns of table 4.4 display these calculated values for U Cep and the solar photosphere on the astronomical logarithmic scale, where element abundances are taken relative to 10^{12} hydrogen atoms (e.g., there are $10^{6.5}$ aluminum atoms in the sun for every 10^{12} hydrogen atoms). Although our relative abundance calculations are slightly higher than the solar case (assumed to be similar for the B star), they are correctly ordered. The solar abundances are taken from Lodders [66], except in the case of carbon, which we averaged with an older, but more commonly reported abundance value.

4.11.2 Flow Feature

The estimation of flow-feature gas densities is susceptible to more uncertainty. With only the data presented here, there is no way to estimate the gas depth accurately. Since the stream effects are mainly present in the phase range of 0.48 to 0.58, we can safely assume that the gas is passing across the observable disk of the B-star, while the G-star is behind the B-star. As mentioned earlier, the flow features essentially disappear within one orbital period, suggesting either a quick dispersion of the gas, or a quickly decaying orbit. Previous works have measured transitory accretion structures on the order of 1.1 – 1.7 R_B. We will adopt a value of 1.5 R_B for estimating

Table 4.5: Measured and Calculated Densities

Ion	**Phase**	σ	W_{eqv} **(Å)**	$\mathscr{N}_{SqrtApprx}$	$\mathscr{N}_{Fit}$	**n** (cm^{-3})
C II 1334	0.48	0.25	0.372	1.3E+18	1.3E+18	5.7E+06
	0.51	0.25	0.416	1.6E+18	1.6E+18	7.2E+06
	0.56	0.15	0.372	1.3E+18	1.3E+18	5.7E+06
	0.58	0.15	0.334	1.0E+18	1.0E+18	4.5E+06
	0.68	0.15	0.189	3.3E+17	2.5E+17	1.1E+06
Al II 1670	0.48	0.25	0.384	6.2E+15	6.3E+15	2.9E+04
	0.51	0.35	0.480	9.8E+15	1.0E+16	4.5E+04
	0.51	0.25	0.275	3.2E+15	3.2E+15	1.4E+04
	0.56	0.25	0.275	3.2E+15	3.2E+15	1.4E+04
	0.58	0.25	0.537	1.2E+16	1.3E+16	5.7E+04
Si II 1260	0.33	0.35	1.038	1.5E+17	1.6E+17	7.2E+05
	0.36	0.55	1.038	1.4E+17	1.6E+17	7.2E+05
	0.48	0.35	1.038	1.5E+17	1.6E+17	7.2E+05
	0.51	0.35	0.929	1.2E+17	1.3E+17	5.7E+05
	0.56	0.25	1.038	1.5E+17	1.6E+17	7.2E+05
	0.58	0.45	1.998	5.3E+17	6.3E+17	2.9E+06
Si II 1264	0.36	0.25	0.326	1.6E+16	1.6E+16	7.2E+04
	0.48	0.25	0.326	1.6E+16	1.6E+16	7.2E+04
	0.51	0.25	0.408	2.5E+16	2.5E+16	1.1E+05
	0.56	0.25	0.511	3.9E+16	4.0E+16	1.8E+05
	0.58	0.25	0.511	3.9E+16	4.0E+16	1.8E+05
Si II 1526	0.56	0.45	0.436	2.4E+17	2.5E+17	1.1E+06
	0.58	0.45	0.436	2.4E+17	2.5E+17	1.1E+06
Si II 1533	0.56	0.55	0.551	3.8E+17	4.0E+17	1.8E+06
	0.58	0.55	0.551	3.8E+17	4.0E+17	1.8E+06

the ionic number densities. Table 4.5 gives the range of values obtained using these estimates: values listed under $\mathscr{N}_{Fit}$ are the estimated column densities, and under n are the number densities. The listed σ value in the third column is the width parameter of the Gaussian (velocity) dispersion profile used to fit the Tupaspec simulated

line. The flow-feature number densities are about four or five orders of magnitude lower than the photospheric values, which is to be expected. The proportions of the ions relative to one another is on par with the abundance ratios list in table 4.4: the number density of aluminum is 2 orders of magnitude less than carbon and one order of magnitude less than silicon. Averaging the carbon number densities in table 4.5, we find a carbon number density of $5 \times 10^6 \mathrm{cm}^{-3}$. Using the solar abundance number from table 4.4, we estimate a flow feature hydrogen density of

$$n_H \simeq \frac{5 \times 10^6}{6 \times 10^{-4}} \simeq 8 \times 10^9 \mathrm{cm}^{-3}. \tag{4.4}$$

This is approximately five orders of magnitude less dense than the photospheric average, which is not surprising since the gas extends over a linear dimension greater by a factor of four orders of magnitude. Since hydrogen constitutes about 93% of the number of atoms in the sun, and approximately that in a B-star, the total gas flow number density is $n_{total} = n_H/0.93 \simeq n_H \simeq 8 \times 10^9 \mathrm{cm}^{-3}$.

Using the standard deviation from our carbon values yields $n_C \simeq (5 \pm 2) \times 10^6 \mathrm{cm}^{-3}$ and $n_{total} \simeq n_H \simeq (8 \pm 0.3) \times 10^9 \mathrm{cm}^{-3}$. This error estimate is similar to that which would follow from a $\sim 20\%$ error in the continuum determination, which we believe to be the primary source of systematic error. However, a greater source of error lies in additional but unresolved spectral features blending with our flow feature. Therefore, in the absence of additional information, we report our value with a conservatively estimated uncertainty; hence,

$$n_{total} \simeq (8 \pm 2) \times 10^9 \mathrm{cm}^{-3}. \tag{4.5}$$

Incidentally, since n_e is a Tupaspec input parameter, this number was lowered from the photospheric value to that of equation (4.4) in the collisional damping term. However, this made no change in the result since the electron density was so low that collisional damping was already at the threshold of barely contributing with respect to other broadening mechanisms.

We note that in 1981 Kondo, Harvel and McCluskey [30] estimated the electron density of a another gas stream (during a different epoch) to be around $\sim 10^{13}\text{cm}^{-3}$. (Note that changes in U Cep over epochs are common.) They also gave a possible range of densities. Since all ions appeared to be in the ground state, the gas density must be less than 10^{15}cm^{-3}, and the lack of forbidden lines (i.e. C III 1909) suggested a minimum electron density of around 10^{11}–10^{12}cm^{-3} [30]. Our result for the flow feature observed here is about one order of magnitude lower than their minumum value.

A further check on the reliability of the approximations used by the Tupaspec program can be done utilizing the equivalent width. All lines measured could be considered saturated, and thus within the square root regime on the curve of growth. Using equation (3.275), the equivalent widths of the measured lines were used to find the column densities,

$$\mathscr{N}(\phi) = \frac{mc^3}{\Gamma f e^2}\left(\frac{W(\phi)}{\lambda_0^2}\right)^2. \tag{4.6}$$

The fourth and fifth columns of table 4.5 list the average equivalent width and calculated column density. The column density calculated from the equivalent width shows good agreement with the $\mathscr{N}$ value used to fit the lines (column six).

4.11.3 Mass Transfer Rate

With the gas flow densities and radial velocities calculated, we can make an estimate of the mass transfer rate. While some of the values we use are somewhat uncertain, we will choose values to obtain an upper bound for the possible mass transfer rate. First, since the gas flow observed occurred primarily during the secondary eclipse phase, we know that at least a substantial portion of the B-star was occulted by the gas. Hence, we can assume that the cross-sectional dimension of the gas stream was on the order of the size of the B-star. We will then assume that the volume of gas moving towards the observer has the form of a cylinder, with a cross sectional area of the disk surface of the B-star ($A = \pi R_B^2$, the maximum possible area in this case). The number of particles, N, moving out of the cylinder per unit time with velocity

v, which is also the particle flux, can be approximated by,

$$\frac{N}{\Delta t} = \frac{nV}{\Delta t} = \frac{nAv\Delta t}{\Delta t} = nAv. \tag{4.7}$$

The mass flow rate can be found by multiplying equation (4.7) by the mass of hydrogen, hence

$$\left(\frac{\mathrm{d}m}{\mathrm{d}t}\right)_H = n_H A v m_H = 4.92 \times 10^{13}\ kg/s \approx 8x10^{-10} M_\odot/\mathrm{yr}, \tag{4.8}$$

where we have used the hydrogen density from equation (4.4). Accounting for the remaining mass (about 25% of the star) of the other atomic species (He, C, etc.), an upper limit on the total mass flow rate is estimated to be

$$\left(\frac{\mathrm{d}m}{\mathrm{d}t}\right)_{total} = \frac{1}{0.75} \times \left(\frac{\mathrm{d}m}{\mathrm{d}t}\right)_H \simeq 1 \times 10^{-9} M_\odot/\mathrm{yr}. \tag{4.9}$$

The mass transfer rate for U Cep has been estimated to be as high as $10^{-6} M_\odot$/yr from previous works [2], but those values were calculated during times of very high activity. U Cep during the September 1989 epoch was in a relatively quiescent state. For reference, Wecht calculated for Algol (a less active system than U Cep) a rate of $1.9x10^{-14} M_\odot/yr$ during one of its quiescent epochs [59]. It should be noted, that this calculation is the instantaneous mass transfer rate for the short duration of the observed gas flow in U Cep.

Chapter 5

Discussion

U Cep is a fascinating and extremely complex system that blends the behaviors of multiple structures, such as photosphere, gas flow effects, and accretion disks, that vary on remarkably short timescales. Considering the combination of noise in the data along with the multitude of time dependent contributions to the spectra, it is not surprising that U Cep is such a challenge to comprehend fully. In this final chapter, we review our work and our new understanding of U Cep, and consider possible directions for future work.

Our analysis of this system has led to the model summarized here. Our analysis of the photosphere is largely consistent with previous work done on the system. Our radial velocity curves match the predicted sinusoidal (orbital) oscillations of the system with nearly the same K_1 value [2]. Analysis of the photospheric absorption lines yields gas number densities and abundance ratios, relative to the sun, one would expect with this type of B-star. Isolating non-photospheric anomalous features has led to the conclusion that the images taken over the course of the September 1989 epoch bore witness to a short duration burst of mass flow from the G-star to the B-star.

The orbital period of the system is short enough that mass streaming off the G-star would likely pass through the inner Lagrange point and directly impact the trailing surface of the B-star. Our observations suggest that a transient absorbing medium crosses the side of the B-star opposite the G-star. It is possible that the observed

flow feature is matter that was ejected from the surface of the B-star during impact at a high velocity. Alternatively, it could be matter that has yet to make contact with the B-star. While it is possible that some of this matter may have been ejected from the system, the range of velocities that we observed, 200 to 350 km/s, are far short of the escape velocities. Escape velocity calculations show that it would require at least 400 km/s to leave the system from the surface of the G-star and 750 km/s to escape from the surface of the B-star, both of which exceed the observed gas flow speeds. Even from a distance of twice the B-star radius, a speed of 530 km/s would still be required for escape. This suggests that the matter witnessed did not leave the system, but in fact fell back onto the B-star. This process finished rather quickly, as there is little evidence of a sustained stream or any substantial flow during the period of the second orbit.

Nazarenko and Glazunova conducted a 2-dimensional hydrodynamic simulation of U Cep and predicted similar results [18]. Figure 5.1 shows the velocity field of mass flows in the system that they produced. According to their graph, phases between roughly 0.2 and 0.4 have velocity fields moving mostly tangent with respect to the B-star's face. These fields would not produce significantly Doppler shifted gas stream effects, but internal turbulence may contribute to accretion disk features. Phases 0.45 through 0.75 begin to show velocity fields with significant motion directed outward from the B-star, which is consistent with the data we have obtained. From about phase 0.75 to eclipse, the observer could view portions of the gas stream moving towards the B-star from behind. The image taken by IUE at phase 0.82 does suggest red shifted gas motion away from the observer; however these features were too small and too mixed with the photosphere to permit an accurate analysis. The model of Nazarenko and Glazunova, assuming that the mass transfer from the G-star is of a short duration, is consistent with our results.

Figure 5.2 shows our proposed model for the system during the mass flow event. Matter overflows the Roche lobe of the secondary companion, passes across the inner Lagrange point and strikes the trailing surface of the B-star. Matter is then ejected into orbit around the B-star for a short time before falling back onto the surface of the

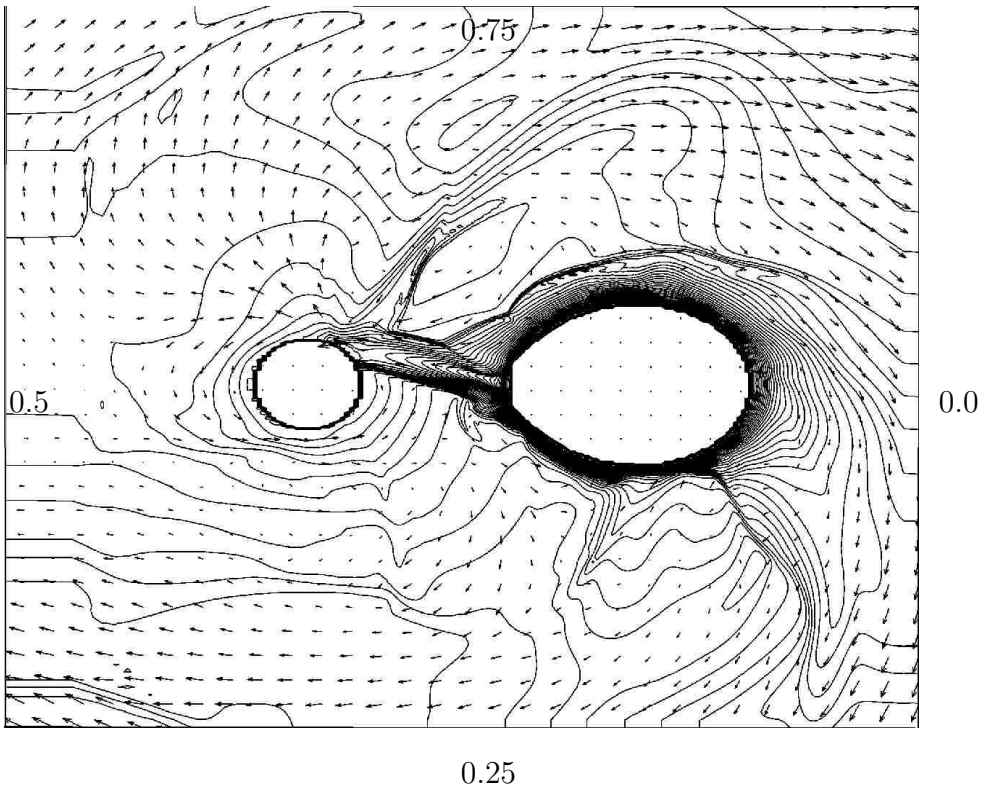

Figure 5.1: Hydrodynamic simulation produced by Nazarenko and Glazunova. Contours indicate regions of constant density and arrows give relative velocity vectors. [18]

star. This is the model most consistent with our observations. We estimate an upper limit of $1 \times 10^{-9} M_{\odot}$/yr deposited on the B-star from the G-star, but we suspect that gas flow rate is not sustained for any appreciable duration. We estimate the flow density to be $(8 \pm 2) \times 10^{9} \mathrm{cm}^{-3}$.

Much of the effort in this work has been focused on isolating and interpreting data from different components of the U Cep system. The TLUSTY & SYNSPEC programs allowed for detailed analysis of the photosphere, and the segregation of the gas stream effects from those of the primary star's atmosphere. The flexibility of adjusting rotational velocities and selectively omitting certain atomic species from the simulations facilitated our reinterpretation of several line formations, indicating

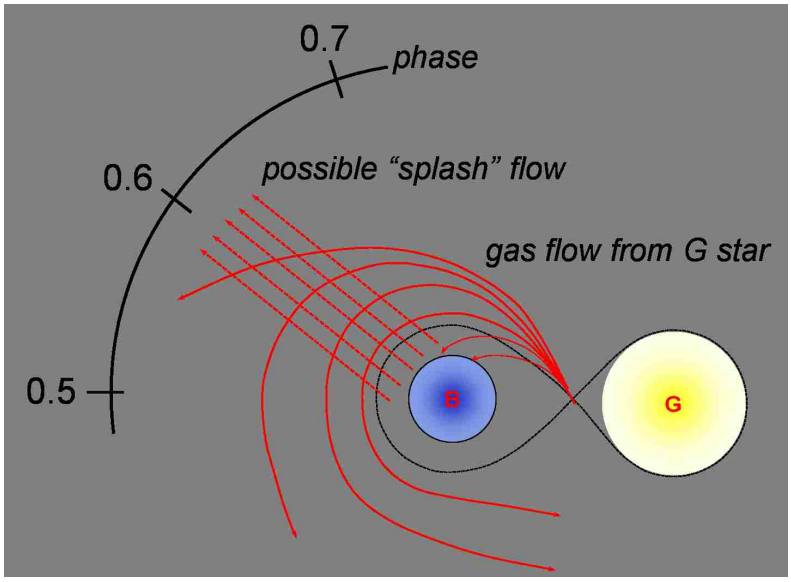

Figure 5.2: Proposed model of U Cep for the September 1989 epoch mass transfer event.

the questionable nature of C IV and Si IV line identifications. This also suggested caution when dealing with contaminated lines, such as Si II and Al III. Being unaware of these overly blended lines could have led to vastly erroneous conclusions. The TLUSTY simulations also allowed us to account for the effects of high rotational velocities and acquire more reliable continuum values. There were discrepancies between the simulated spectra and the data, such as line core depth, which could be attributed to a combination of differential rotation, equatorial bulges, and accretion structures (which TLUSTY cannot simulate). However, the simulations provided a tremendously helpful tool that aided in the analysis of the photosphere of the primary star, which led to data largely consistent with previous work done on this system.

The Tupaspec program, used in conjunction with the TLUSTY & SYNSPEC package, proved to be a versatile tool set. Once the photospheric absorption lines had been divided out of the spectral data, Tupaspec could easily be adjusted to fit the properties of the gas flow. Using the column density as the free parameter when fitting absorption lines was extremely powerful in that we could directly fit the optical depth and subsequently the abundance of a particular ion. The program's strongest suit is the ability to switch between different broadening mechanisms, be they stellar

rotation, macroturbulence, or modeling a gas stream's velocity distribution. Hence, Tupaspec was also used in determining the densities of the B-star's photospheric features. Many improvements can be made in the future. For example, the addition of a least squares fitting routine could vastly improve the the efficiency of the data taking process as well as remove several levels of human subjectivity.

The derivations and equations presented in the third chapter are improvements over what can be found in many source books. All too frequently, important steps are omitted, nomenclature is used inconsistently, and interchanged variables have led to much confusion. We endeavored here to create more uniform and intuitive systems of equations. While some minor changes have been made to variables representing physical quantities, the overall progression should be easy enough for one familiar with the topic to follow along. Many of the derivations follow a traditional progression, but with expanded detail. Other sections strove to make abundantly clear the difference between commonly misused concepts, such as absorption coefficients and profile shapes, or when it is or is not correct to carry out a convolution.

This dissertation was also just a start in our analysis of U Cep and other Algol systems using IUE data. Many more images of U Cep were taken during IUE's mission lifetime. These pictures can be used to examine repetitions of the behaviors studied in this work, or interesting divergences. Additionally, further study is recommended on the issue of U Cep's rotational rate. This aspect of the primary star has been little studied, yet rotation is the most dominant effect on the photospheric spectra.

U Cep is both a challenging and fascinating example of the Algol type binary system, and the author hopes, with time, even more of its secrets can be unlocked.

Appendix A

Ionic Transitions

Table A.1 contains full parameters and information regarding electronic transitions used in this dissertation. Transitions that are likely or expected to appear in some form have been included as well. The table lists information on laboratory wavelength, electron configuration, quantum numbers, oscillator strengths (f_{ik}), Einstein coefficients (A_{ki}). Data obtained through the NIST Atomic Spectra Database [67]. Final two columns contain the natural, Γ_N, and collisional, Γ_C, damping parameters, compiled by Kurucz [68].

Table A.1: Ionic transitions studied in this analysis.

Ion	λ_0 (Å)	Configuration	$J_i - J_k$	f_{ik}	$A_{ki}(10^8 \frac{1}{s})$	$log(\Gamma_N)$	$log(\Gamma_C)/N_e$
N V 1238	1238.82	$1s^2 2s - 1s^2 2p$	$\frac{1}{2} - \frac{3}{2}$	0.156	3.4	8.53	-6.36
N V 1242	1242.8	$1s^2 2s - 1s^2 2p$	$\frac{1}{2} - \frac{1}{2}$	0.078	3.37	8.53	-6.36
S II 1250	1250.58	$3s^2 3p^3 - 3s^2 3p^4$	$\frac{3}{2} - \frac{1}{2}$	5.4e-3	0.46	7.71	0
S II 1253	1253.81	$3s^2 3p^3 - 3s^2 3p^4$	$\frac{3}{2} - \frac{3}{2}$	9.9e-3	0.42	0.63	0
S II 1259	1259.52	$3s^2 3p^3 - 3s^2 3p^4$	$\frac{3}{2} - \frac{5}{2}$	0.012	0.34	7.53	0
Si II 1260	1260.42	$3s^2 3p - 3s^2 3d$	$\frac{1}{2} - \frac{3}{2}$	1.22	25.7	9.39	-5.21
Si II 1264	1264.74	$3s^2 3p - 3s^2 3d$	$\frac{3}{2} - \frac{5}{2}$	1.09	30.4	9.4	-5.21
Si II 1265	1265.02	$3s^2 3p - 3s^2 3d$	$\frac{3}{2} - \frac{3}{2}$	0.113	4.73	9.39	-5.21
Si III 1294	1294.54	$3s3p - 3p^2$	1 – 2	0.224	5.35	9.33	-5.74
Si III 1296	1296.73	$3s3p - 3p^2$	0 – 1	0.537	7.1	9.33	-5.74
Si III 1298	1298.89	$3s3p - 3p^2$	1 – 1	0.134	5.29	9.33	-5.74
Si III 1299	1298.96	$3s3p - 3p^2$	2 – 2	0.401	15.9	9.33	-5.74
Si III 1301	1301.15	$3s3p - 3p^2$	1 – 0	0.178	21.1	9.33	-5.74
Si III 1303	1303.32	$3s3p - 3p^2$	2 – 1	0.133	8.71	9.33	-5.74
C II 1334	1334.53	$2s^2 2p - 2s2p^2$	$\frac{1}{2} - \frac{3}{2}$	0.127	2.37	8.45	-6.52
C II 1335	1335.66	$2s^2 2p - 2s2p^2$	$\frac{3}{2} - \frac{3}{2}$	0.013	0.474	8.45	-6.52
C II 1335	1335.71	$2s^2 2p - 2s2p^2$	$\frac{3}{2} - \frac{5}{2}$	0.114	2.84	8.46	-6.52
Si IV 1393	1393.76	$2p^6 3s - 2p^6 3p$	$\frac{1}{2} - \frac{3}{2}$	0.513	8.8	8.96	-6
Si IV 1402	1402.77	$2p^6 3s - 2p^6 3p$	$\frac{1}{2} - \frac{1}{2}$	0.255	8.63	8.96	-6

continues ...

Ion	λ_0 (Å)	Configuration	$J_i - J_k$	f_{ik}	$A_{ki}(10^8 \frac{1}{s})$	$log(\Gamma_N)$	$log(\Gamma_C)/N_e$
Si III 1417	1417.24	$3s3p - 3p^2$	1 0	0.218	21.7	9.72	0
Ni II 1454	1454.84	–	–	–	–	0	0
Si II 1526	1526.72	$3s^2 3p - 3s^2 4s$	$\frac{1}{2} - \frac{1}{2}$	0.133	3.81	9.04	-5.42
Si II 1533	1533.45	$3s^2 3p - 3s^2 4s$	$\frac{3}{2} - \frac{1}{2}$	0.133	7.52	9.04	-5.42
C IV 1548	1548.2	$1s^2 2s - 1s^2 2p$	$\frac{1}{2} - \frac{3}{2}$	0.19	2.65	8.42	-6.1
C IV 1550	1550.77	$1s^2 2s - 1s^2 2p$	$\frac{1}{2} - \frac{1}{2}$	0.095	2.64	8.42	-6.1
Al II 1670	1670.79	$2p^6 3s^2 - 3s3p$	0 – 1	1.83	14.6	9.16	0
Si II 1808	1808.01	$3s^2 3p - 3s3p^2$	$\frac{1}{2} - \frac{3}{2}$	2.5e-3	0.003	6.69	-6.15
Si II 1816	1816.93	$3s^2 3p - 3s3p^2$	$\frac{3}{2} - \frac{5}{2}$	2.0e-3	0.003	6.69	-6.15
Si II 1817	1817.45	$3s^2 3p - 3s3p^2$	$\frac{3}{2} - \frac{3}{2}$	1.6e-4	0	6.69	-6.15
Al III 1854	1854.72	$2p^6 3s - 2p^6 3p$	$\frac{1}{2} - \frac{3}{2}$	0.557	5.4	8.73	-5.72
Al III 1862	1862.79	$2p^6 3s - 2p^6 3p$	$\frac{1}{2} - \frac{1}{2}$	0.277	5.33	8.73	-5.72
Fe III 1895	1895.46	–	–	–	–	8.78	-6.69

Appendix B

IUE IMAGES

Table B.2: IUE LWP/LWR Observations of UCep

Data ID	Obs. Start Time (UT)	Exp. Time (s)	Disp.	UCep Phase
LWR01597	06/02/78 11:46	1200	HIGH	0.19
LWR02118	08/20/78 04:54	1200	HIGH	0.76
LWR02301	09/07/78 14:33	1200	HIGH	0.14
LWR02302	09/07/78 15:25	1500	HIGH	0.16
LWR02292	09/07/78 00:57	1440	HIGH	0.91
LWR02314	09/11/78 00:37	2160	HIGH	0.52
LWR02315	09/11/78 01:47	2400	HIGH	0.54
LWR02321	09/11/78 13:39	2040	HIGH	0.73
LWR02322	09/11/78 14:47	1920	HIGH	0.75
LWR02836	11/05/78 22:28	1500	HIGH	0.94
LWR03915	03/03/79 00:28	2160	HIGH	0.9
LWR03965	03/09/79 02:21	2400	HIGH	0.34
LWR04107	03/24/79 21:08	2400	HIGH	0.67
LWR04108	03/24/79 22:57	2400	HIGH	0.7
LWR04490	05/09/79 21:29	2400	HIGH	0.13
LWR04493	05/10/79 15:20	1800	HIGH	0.43
LWR04751	06/10/79 15:00	2400	HIGH	0.86

Continued on next page

Table B.2 – continued from previous page

Data ID	Obs. Start Time (UT)	Exp. Time (s)	Disp.	UCep Phase
LWR06677	01/16/80 05:13	1200	HIGH	0.93
LWR06678	01/16/80 06:00	1500	HIGH	0.95
LWR06679	01/16/80 06:52	3120	HIGH	0.97
LWR07873	05/27/80 14:51	3300	HIGH	0.05
LWR07874	05/27/80 16:16	1500	HIGH	0.07
LWP08337	06/04/86 18:15	1500	HIGH	0.14
LWP08338	06/04/86 19:32	1500	HIGH	0.16
LWP08343	06/06/86 20:40	900	HIGH	0.98
LWP08395	06/15/86 17:19	1500	HIGH	0.53
LWP08396	06/15/86 18:32	1800	HIGH	0.55
LWP08397	06/15/86 20:11	2400	HIGH	0.58
LWP08401	06/16/86 13:43	1800	HIGH	0.87
LWP09386	10/22/86 10:39	1500	HIGH	0.16
LWP09387	10/22/86 11:54	1200	HIGH	0.18
LWP16328	09/11/89 11:29	1320	HIGH	0.35
LWP16331	09/11/89 19:09	1200	HIGH	0.47
LWP16332	09/11/89 20:26	1260	HIGH	0.5
LWP16334	09/12/89 00:48	1200	HIGH	0.57
LWP16335	09/12/89 02:18	1200	HIGH	0.59
LWP16337	09/12/89 07:17	1200	HIGH	0.68
LWP16341	09/12/89 16:20	1200	HIGH	0.83
LWP16344	09/12/89 22:28	1800	HIGH	0.93
LWP16346	09/13/89 02:14	4200	HIGH	0
LWP16348	09/13/89 08:39	1800	HIGH	0.1
LWP16351	09/13/89 14:59	1200	HIGH	0.21
LWP16354	09/13/89 21:13	1200	HIGH	0.31
LWP16345	09/13/89 00:34	3000	HIGH	0.97
LWP16357	09/14/89 05:05	1200	HIGH	0.44
LWP16359	09/14/89 10:50	1200	HIGH	0.54

Table B.1: IUE SWP Observations of UCep

Data ID	Obs. Start Time (UT)	Exp. Time (s)	Disp.	UCep Phase
SWP01580	05/19/78 22:06	3600	HIGH	0.750
SWP01693	06/02/78 12:19	3000	HIGH	0.201
SWP03230	11/05/78 22:59	3000	HIGH	0.952
SWP04457	03/03/79 01:10	2700	HIGH	0.917
SWP04746	03/24/79 21:52	3600	HIGH	0.688
SWP14624	08/02/81 07:21	3600	HIGH	0.201
SWP28429	06/04/86 17:38	1800	HIGH	0.126
SWP28430	06/04/86 18:49	2100	HIGH	0.147
SWP28431	06/04/86 20:04	2400	HIGH	0.168
SWP28494	06/15/86 17:51	2100	HIGH	0.543
SWP28495	06/15/86 19:10	3300	HIGH	0.568
SWP28502	06/16/86 14:18	2700	HIGH	0.886
SWP28931	08/18/86 14:06	4500	HIGH	0.157
SWP29513	10/22/86 10:06	1500	HIGH	0.155
SWP29514	10/22/86 11:11	2100	HIGH	0.174
SWP36990	09/11/89 10:35	2700	HIGH	0.335
SWP36991	09/11/89 12:01	2400	HIGH	0.358
SWP36994	09/11/89 19:37	2400	HIGH	0.485
SWP36995	09/11/89 21:02	2520	HIGH	0.509
SWP36997	09/12/89 00:00	2280	HIGH	0.558
SWP36998	09/12/89 01:24	2520	HIGH	0.582
SWP37000	09/12/89 07:46	2400	HIGH	0.688
SWP37004	09/12/89 15:32	2400	HIGH	0.818
SWP37007	09/12/89 23:26	3600	HIGH	0.953
SWP37012	09/13/89 07:19	3600	HIGH	0.084
SWP37015	09/13/89 14:09	2400	HIGH	0.196
SWP37018	09/13/89 20:24	2400	HIGH	0.300
SWP37022	09/14/89 04:14	2400	HIGH	0.431
SWP37024	09/14/89 10:02	2400	HIGH	0.528

Appendix C

Data Plots

Included here are detailed plots of all of the ion studied from the September 1989 data run. Subsequent plots will show the progression of the data analysis and reduction. The normalized fluxes are layered in chronological order from the bottom to the top. The x-axis gives the wavelength range, while the vertical axis is the normalized flux. Each image's associated phase is listed to the right. Vertical black lines indicate the location of the laboratory rest wavelength.

The series of plots will show the line analysis progression as follows:

- [A] Data taken with respect to the Sun. In these plots the lines will appear to shift left and right according to phase and is indictative of the binary orbit of the primary star. Dashed lines indicate TLUSTY simulated spectra.
- [B] Doppler corrected images with respect to B7/8 V star. Thus, the photospheric motion is eliminated. In these images interstellar lines will appear to oscillate according to phase. These plots are best used to locate non-photospheric gas flows or other anomalous absorption features.
- [C] Division spectra of U Cep and the simulated photospheric spectra. Gaussians have been fit to obvious absorption excess features to measure radial velocity of flow features.
- [D] Tupaspec fit of photospheric lines.
- [E] Tupaspec fit of flow feature, in terms of optical depth.

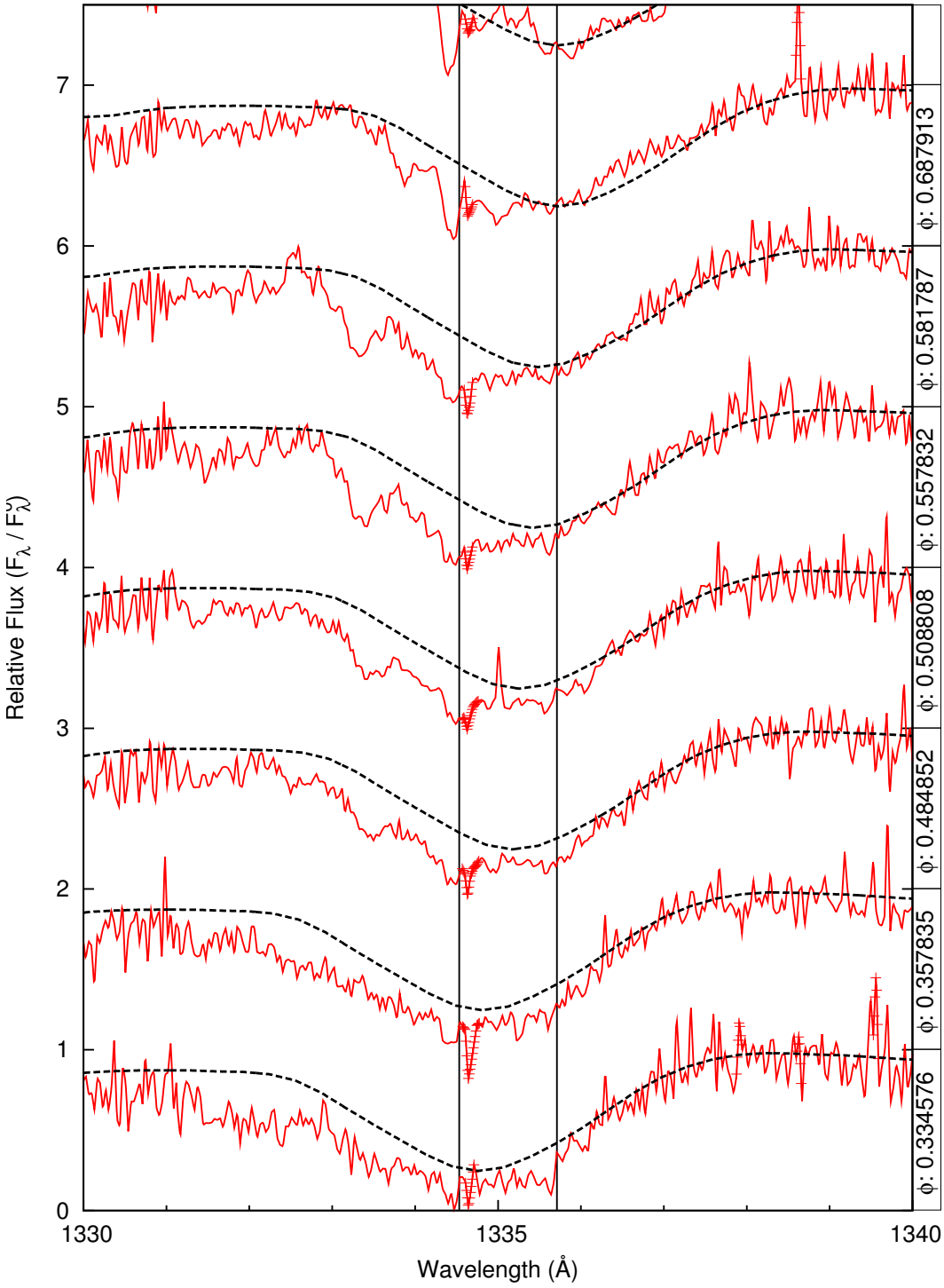

Figure C.1: [A] (a) C II 1334 & 1335: Normalized U Cep data. Doppler motion with respect to the Sun. Synthetic spectra matched to data.

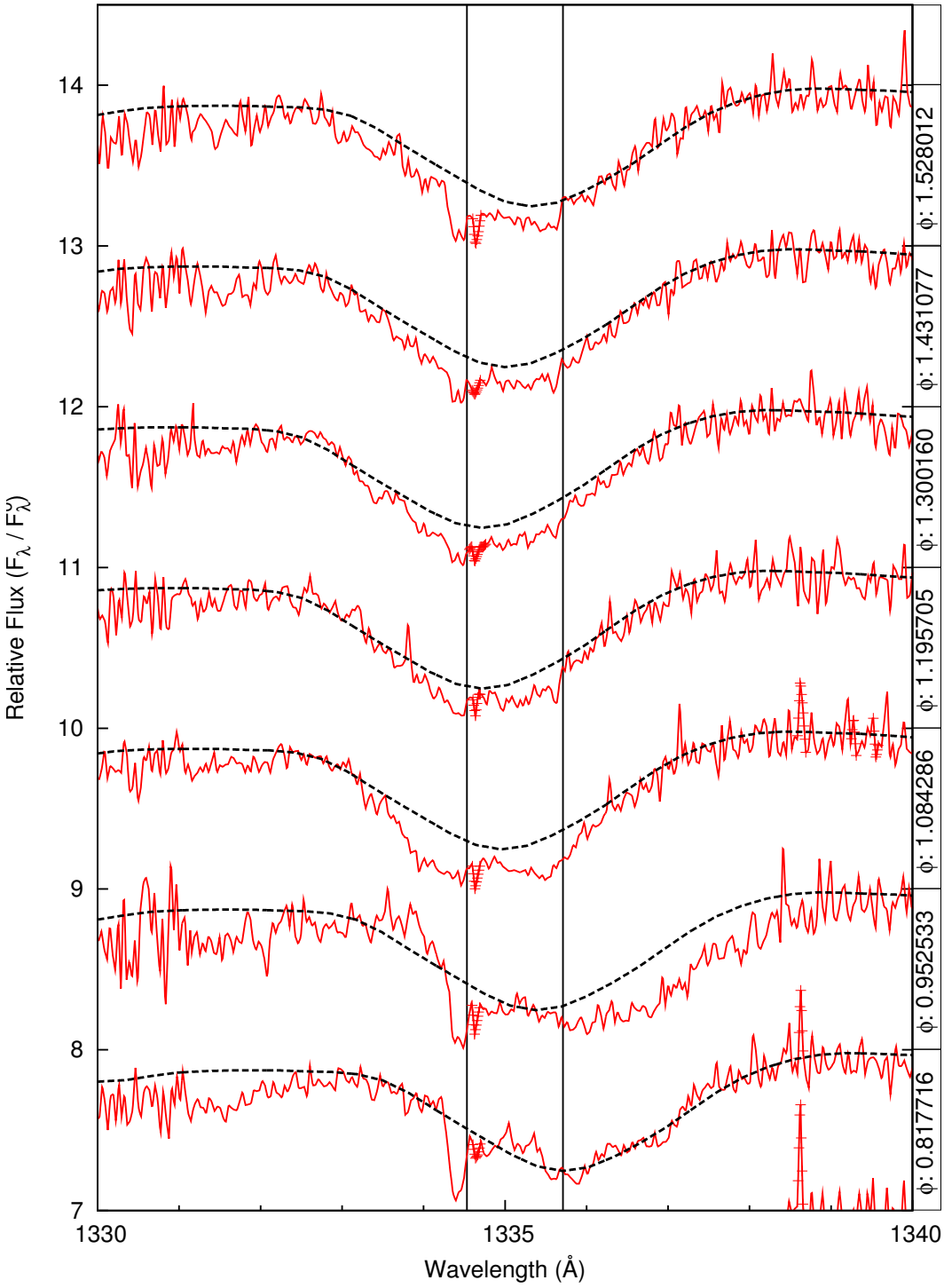

Figure C.2: [A] (b) C II 1334 & 1335: Normalized U Cep data. Doppler motion with respect to the Sun. Synthetic spectra matched to data.

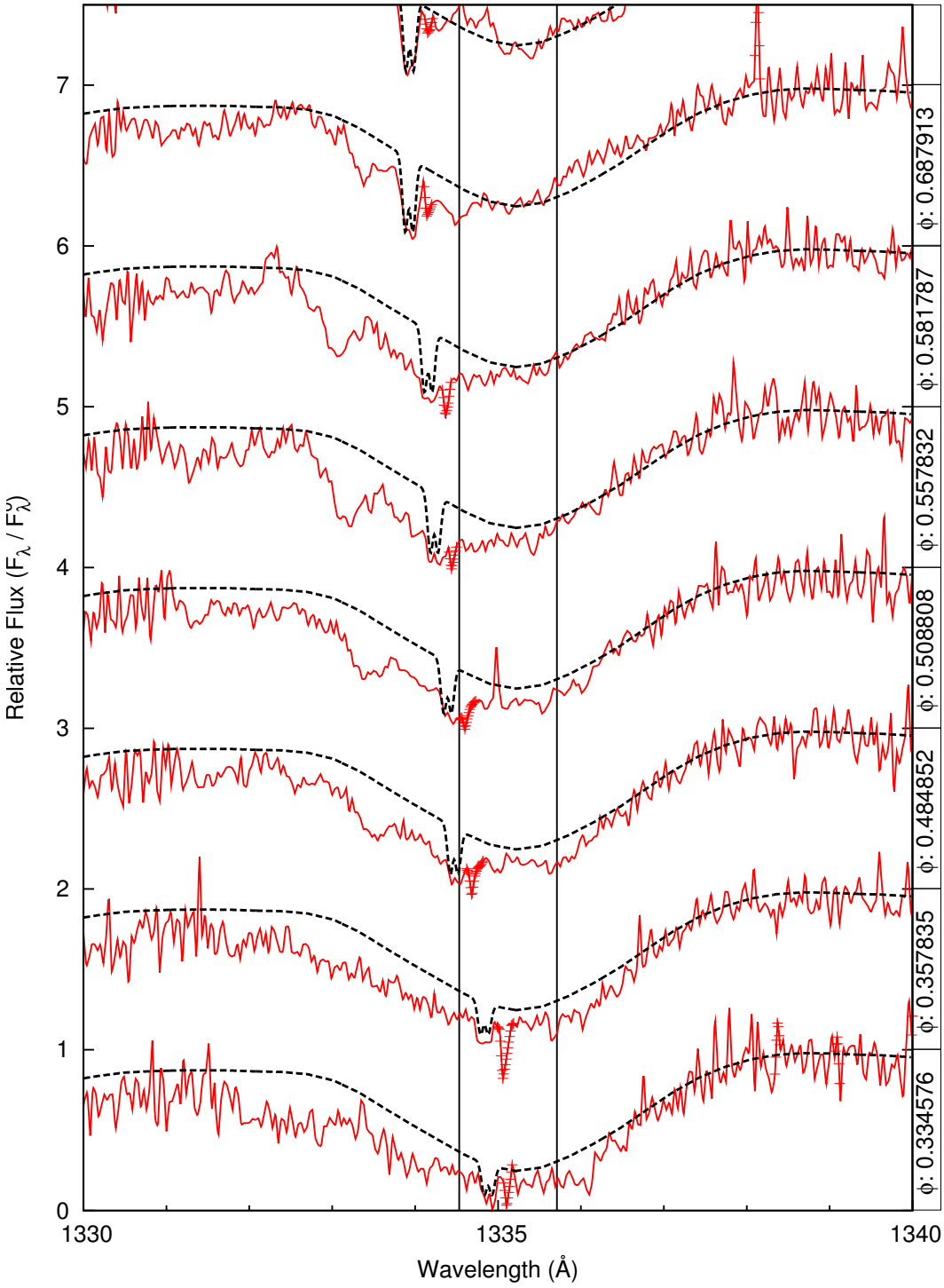

Figure C.3: [B] (a) C II 1334 & 1335: Normalized U Cep data. Synthetic spectra and interstellar absorption lines matched to data.

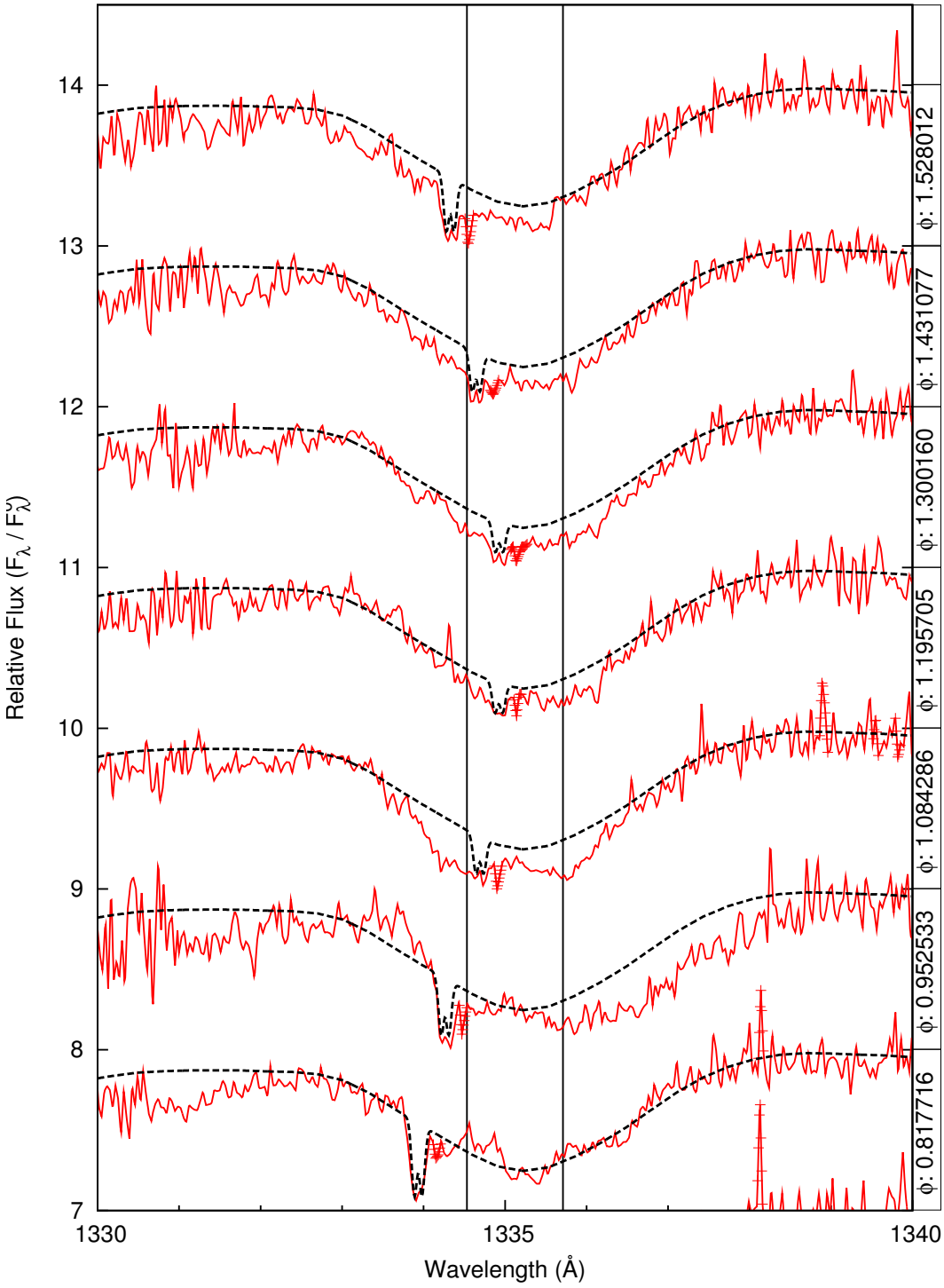

Figure C.4: [B] (b) C II 1334 & 1335: Normalized U Cep data. Synthetic spectra and interstellar absorption lines matched to data.

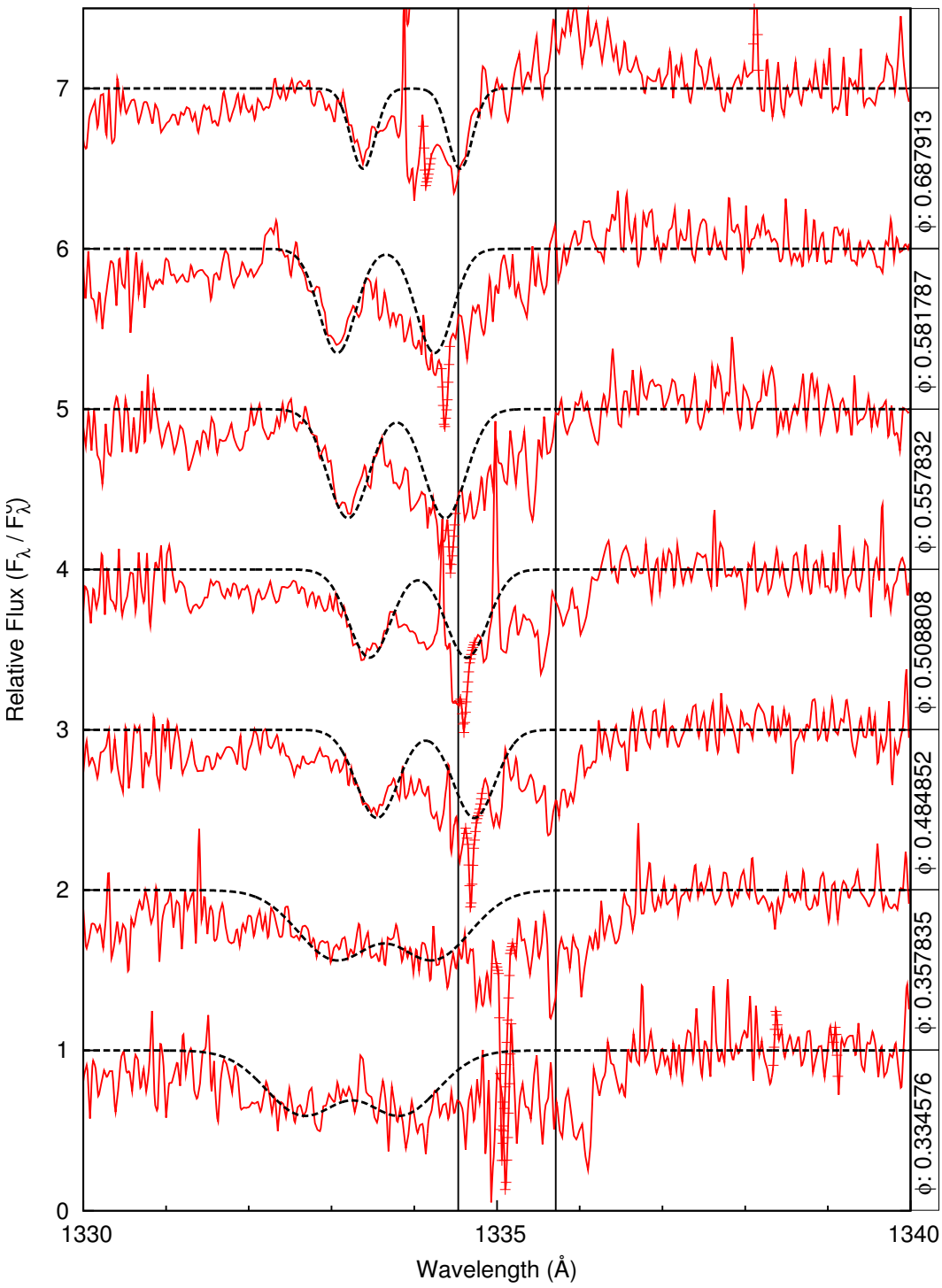

Figure C.5: [C] (a) C II 1334 & 1335: Synthetic photosphere and interstellar lines divided out of U Cep data. Doublet Gaussian fitting added to to strongest flow features.

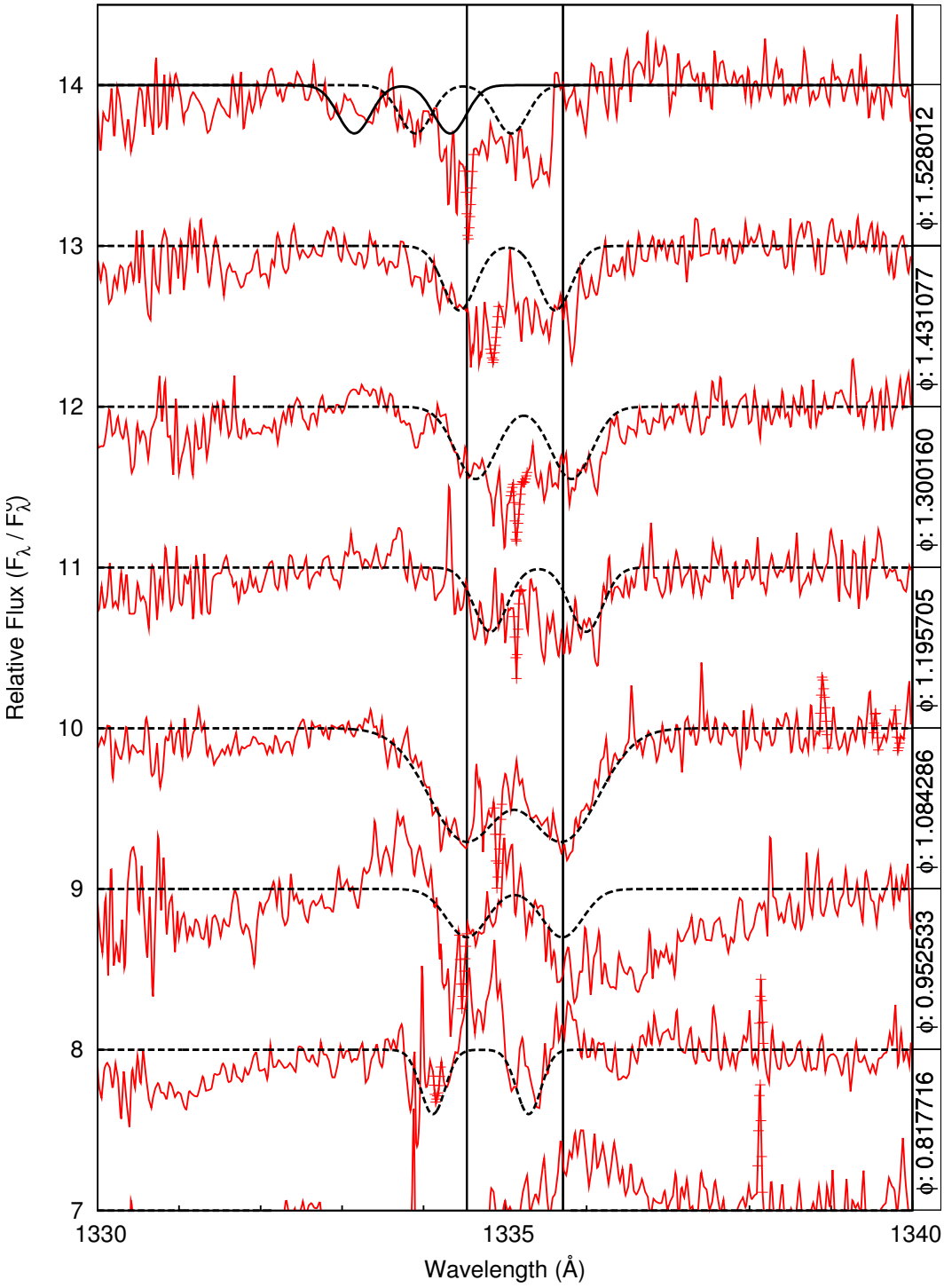

Figure C.6: [C](b) C II 1334 & 1335: Synthetic photosphere and interstellar lines divided out of U Cep data. Doublet Gaussian fitting added to to strongest flow features.

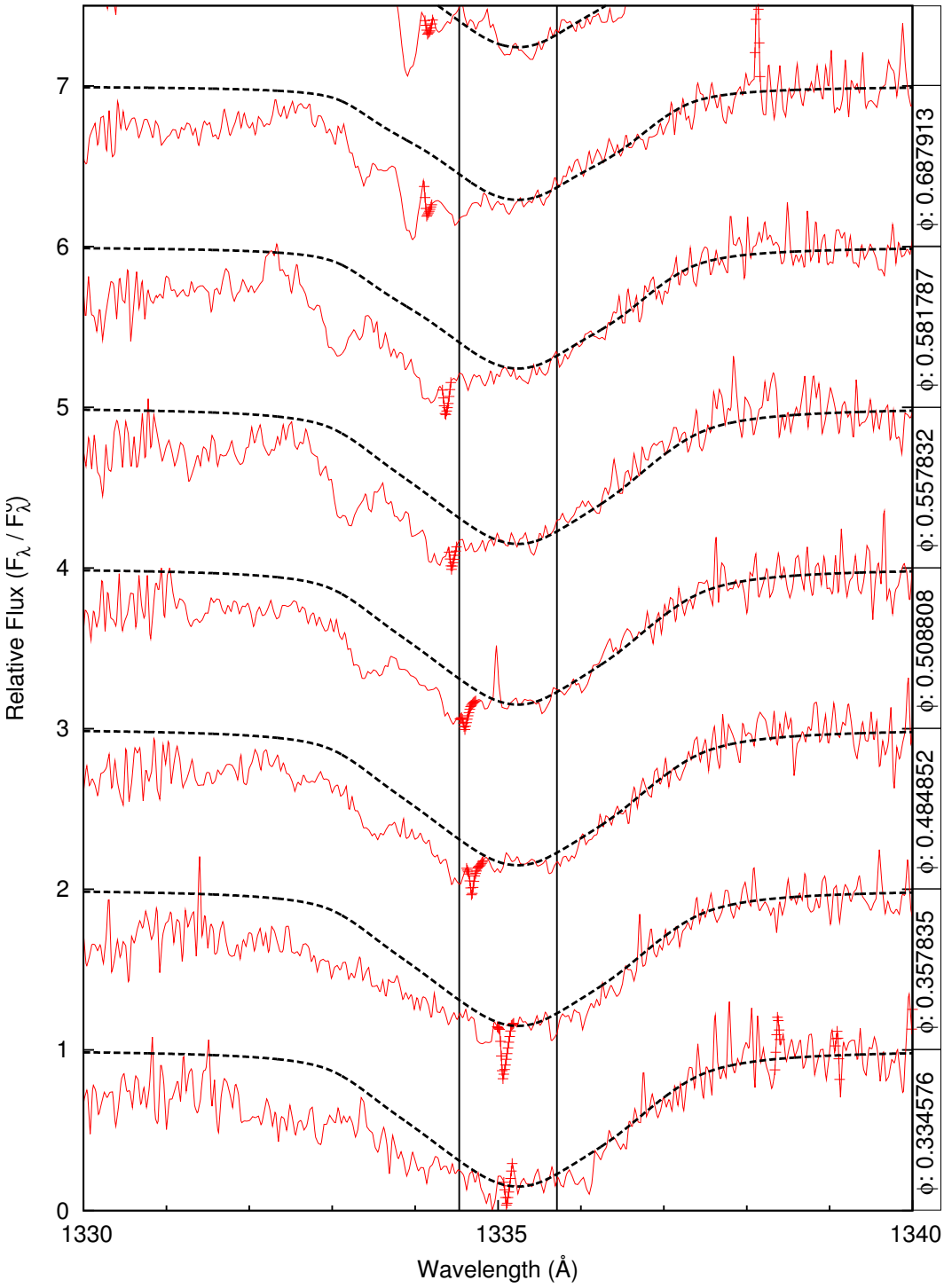

Figure C.7: [D] (a) C II 1334 & 1335: Tupaspec fit to photosphere.

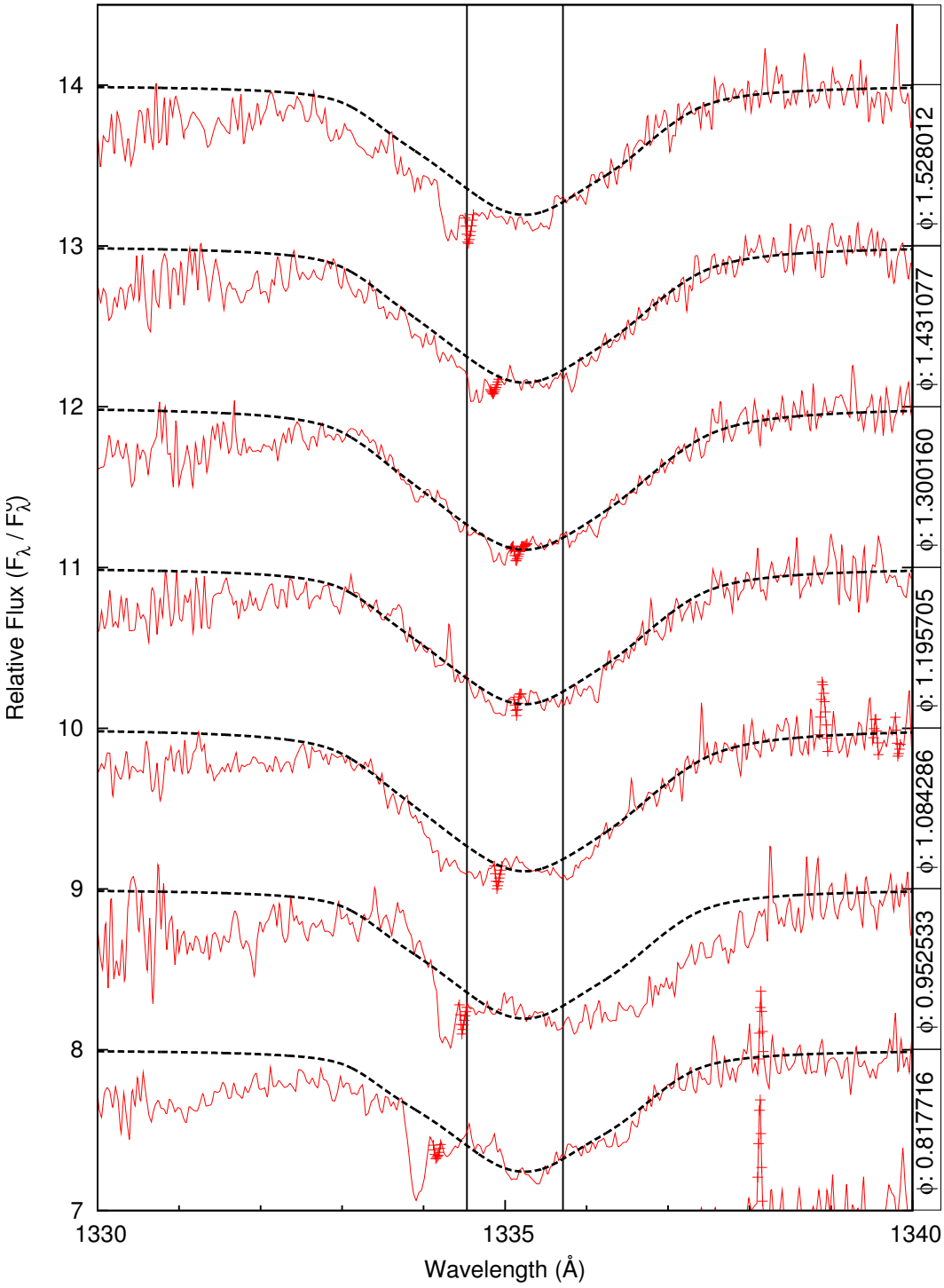

Figure C.8: [D](b) C II 1334 & 1335: Tupaspec fit to photosphere.

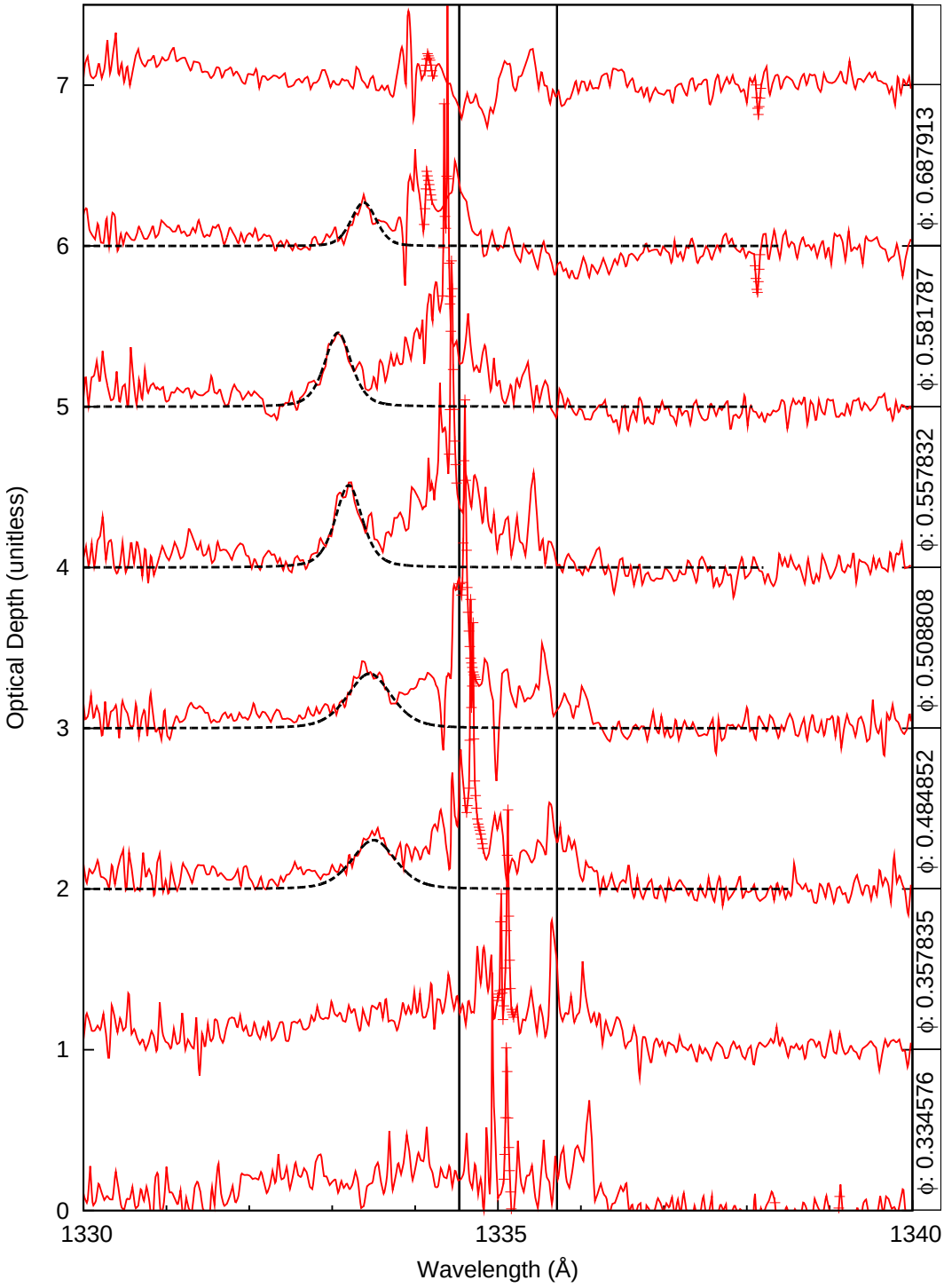

Figure C.9: [E] C II 1334 & 1335: Tupaspec fit to optical depth of flow features isolated through divsion spectra method.

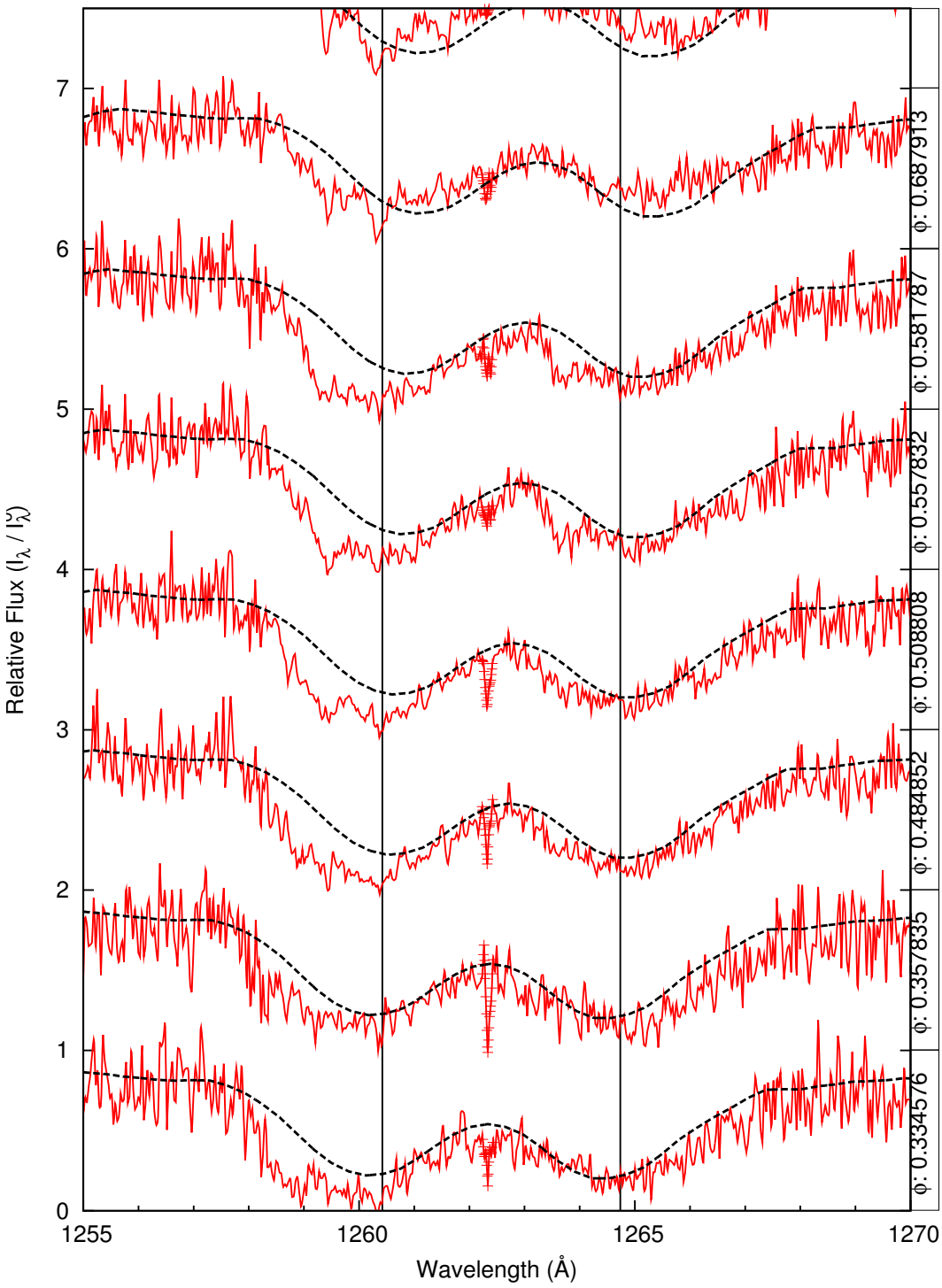

Figure C.10: [A] (a) Si II 1260 & 1264: Normalized U Cep data. Doppler motion with respect to the Sun. Synthetic spectra matched to data.

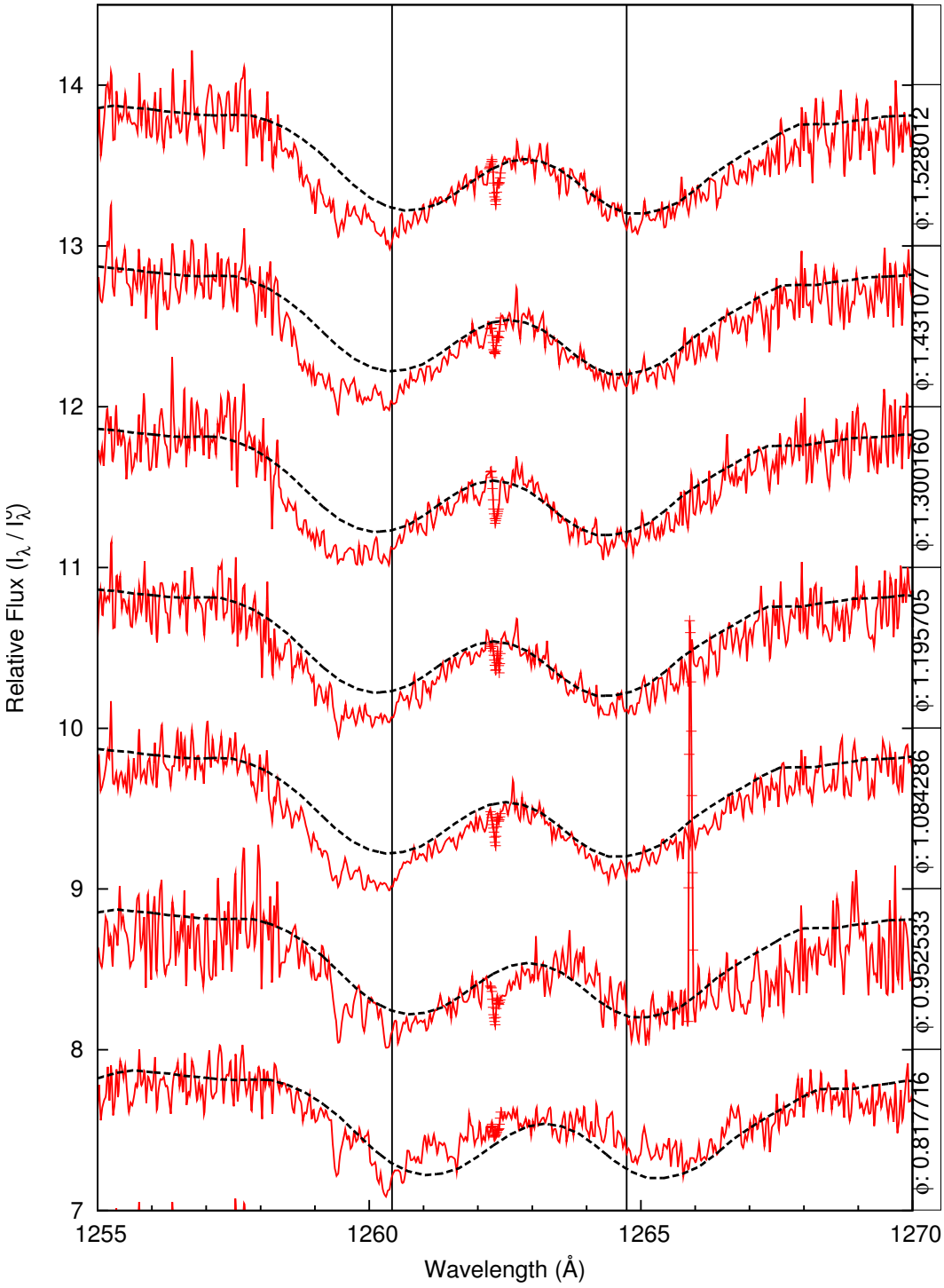

Figure C.11: [A] (b) Si II 1260 & 1264: Normalized U Cep data. Doppler motion with respect to the Sun. Synthetic spectra matched to data.

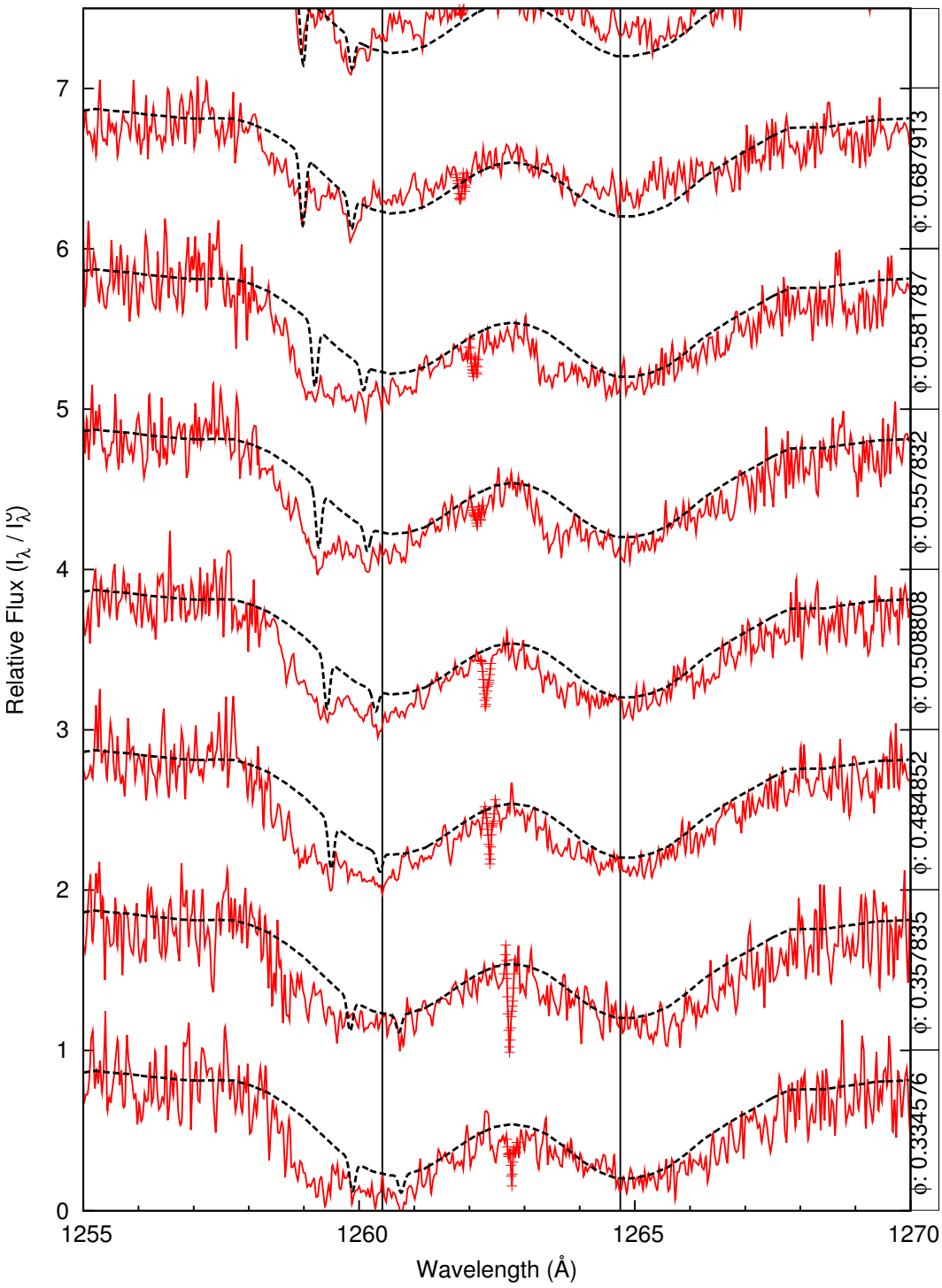

Figure C.12: [B] (a) Si II 1260 & 1264: Normalized U Cep data. Synthetic spectra and interstellar absorption lines matched to data.

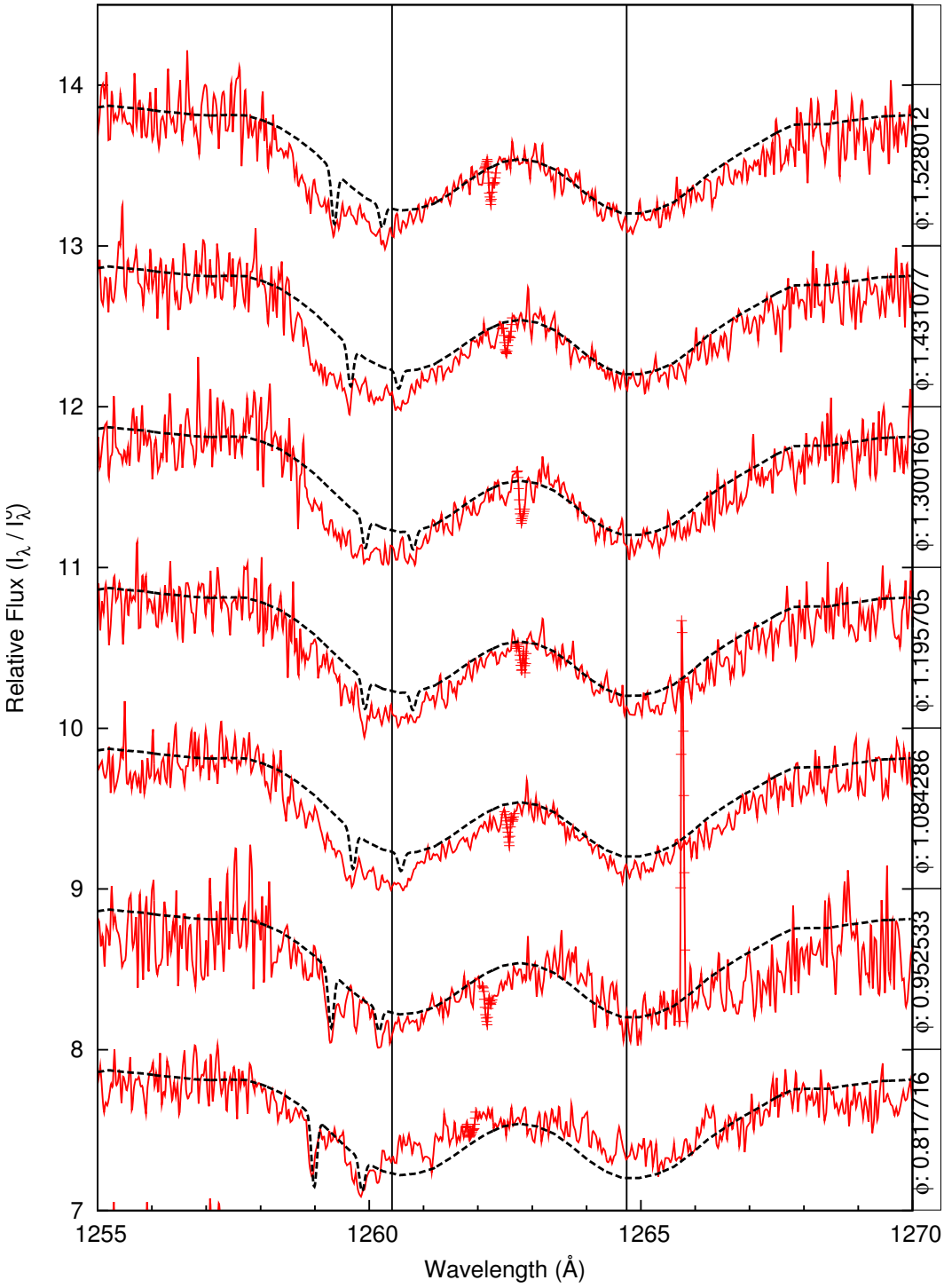

Figure C.13: [B] (b) Si II 1260 & 1264: Normalized U Cep data. Synthetic spectra and interstellar absorption lines matched to data.

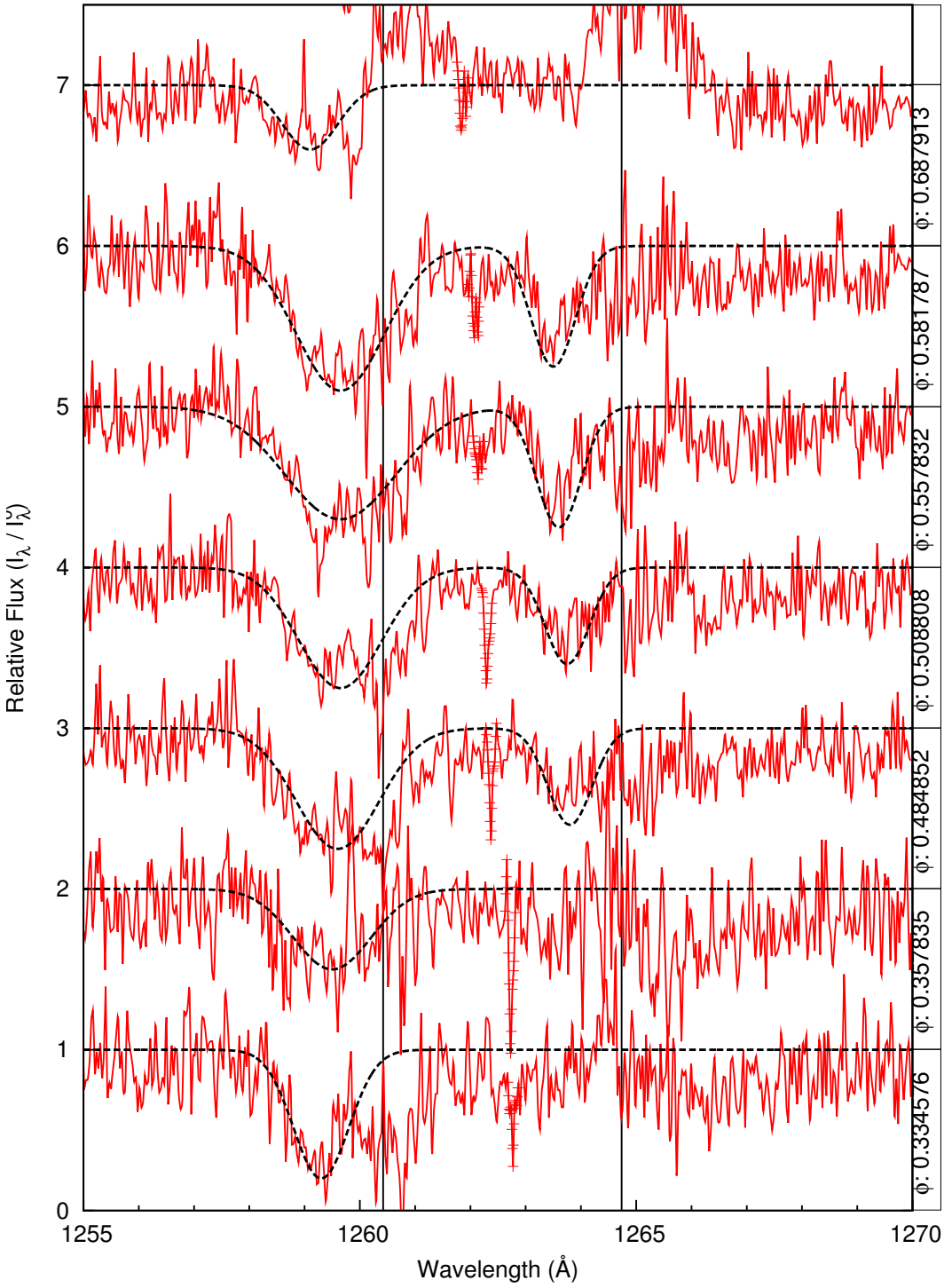

Figure C.14: [C] (a) Si II 1260 & 1264: Synthetic photosphere and interstellar lines divided out of U Cep data. Doublet Gaussian fitting added to to strongest flow features.

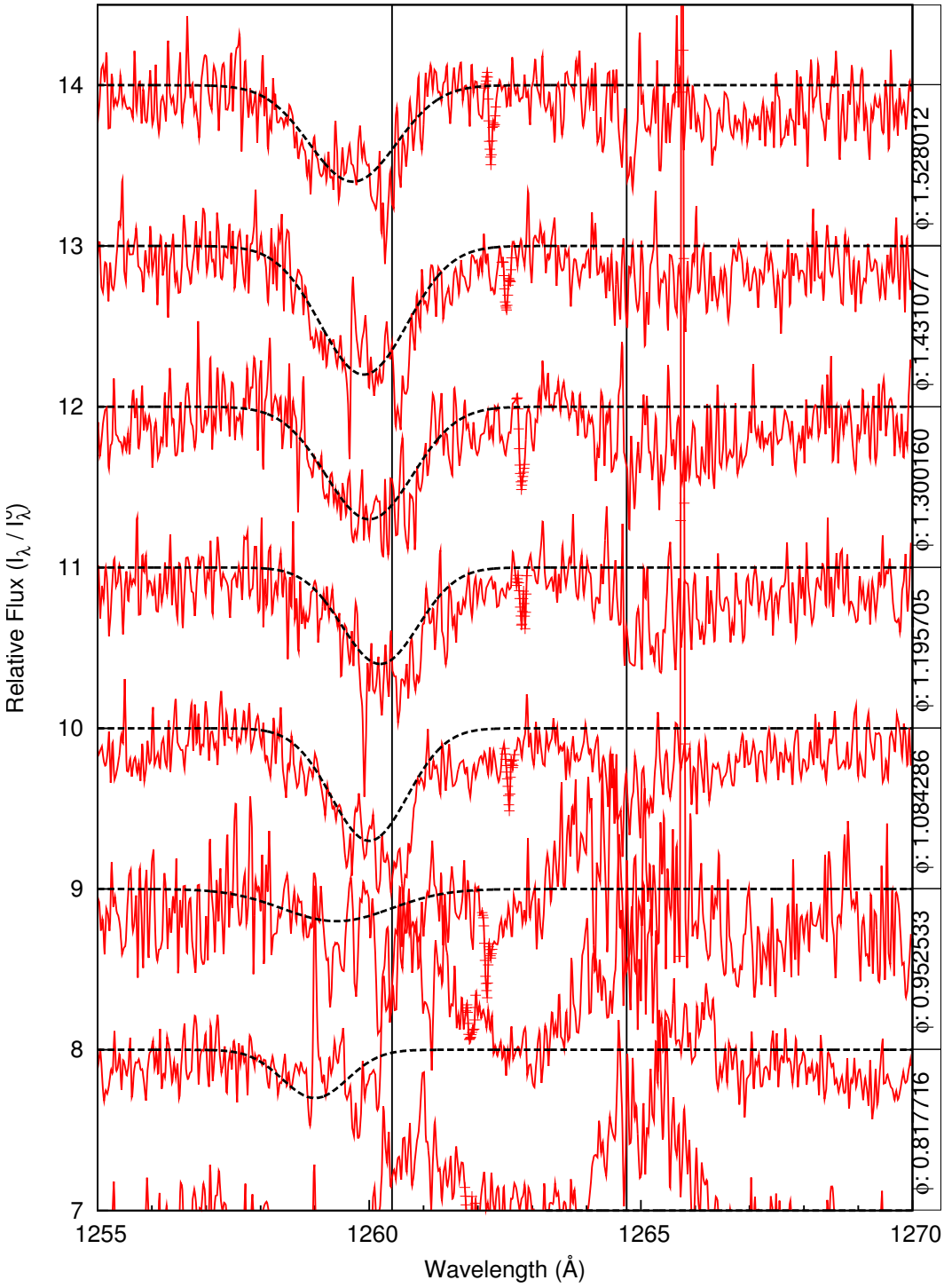

Figure C.15: [C](b) Si II 1260 & 1264: Synthetic photosphere and interstellar lines divided out of U Cep data. Doublet Gaussian fitting added to to strongest flow features.

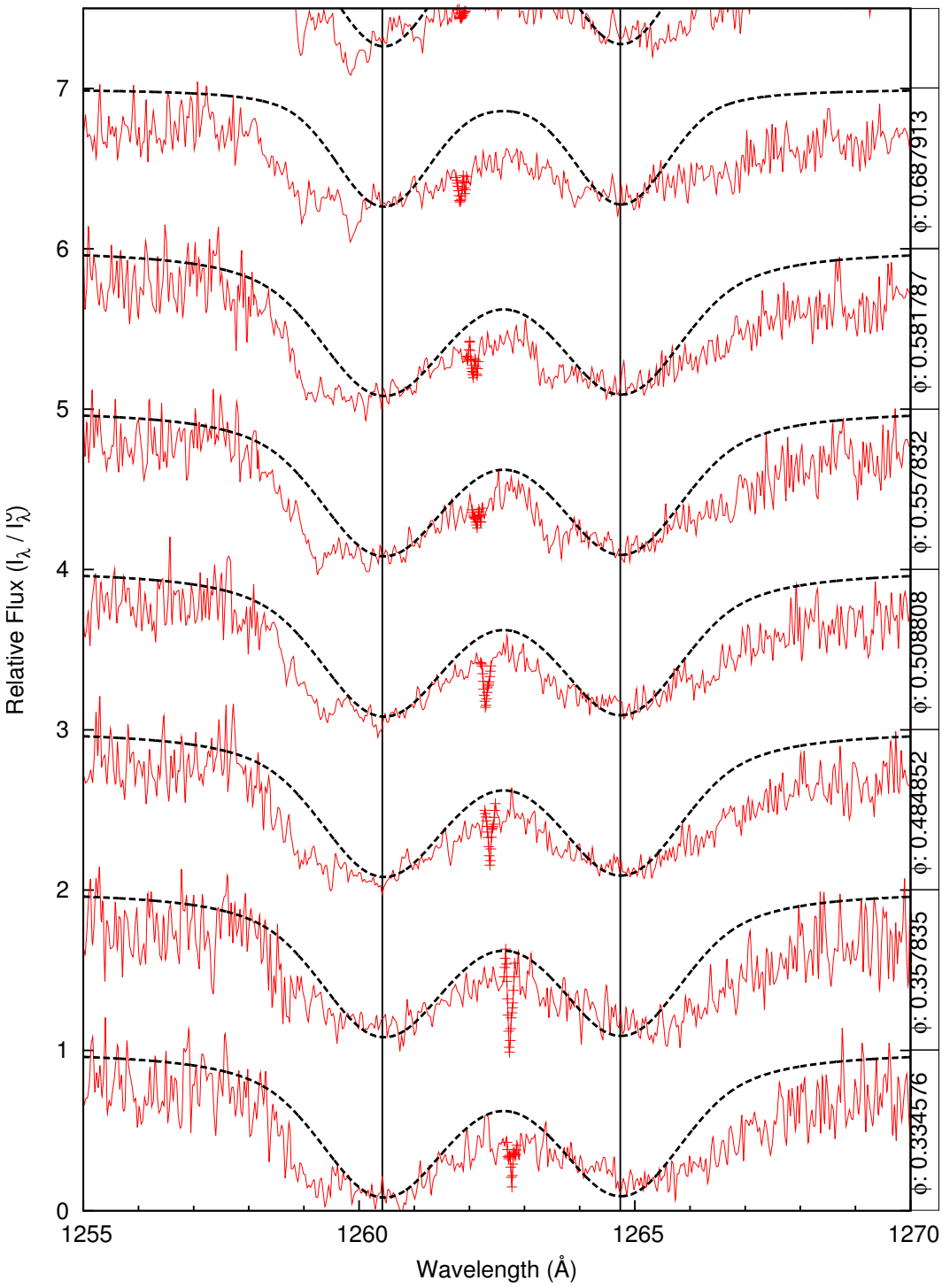

Figure C.16: [D] (a) Si II 1260 & 1264: Tupaspec fit to photosphere.

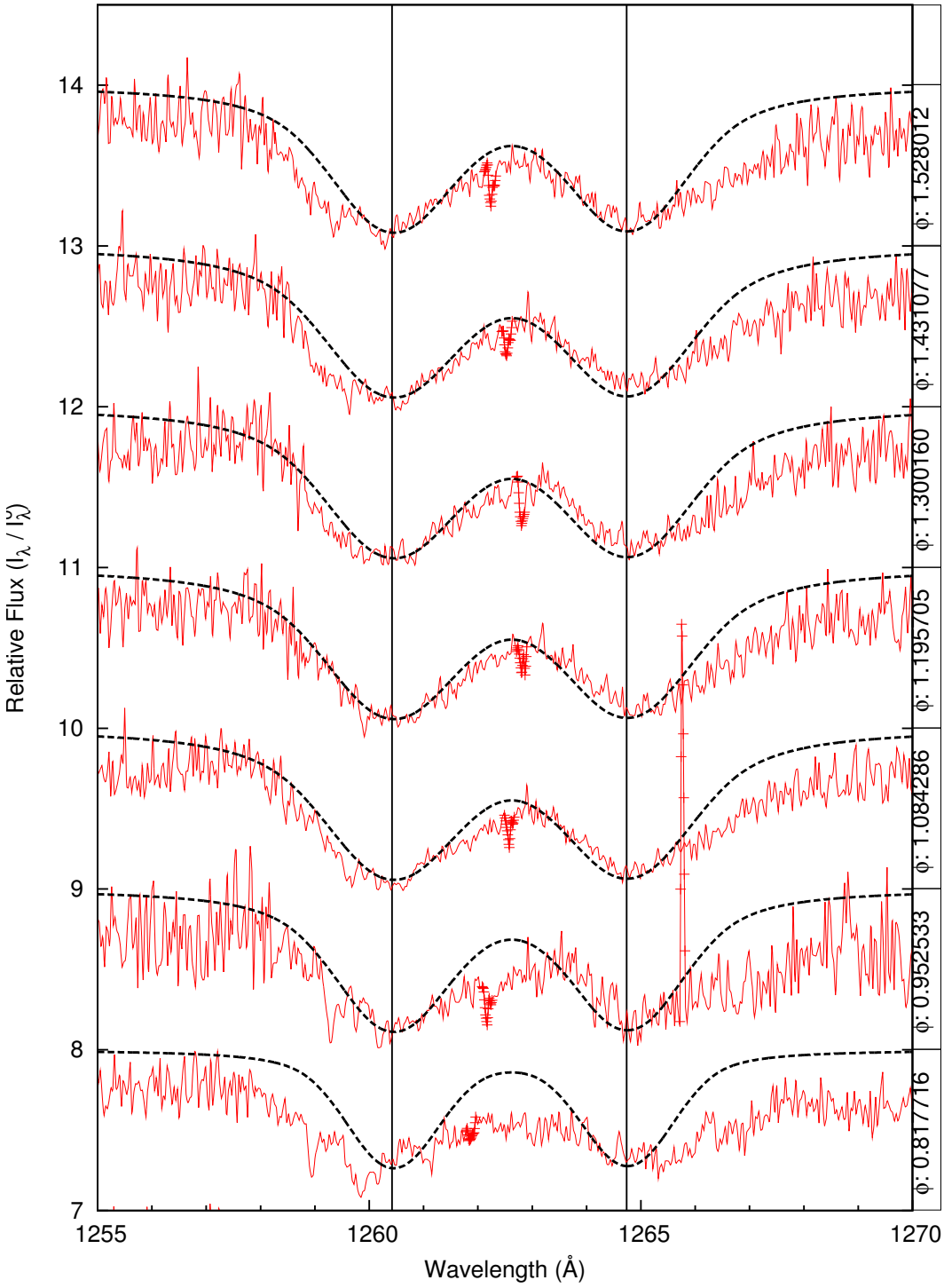

Figure C.17: [D](b) Si II 1260 & 1264: Tupaspec fit to photosphere.

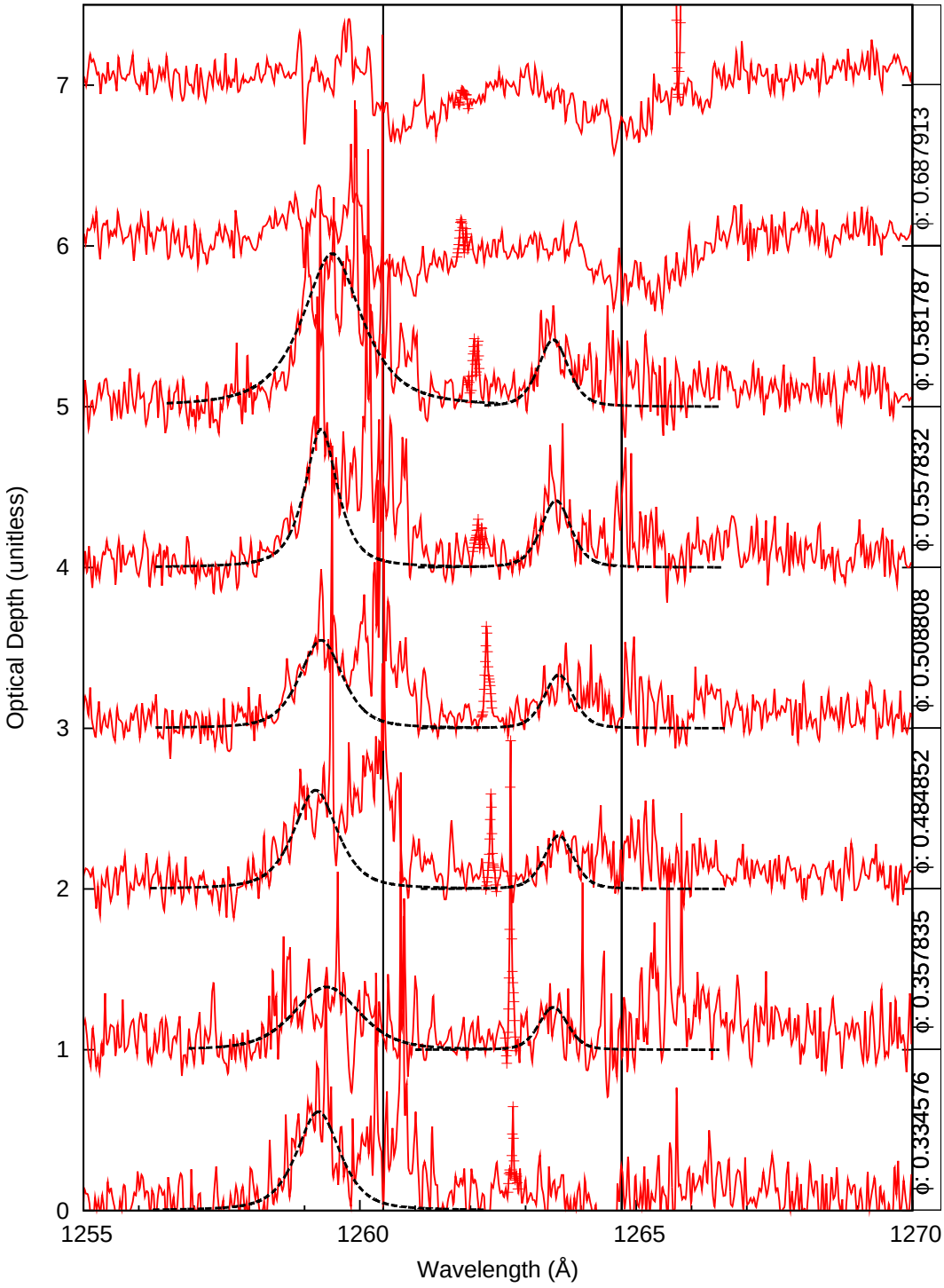

Figure C.18: [E] Si II 1260 & 1264: Tupaspec fit to optical depth of flow features isolated through divsion spectra method.

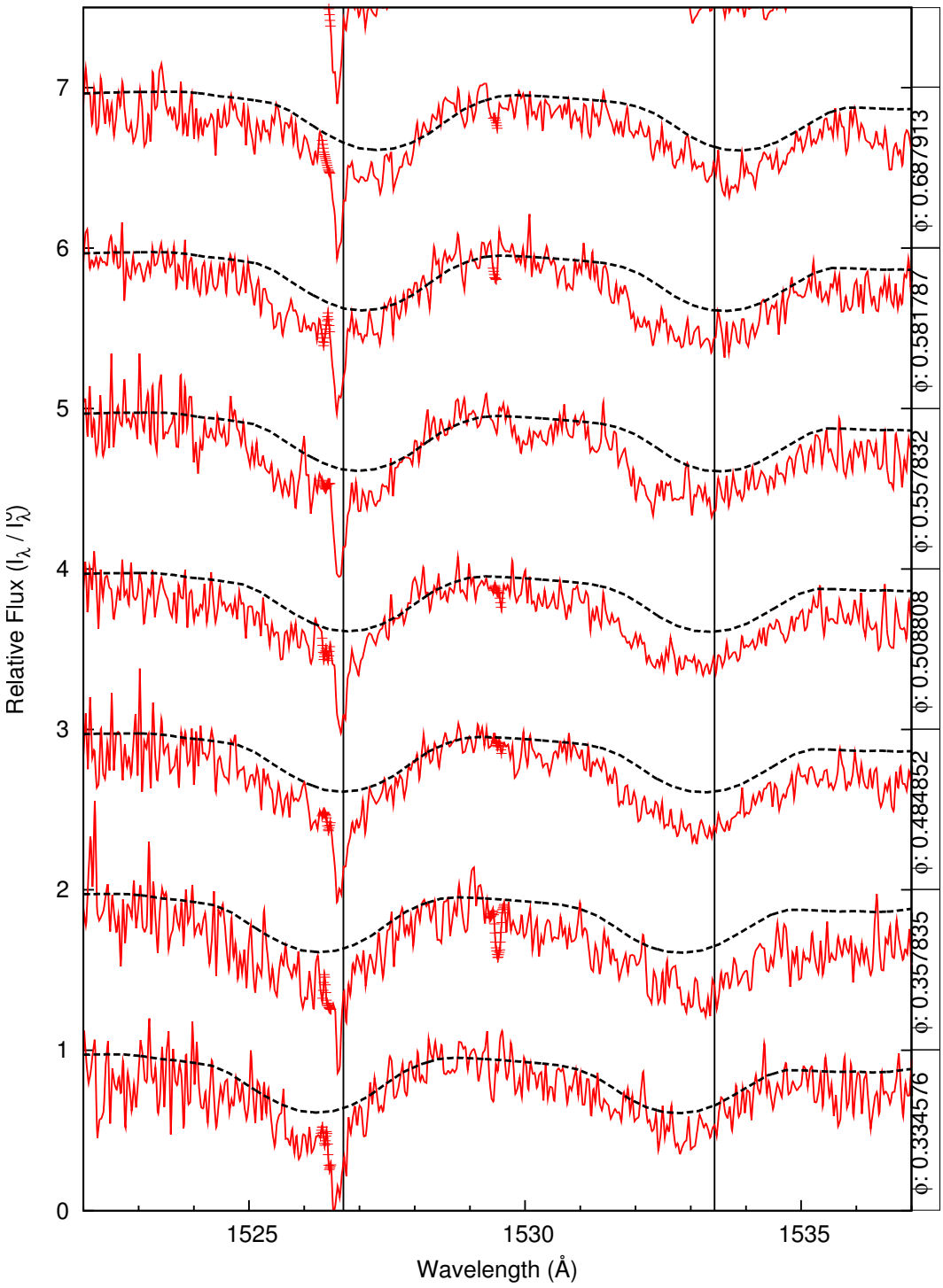

Figure C.19: [A] (a) Si II 1526 & 1533: Normalized U Cep data. Doppler motion with respect to the Sun. Synthetic spectra matched to data.

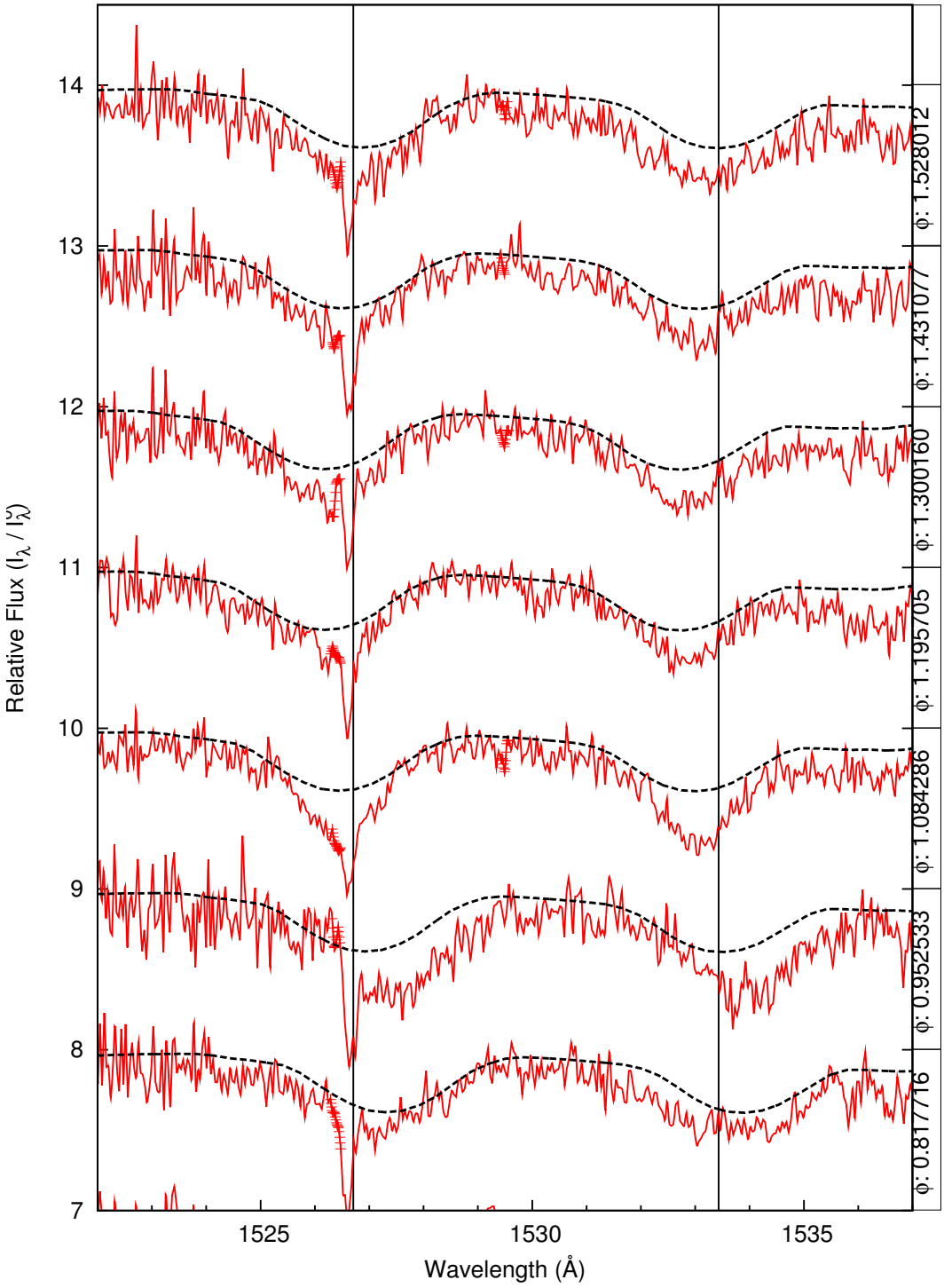

Figure C.20: [A] (b) Si II 1526 & 1533: Normalized U Cep data. Doppler motion with respect to the Sun. Synthetic spectra matched to data.

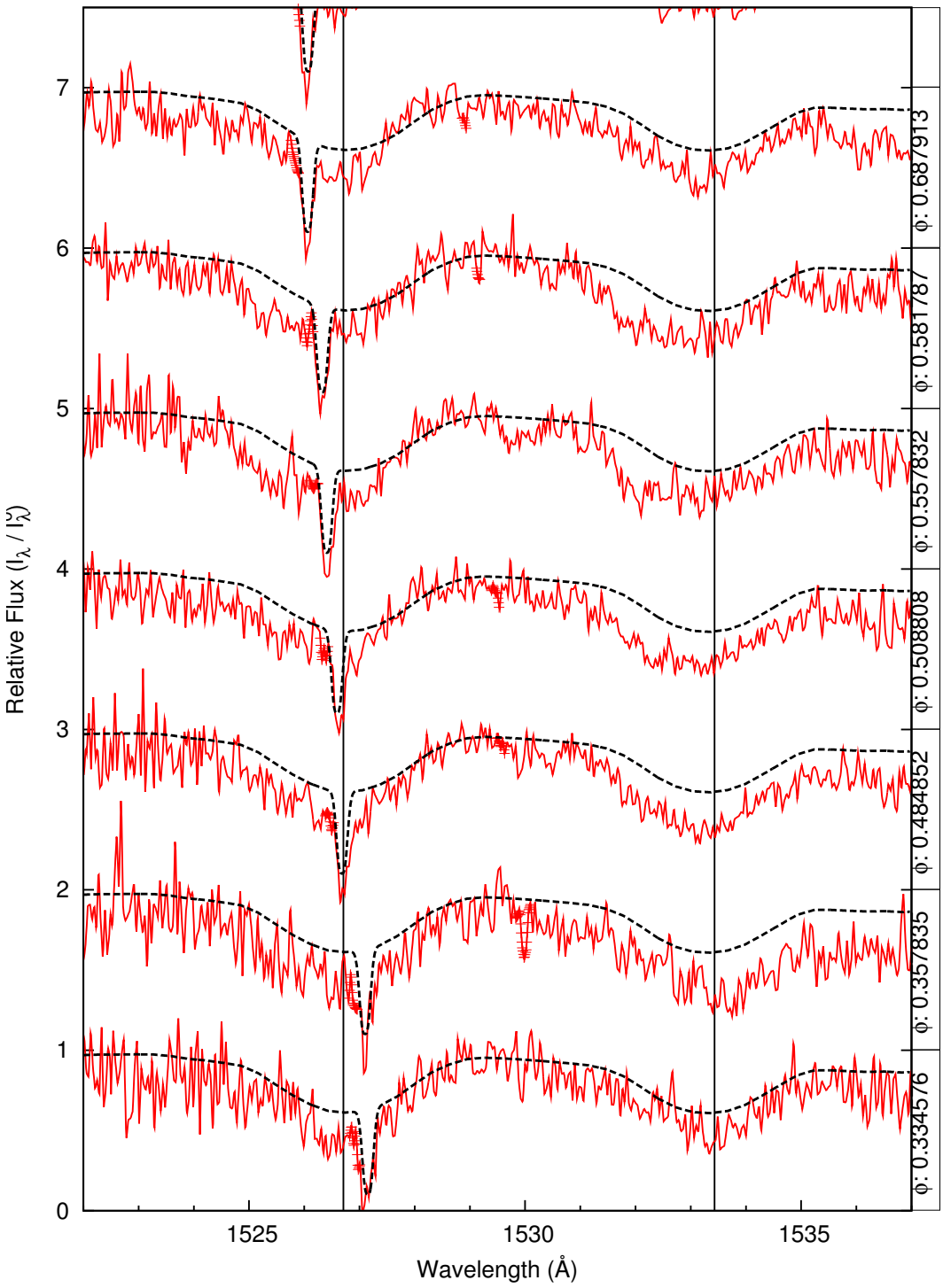

Figure C.21: [B] (a) Si II 1526 & 1533: Normalized U Cep data. Synthetic spectra and interstellar absorption lines matched to data.

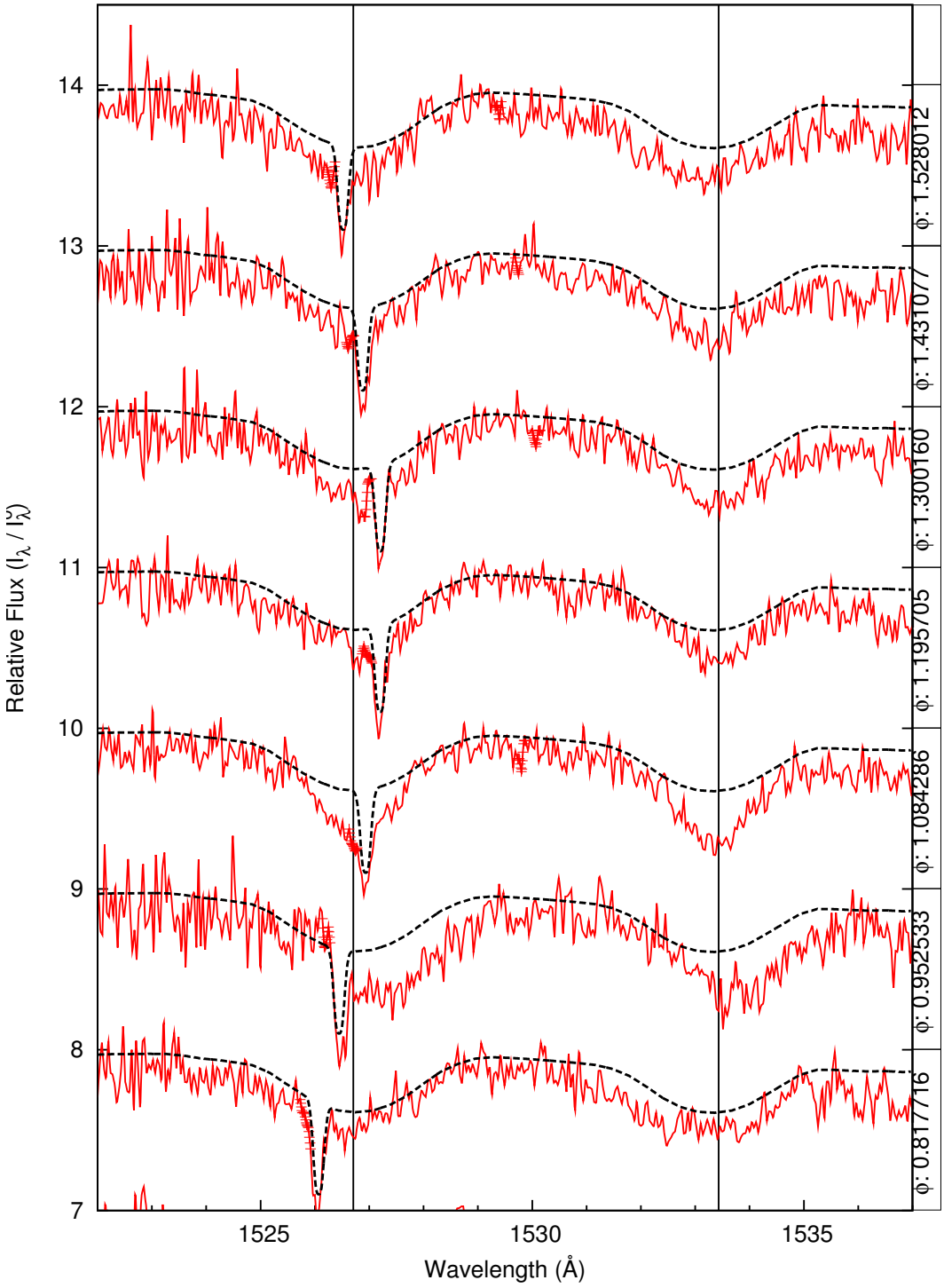

Figure C.22: [B] (b) Si II 1526 & 1533: Normalized U Cep data. Synthetic spectra and interstellar absorption lines matched to data.

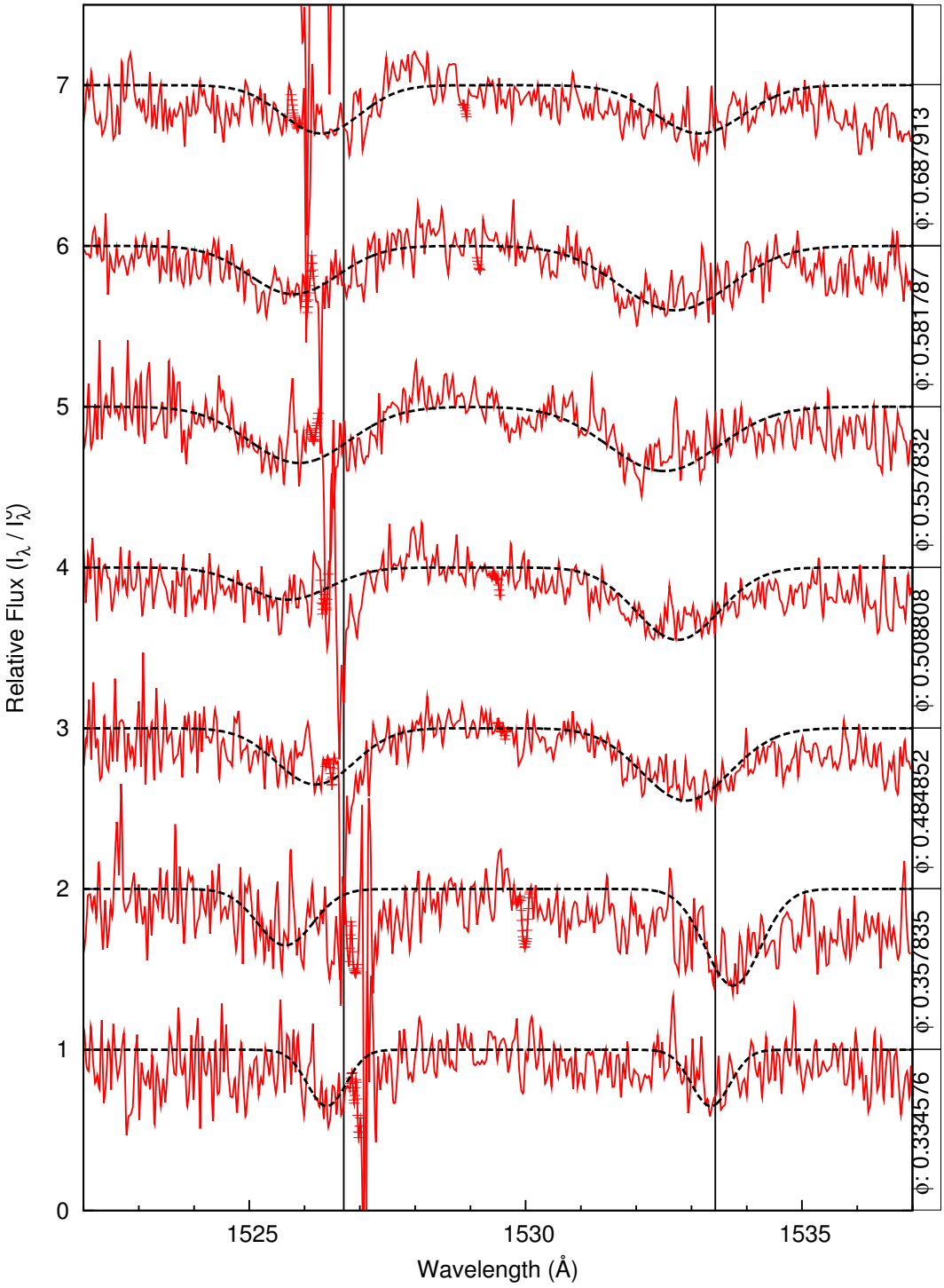

Figure C.23: [C] (a) Si II 1526 & 1533: Synthetic photosphere and interstellar lines divided out of U Cep data. Doublet Gaussian fitting added to to strongest flow features.

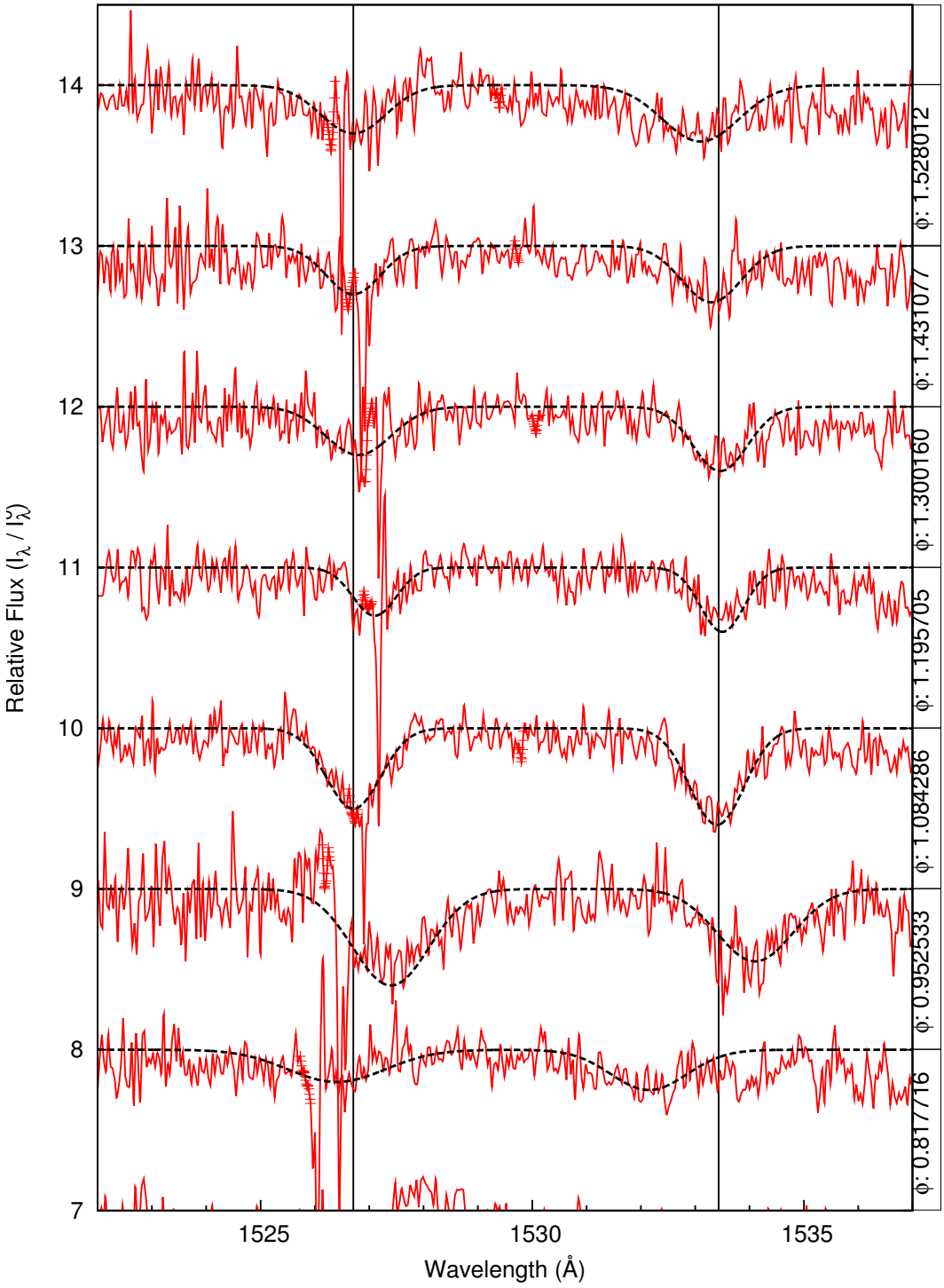

Figure C.24: [C](b) Si II 1526 & 1533: Synthetic photosphere and interstellar lines divided out of U Cep data. Doublet Gaussian fitting added to to strongest flow features.

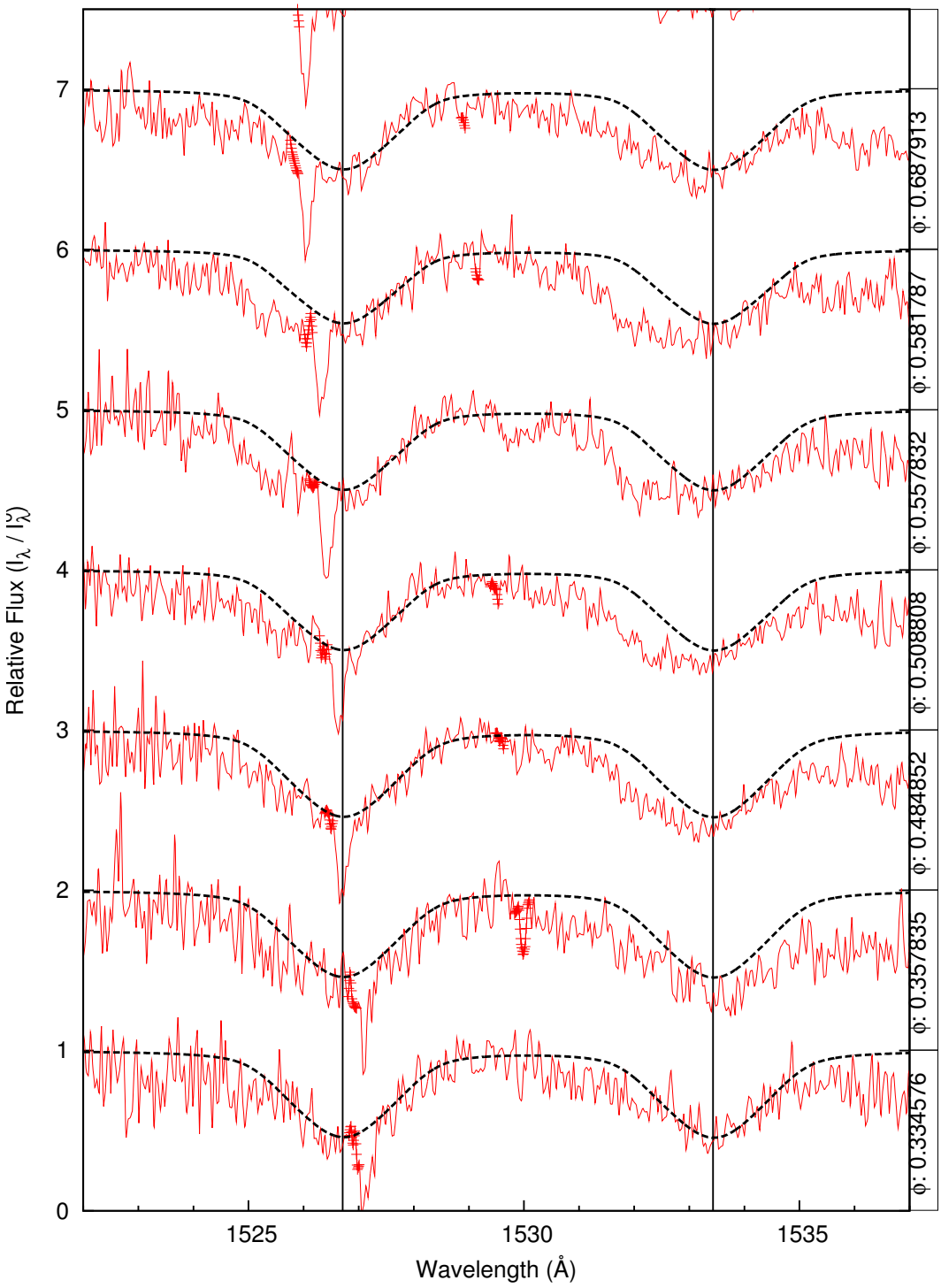

Figure C.25: [D] (a) Si II 1526 & 1533: Tupaspec fit to photosphere.

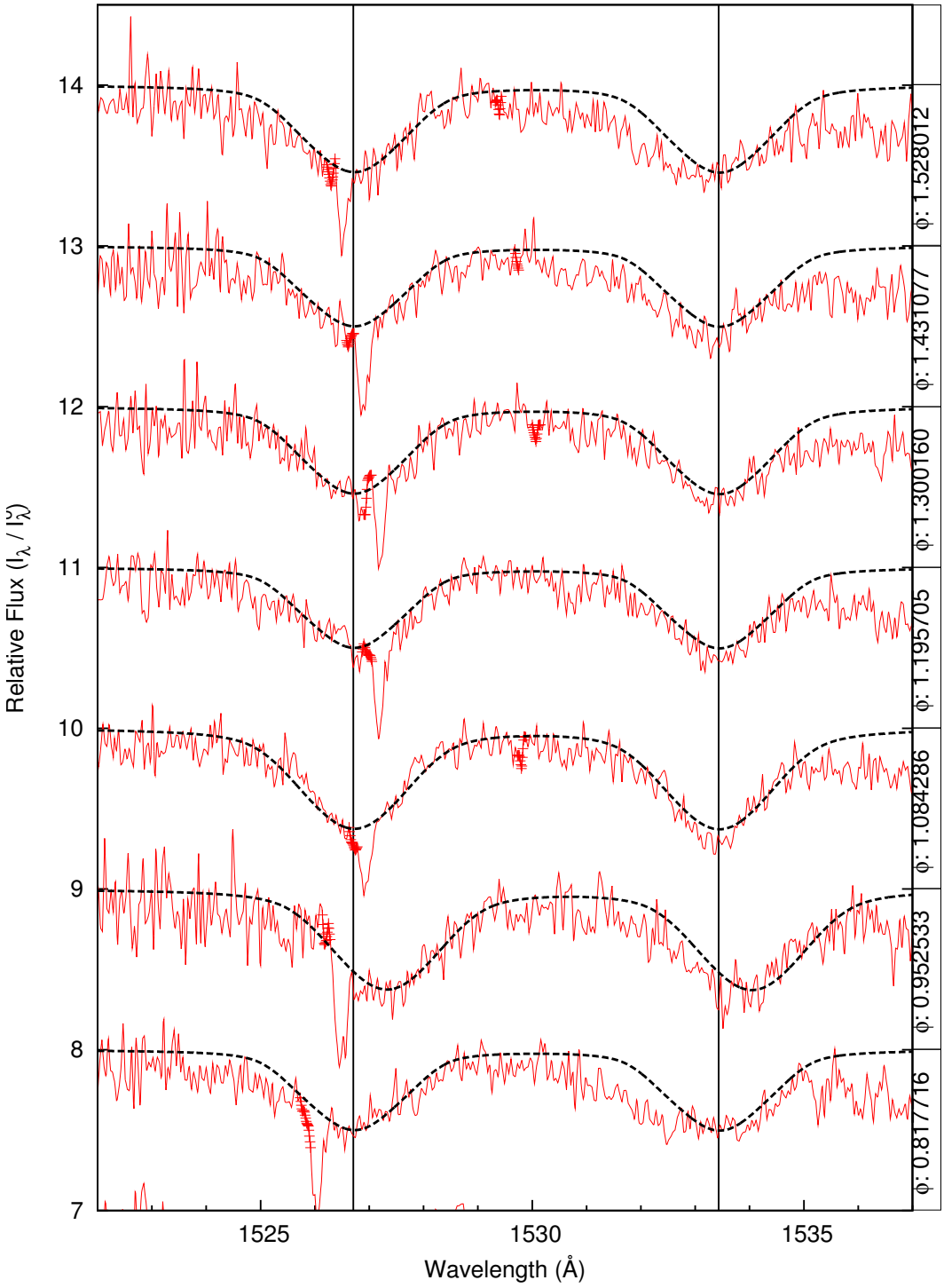

Figure C.26: [D](b) Si II 1526 & 1533: Tupaspec fit to photosphere.

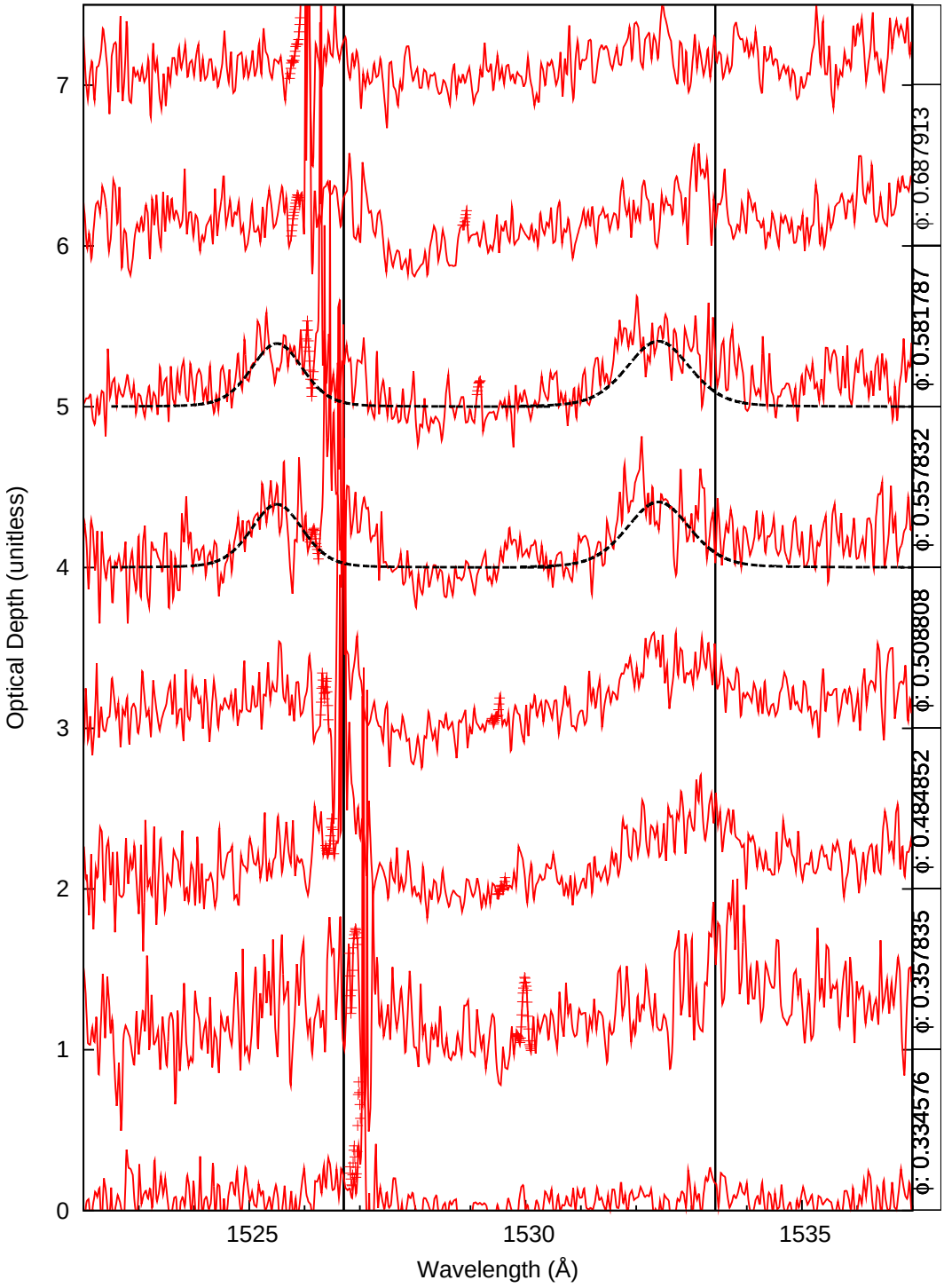

Figure C.27: [E] Si II 1526 & 1533: Tupaspec fit to optical depth of flow features isolated through divsion spectra method.

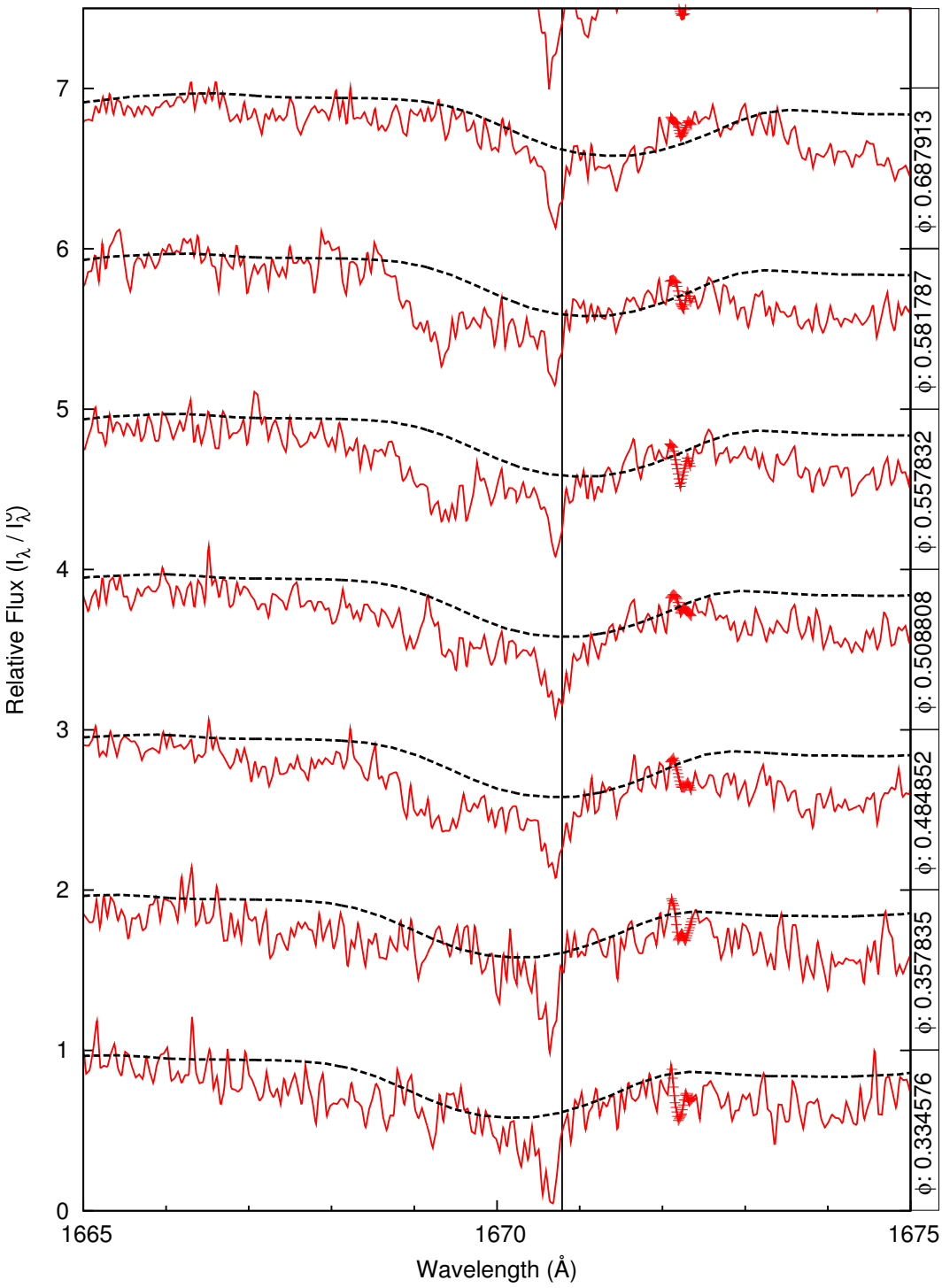

Figure C.28: [A] (a) Al II 1670: Normalized U Cep data. Doppler motion with respect to the Sun. Synthetic spectra matched to data.

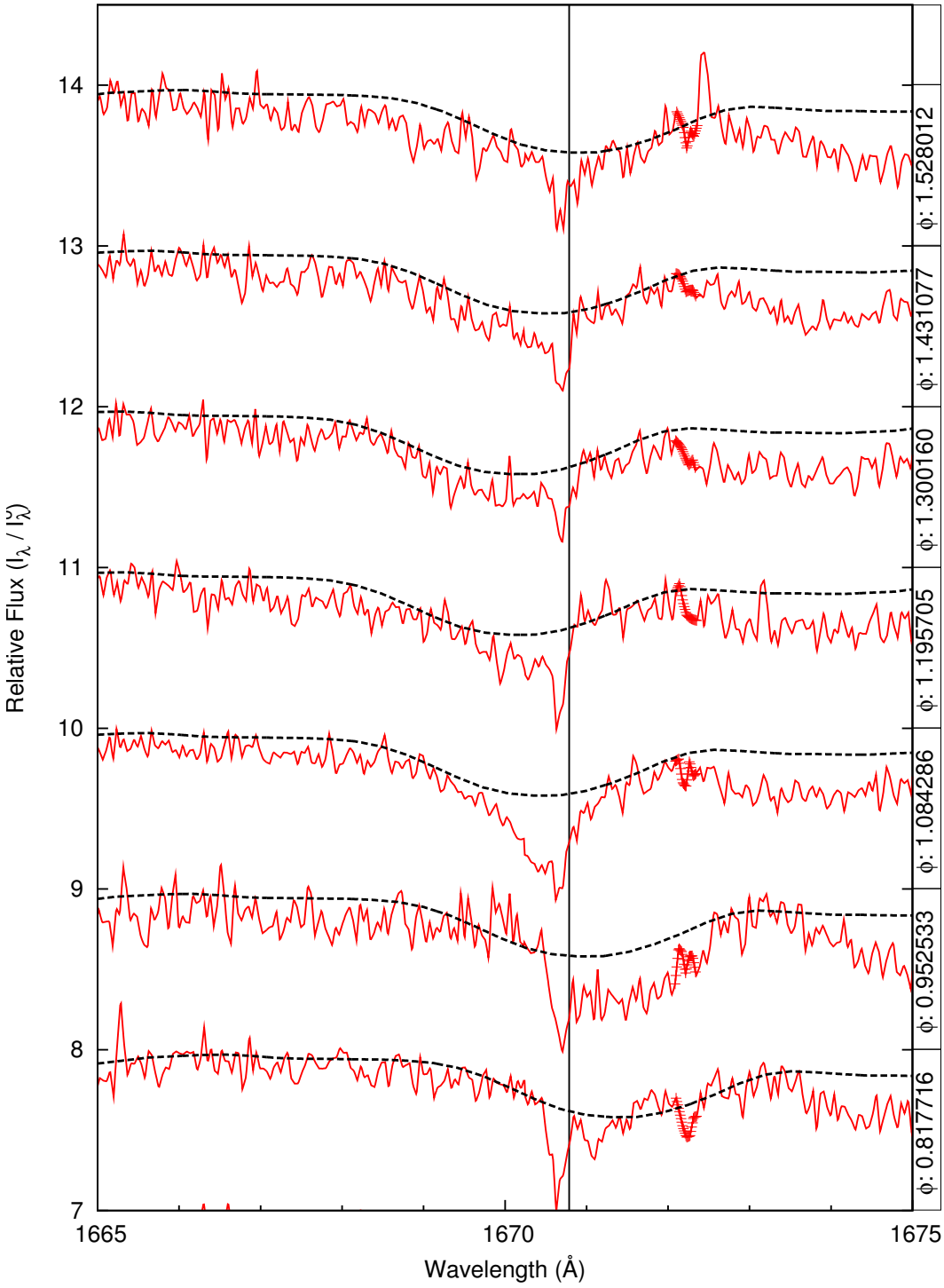

Figure C.29: [A] (b) Al II 1670: Normalized U Cep data. Doppler motion with respect to the Sun. Synthetic spectra matched to data.

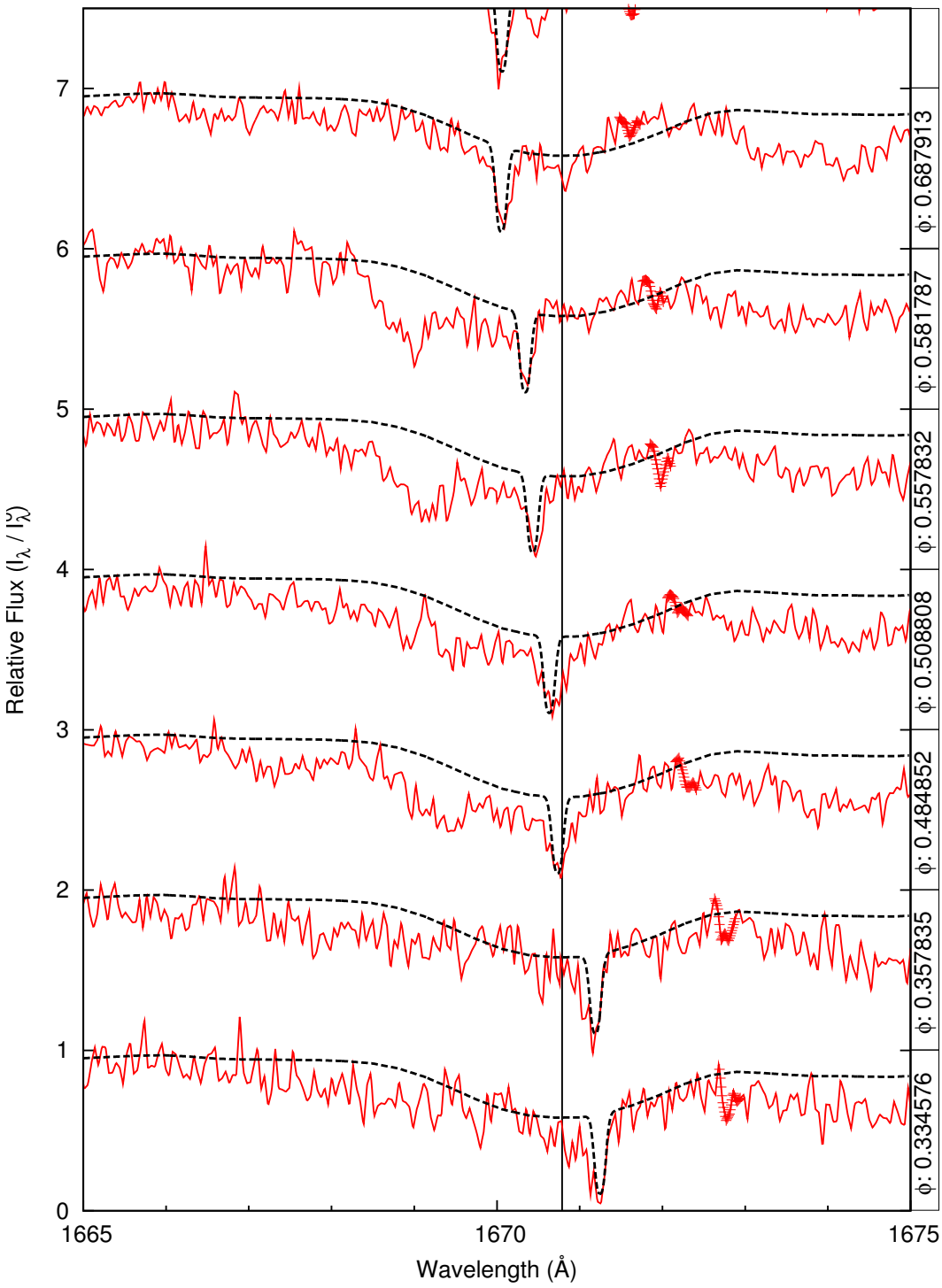

Figure C.30: [B] (a) Al II 1670: Normalized U Cep data. Synthetic spectra and interstellar absorption lines matched to data.

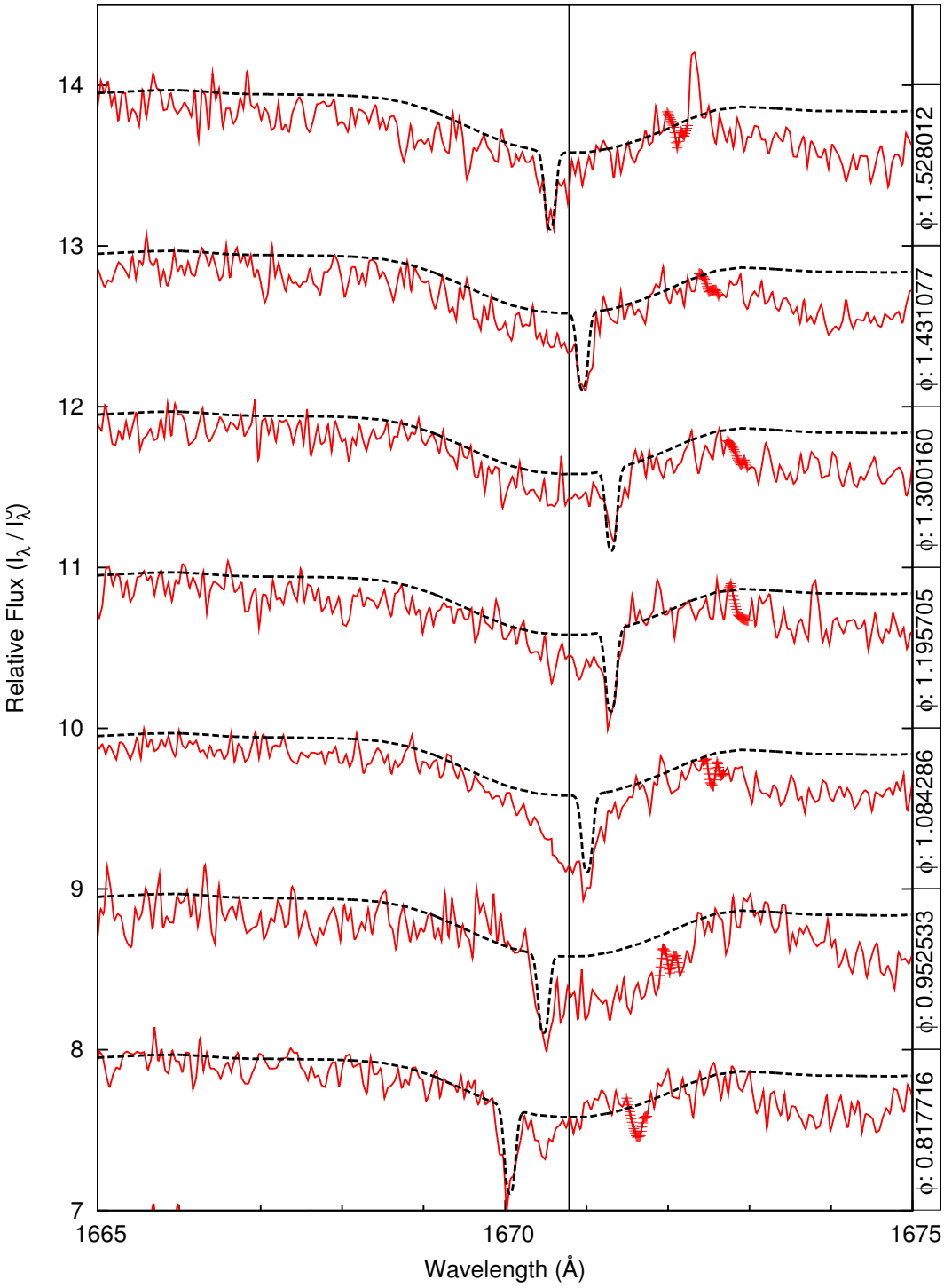

Figure C.31: [B] (b) Al II 1670: Normalized U Cep data. Synthetic spectra and interstellar absorption lines matched to data.

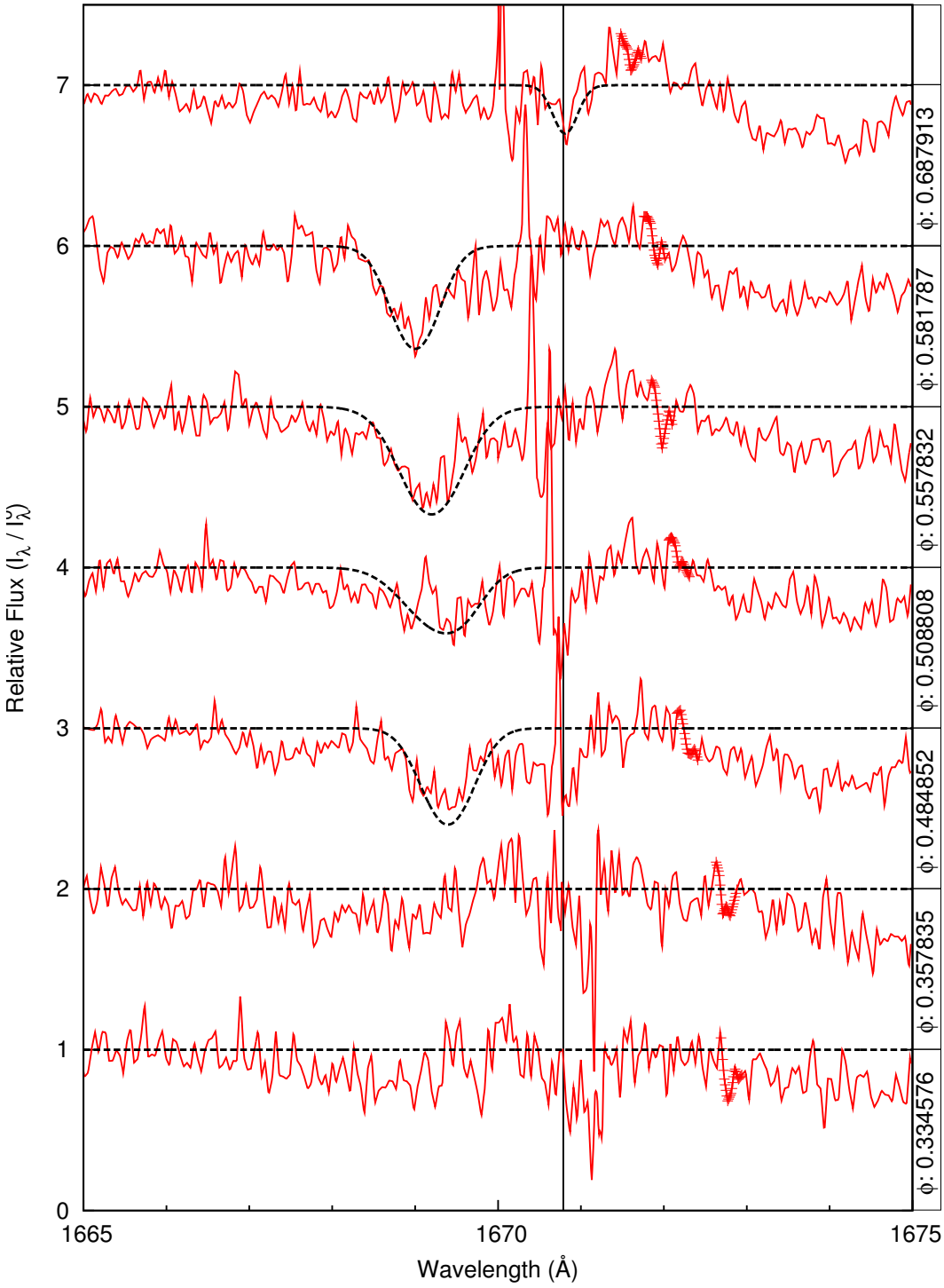

Figure C.32: [C] (a) Al II 1670: Synthetic photosphere and interstellar lines divided out of U Cep data. Gaussian fitting added to strongest flow features.

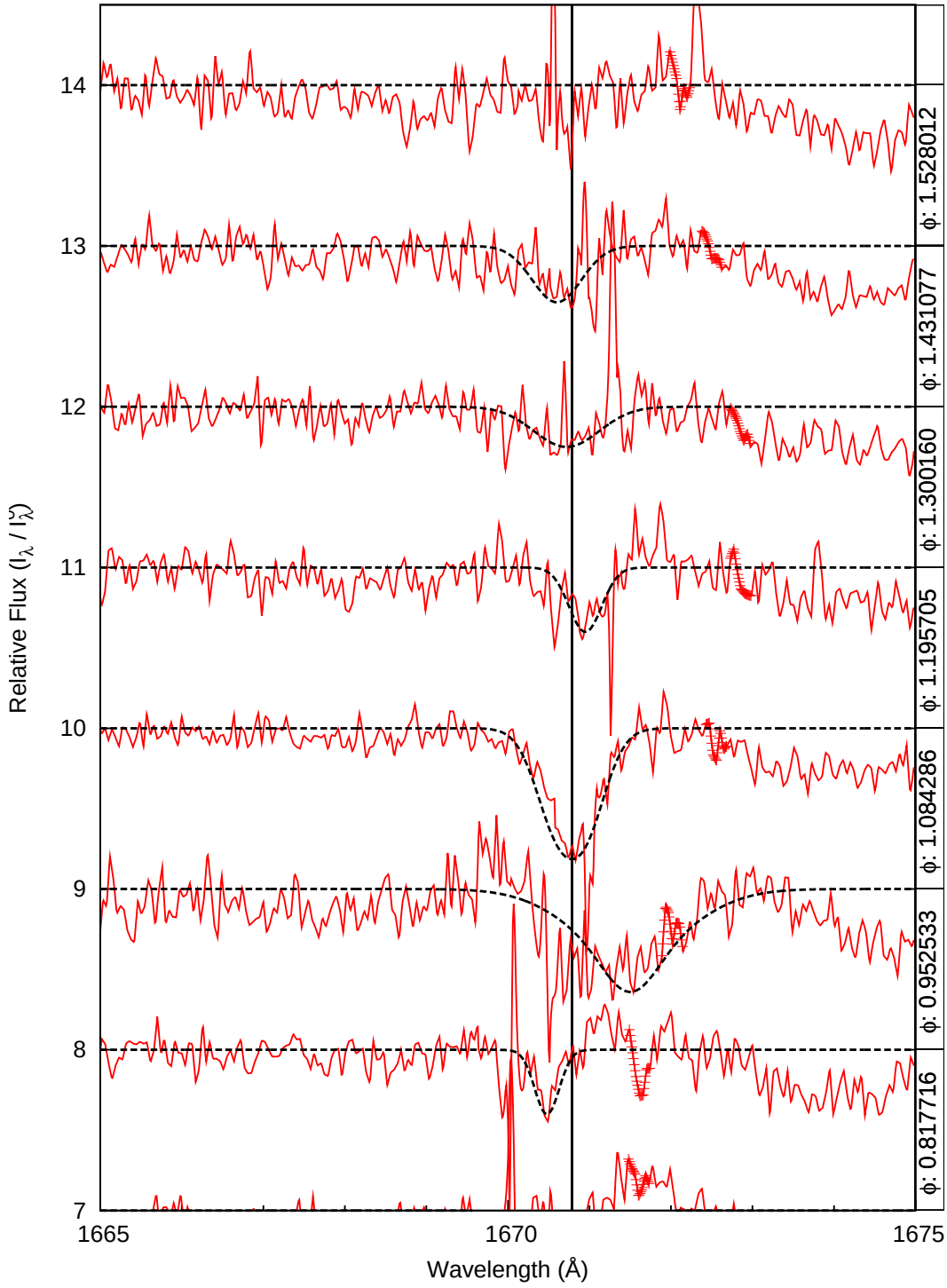

Figure C.33: [C](b) Al II 1670: Synthetic photosphere and interstellar lines divided out of U Cep data. Gaussian fitting added to strongest flow features.

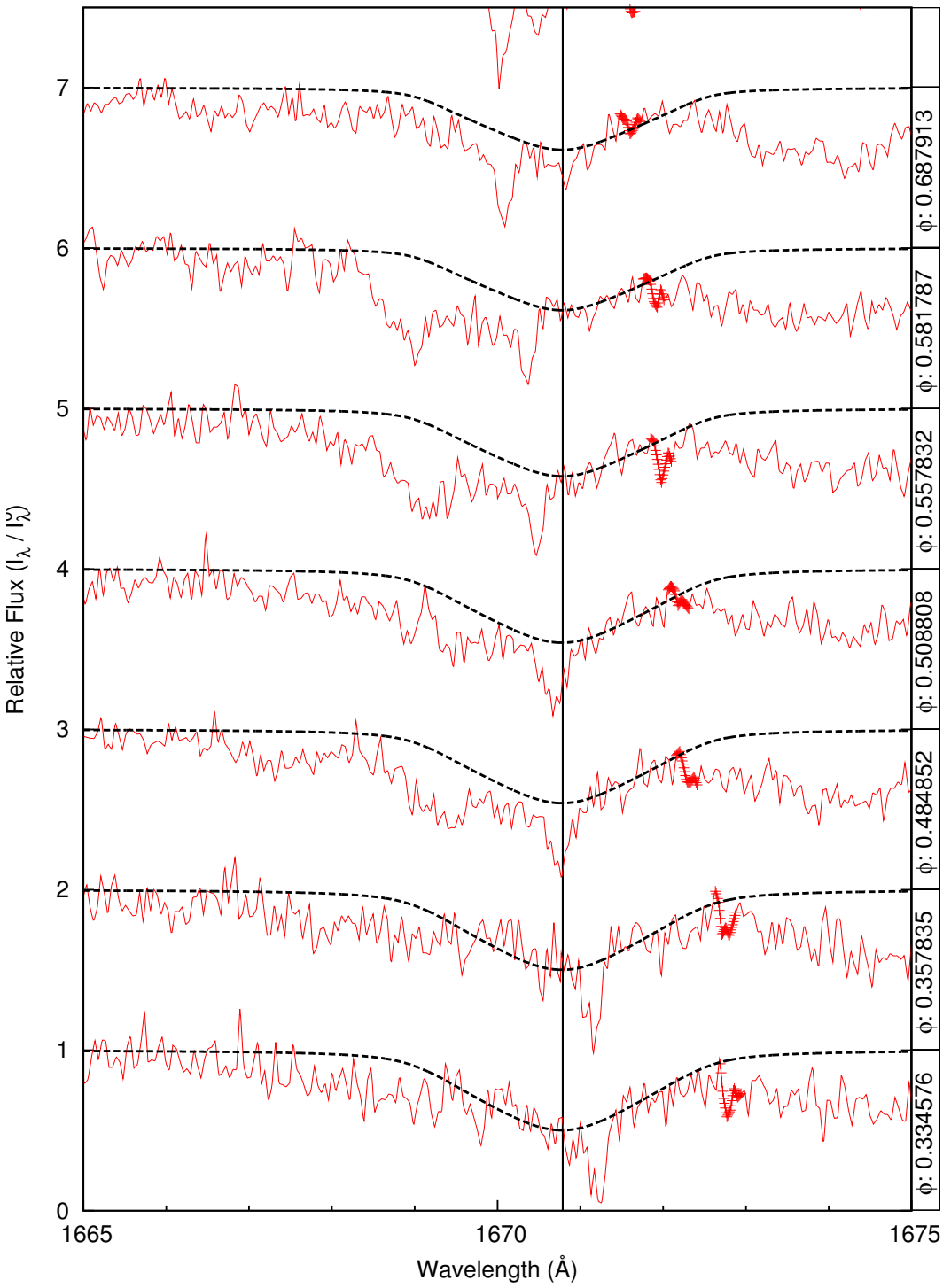

Figure C.34: [D] (a) Al II 1670: Tupaspec fit to photosphere.

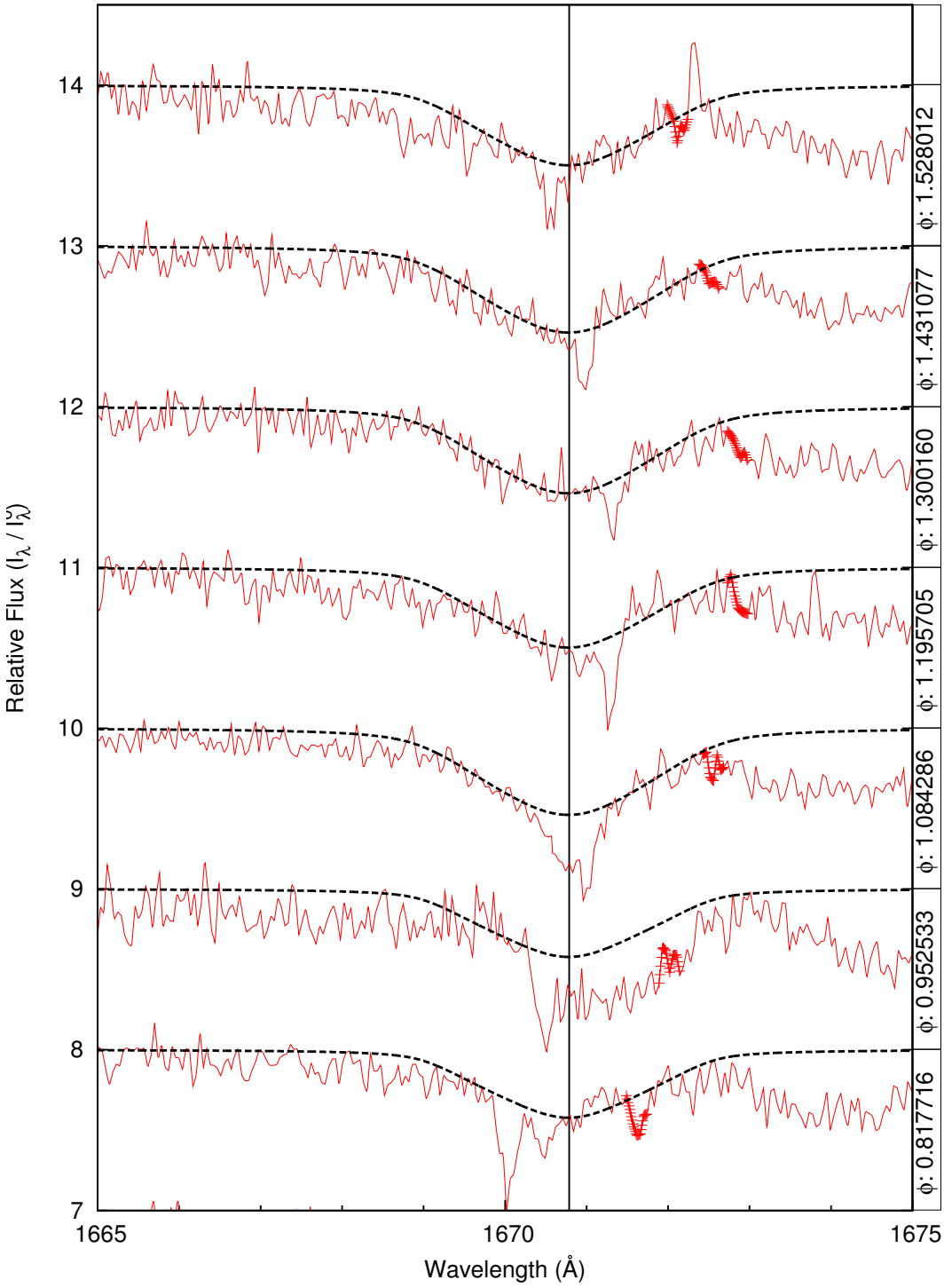

Figure C.35: [D](b) Al II 1670: Tupaspec fit to photosphere.

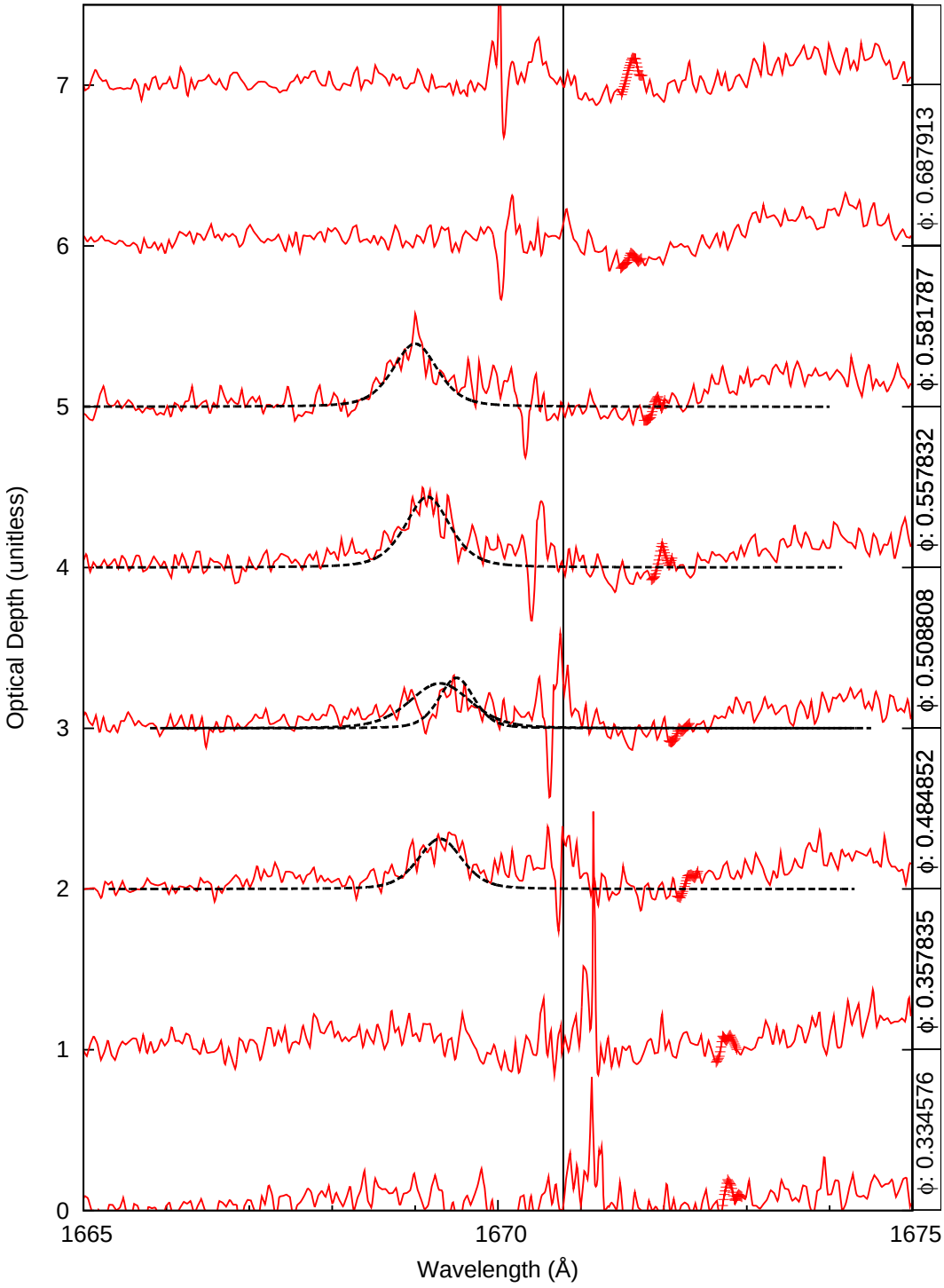

Figure C.36: [E] Al II 1670: Tupaspec fit to optical depth of flow features isolated through divsion spectra method.

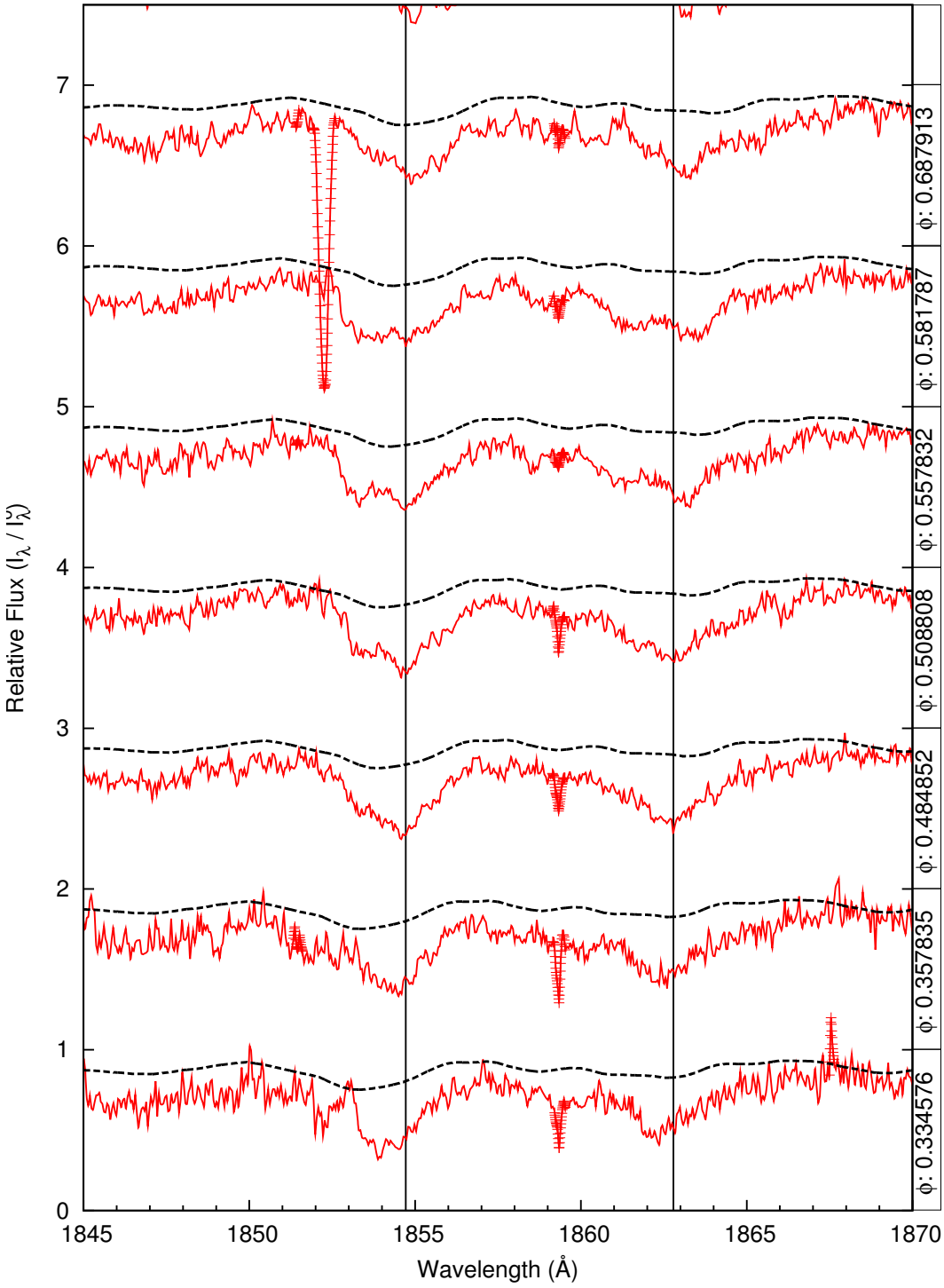

Figure C.37: [A] (a) Al III 1854 & 1862: Normalized U Cep data. Doppler motion with respect to the Sun. Synthetic spectra matched to data.

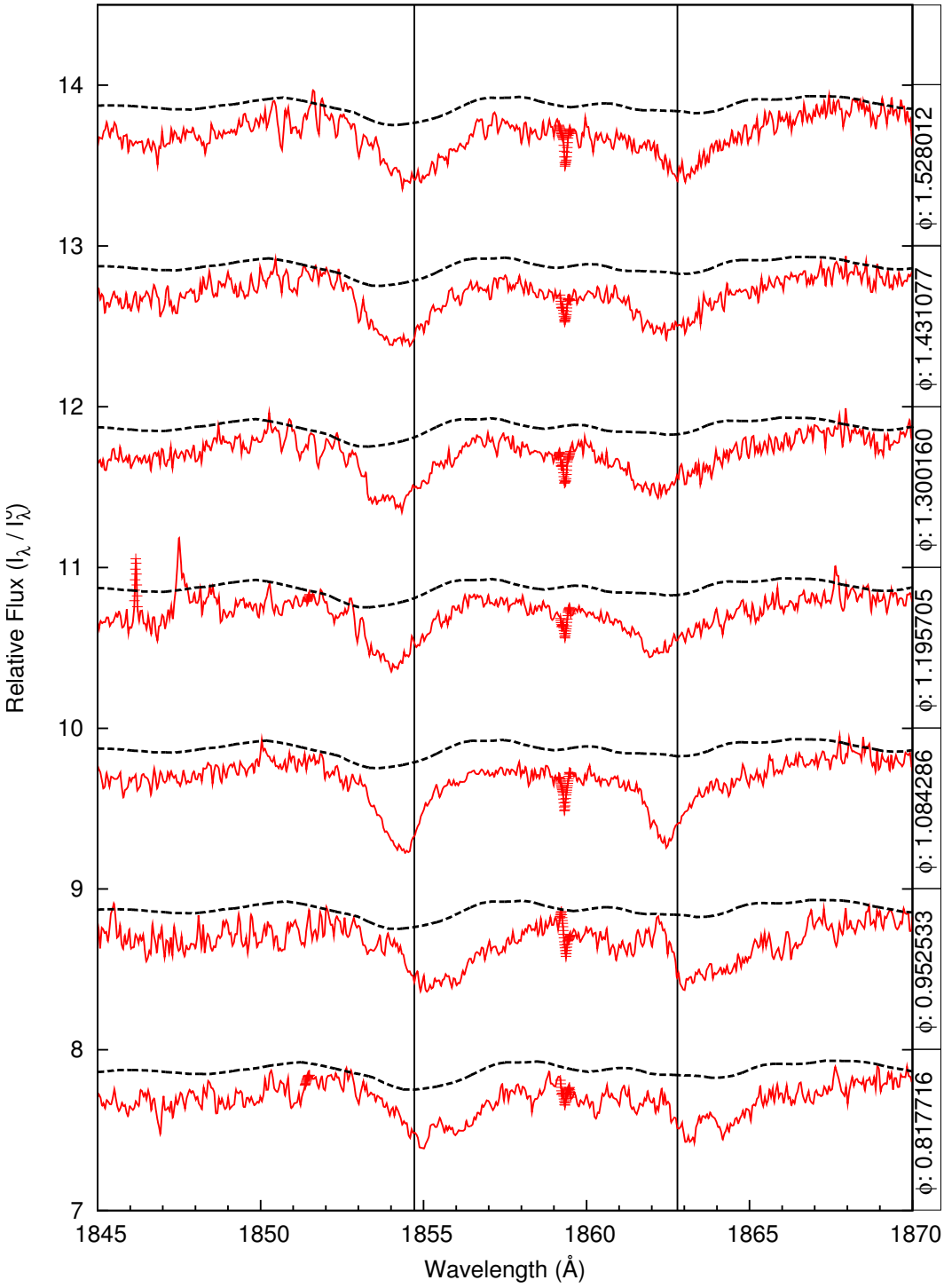

Figure C.38: [A] (b) Al III 1854 & 1862: Normalized U Cep data. Doppler motion with respect to the Sun. Synthetic spectra matched to data.

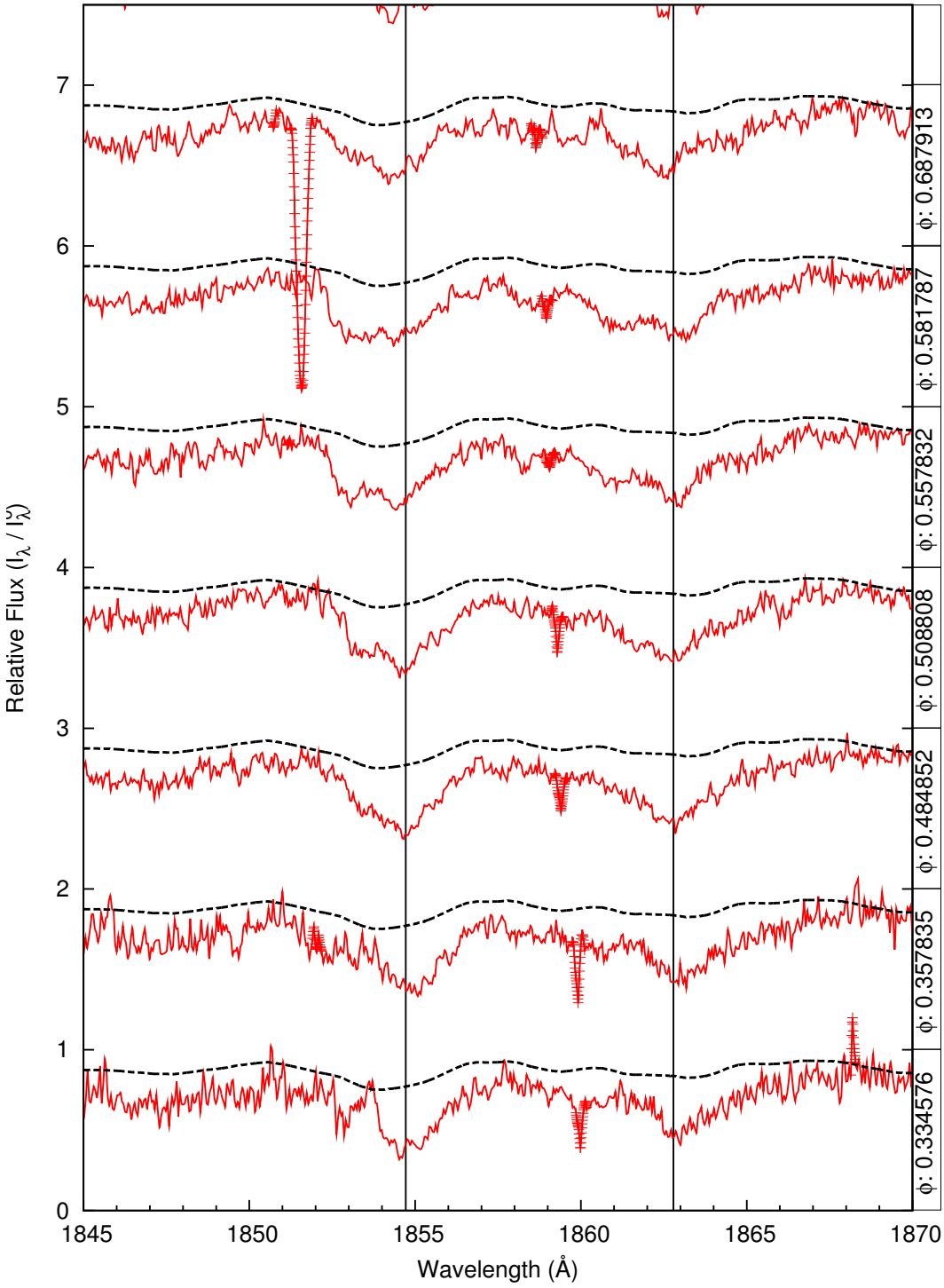

Figure C.39: [B] (a) Al III 1854 & 1862: Normalized U Cep data. Synthetic spectra and interstellar absorption lines matched to data.

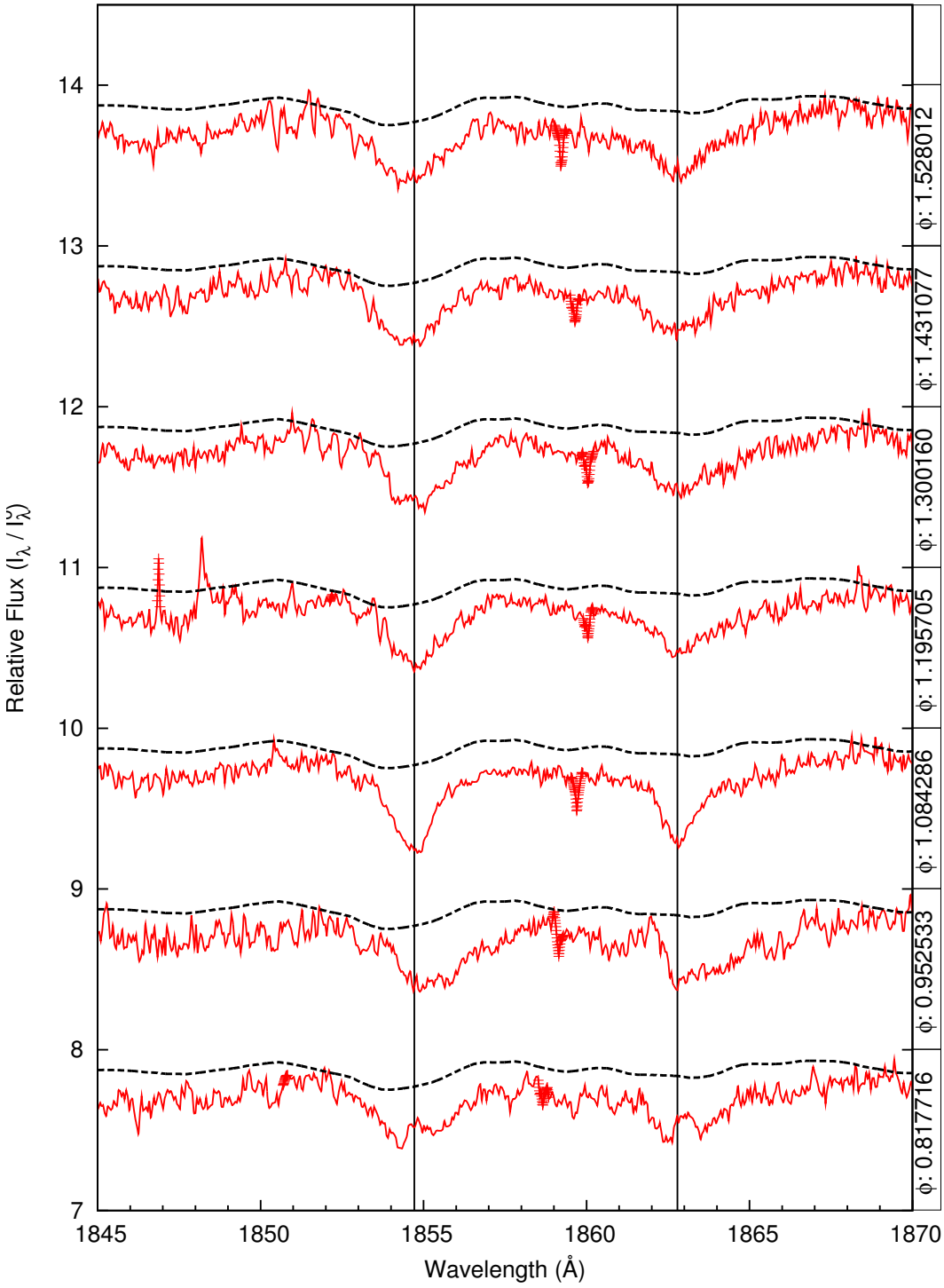

Figure C.40: [B] (b) Al III 1854 & 1862: Normalized U Cep data. Synthetic spectra and interstellar absorption lines matched to data.

Appendix D

Ionization Fractions

In this appendix is a collection of plots of ionization fractions computed under various conditions. The elements considered, C, Si, Al, N, O, Fe, and Mg are commonly found in B star systems. The first set of plots hold the average temperature constant, and shows the fractional change with increasing electron pressure. The second set of images holds electron pressure to be constant and displays the change in ionization ratios at temperature increases.

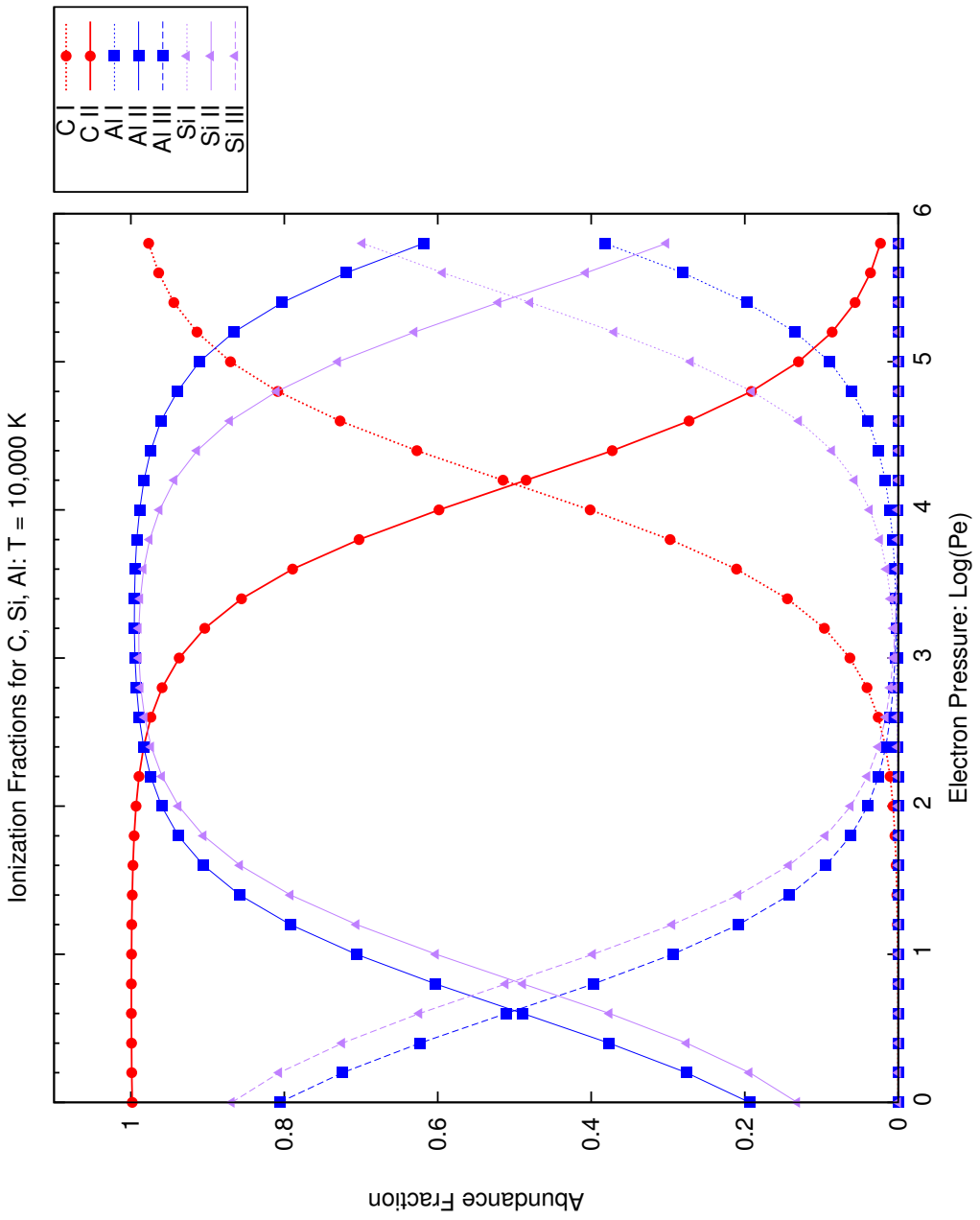

Figure D.1: Abundance ratios for the elements C, Si, and Al at an average temperature of 10,000 K varying with electron pressure, P_e. As P_e increases, it is more likely for an atom to capture an electron and exist in a lower ionization state.

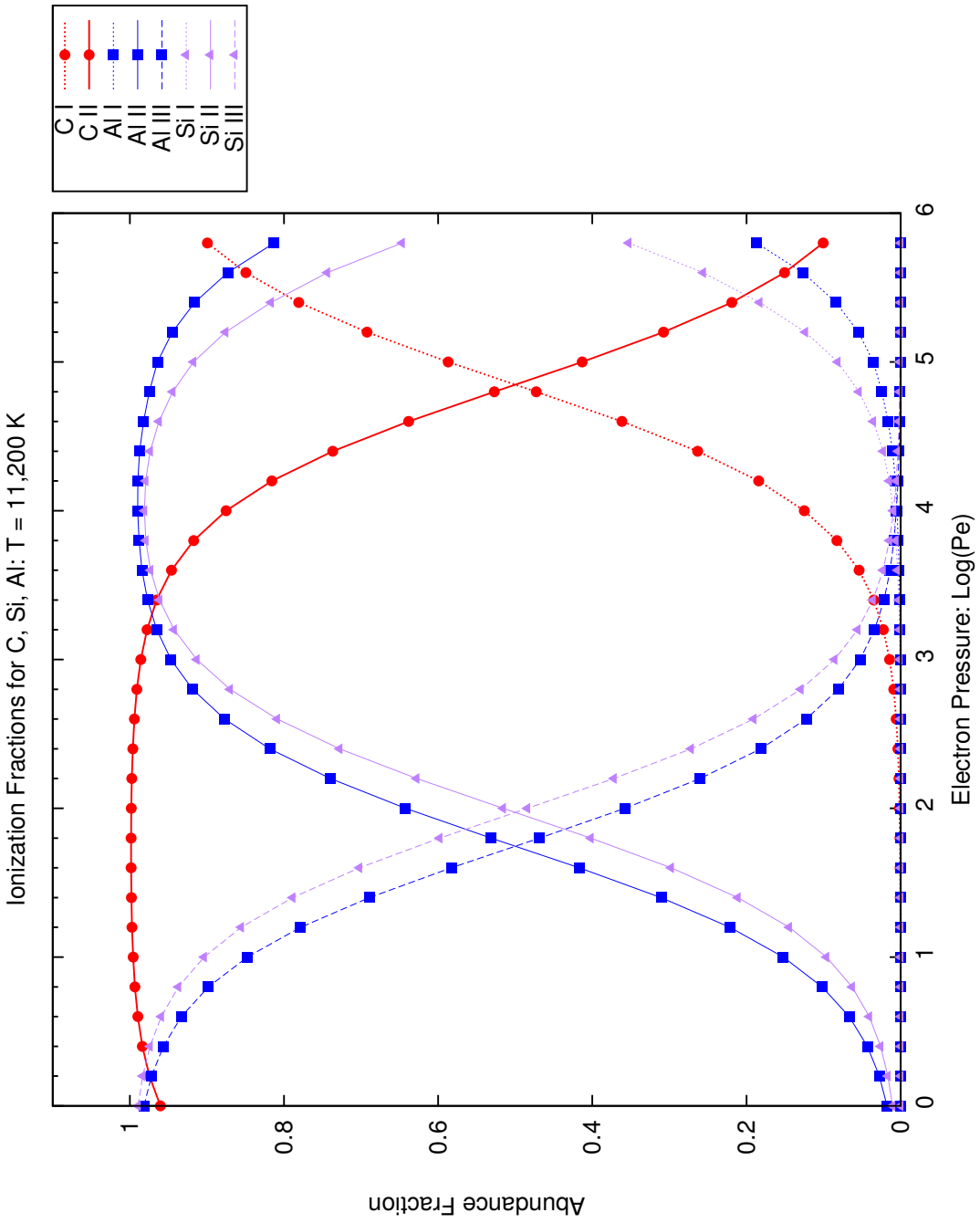

Figure D.2: Abundance ratios for the elements C, Si, and Al at an average temperature of 11,000 K varying with electron pressure, P_e. As P_e increases, it is more likely for an atom to capture an electron and exist in a lower ionization state.

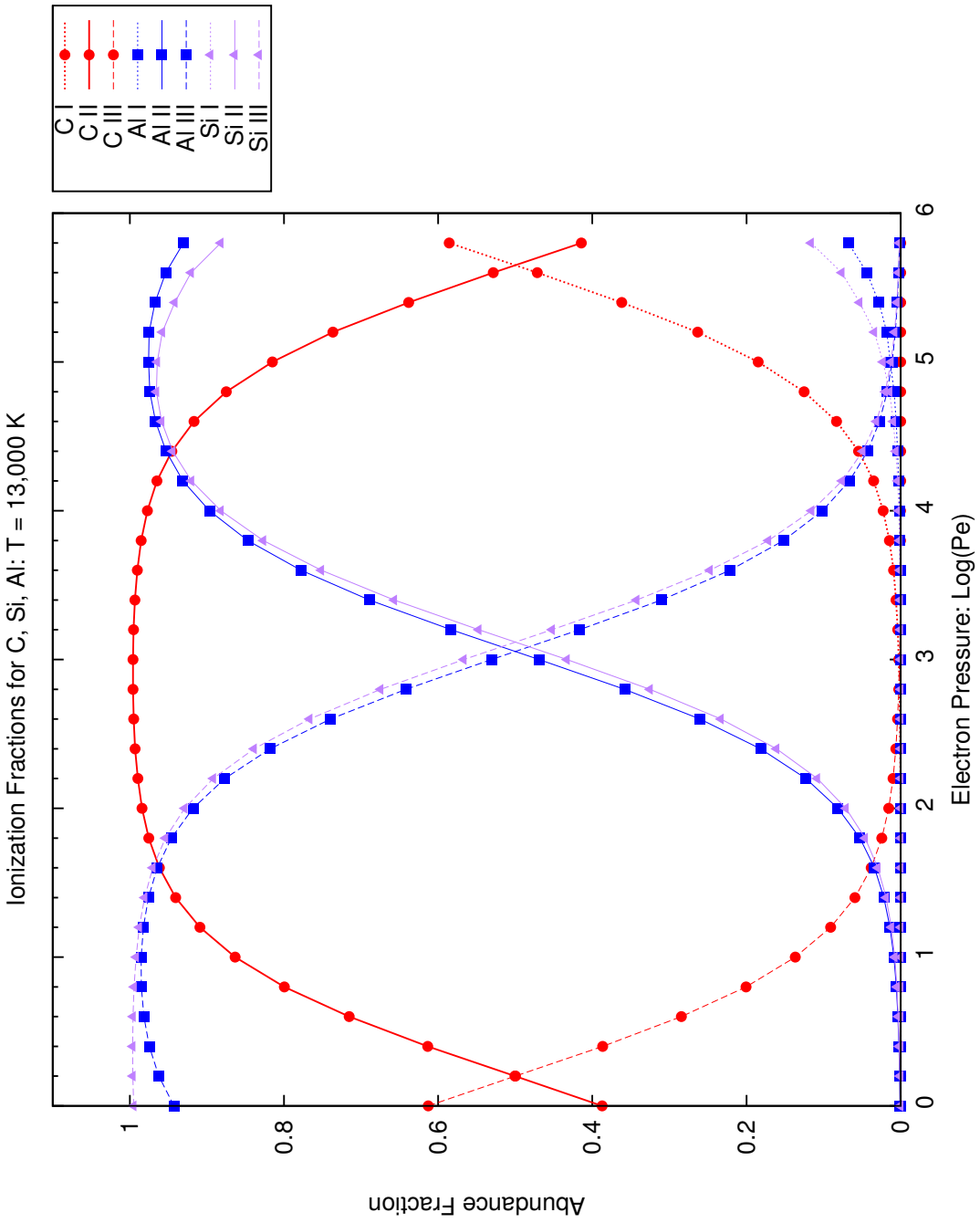

Figure D.3: Abundance ratios for the elements C, Si, and Al at an average temperature of 13,000 K varying with electron pressure, P_e. As P_e increases, it is more likely for an atom to capture an electron and exist in a lower ionization state.

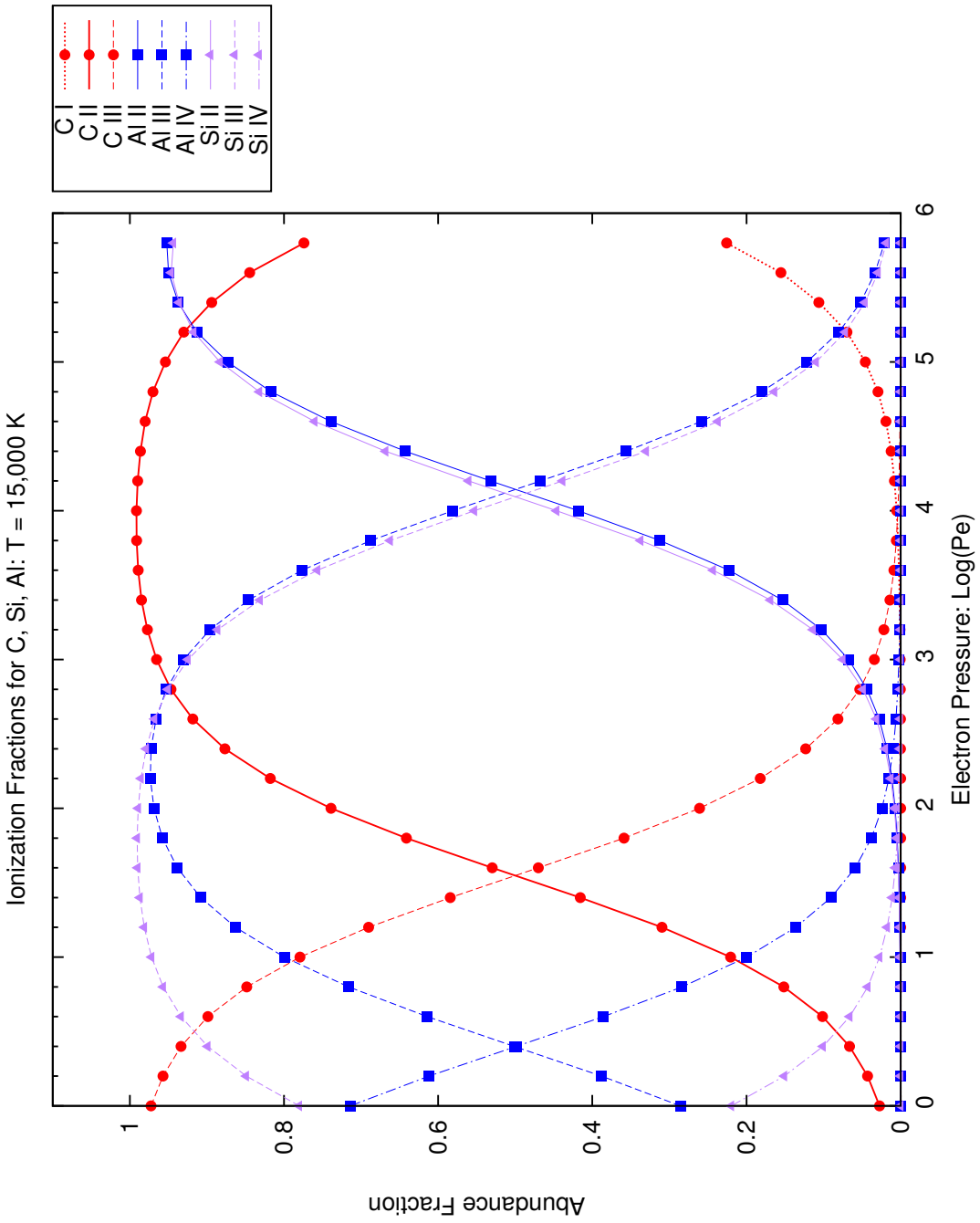

Figure D.4: Abundance ratios for the elements C, Si, and Al at an average temperature of 15,000 K varying with electron pressure, P_e. As P_e increases, it is more likely for an atom to capture an electron and exist in a lower ionization state.

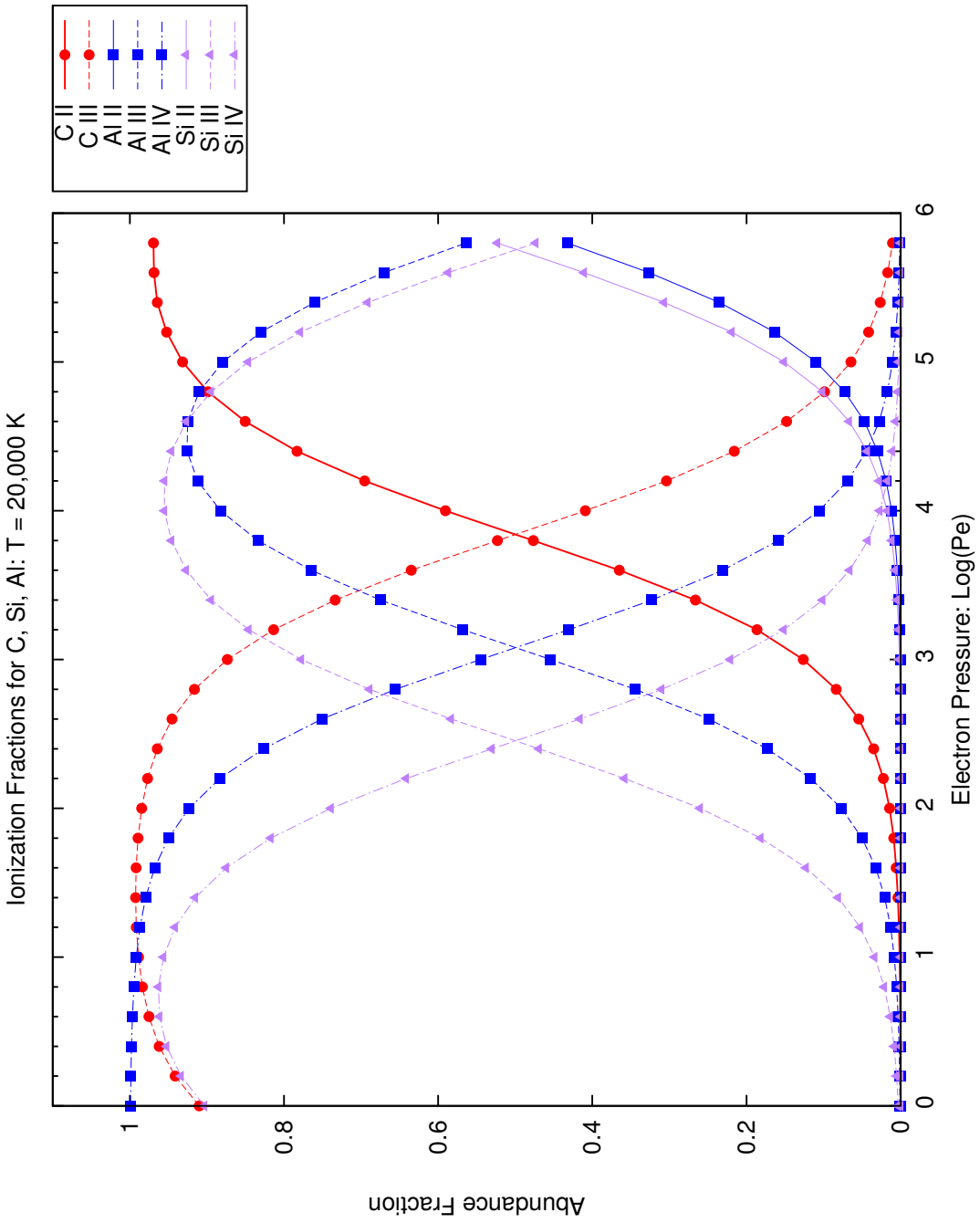

Figure D.5: Abundance ratios for the elements C, Si, and Al at an average temperature of 20,000 K varying with electron pressure, P_e. As P_e increases, it is more likely for an atom to capture an electron and exist in a lower ionization state.

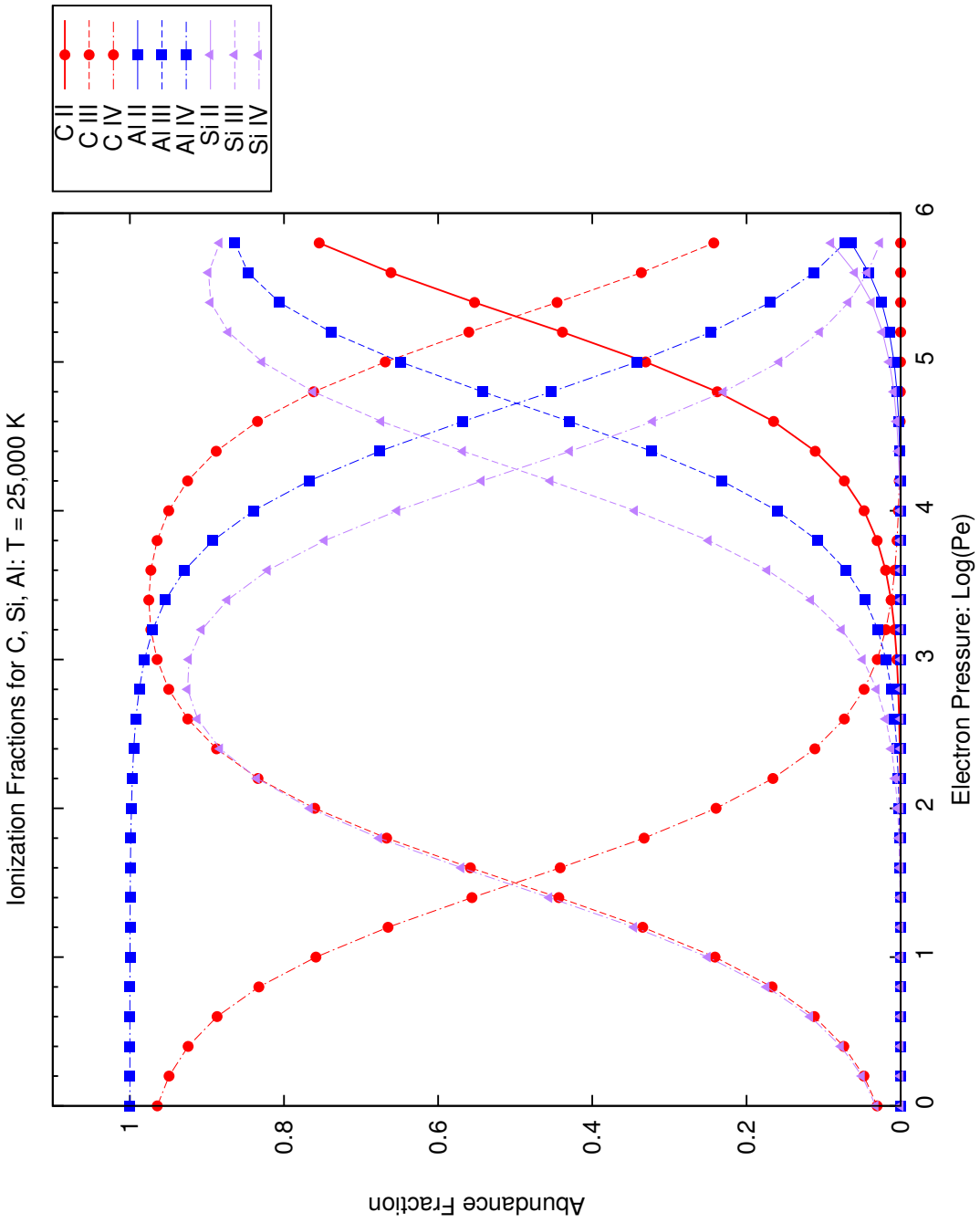

Figure D.6: Abundance ratios for the elements C, Si, and Al at an average temperature of 25,000 K varying with electron pressure, P_e. As P_e increases, it is more likely for an atom to capture an electron and exist in a lower ionization state.

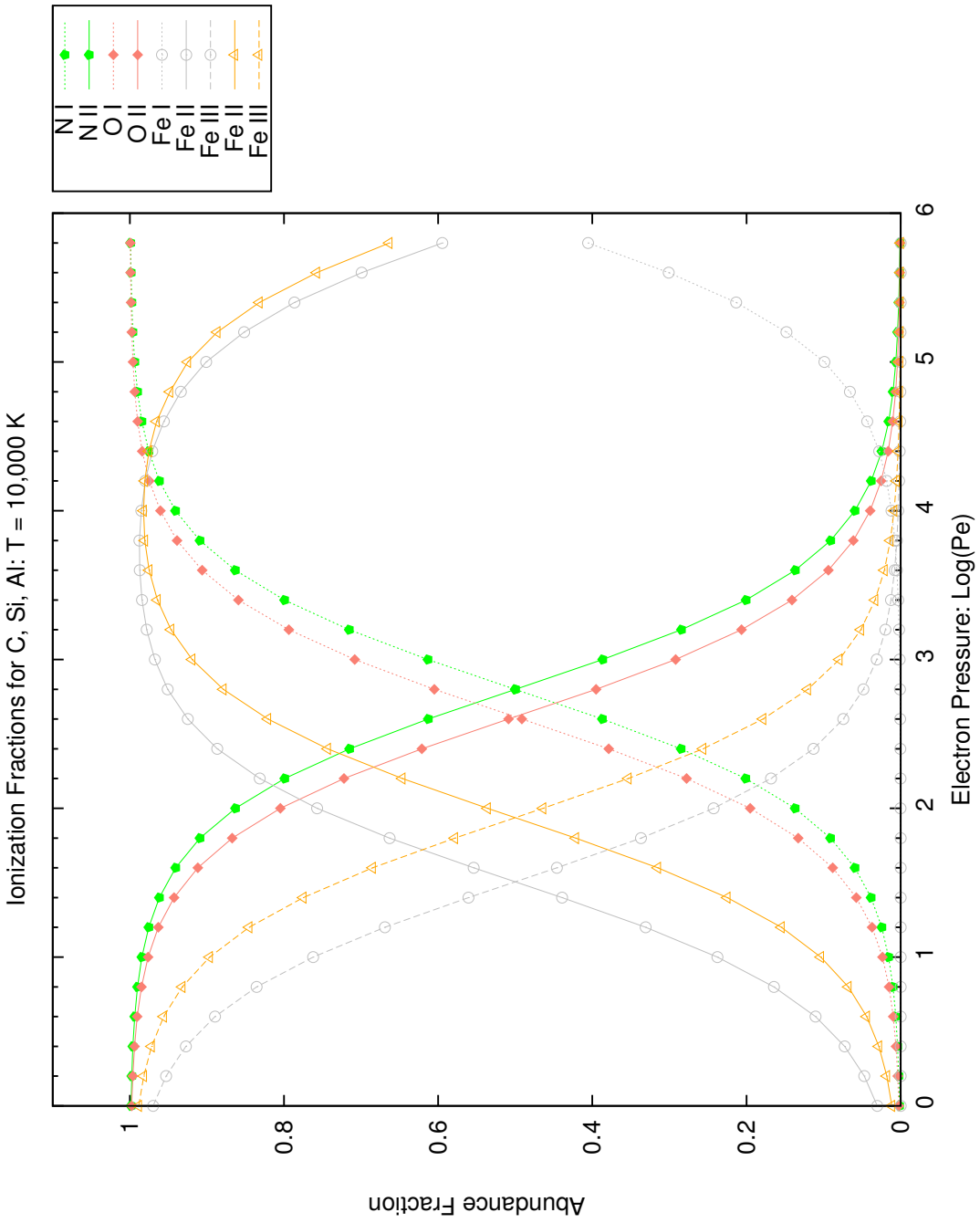

Figure D.7: Abundance ratios for the elements N, O, Mg, and Fe at an average temperature of 10,000 K varying with electron pressure, P_e. As P_e increases, it is more likely for an atom to capture an electron and exist in a lower ionization state.

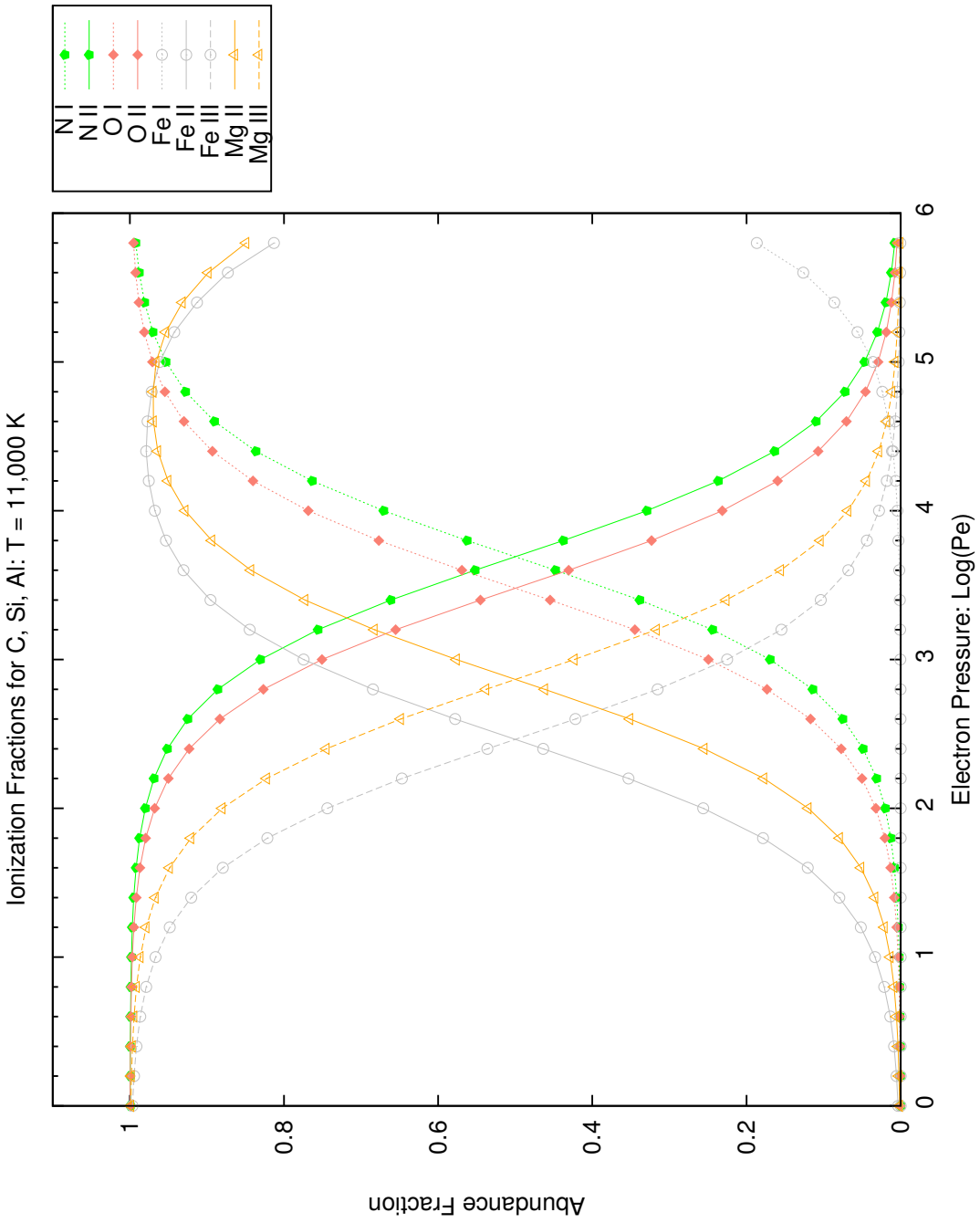

Figure D.8: Abundance ratios for the elements N, O, Mg, and Fe at an average temperature of 11,000 K varying with electron pressure, P_e. As P_e increases, it is more likely for an atom to capture an electron and exist in a lower ionization state.

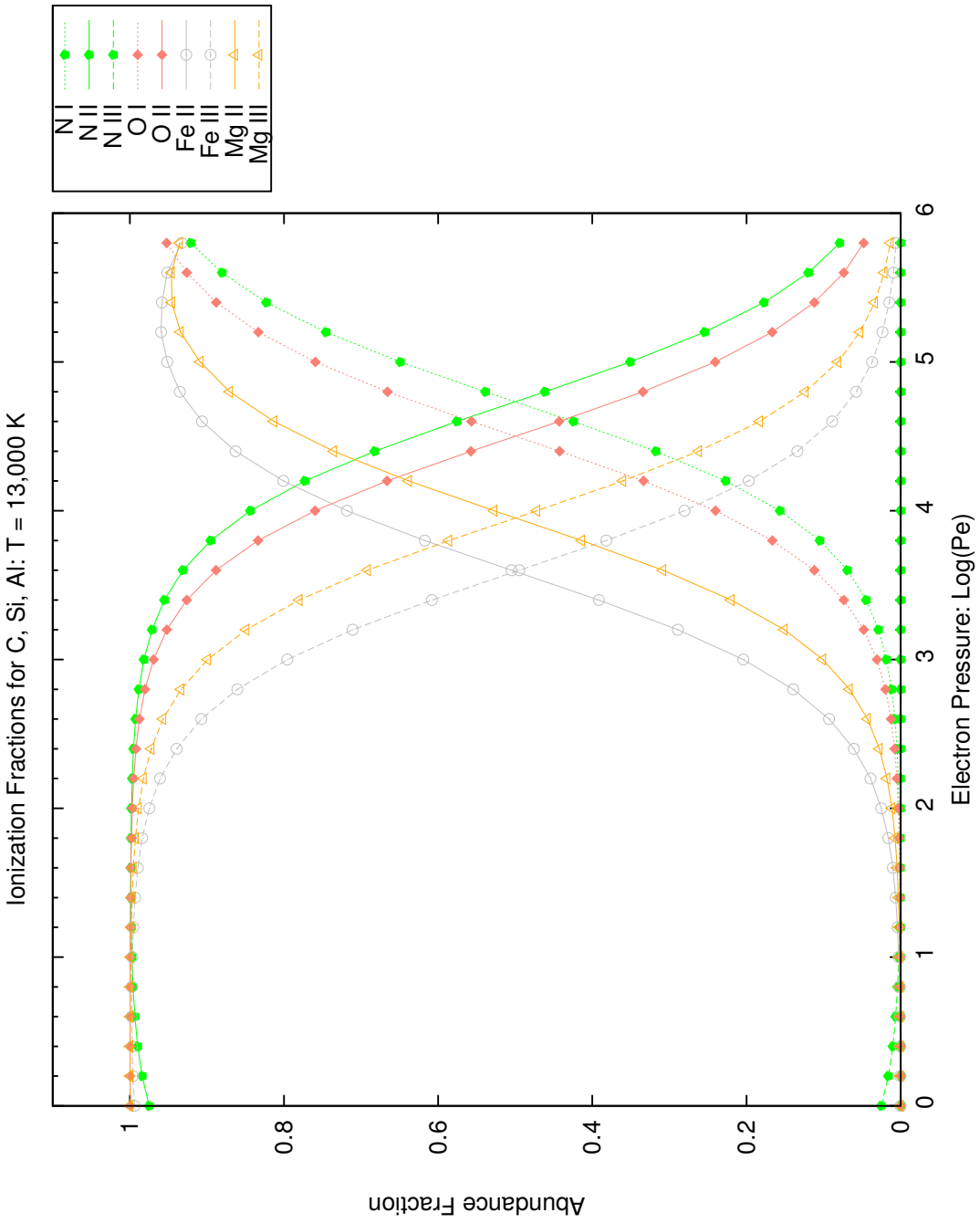

Figure D.9: Abundance ratios for the elements N, O, Mg, and Fe at an average temperature of 13,000 K varying with electron pressure, P_e. As P_e increases, it is more likely for an atom to capture an electron and exist in a lower ionization state.

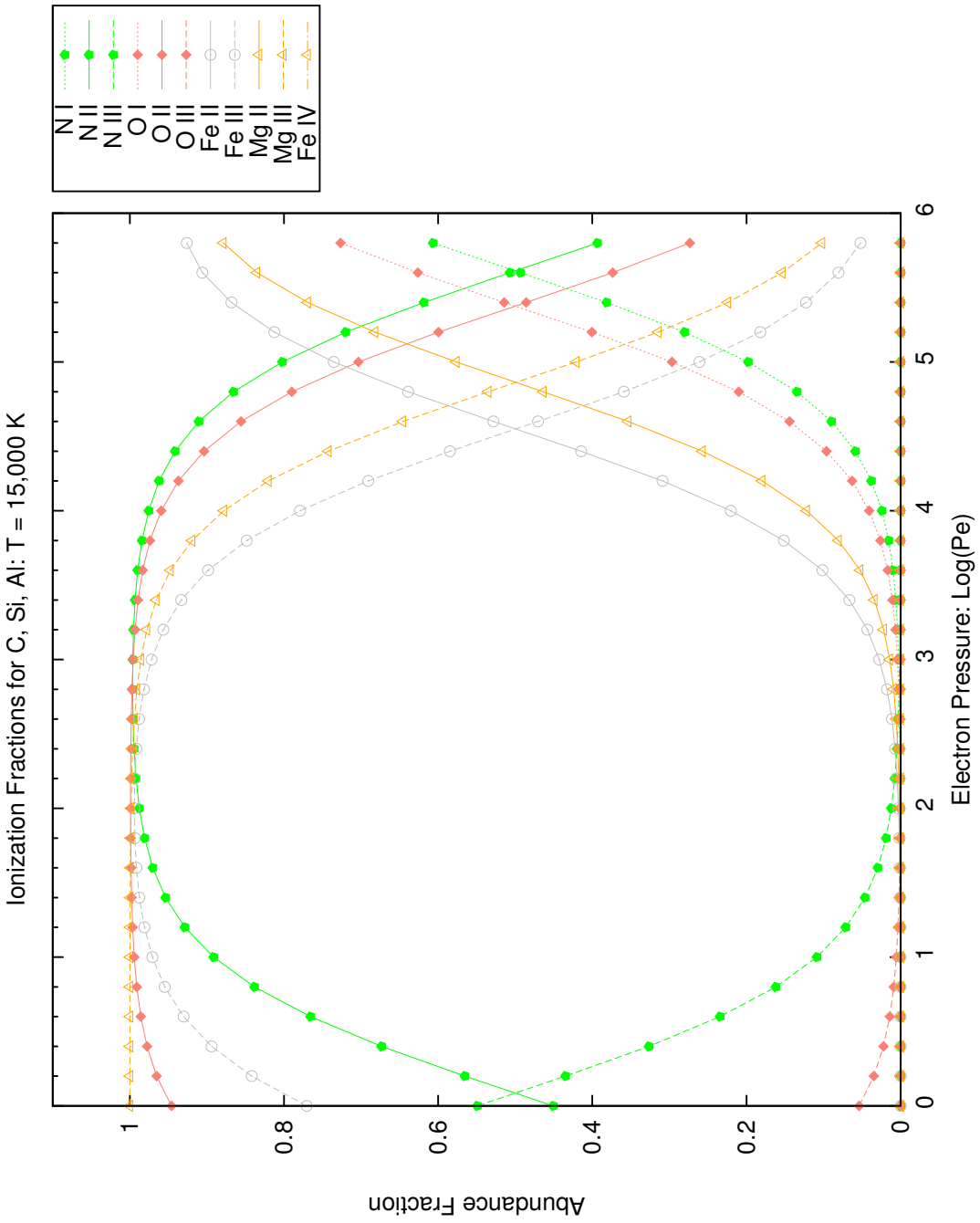

Figure D.10: Abundance ratios for the elements N, O, Mg, and Fe at an average temperature of 15,000 K varying with electron pressure, P_e. As P_e increases, it is more likely for an atom to capture an electron and exist in a lower ionization state.

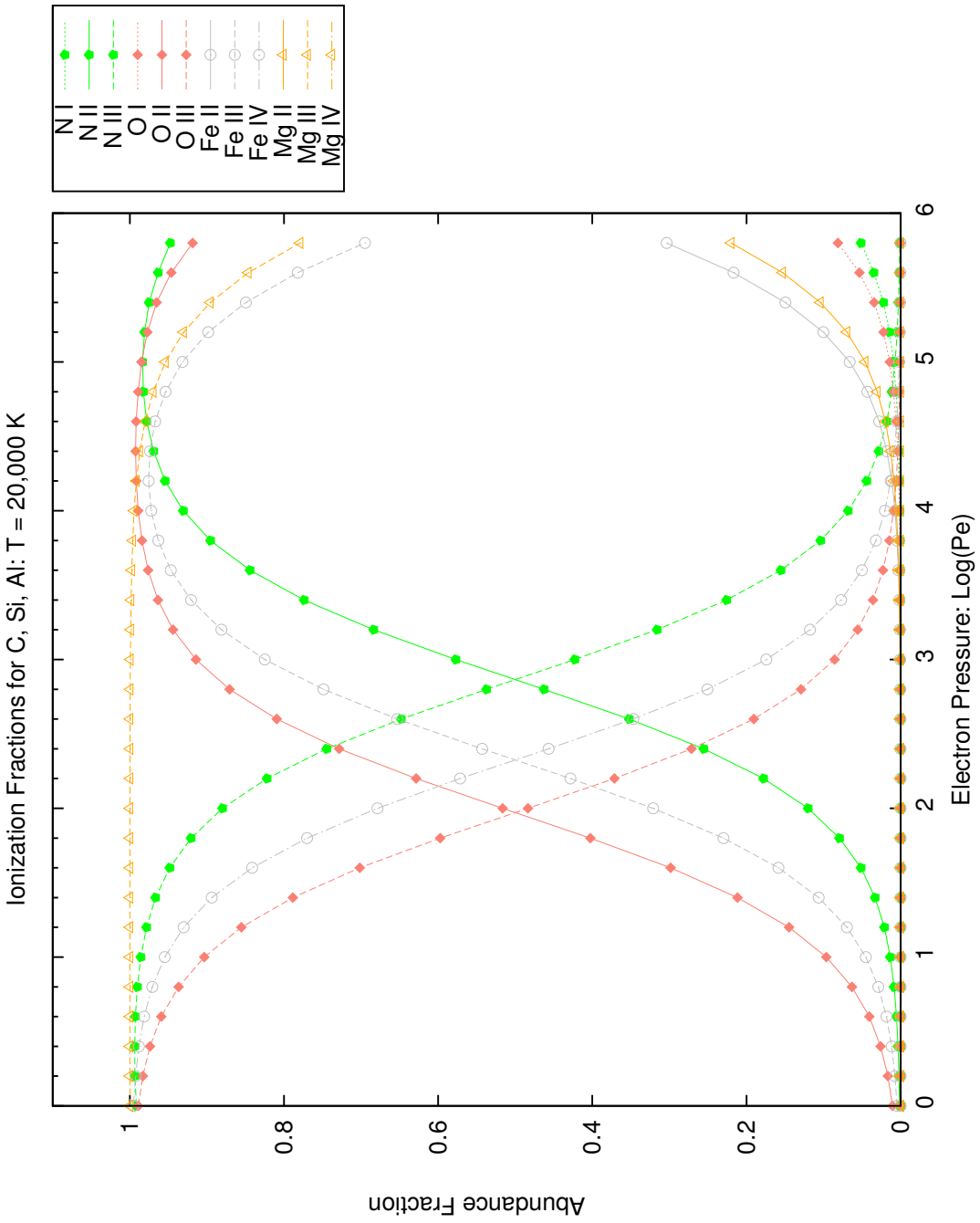

Figure D.11: Abundance ratios for the elements N, O, Mg, and Fe at an average temperature of 20,000 K varying with electron pressure, P_e. As P_e increases, it is more likely for an atom to capture an electron and exist in a lower ionization state.

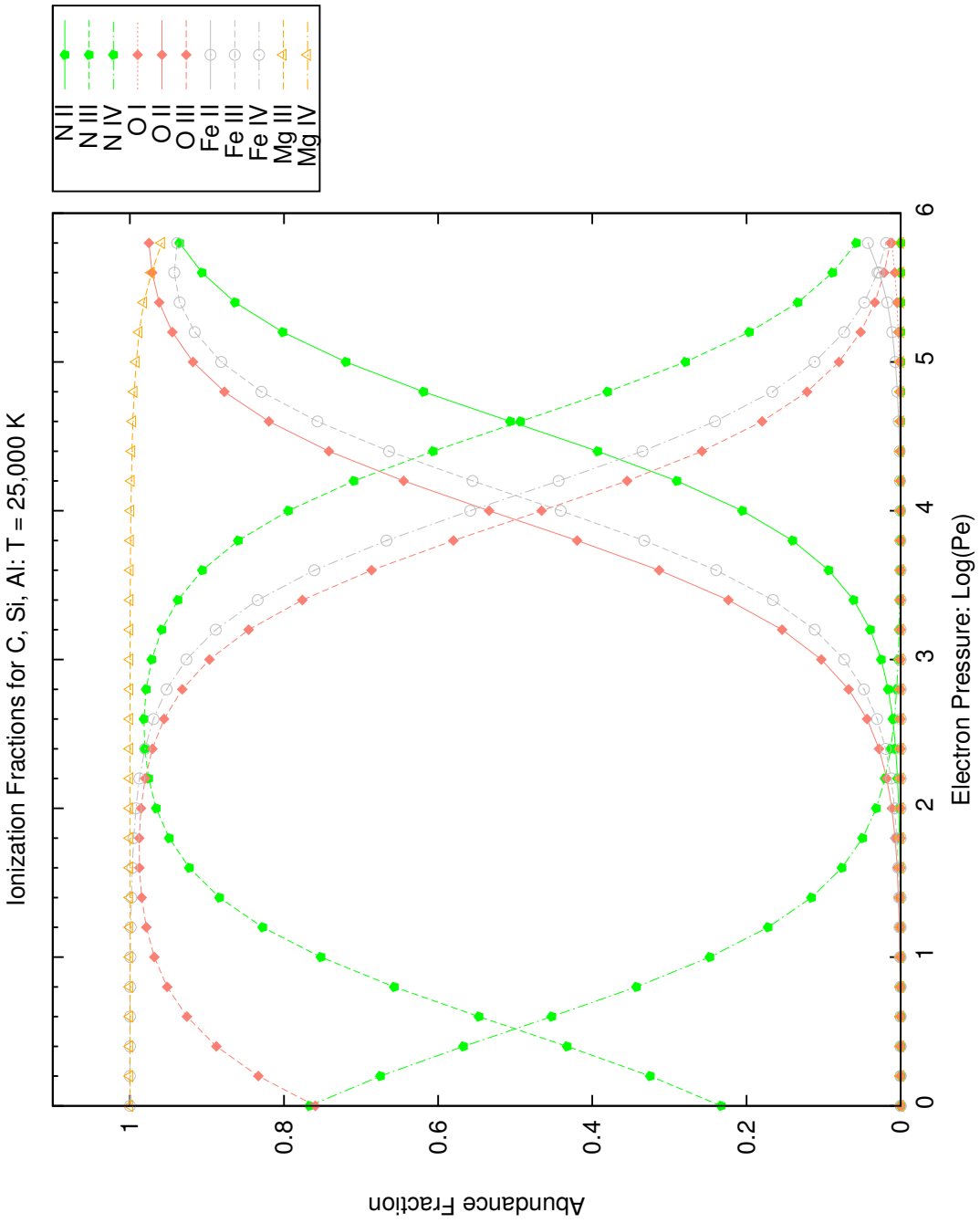

Figure D.12: Abundance ratios for the elements N, O, Mg, and Fe at an average temperature of 25,000 K varying with electron pressure, P_e. As P_e increases, it is more likely for an atom to capture an electron and exist in a lower ionization state.

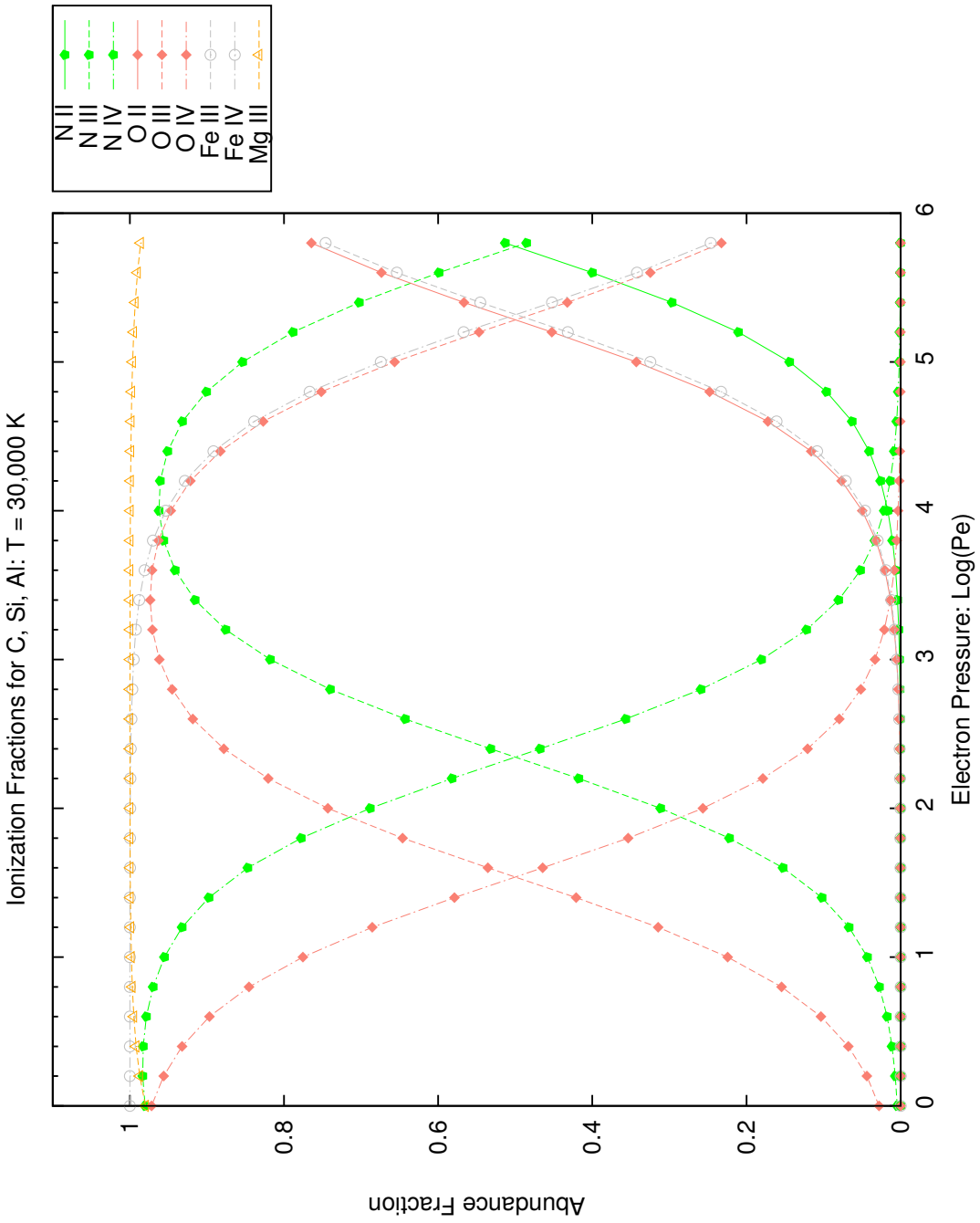

Figure D.13: Abundance ratios for the elements N, O, Mg, and Fe at an average temperature of 30,000 K varying with electron pressure, P_e. As P_e increases, it is more likely for an atom to capture an electron and exist in a lower ionization state.

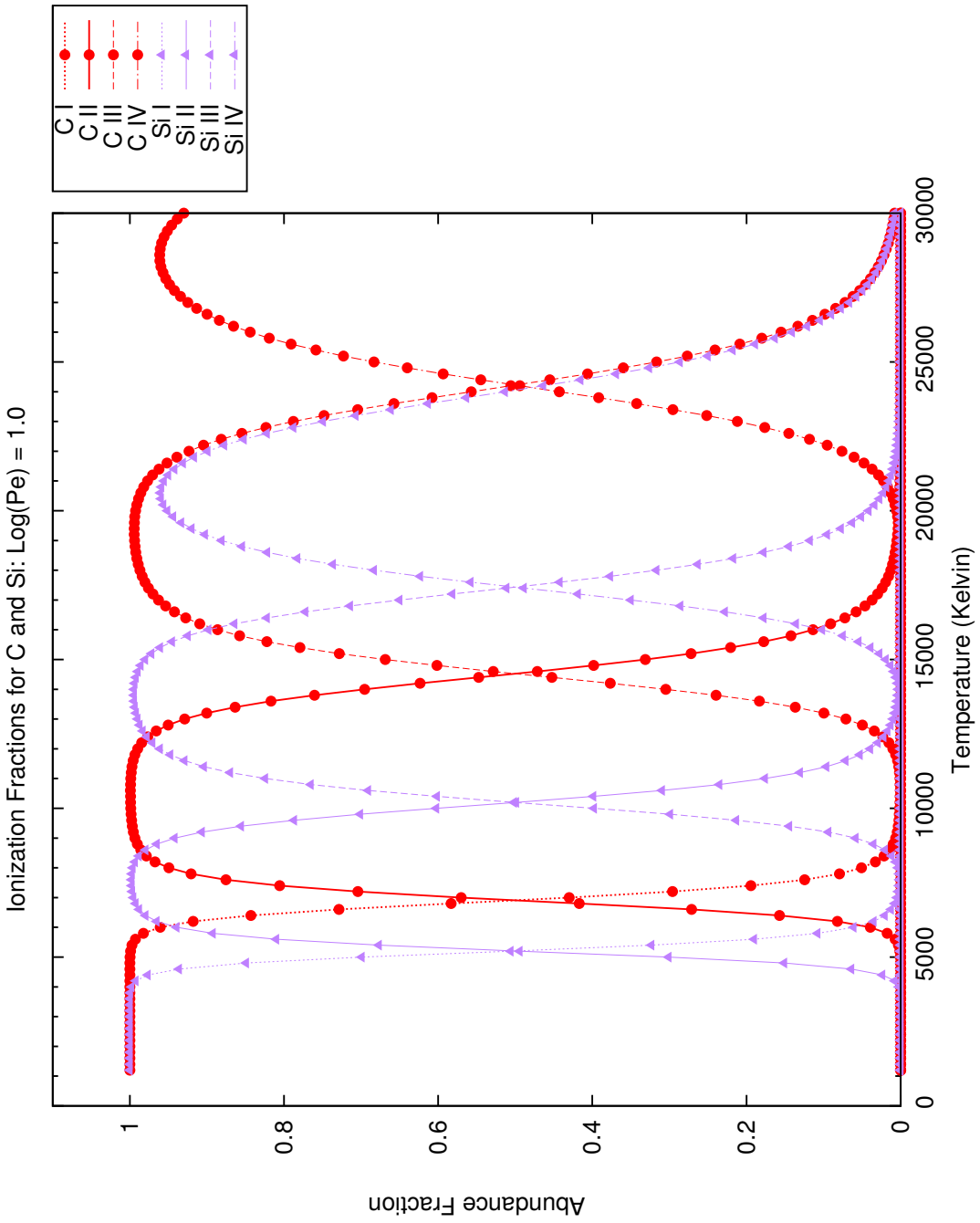

Figure D.14: Abundance ratios for the elements C and Si at a given $log(P_e) = 1.0$ varying with temperature. As T increases, it is more likely for an electron to be stripped from its parent atom, leading to higher and higher ionization states.

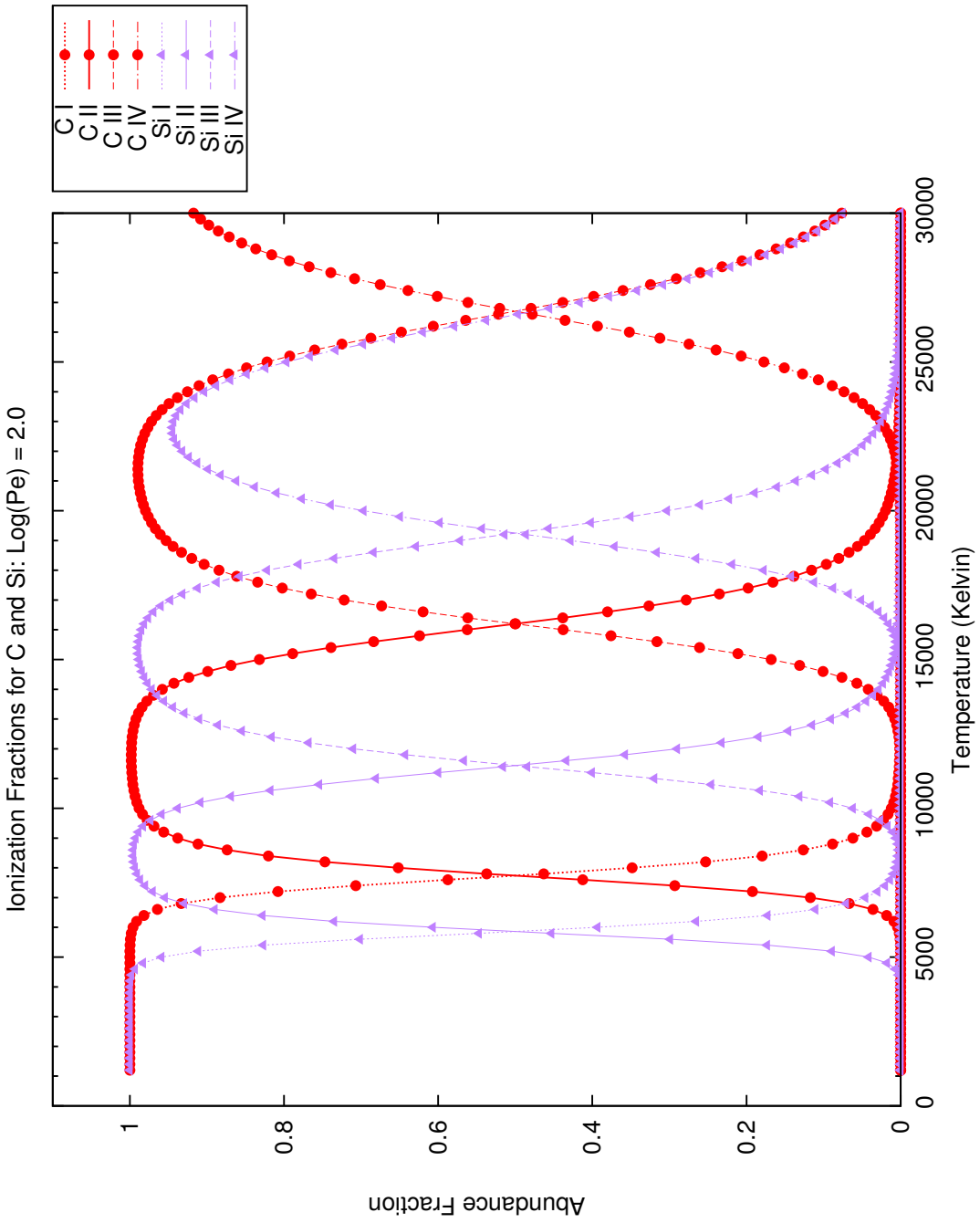

Figure D.15: Abundance ratios for the elements C and Si at a given $log(P_e) = 2.0$ varying with temperature. As T increases, it is more likely for an electron to be stripped from its parent atom, leading to higher and higher ionization states.

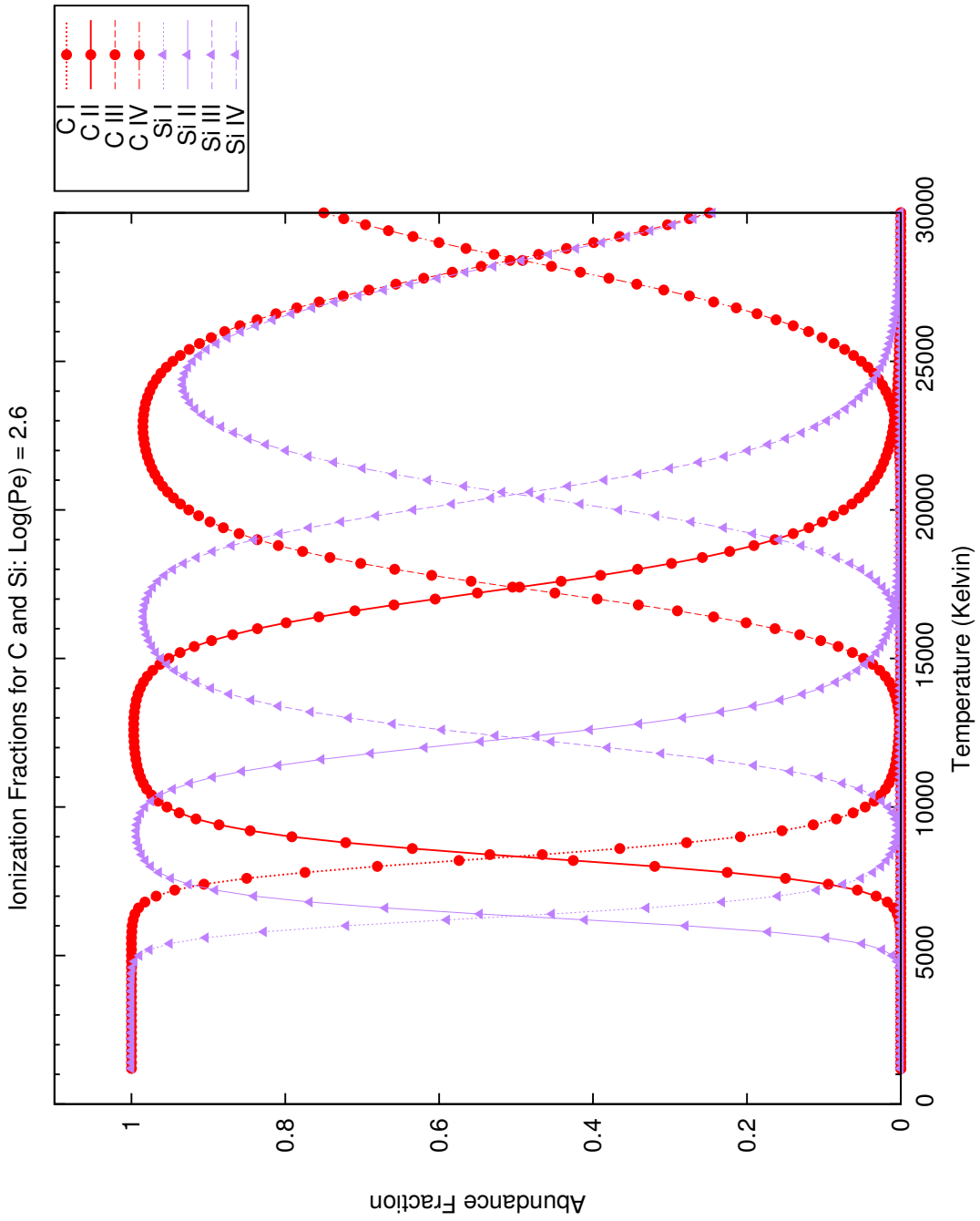

Figure D.16: Abundance ratios for the elements C and Si at a given $log(P_e) = 2.6$ varying with temperature. As T increases, it is more likely for an electron to be stripped from its parent atom, leading to higher and higher ionization states.

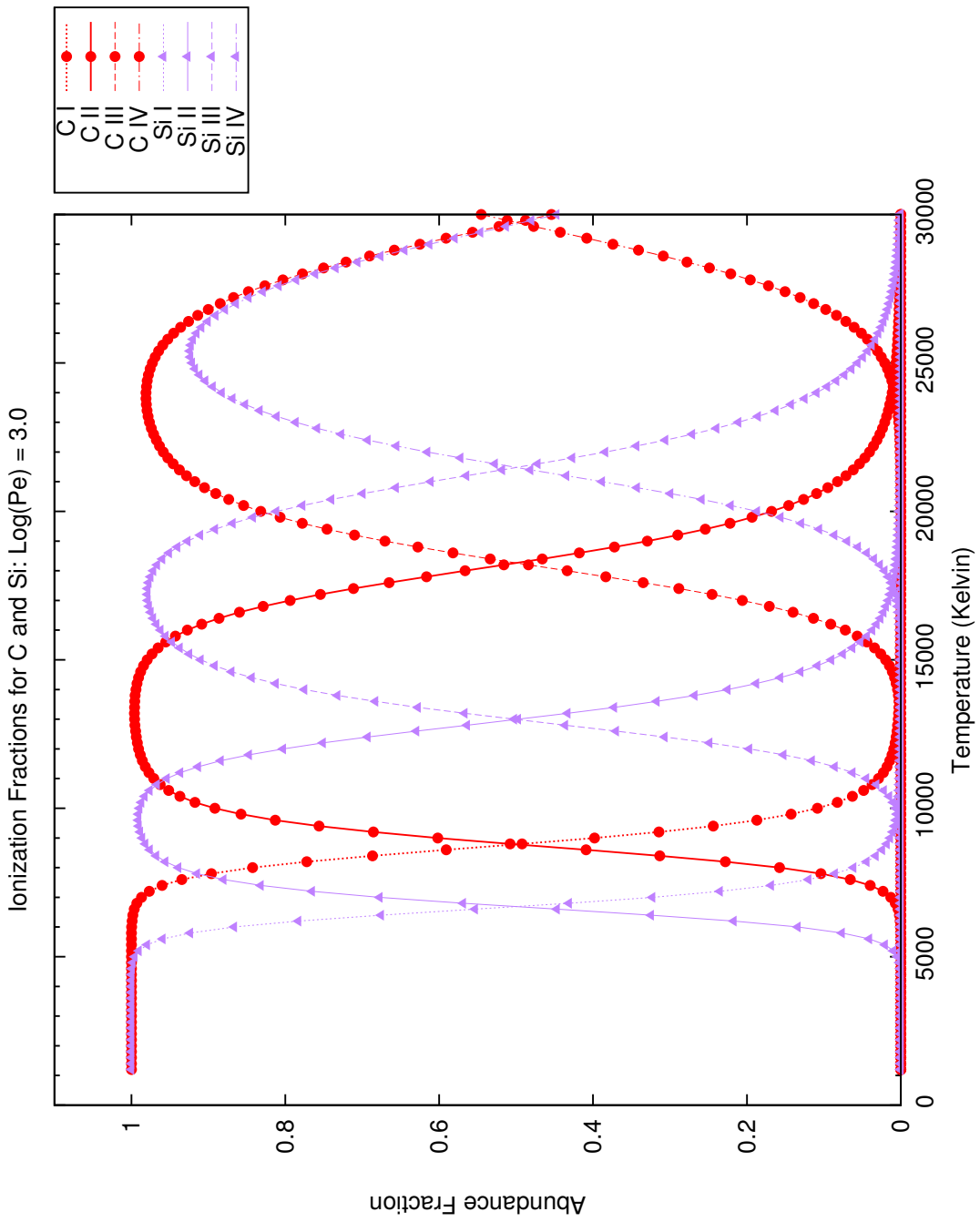

Figure D.17: Abundance ratios for the elements C and Si at a given $log(P_e) = 3.0$ varying with temperature. As T increases, it is more likely for an electron to be stripped from its parent atom, leading to higher and higher ionization states.

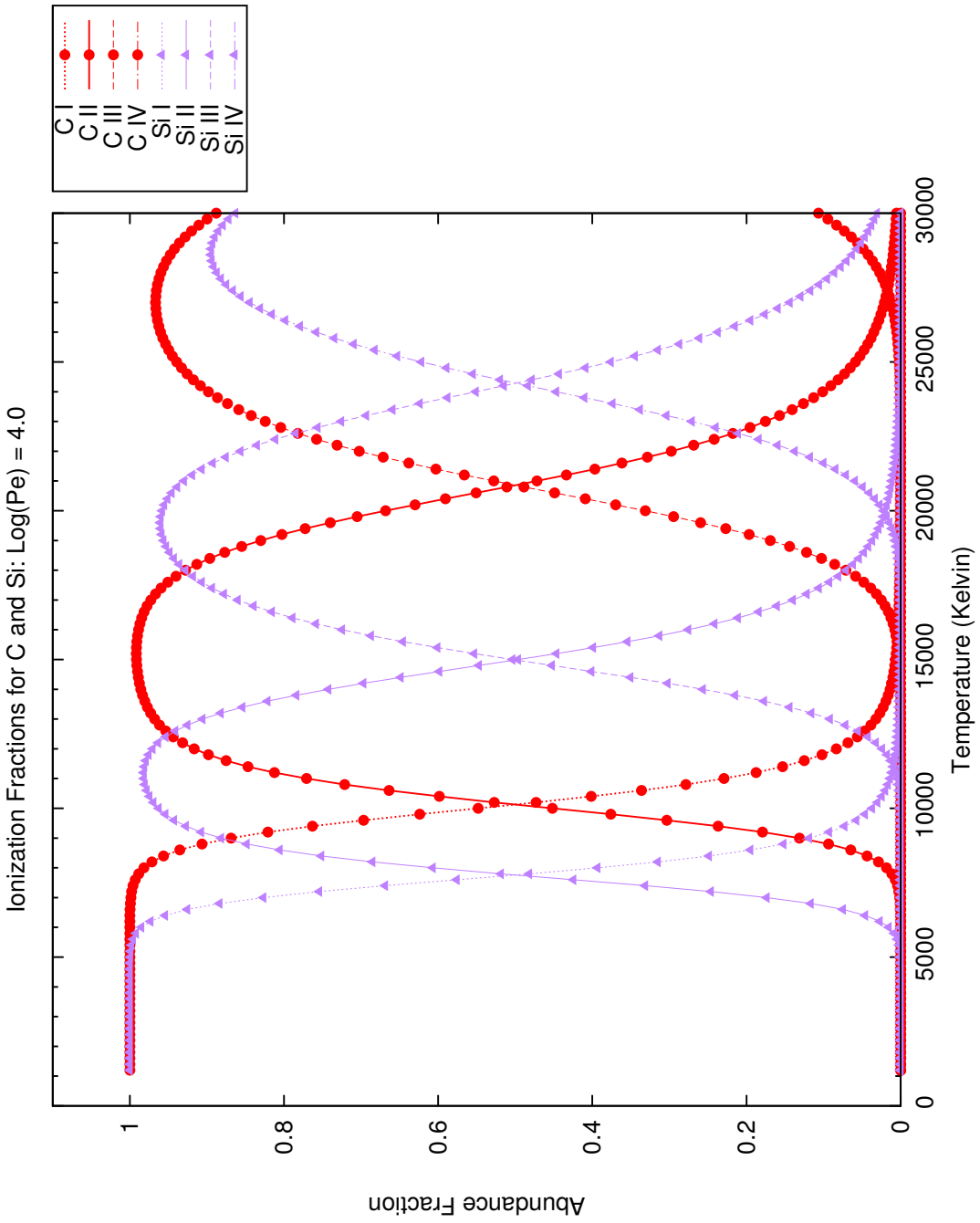

Figure D.18: Abundance ratios for the elements C and Si at a given $log(P_e) = 4.0$ varying with temperature. As T increases, it is more likely for an electron to be stripped from its parent atom, leading to higher and higher ionization states.

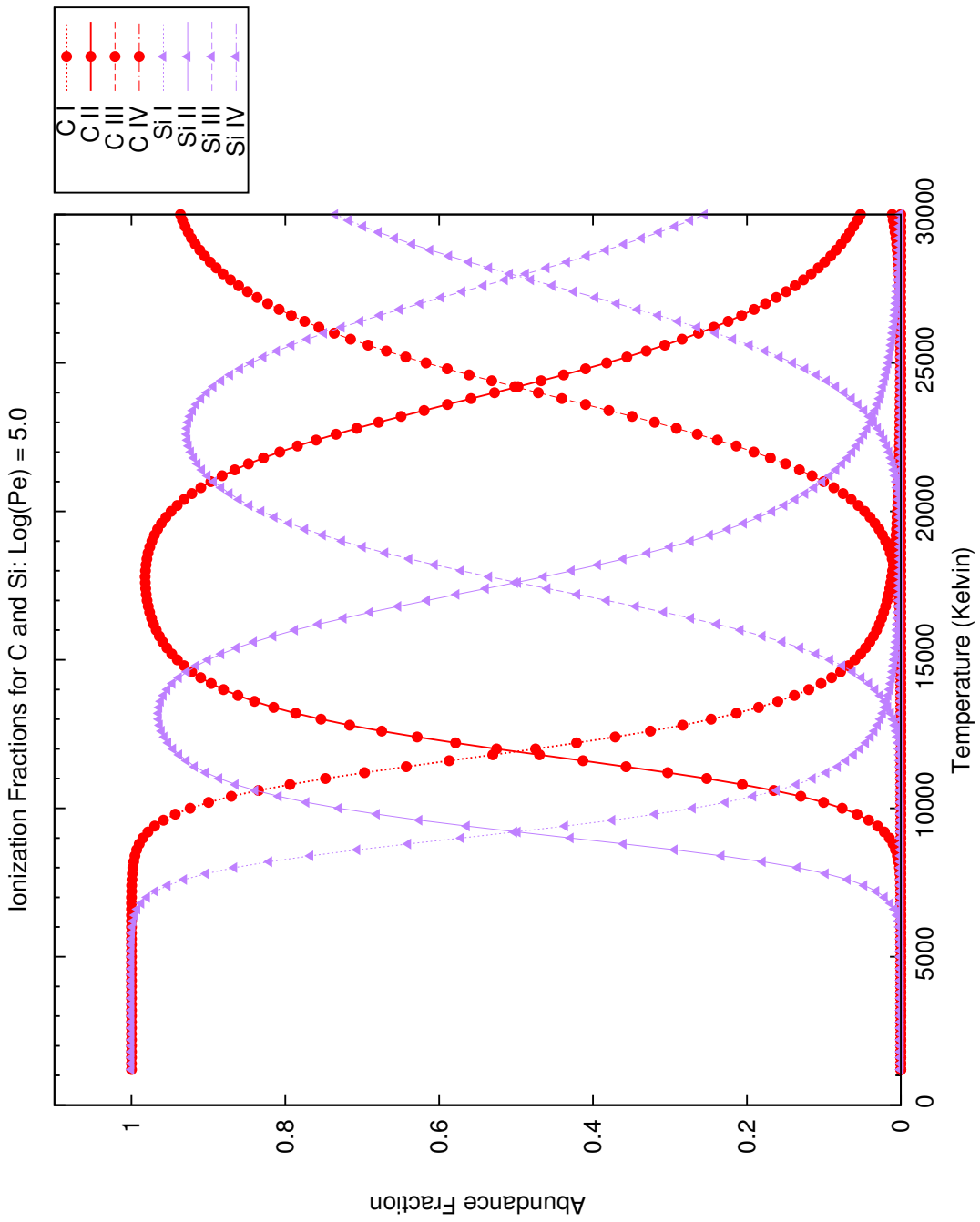

Figure D.19: Abundance ratios for the elements C and Si at a given $log(P_e) = 5.0$ varying with temperature. As T increases, it is more likely for an electron to be stripped from its parent atom, leading to higher and higher ionization states.

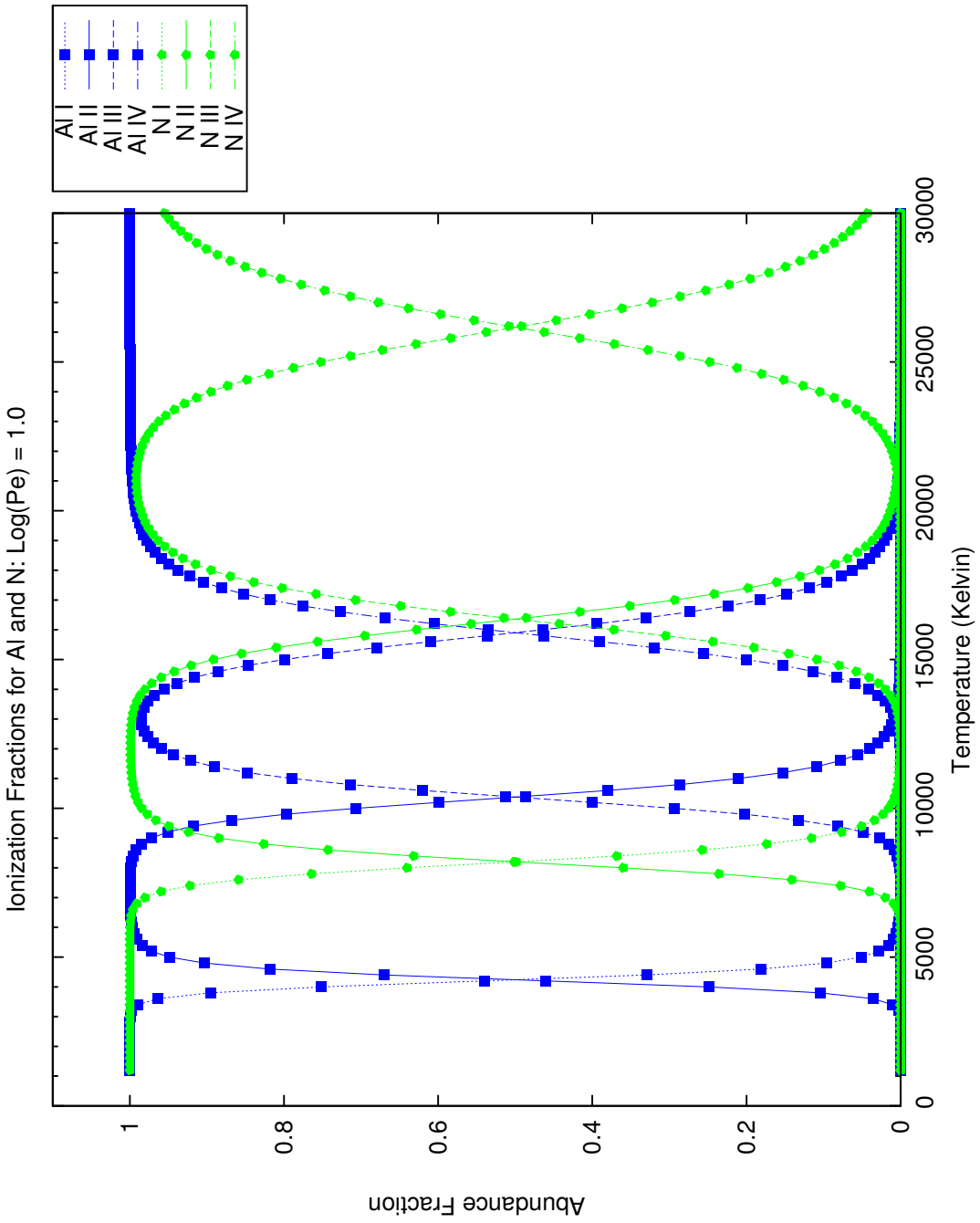

Figure D.20: Abundance ratios for the elements Al and N at a given $log(P_e) = 1.0$ varying with temperature. As T increases, it is more likely for an electron to be stripped from its parent atom, leading to higher and higher ionization states.

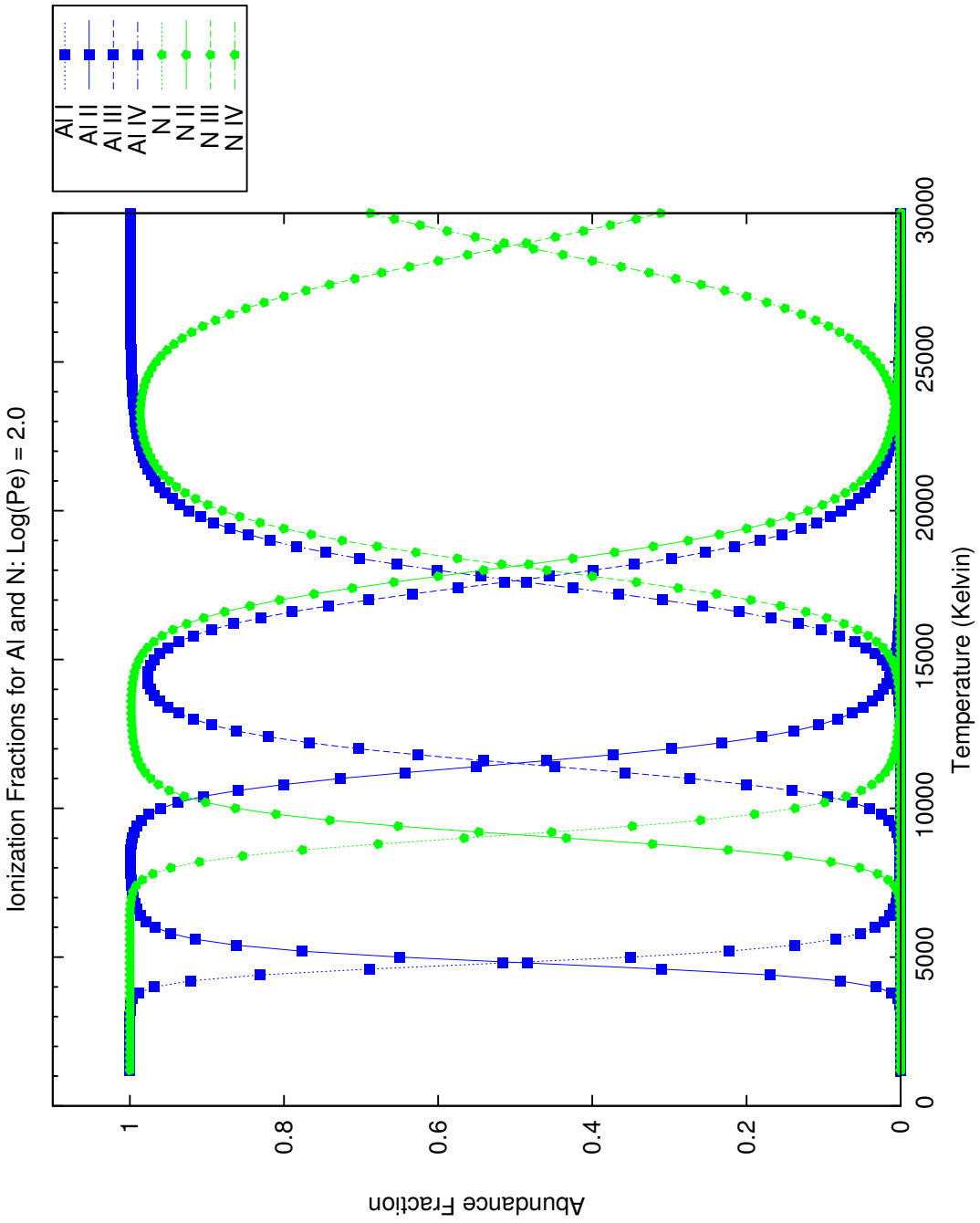

Figure D.21: Abundance ratios for the elements Al and N at a given $log(P_e) = 2.0$ varying with temperature. As T increases, it is more likely for an electron to be stripped from its parent atom, leading to higher and higher ionization states.

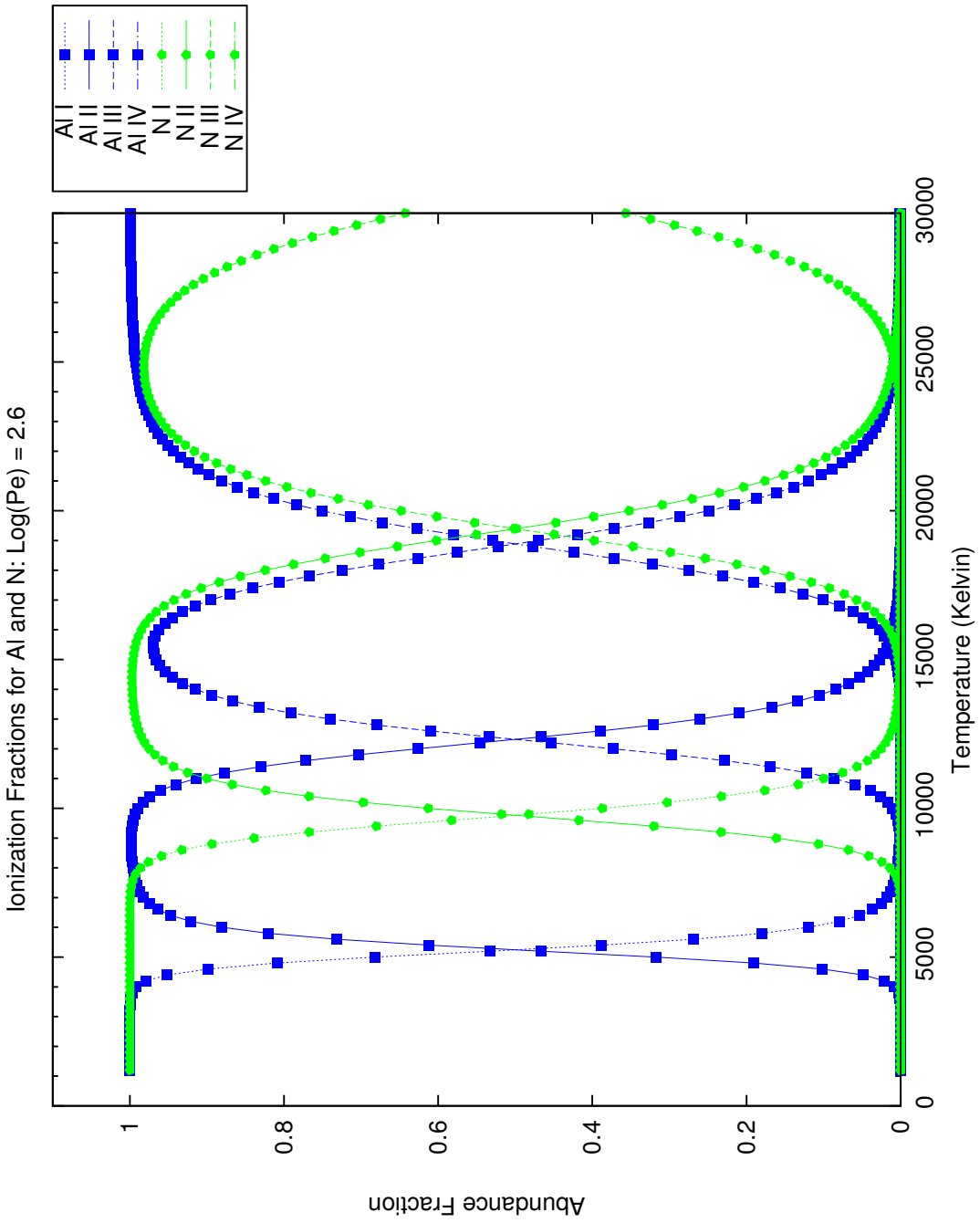

Figure D.22: Abundance ratios for the elements Al and N at a given $log(P_e) = 2.6$ varying with temperature. As T increases, it is more likely for an electron to be stripped from its parent atom, leading to higher and higher ionization states.

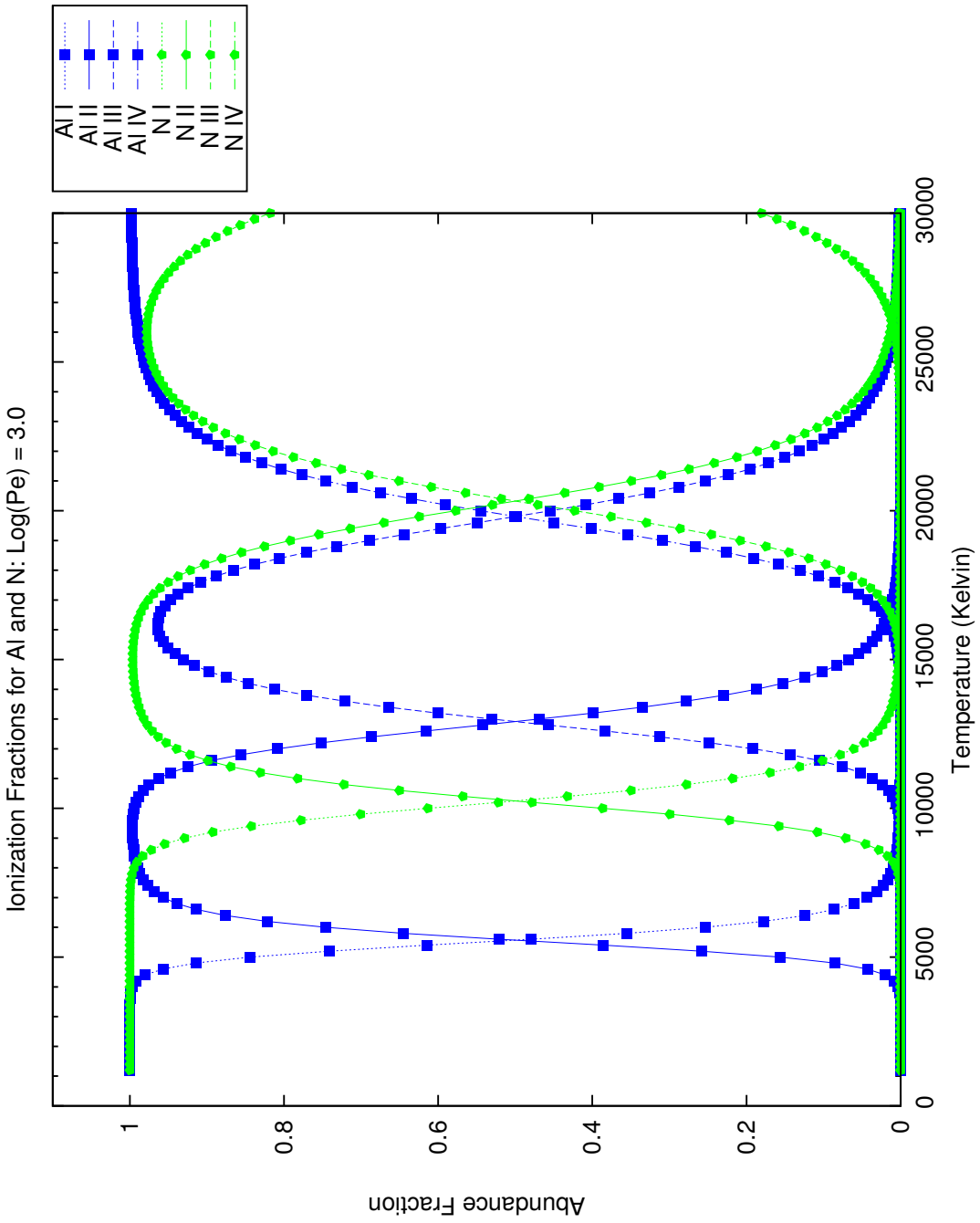

Figure D.23: Abundance ratios for the elements Al and N at a given $log(P_e) = 3.0$ varying with temperature. As T increases, it is more likely for an electron to be stripped from its parent atom, leading to higher and higher ionization states.

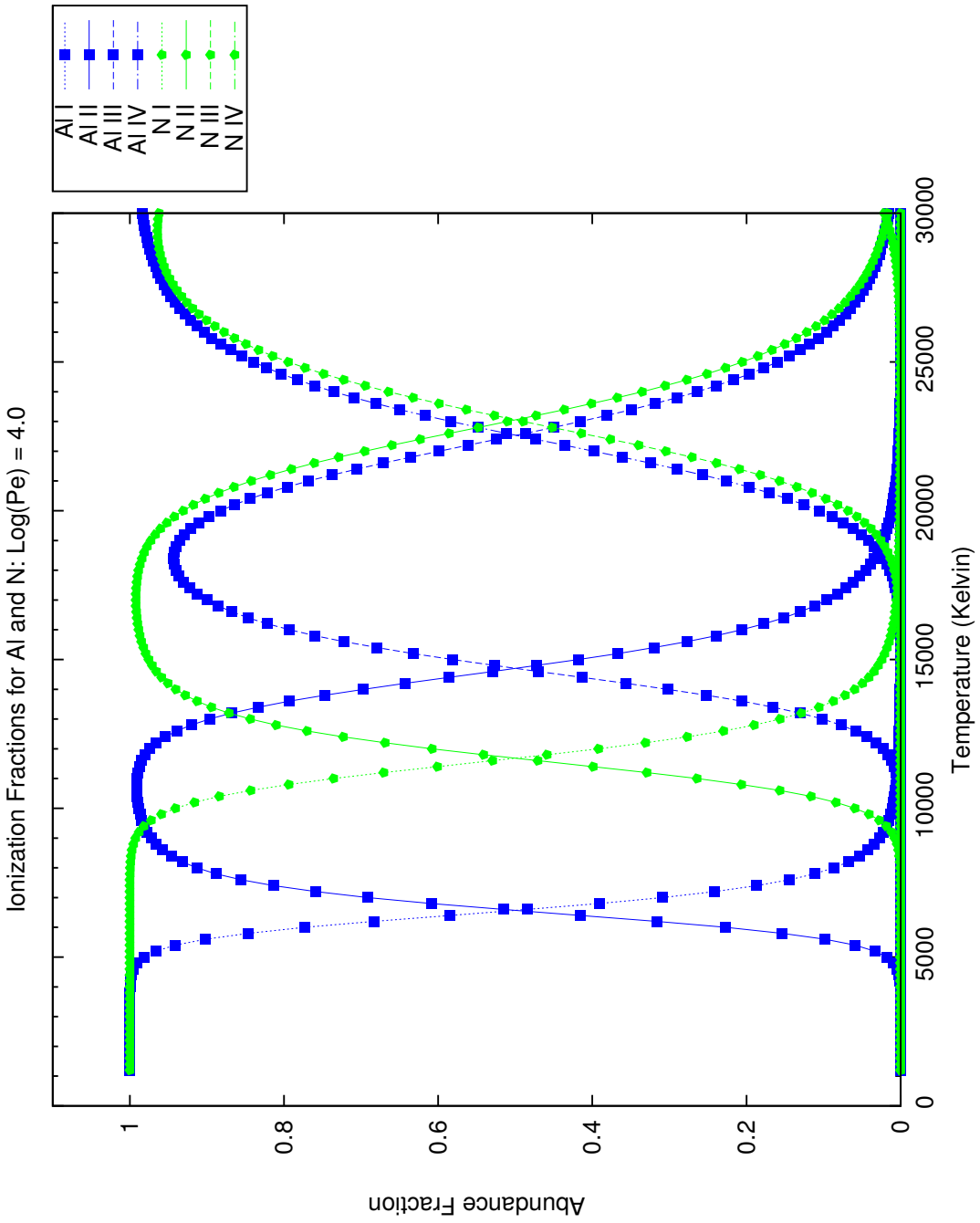

Figure D.24: Abundance ratios for the elements Al and N at a given $log(P_e) = 4.0$ varying with temperature. As T increases, it is more likely for an electron to be stripped from its parent atom, leading to higher and higher ionization states.

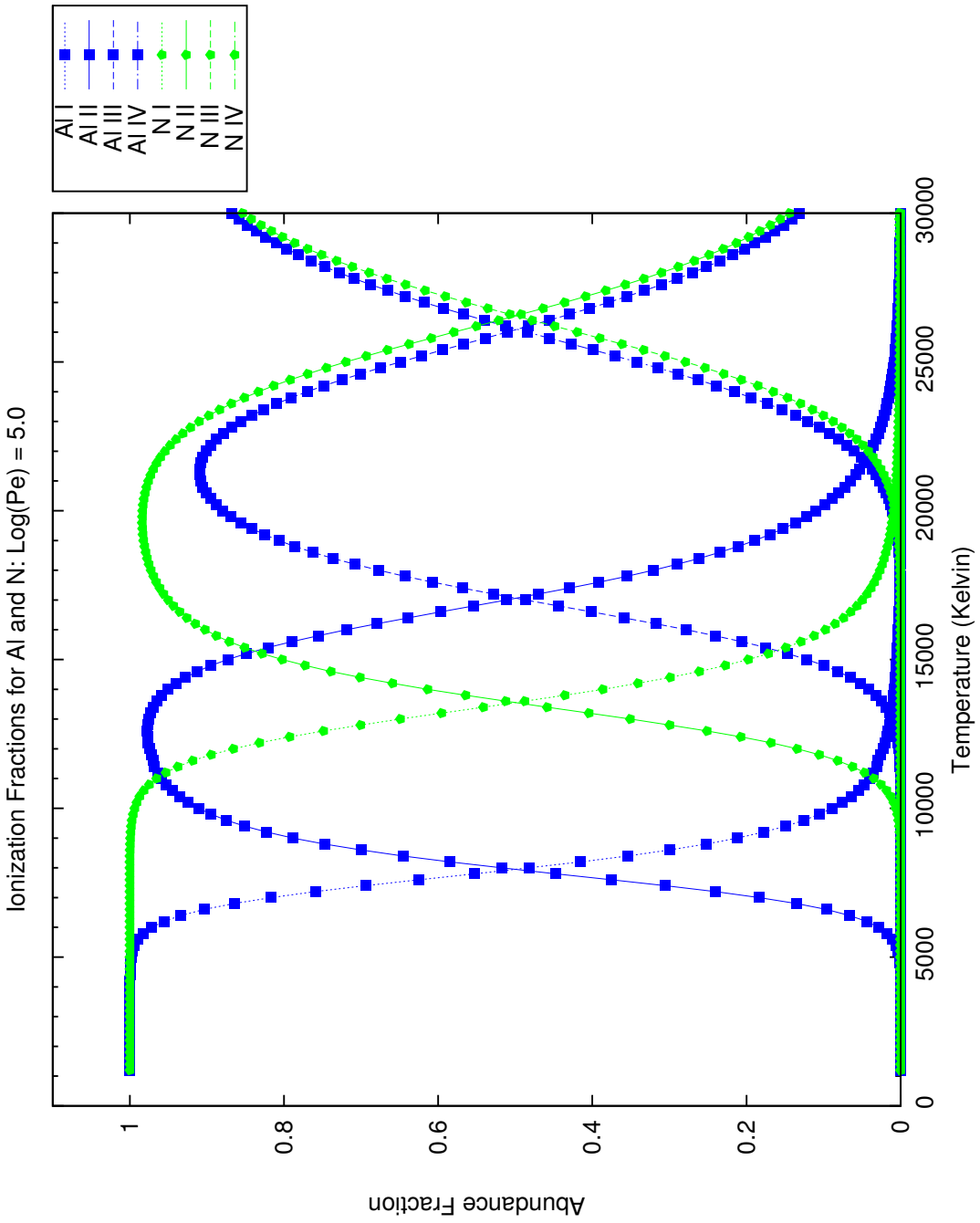

Figure D.25: Abundance ratios for the elements Al and N at a given $log(P_e) = 5.0$ varying with temperature. As T increases, it is more likely for an electron to be stripped from its parent atom, leading to higher and higher ionization states.

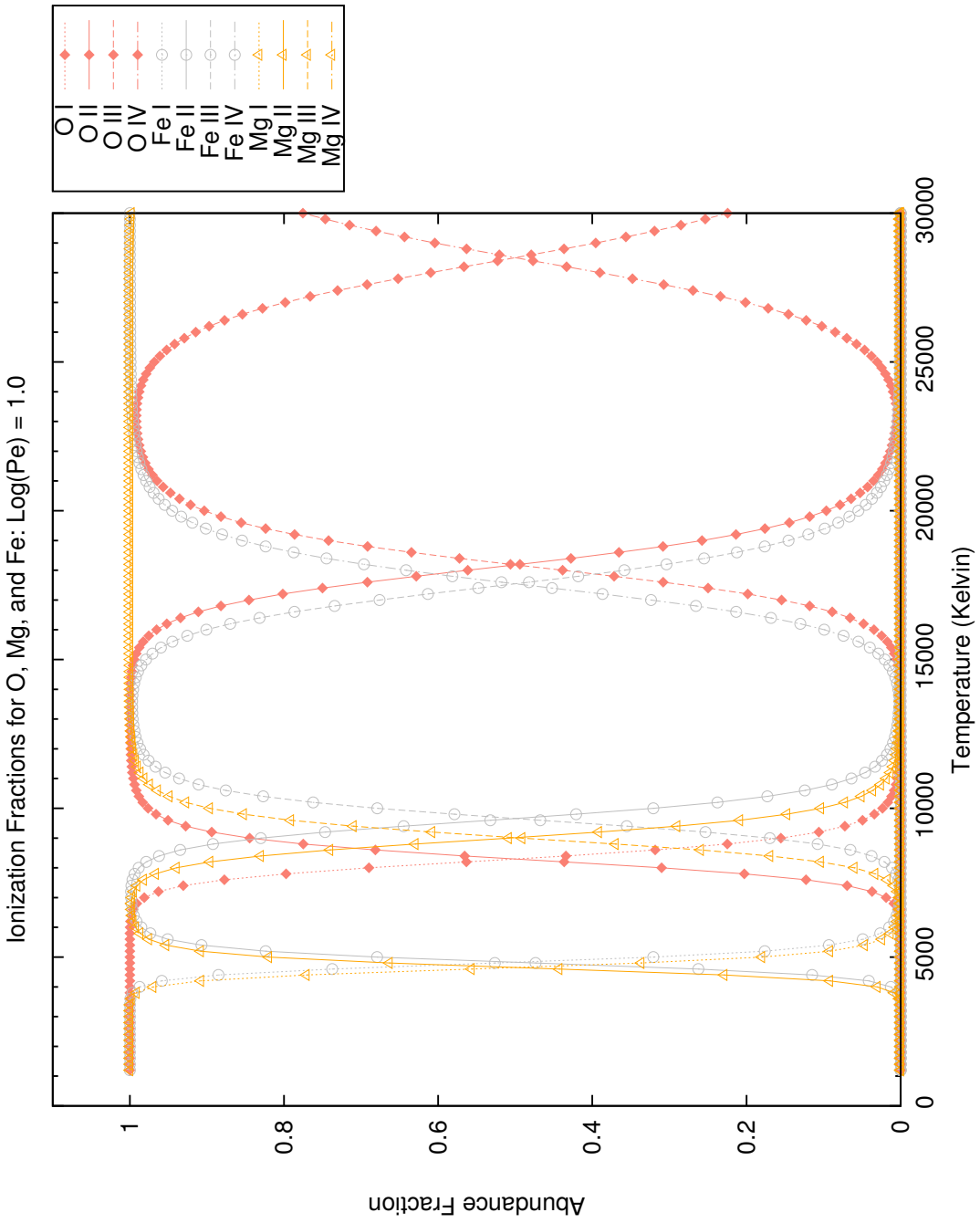

Figure D.26: Abundance ratios for the elements Mg, O, and Fe at a given $log(P_e) = 1.0$ varying with temperature. As T increases, it is more likely for an electron to be stripped from its parent atom, leading to higher and higher ionization states.

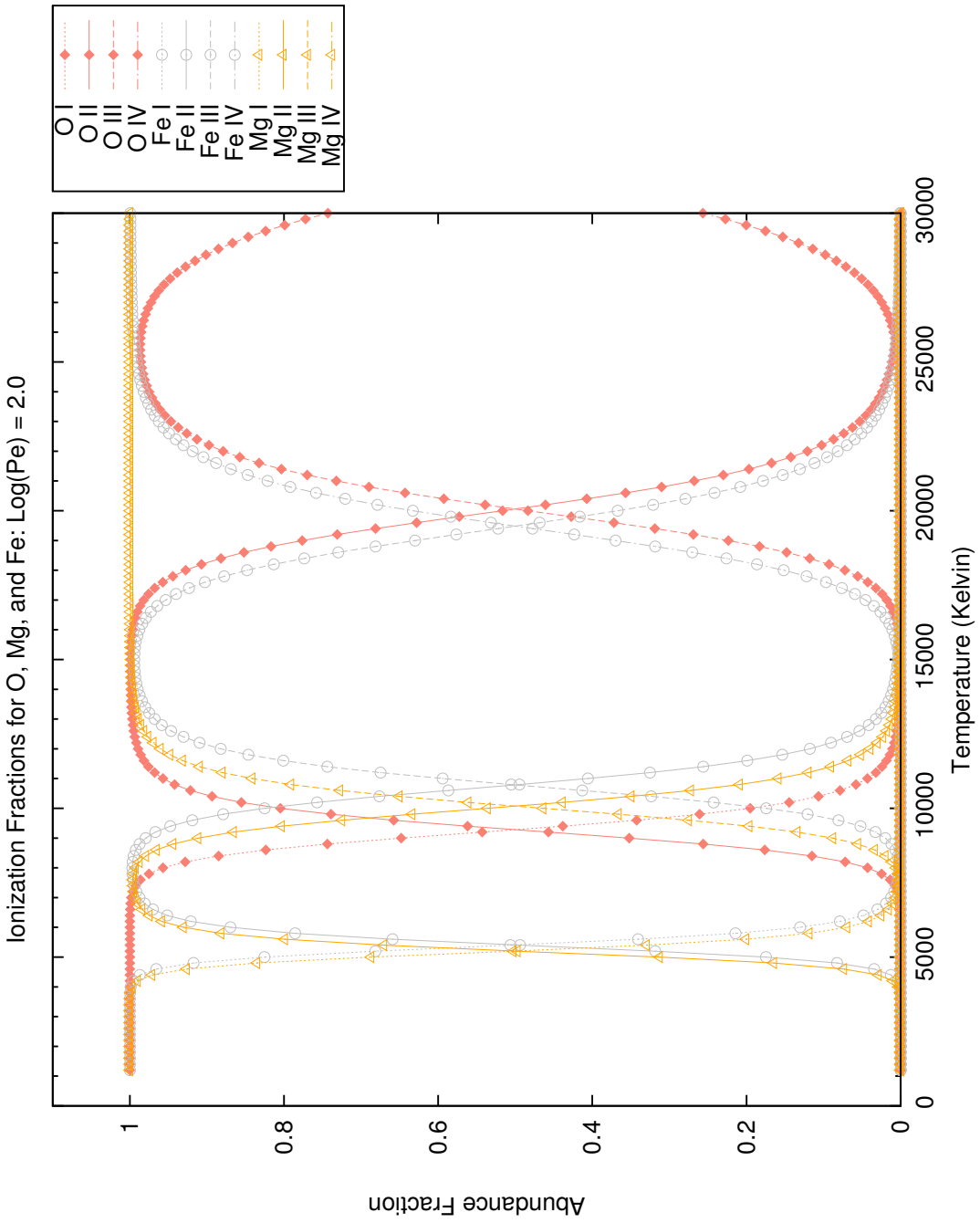

Figure D.27: Abundance ratios for the elements Mg, O, and Fe at a given $log(P_e) = 1.0$ varying with temperature. As T increases, it is more likely for an electron to be stripped from its parent atom, leading to higher and higher ionization states.

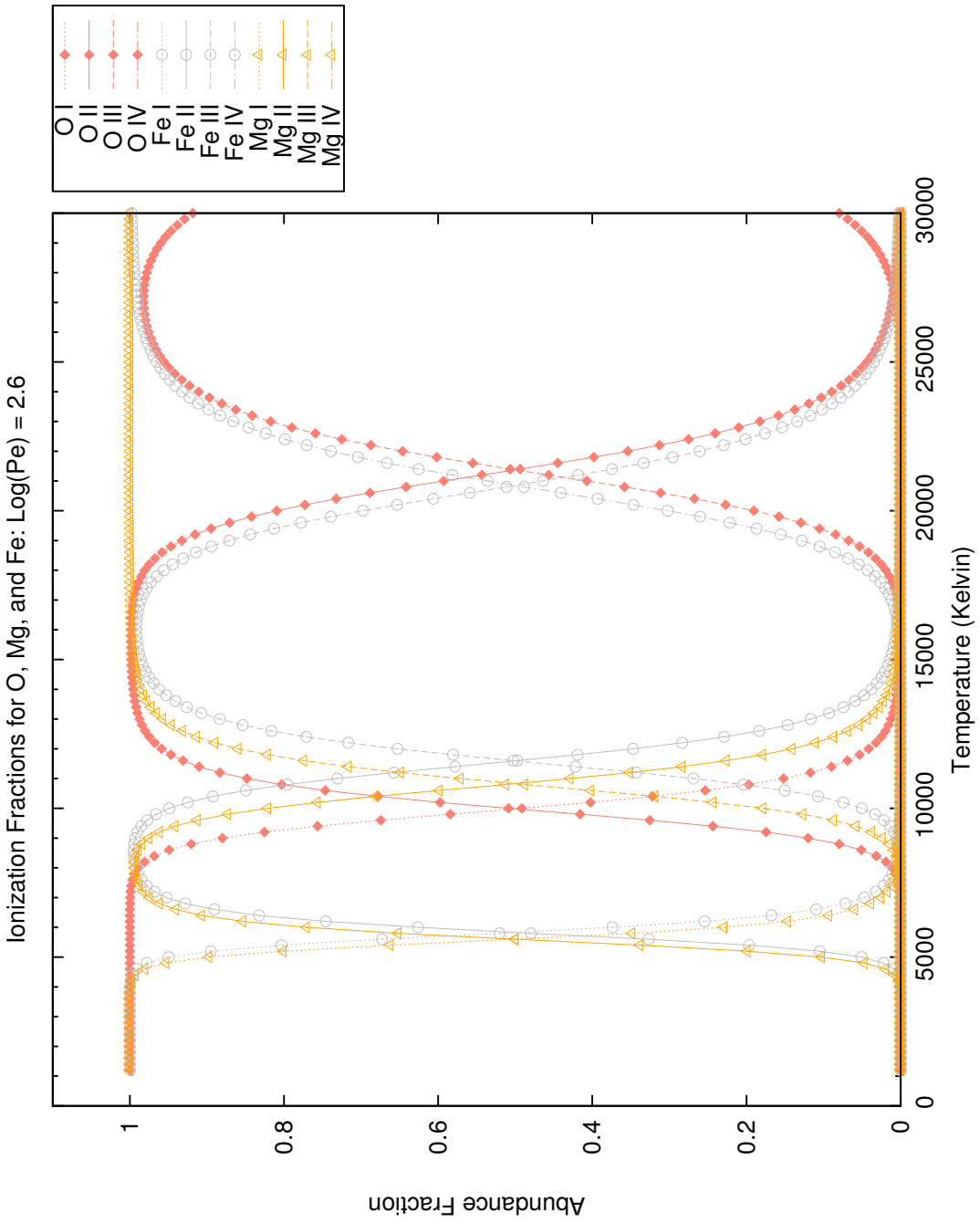

Figure D.28: Abundance ratios for the elements Mg, O, and Fe at a given $log(P_e) = 2.6$ varying with temperature. As T increases, it is more likely for an electron to be stripped from its parent atom, leading to higher and higher ionization states.

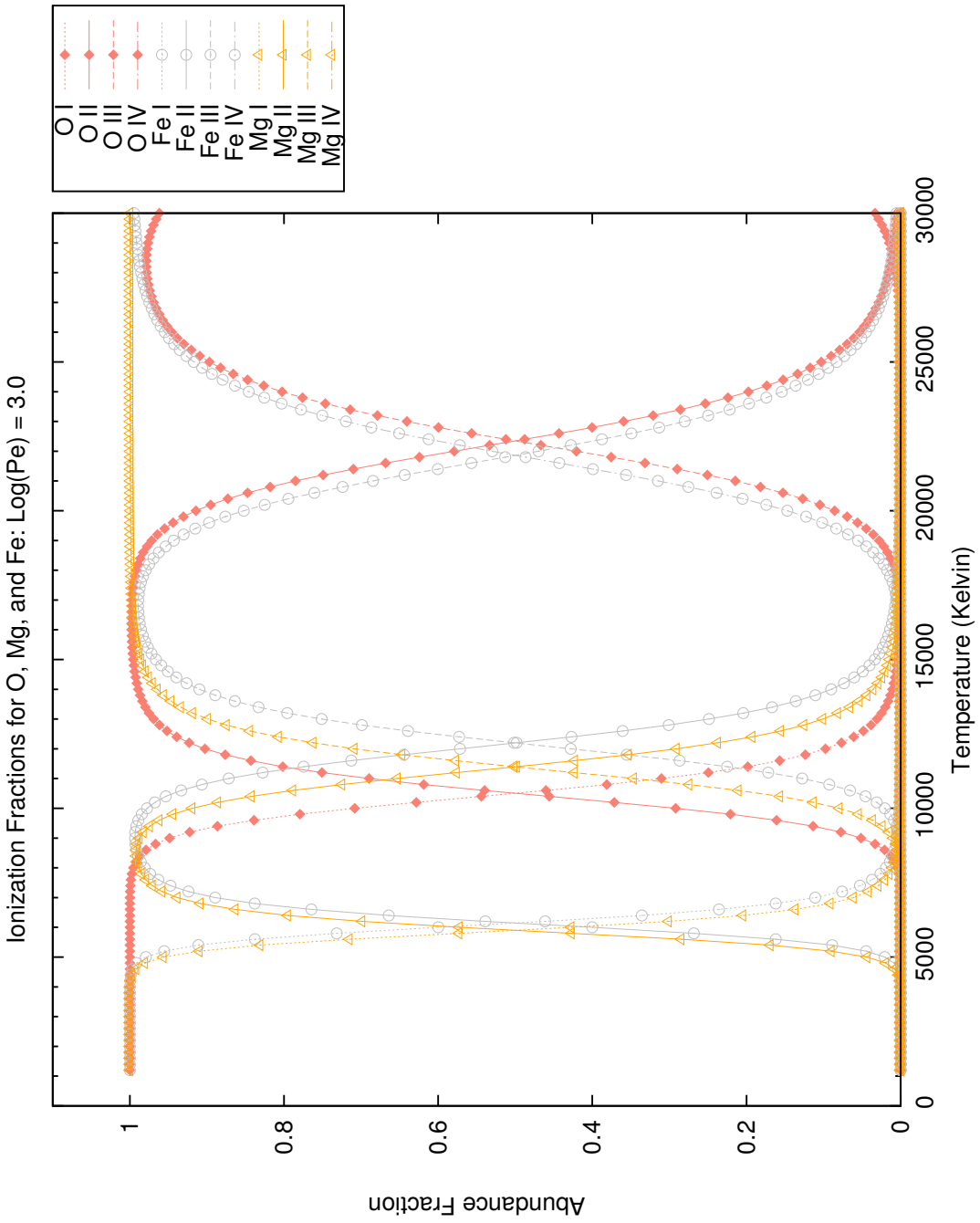

Figure D.29: Abundance ratios for the elements Mg, O, and Fe at a given $log(P_e) = 3.0$ varying with temperature. As T increases, it is more likely for an electron to be stripped from its parent atom, leading to higher and higher ionization states.

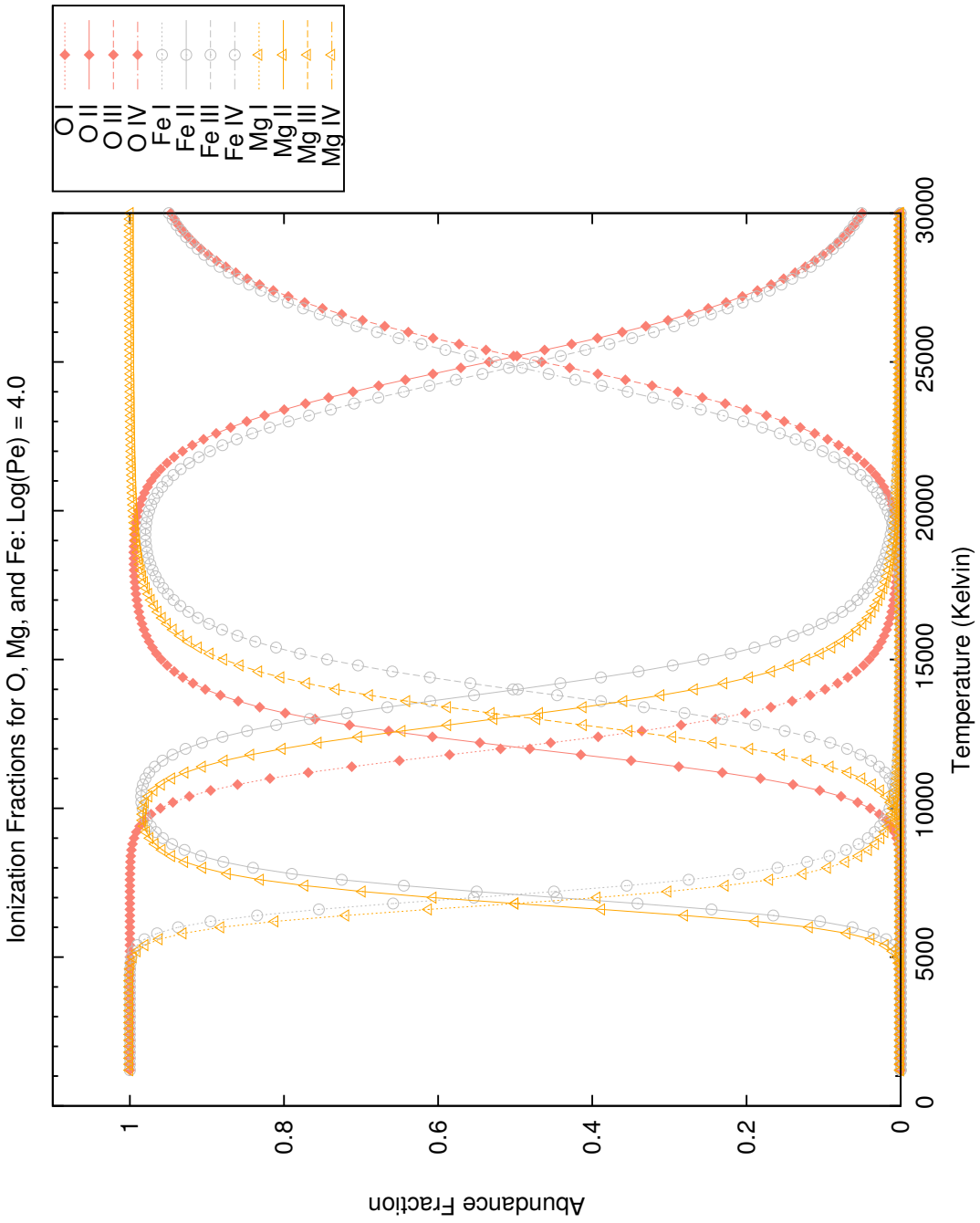

Figure D.30: Abundance ratios for the elements Mg, O, and Fe at a given $log(P_e) = 4.0$ varying with temperature. As T increases, it is more likely for an electron to be stripped from its parent atom, leading to higher and higher ionization states.

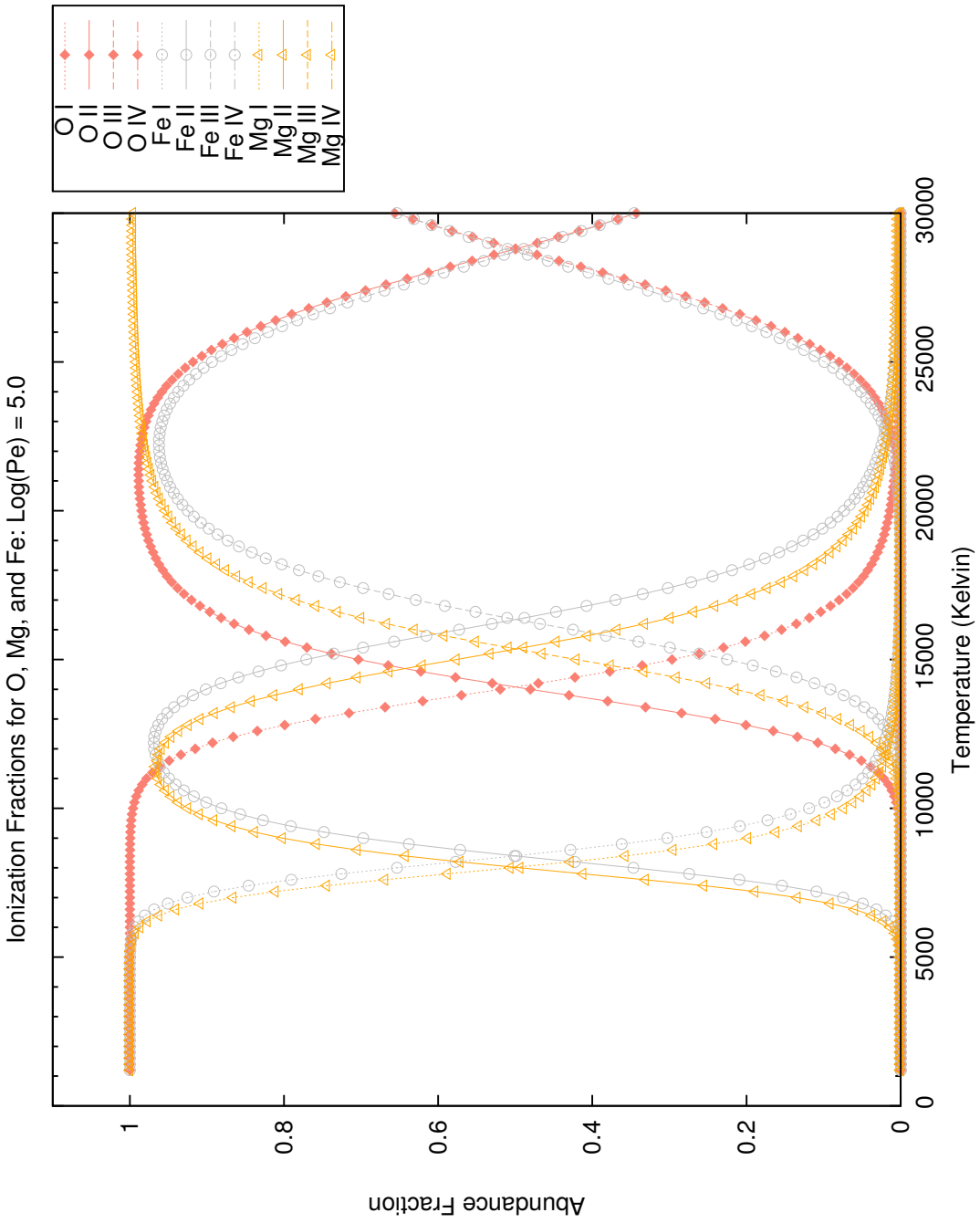

Figure D.31: Abundance ratios for the elements Mg, O, and Fe at a given $log(P_e) = 5.0$ varying with temperature. As T increases, it is more likely for an electron to be stripped from its parent atom, leading to higher and higher ionization states.

Bibliography

[1] Zombeck, M. V. *Handbook of Space Astronomy and Astrophysics* (Cambridge University Press, 1990).

[2] Batten, A. H. A new, unified interpretation of U Cephei. *Publications of the Dominion Astrophysical Observatory Victoria* **14**, 191–269 (1974).

[3] Rohde, R. Solar Radiation Spectrum (2007). URL `"http://en.wikipedia.org/wiki/File:Solar_Spectrum.png"`.

[4] Carroll, B. W. & Ostlie, D. A. *An Introduction to Modern Astrophysics* (Addison-Wesley Publishing Company, 1996).

[5] Bradstreet, D. H. & Steelman, D. P. Binary Maker 3.0 - An Interactive Graphics-Based Light Curve Synthesis Program Written in Java. In *American Astronomical Society Meeting Abstracts*, vol. 34 of *Bulletin of the American Astronomical Society*, 1224–+ (2002).

[6] Terrell, D., Mukherjee, J. & Wilson, R. E. *Binary Stars: A Pictorial Atlas* (Krieger Publishing Company, 1992).

[7] Reed, P. A. *et al.* Ultraviolet study of the active interacting binary star R Arae using archival IUE data. *Monthly Notices of the RAS* **401**, 913–923 (2010). `0909.4047`.

[8] Carpenter, E. F. U Cephei: an anomalous spectrographic result. *Astrophysical Journal* **72**, 205–220 (1930).

[9] Hardie, R. H. A Study of the Spectroscopic Binary U Cephei. *Astrophysical Journal* **112**, 542–+ (1950).

[10] Hall, D. S. A Period Study for U Cephei and Implications for the Mass-Transfer Theory. *Acta Astronomica* **25**, 1–20 (1975).

[11] Olson, E. C. *et al.* Further period changes in U Cephei. *Publications of the ASP* **93**, 464–469 (1981).

[12] Olson, E. C. U Cephei - Effects of disk, hot spot, and stream on primary eclipse light curves. *Astrophysical Journal* **241**, 257–268 (1980).

[13] Gray, D. F. *The Observation and Analysis of Stellar Photospheres.* (Cambridge University Press, 1992).

[14] Pradhan, A. K. & Nahar, S. N. *Atomic Astrophysics and Spectroscopy* (Cambridge University Press, 2011).

[15] NASA. IUE Promotional Image (2009). URL `http://ecolloq.gsfc.nasa.gov/archive/2009-Spring/images/RomanPix/IUE.jpg`.

[16] MAST IUE. Figure of IUE Satellite Scientific Instruments (2007). URL `http://archive.stsci.edu/iue/instrument.html`.

[17] McCluskey, G. E., Jr., Johnson, J., DeLeo, G.G., et al. Ultraviolet Spectroscopic Analysis of Mass Flow in the Interacting Binary U Cephei (2002).

[18] Nazarenko, V. V. & Glazunova, L. V. Two-Dimensional Hydrodynamical Modeling of Mass Transfer in Semidetached Binaries with Asynchronously Rotating Components. *Astronomy Reports* **47**, 1027–1037 (2003).

[19] Kallrath, J. & Milone, E. F. *Eclipsing Binary Stars: Modeling and Analysis* (Springer, 2009).

[20] Ceraski, W. Schreiben an den Herausgeber. *Astronomische Nachrichten* **97**, 319–+ (1880).

[21] Cannon, A. J. & Pickering, E. C. The Henry Draper catalogue 0h, 1h, 2h, and 3h. *Annals of Harvard College Observatory* **91**, 1–290 (1918).

[22] Struve, O. The Spectrographic Problem of U Cephei. *Astrophysical Journal* **99**, 222–+ (1944).

[23] Struve, O. The Problem of U Cephei. *Publications of the ASP* **75**, 207–+ (1963).

[24] Olson, E. C. Spectral Classification and Surface Gravities for Some Bright Eclipsing Binaries. *Astrophysical Journal* **153**, 187–+ (1968).

[25] Biermann, P. & Hall, D. S. A model to explain alternate period changes in Algol-like binaries. *Astronomy and Astrophysics* **27**, 249–253 (1973).

[26] Piirola, V. Polarimetric Observations of U Cephei during the Primary Eclipse. *Information Bulletin on Variable Stars* **1061**, 1–+ (1975).

[27] Hall, D. S. & Keel, W. C. The recent behavior of the period of U Cephei. *Acta Astronomica* **27**, 167–177 (1977).

[28] Kondo, Y., McCluskey, G. E. & Stencel, R. E. IUE observations of gas stream effects in the ultraviolet spectrum of U Cephei. *Astrophysical Journal* **233**, 906–912 (1979).

[29] Piirola, V. A polarimetric study of U Cephei. I. *Astronomy and Astrophysics* **90**, 48–53 (1980).

[30] Kondo, Y., Harvel, C. A. & McCluskey, G. E., Jr. IUE ultraviolet spectra of the interacting binary U Cephei. *Astrophysical Journal* **247**, 202–209 (1981).

[31] Plavec, M. J. Far-ultraviolet emission lines in U Cephei - Evidence for a hot, turbulent circumstellar envelope. *Astrophysical Journal* **275**, 251–270 (1983).

[32] McCluskey, G. E., Jr., Kondo, Y. & Olson, E. C. IUE spectroscopy of U Cephei during the mass flow outburst of 1986 June. *Astrophysical Journal* **332**, 1019–1029 (1988).

[33] Kaitchuck, R. H., Honeycutt, R. K. & Faulkner, D. R. Spectroscopic and photometric observations of transient accretion disks in U Cephei. *Astrophysical Journal* **339**, 420–433 (1989).

[34] Rafert, J. B. & Markworth, N. L. Simultaneous light and radial velocity curve solutions for U Cephei. *Astrophysical Journal* **377**, 278–284 (1991).

[35] Burnett, B. J., Etzel, P. B. & Olson, E. C. New six-color intermediate-band photometry and photometric solutions for U Cephei. *Astronomical Journal* **106**, 1627–1638 (1993).

[36] Mukherjee, J., Peters, G. J. & Wilson, R. E. Rotation of Algol binaries - a line profile model applied to observations. *Monthly Notices of the RAS* **283**, 613–625 (1996).

[37] Sahade, J., McCluskey, G. E. & Kondo, Y. *The Realm of Interacting Binary Stars* (Springer, 1993).

[38] McCluskey, G. E., Jr. & Sahade, J. Interacting Binaries. In Y. Kondo (ed.) *Exploring the Universe with the IUE Satellite*, vol. 129 of *Astrophysics and Space Science Library*, 427–444 (1987).

[39] Boyarchuk, A. A., Bisikalo, D. V., Kuznetsov, O. A. & Chechetkin, V. M. *Mass transfer in close binary stars* (CRC Press, 2002).

[40] Tatum, J. Celestial mechanics (2011).

[41] Bowers, R. L. & Deeming, T. *Astrophysics. Volume 1 - Stars* (Jones & Bartlett Publishers, 1984).

[42] Drake, J. J. From the Heart of the Ghoul: C and N Abundances in the Corona of Algol B. *Astrophysical Journal* **594**, 496–509 (2003). `arXiv:astro-ph/0308230`.

[43] Crawford, J. A. On the Subgiant Components of Eclipsing Binary Systems. *Astrophysical Journal* **121**, 71–+ (1955).

[44] Hubeny, I. A computer program for calculating non-LTE model stellar atmospheres. *Computer Physics Communications* **52**, 103–132 (1988).

[45] DeLeo, G. G. Private communication (2011).

[46] Merzbacher, E. *Quantum Mechanics* (Wiley, 1998).

[47] Jackson, J. D. *Classical Electrodynamics, 3rd Edition* (Wiley, 1998).

[48] Heald, M. A. & Marion, J. B. *Classical electromagnetic radiation, 3rd ed.* (Saunders College Publishing, 1995).

[49] Aller, L. H. *Astrophysics: The Atmospheres of the Sun and Stars* (Ronald Press, 1963).

[50] Emerson, D. *Interpreting Astronomical Spectra* (Wiley, 1999).

[51] Lorentz, H. *The theory of electrons and its applications to the phenomena of light and radiant heat: a course of lectures delivered in Columbia University, New York, in March and April, 1906* (Leipzig : B.G. Teubner ; New York : G.E. Stechert, 1916).

[52] Lee, J. F., Sears, F. W. & Turcotte, D. L. *Statistical Thermodynamics* (Addison-Wesley Pub. Co. Reading, Mass.,, 1973), 2d ed. edn.

[53] Kurucz, R. L. & Avrett, E. H. Solar Spectrum Synthesis. I. A Sample Atlas from 224 to 300 nm. *SAO Special Report* **391** (1981).

[54] Harris, D. L., III. On the Line-Absorption Coefficient due to Doppler Effect and Damping. *Astrophysical Journal* **108**, 112–+ (1948).

[55] Hummer, D. G. The Voigt function: An eight-significant-figure table and generating procedure. *Memoirs of the RAS* **70**, 1–+ (1965).

[56] Gray, D. F. Atmospheric turbulence measured in stars above the main sequence. *Astrophysical Journal* **202**, 148–164 (1975).

[57] Reiners, A. & Schmitt, J. H. M. M. On the feasibility of the detection of differential rotation in stellar absorption profiles. *Astronomy and Astrophysics* **384**, 155–162 (2002).

[58] Hubeny, I. & Lanz, T. Non-LTE line-blanketed model atmospheres of hot stars. 1: Hybrid complete linearization/accelerated lambda iteration method. *Astrophysical Journal* **439**, 875–904 (1995).

[59] Wecht, K. *Determination of mass loss and mass transfer rates of Algol (Beta Persei) from the analysis of absorption lines in the UV spectra obtained by the IUE satellite.* Ph.D. thesis, Lehigh University (2006).

[60] Prialnik, D. *An Introduction to the Theory of Stellar Structure and Evolution* (Cambridge University Press, 2000).

[61] Peréz Calpena, A., Pepoy, J., Wamsteker, W. & Harris, R. A. *IUE spacecraft operations. Final report.* (1997).

[62] Nichols, J. S. & Linsky, J. L. The Final Archive and Recalibration of the International Ultraviolet Explorer (IUE) Satellite. *Astronomical Journal* **111**, 517–+ (1996).

[63] McAlister, H. A. *et al.* First Results from the CHARA Array. I. An Interferometric and Spectroscopic Study of the Fast Rotator α Leonis (Regulus). *Astrophysical Journal* **628**, 439–452 (2005). `arXiv:astro-ph/0501261`.

[64] Hubeny, I., Harmanec, P. & Stefl, S. How strong is the evidence of superionization and large mass outflows in B/Be stars? II - The C IV and SI IV lines in the UV spectra of V 767 Cen, omicron And, Theta CrB, Lambda Eri, and 59 CYG. *Bulletin of the Astronomical Institutes of Czechoslovakia* **37**, 370–382 (1986).

[65] Novotny, E. *Introduction to Stellar Atmospheres and Interiors* (Oxford University Press, 1973).

[66] Lodders, K. Solar System Abundances and Condensation Temperatures of the Elements. *Astrophysical Journal* **591**, 1220–1247 (2003).

[67] Ralchenko, Y., Kramida, A. E., Reader, J. & Team, N. A. *NIST Atomic Spectra Database* (National Institute of Standards and Technology, 2008).

[68] Kurucz, R. L. Kurucz/linelists (2008). URL `http://kurucz.harvard.edu/`.

Vita

Peter Robert Tupa was born in Warrensville Heights, Ohio on April 28, 1981 to Robert and Terry Tupa. Peter was homeschooled through highschool. He graduated from Hiram College (Hiram, OH) with a B. A. in 2005, majoring in physics and a minor in international studies of Asia & Japan and earning the honors of magna cum laude and phi beta kappa membership. He received a M. S. in phyics from Lehigh University (Bethlehem, PA) in 2008. He taught as a teaching assistant for the introductory physics course at Lehigh for six years. He married Hisako Masuda in 2006 and has two daughters, Katharine and Abigail.